

**Horizontal, Oil-Water Flows
in the
Dual Continuous Flow Regime**

By

Jonathon Lovick

March 2004

A thesis submitted for the degree of
Doctor of Philosophy of the University of London

Department of Chemical Engineering
University College London
Torrington Place
London WC1E 7JE, UK



ABSTRACT

The research presented in this thesis is concerned with the flow behaviour of two-phase, liquid-liquid, oil-water flow through horizontal pipes. The test liquids used were oil (density 828kg/m^3 , viscosity $6 \times 10^{-3}\text{ Pa s}$) and water, with experiments carried out in a purpose built test facility with a stainless steel pipe (internal dia. 38mm, length 8m). Visual observation of the flow was possible at low mixture velocities through a 1m transparent pipe at the end of the test section. At higher mixture velocities local probes were used for flow pattern identification. These local probes were a conductivity probe for identifying the continuous phase, and a high frequency impedance probe for measuring local phase distribution. A dual sensor impedance probe was also developed for measuring local drop velocity and also the drop chord length distributions. Pressure gradient was also measured using a differential pressure transducer, and in-situ phase fractions were obtained using Quick Closing Valves.

Experimental results show that the dual continuous flow regime, where both phases retain their continuity while there is mixing at the interface, dominates at all input oil fractions at low mixture velocities and intermediate oil fractions at high mixture velocities. In general the pressure drop of the two-phase mixture is lower than that of single phase oil. At higher mixture velocities a minimum in pressure gradient appeared at high oil fractions perhaps as a combination of the drag reduction phenomenon and the relative fraction of the oil and water layers in the pipe. At the highest mixture velocity this minimum was at the boundary of fully dispersed oil continuous flow with dual continuous flow. Velocity ratios are shown to increase with increasing oil fraction at low mixture velocities, with this trend reversing at high mixture velocities. These trends in the pressure gradient and velocity ratio can be explained using the phase distribution diagrams, with the interfacial curvature greatly affecting velocity ratio. Local chord length data shows that, in general, drop sizes decrease with increasing distance from the interface and that oil drops tend to be slightly larger than water drops. Mixture velocity did not significantly affect the drop size of either phase in dual continuous flow. A modified version of the two-fluid model was suggested for dual continuous flow that treats the upper and lower layers as dispersions and uses

experimental entrainment to calculate their properties. Better predictions were obtained when friction factors that accounted for the drag reduction phenomenon were used to calculate wall shear stresses.

ACKNOWLEDGEMENTS

Foremost I would like to thank Dr Panagiota Angeli, my supervisor during my Ph.D. She has taken my knowledge of two-phase flow from zero to what you see in the following pages. She has also given guidance to the direction of my research, and by applying gentle but constant pressure, ensured completion of my work.

I would also like to thank all the members of the mechanical workshop in the Department, especially Barry Bartram who originally built the test rig, and Martin Town who has always been able to 'see me right' whenever I have needed something doing. Thanks also goes to the electronic workshop in the department, especially Sarah Bailey whose ability to produce the impedance hardware, given the vaguest of descriptions, and then be on hand for the odd bit of soldering has been invaluable.

My research colleague, Jason Lum, has been a constant source of help during the final two years of my research. His assistance as an extra set of hands in some of the more involved experiments, and as someone to chat to during the more boring ones has probably kept me sane in the basement lab. His maths isn't bad either! I hope that the team working culture in the group remains.

To everyone else in the department who has helped me in one way or another, whether it be with learning Fortran, Matlab, or just for a gossip in the corridor, thank you very much.

Lastly I would like to thank my parents. I suspect that they are not totally sure what I have been doing for the last 4 years, but they have been happy to support me regardless. And also to Ros, who has been a great support to me during my research, and been a fantastic tonic to the emotional rollercoaster that is research; I am just annoyed that she finished first!

CONTENTS

CONTENTS	1
LISTS OF TABLES AND FIGURES	4
1. INTRODUCTION	14
1.1 Objectives.....	15
1.2 Thesis Structure.....	16
2. LITERATURE REVIEW.....	17
2.1 Liquid-Liquid Flows	17
2.1.1 <i>Separated flow</i>	19
2.1.2 <i>Dual Continuous Flow</i>	20
2.1.3 <i>Dispersed Flow</i>	24
2.1.4 <i>Phase Inversion</i>	26
2.2 Drop Size Distribution	28
2.2.1 <i>Drop Break-up</i>	28
2.2.2 <i>Drop Coalescence</i>	34
2.2.3 <i>Drop Distribution</i>	37
2.3 Chord Length / Drop Diameter Transformation	41
2.3.1 <i>Clarke and Turton (1988)</i>	43
2.3.2 <i>Probability Apportioning Method (PAM)</i>	46
2.3.3 <i>Finite Element Method (FEM)</i>	47
2.3.4 <i>Probability Apportioning Method 2 (PAM2)</i>	49
2.4 Pressure Gradient and Hold-up Modelling	51
2.4.1 <i>Homogeneous Model</i>	53
2.4.2 <i>Two-fluid Model</i>	55
3. INSTRUMENTATION AND EXPERIMENTAL METHODS.....	66

3.1 Experimental Flow Facility.....	66
3.2 Pressure Gradient Measurements – Pressure Transducers.....	69
3.3 Average In-situ Hold-up and Slip Ratio - Quick Closing Valves (QCV).....	70
3.4 In-situ Flow Behaviour - Local Probes	70
3.4.1 High Frequency Impedance Probes – Phase Distribution	71
3.4.2 High Frequency Dual Impedance Probe–Drop Size Distribution...	75
3.4.2.1 Drop Velocity Measurement–Cross-correlation	76
3.4.2.2 Chord length measurement	77
3.4.2.3 Chord Length to Drop Size Conversion	79
3.4.3 Conductivity Probes – Phase Continuity	79
4. EXPERIMENTAL RESULTS.....	91
4.1 Flow Patterns.....	91
4.2. Flow Development.....	92
4.3 Pressure Gradient Experiments	96
4.3.1 Single phase pressure gradient	96
4.3.2 Pre-wetting comparisons	97
4.3.3 Mixture velocity comparisons	98
4.4 Velocity Ratio and Phase Distribution.....	101
4.5 Conclusions	104
5. CHORD LENGTH/DROP SIZE AND DISTRIBUTION RESULTS	125
5.1 Velocity Profiles.....	125
5.2. Chord Length to Drop Diameter Transformations.....	127
5.3 Chord Length Distributions	128
5.4. Comparisons With Models.....	131
6. PREDICTIVE MODEL FOR DUAL CONTINUOUS FLOW	150

6.1. Model Development.....	150
6.2. Comparisons of Experimental Pressure Gradient Data with the Predictions of the Two-Fluid Model with Entrainment	156
6.2.1. <i>Pressure gradient predictions</i>	156
6.2.1.1. <i>Flat interface</i>	157
6.2.1.2. <i>Curved interface</i>	159
6.3. Comparisons of Experimental Velocity Ratio Data with the Predictions of the Two-Fluid Model with Entrainment.....	160
6.3.1. <i>Flat interface</i>	160
6.3.2. <i>Curved interface</i>	161
7. CONCLUSIONS.....	170
7.1 Experimental Results	170
7.1.1 <i>Flow patterns</i>	171
7.1.2 <i>Pressure gradient</i>	171
7.1.3 <i>Velocity Ratio and Phase Distribution</i>	172
7.1.4 <i>Drop size distributions</i>	172
7.1.5 <i>Modified two-fluid model</i>	174
7.2 Future Work	175
NOMENCLATURE.....	177
REFERENCES.....	181
APPENDIX A1 IMPEDANCE PROBE CODE	192
APPENDIX A2 CROSS-CORRELATION CODE.....	194
APPENDIX A3 SQUARE WAVE TRANSFORMATION CODE	197
APPENDIX A4 COMPLETE PHASE DISTRIBUTION DATA	201
APPENDIX A5 COMPLETE CHORD DISTRIBUTION DATA	209
APPENDIX A6 MODIFIED 2-FLUID MODEL CODE	221

LIST OF FIGURES

Section 2

Fig. 2.1. Flow patterns as described by Trallero (1995)	60
Fig. 2.2. Flow pattern map by Charles et al. (1961).....	61
Fig. 2.3. Flow pattern map by Guzhov et al. (1973)	61
Fig. 2.4. Velocity profile of oil-water flow showing water flowing faster than oil ($S=0.5$) (Ng, 2002).....	62
Fig. 2.5. Flow pattern map by Nädler and Mewes (1995)	62
Fig. 2.6. Pressure gradient data by Nädler and Mewes (1995), where j_f is the mixture velocity.....	63
Fig. 2.7. Pressure gradient data by Soleimani (1997) showing peak at phase inversion. .	63
Fig. 2.8. Pressure gradient against input oil concentration by Guzhov et al. (1973)	64
Fig. 2.9. Relevant geometric parameters when a sensor tip is cutting a drop (Weimer et al., 1985)	64
Fig. 2.10. Relevant dimensions in Probe-droplet interaction (Clarke and Turton, 1988). 65	
Fig. 2.11. Geometry used for modelling the dual continuous flow pattern (Guzhov and Medvedev, 1971)	65

Section 3

Fig. 3.1a. Experimental liquid-liquid flow facility	81
Fig. 3.1b. Photograph of measurement of test section. Measurement location at far end above PC. Inlet to the left of picture	82

Fig. 3.1c. Photograph of experimental facility showing storage tanks, separator, and inlet to test section. Measurement location to the right of picture	82
Fig. 3.2. Photograph of modified 'T-piece' where the oil and water phases come together	83
Fig. 3.3. Pressure tapping port	83
Fig. 3.4. Assembly for pressure gradient measurements	84
Fig. 3.5. Electrical field around impedance probe tip	84
Fig. 3.6. Measuring cycles of impedance probe.....	85
Fig. 3.7. Low sample frequency allowing drops to go undetected	85
Fig. 3.8. High sample frequency with many cycles per drop.....	85
Fig. 3.9. Wire used for high frequency impedance probe	86
Fig. 3.10a. Impedance probe mounting.....	87
Fig. 3.10b. Photograph of impedance probe mounting between two sections of pipe	87
Fig. 3.11. Measurement planes for impedance probe	88
Fig. 3.12. Dual impedance and conductivity probe mounting	88
Fig. 3.13. Cross-correlation function against lag time, with time delay between sensors at $6000\mu s$	89
Fig. 3.14. Probe tip interaction with interface (Cartellier and Achard, 1991)	89
Fig. 3.15. Signal from the impedance probe in the raw and processed square wave form.....	90

Section 4

Fig. 4.1a-d. Phase distribution diagram at mixture velocity 1m/s and input oil fraction 50%, at different distances from test section inlet	105
Fig. 4.2a-d. Phase distribution diagram at mixture velocity 2m/s and input oil fraction 72%, at different distances from test section inlet	106
Fig. 4.3. Profile of conductivity probe data for 60% input oil fraction, 0.8m/s mixture velocity.....	107
Fig. 4.4. Flow pattern map for current study	107
Fig. 4.5. Phase distribution diagram at mixture velocity 0.8m/s and input oil fraction 80%	108
Fig. 4.6. Phase distribution diagram at mixture velocity 1.5m/s and input oil fraction 68%	108
Fig. 4.7. Phase distribution diagram at mixture velocity 2 m/s and input oil fraction 90%	109
Fig. 4.8a Photograph of Stratified Wavy flow.....	110
Fig. 4.8b. Photograph of Dual Continuous flow pattern with low entrainment.....	110
Fig. 4.8c. Photograph of Dual Continuous flow pattern with increased entrainment.....	110
Fig. 4.8d. Photograph of Dual continuous flow pattern, referred to in previous studies as a Dispersion of oil in water and water in oil	110
Fig. 4.9. Entrainment concentration in the upper (oil continuous) and lower (water continuous) phases during dual continuous flow at different mixture velocities	111
Fig. 4.10. Comparison of flow pattern map from current study, with that of Laflin & Oglesby (1976).....	112

Fig. 4.11. Comparison of flow pattern map from current study, with that of Malinowsky (1975).....	112
Fig. 4.12. Friction factor vs. Reynolds number for single phase flows	113
Fig. 4.13. Pressure gradient comparison for oil and water pre-wetted pipes at mixture velocity 2m/s.....	114
Fig. 4.14. Pressure gradient comparison for oil and water pre-wetted pipes at mixture velocity 3m/s.....	114
Fig. 4.15. Pressure gradient comparisons for low mixture velocities	115
Fig. 4.16. Pressure gradient comparisons for high mixture velocities.....	115
Fig. 4.17a. Phase distribution diagram at mixture velocity 1.5m/s and input oil fraction 50%	116
Fig. 4.17b. Phase distribution diagram at mixture velocity 1.5m/s and input oil fraction 68%	116
Fig. 4.17c. Phase distribution diagram at mixture velocity 1.5m/s and input oil fraction 80%	116
Fig. 4.18. Phase distribution diagram at mixture velocity 2.5m/s and input oil fraction 80%	117
Fig. 4.19. Phase distribution diagram at mixture velocity 2.5m/s and input oil fraction 50%	117
Fig. 4.20. Phase distribution diagram at mixture velocity 2m/s and input oil fraction 10%	118
Fig. 4.21. Comparison of in-situ oil fraction measured by the QCVs and the impedance probe diagrams for different mixture velocities Dotted lined indicate +/- 15% difference	118

Fig. 4.22. Velocity ratio for low mixture velocities. $S > 1$ indicates oil flowing faster than water; $S < 1$ indicates oil flowing slower than water.....	119
Fig. 4.23. Velocity ratio for intermediate mixture velocities. $S > 1$ indicates oil flowing faster than water; $S < 1$ indicates oil flowing slower than water.....	119
Fig. 4.24. Velocity ratio for high mixture velocities. $S > 1$ indicates oil flowing faster than water; $S < 1$ indicates oil flowing slower than water.....	120
Fig. 4.25a. Phase distribution diagram at mixture velocity 1.5m/s and input oil fraction 20%	121
Fig. 4.25b. Phase distribution diagram at mixture velocity 1.5m/s and input oil fraction 50%	121
Fig. 4.25c. Phase distribution diagram at mixture velocity 1.5m/s and input oil fraction 80%	121
Fig. 4.26a. Phase distribution diagram at mixture velocity 2m/s and input oil fraction 68%	122
Fig. 4.26b. Phase distribution diagram at mixture velocity 2.5m/s and input oil fraction 68%	122
Fig. 4.27a. Phase distribution diagram at mixture velocity 2m/s and input oil fraction 80%	123
Fig. 4.27b. Phase distribution diagram at mixture velocity 2.5m/s and input oil fraction 80%	123
Fig. 4.28. Velocity ratio at 1m/s mixture velocity compared to data from literature for dual continuous flow.....	124

Section 5

Fig. 5.1. Velocity profile and phase distribution diagram for mixture velocity 2.5m/s, input oil concentration 80%	136
--	-----

Fig. 5.2. Velocity profile and phase distribution diagram for mixture velocity 2.5m/s, input oil concentration 20%	137
Fig. 5.3. Velocity profile and phase distribution diagram for mixture velocity 2m/s, input oil concentration 50%	138
Fig. 5.4. Graph of drop velocity against continuous phase velocity for oil and water drops.....	139
Fig. 5.5. Raw data and data transformed to a square wave.....	139
Fig. 5.6. Chord and derived diameter distributions for a system with initial unimodal particle size distribution at size 10.....	140
Fig. 5.7. Chord and derived diameter distributions for a system with initial bimodal particle size distribution at sizes 5 and 10	140
Fig. 5.8. Chord and derived diameter distributions for an experimental chord distribution	141
Fig. 5.9. Chord length distribution for mixture velocity 2.5m/s, input oil concentration 50 and heights 2mm, 14mm, 22mm, 32mm from the bottom of the pipe	142
Fig. 5.10. Chord length distribution for mixture velocity 2 m/s, input oil concentration 50 %, and heights 2 mm, 16 mm, 26 mm, and 34 mm from the bottom of the pipe.....	143
Fig. 5.11. The effect of the distance from the interface on chord length medians for all mixture velocities and input oil concentrations	144
Fig. 5.12. The effect of the distance from the interface on chord length d_{95} values for all mixture velocities and input oil concentrations	144
Fig. 5.13. The effect of continuous phase velocity on the chord distribution median for all mixture velocities and input oil concentrations	145

Fig. 5.14. The effect of continuous phase velocity on the chord distribution d_{95} values for all mixture velocities and input oil concentrations.....	145
Fig. 5.15. Rosin-Rammler distribution fit to 2m/s mixture velocity, 68% input oil concentration, 8mm from the bottom of the pipe	146
Fig. 5.16. Log-normal distribution fit to 2.5m/s mixture velocity, 68% input oil concentration, 10mm from the bottom of the pipe	146
Fig. 5.17. Log-normal distribution fit to 2.5m/s mixture velocity, 50% input oil concentration, 32mm from the bottom of the pipe	147
Fig. 5.18. Comparisons of the experimental maximum drop sizes with predictions of literature models for fully dispersed flow at 2m/s and 2.5m/s mixture velocities and 20% input oil fraction I	147
Fig. 5.19. Vertical concentration gradient of chord distribution for the Karabelas (1977) model and experimental data for 2m/s mixture velocity and 20% input oil concentration.....	148
Fig. 5.20. Vertical concentration gradient of chord distribution for water drops in oil for the Karabelas (1977) model and experimental data for 2m/s mixture velocity and 50% input oil concentration	148
Fig. 5.21. Vertical concentration gradient of chord distribution for oil drops in water for the Karabelas (1977) model for 2m/s mixture velocity and 50% input oil concentration.....	149
Section 6	
Fig. 6.1. Diagram of dual continuous flow, and key for symbols used in eqs. (6.1) & (6.2).....	163
Fig. 6.2. Comparison between different dispersed phase viscosity correlations used in the homogeneous model	163

Fig. 6.3a. Interfacial curvature (curved up) with $X < r$	164
Fig. 6.3b. Interfacial curvature (curved up) with $X > r$	164
Fig. 6.3c. Interfacial curvature (curved down).....	165
Fig. 6.4. Comparison of experimental pressure gradient data and predictions of the homogeneous model using different dispersed phase viscosity correlations at a mixture velocity of 1.5m/s	165
Fig. 6.5. Pressure gradient predictions for the Theissing (1980) correlation.....	166
Fig. 6.6. Comparison of experimental pressure gradient data with the model predictions for different interfacial shear stress terms at 1.5m/s mixture velocity.....	166
Fig. 6.7. Comparison of experimental pressure gradient data with the model predictions for different phase friction factors at 1.5m/s mixture velocity	167
Fig. 6.8. Comparison of experimental pressure gradient with the model predictions for different phase friction factors at 1m/s mixture velocity	167
Fig. 6.9. Comparison of experimental pressure gradient data with the model predictions for curved interface with 0.038m radius at 1.5m/s mixture velocity	168
Fig. 6.10. Comparison of experimental pressure gradient data with the model predictions for curved interface with 0.019m radius at 1.5m/s mixture velocity	168
Fig. 6.11. Comparison of experimental velocity ratio data with the model predictions at 1.5m/s mixture velocity	169
Fig. 6.12. Comparison of experimental velocity ratio data with the model predictions for curved interface with 0.038m radius at 1.5m/s mixture velocity.....	169

Appendix A4

Phase distribution diagrams for 0.8m/s.....	201
---	-----

Phase distribution diagrams for 1m/s.....	202
Phase distribution diagrams for 1.5m/s.....	203
Phase distribution diagrams for 2m/s.....	205
Phase distribution diagrams for 2.5m/s.....	207
Phase distribution diagrams for 3m/s.....	208

Appendix A5

Chord distributions 2.5m/s 80% input oil concentration	209
Chord distributions 2.5m/s 68% input oil concentration	210
Chord distributions 2.5m/s 50% input oil concentration	211
Chord distributions 2.5m/s 20% input oil concentration	212
Chord distributions 2m/s 80% input oil concentration	213
Chord distributions 2m/s 68% input oil concentration	214
Chord distributions 2m/s 50% input oil concentration	215
Chord distributions 2m/s 20% input oil concentration	216
Chord distributions 1.5m/s 80% input oil concentration	217
Chord distributions 1.5m/s 68% input oil concentration	218
Chord distributions 1.5m/s 50% input oil concentration	219
Chord distributions 1.5m/s 20% input oil concentration	220

LIST OF TABLES

Section 2

Table. 2.1. Summary of studies carried out at the dual continuous flow pattern..... 59

Section 3

Table. 3.1. Properties of oil used in study..... 66

Section 6

Table 6.1 Geometric parameters used in the model to account for curved interface 170

1. INTRODUCTION

Two-phase flows, liquid-liquid or gas-liquid, occur in many applications in the process industries. Gas-liquid flows occur in distillation columns, two-phase reactors and heat exchangers, while liquid-liquid flows occur in emulsifiers, two-phase reactors with immiscible liquid catalysts and in the petroleum industry. It is this latter case that this thesis is concerned with. During the production of crude oil, it is often the case that oil is brought to the surface with quantities of natural gas and water. The study of two-phase liquid-liquid systems can also offer insight into the more complex three or four phase flows.

In previous years gas-liquid flows have been the focus of much attention, mainly driven by the nuclear industry where steam-water flow occurs in cooling systems. This research has produced large data banks for many different system conditions, and led to the development of flow pattern boundary and pressure gradient predictive models. Some of the earliest liquid-liquid flow research was carried out in the early 1960s when it was hoped that the addition of water to single phase oil would help reduce pressure gradient (Charles et al., 1961). The interest increased again in the 1990s with the need to improve the predictive models for pressure gradient and hold-up in multiphase pipelines. These models required that the oil and water cannot be simply assumed as one homogeneous mixture and that the details of the flow pattern must be considered in determining the mixture behaviour.

As the two liquids flow through a horizontal pipe, different flow patterns can occur depending on the mixture velocity and phase fractions. At low mixture velocities the two phases flow separately with the less dense phase flowing at the top of the pipe. This type of flow is called *separated flow*. As the mixture velocity increases droplets of each phase start to form in the continuum of the other phase resulting in mixing at the interface. As the mixture velocity increases further the degree of interfacial dispersion increases until it reaches the top or bottom of the pipe. Finally at the highest mixture velocities one phase becomes completely dispersed within the other. This flow pattern is called *dispersed flow*. The focus of this thesis is on the partially dispersed flow pattern, which falls between totally separated flow and fully dispersed

flow. This flow pattern has been called *dual continuous flow* as each phase retains its continuity at the top and bottom of the pipe but with some of the opposite phase dispersed in it. Investigators have identified different flow patterns depending on the degree of entrainment of one phase into the other, without, however, providing any quantitative criteria on how to differentiate between them. In order to avoid further ambiguity, the patterns where both phases form continuous layers at the top and bottom of the pipe, separated by an interface, and also contain drops of the opposite phase at various concentrations are classified in this research as dual continuous flow. Any further subdivision would depend on detailed knowledge of the degree and height of dispersed of one phase into the other, which may be difficult to obtain.

1.1 Objectives

The aim of this project was to investigate in detail the dual continuous pattern in horizontal liquid-liquid flows and to use the experimental data in the development and validation of a model for the prediction of pressure gradient and hold-up that is based on the two-fluid model but takes into account the particular characteristics (combination of separated and dispersed flows) of this flow. In particular the objectives were:

- To identify the boundaries of the dual continuous flow pattern on the experimental system used.
- To investigate the variation of overall flow parameters such as pressure gradient and hold-up with the change in operational conditions.
- To investigate the variation of local flow parameters such as phase and drop size distribution with changes in the operational conditions.
- To develop a predictive model for pressure gradient and hold-up based on the two-fluid model.
- To develop instrumentation for the measurement of the local parameters such as drop size and local phase fractions.

1.2 Thesis Structure

The thesis is divided into five main parts. The first part, Chapter 2, gives descriptions of previous research carried out with two-phase, liquid-liquid horizontal flow and reports the results obtained. The section also reports previous research carried out into drop formation and some of the governing equations suggested by previous researchers. A brief reference is also made to some of the models suggested to predict the pressure gradient and hold-up behaviour of two-phase horizontal flows.

Chapter 3 gives a detailed description of the pilot scale facility and the instrumentation used in the experimental work. Emphasis is given on the probes that were developed as part of this study. The methods used for data processing and analysis are also described.

Chapters 4 and 5 present the experimental results obtained and their comparisons with existing models and available literature data. In particular Chapter 4 presents the findings on the overall flow parameters such as flow pattern boundaries, pressure gradient and hold-up. The phase distribution data from the local impedance probe helped to identify the flow patterns and also explain the trends in pressure gradient and velocity ratio.

Chapter 5 presents the results on drop size. These are unique data as drop size and concentration during dual continuous fully dispersed flow are given as a function of vertical height in the pipe.

In Chapter 6 the development of the *two-fluid model with entrainment* is presented, This is based on the two-fluid model but the entrainment of one phase into the other is also taken into account, the effect of interface curvature on predicted pressure gradient and hold-up is also examined. The model predictions are compared with the experimental data obtained in this study.

The final Chapter 7 summarises the conclusions of this work and proposes recommendations for future work.

2. LITERATURE REVIEW

2.1 Liquid - Liquid Flows

The flow of two immiscible liquids can occur in many chemical industries, but it is most prevalent in the petrochemical industry where it is often the case that oil and water are pumped from the wells and transported together before they are separated. It is, therefore, necessary to understand how the different flow patterns form so that accurate predictions of the flow regime boundaries can be made and their characteristics can be taken into account in the design of the process. The literature on liquid-liquid flow is rather limited when compared to gas-liquid flow, and differences between the two systems in *density ratio*, *viscosity ratio*, and *surface and interfacial phenomena* mean that results from gas-liquid systems cannot be directly transferred to liquid-liquid ones. The density ratio for liquid-liquid flow systems is lower than that found in gas-liquid flows, and therefore the separation of the two phases due to gravity is much slower. Viscosity ratio for liquid-liquid flows is also lower than that for gas-liquid flows, and can vary significantly due to the large differences in the liquids used industrially. Normally it lies in the range of $0.3-10^4$ compared to 10^{-2} for gas-liquid flow (Valle, 2000). The result of this difference in viscosity ratio is that the dispersion of the drops of one phase in the other, the drag between the phases, and the slip velocities of the two phases are different from those found in gas-liquid flows. Lastly the interactions between the two liquids, with respect to interfacial tension and the wetting properties of the pipe material, mean that interfacial phenomena are more complex compared to gas-liquid systems.

Due to the large differences in the test fluids used in liquid-liquid experimental studies it is difficult to draw any definitive rules for flow pattern boundaries and properties from the literature. However attempts have been made to construct a general two-phase liquid-liquid flow pattern map, but it has not been rigorously tested due to the limited amount of data available (Brauner and Moalem Maron, 1991).

The flow patterns that have been reported for co-current liquid-liquid flows are subdivided into three main categories for the purposes of the current work. Each of these three groups can be further divided into a number of sub-categories. Since most of the research into flow patterns has been done using measuring techniques based on visual observation, the boundaries of the flow regime changes can be rather objective. The names given to each of the flow regimes also differ between investigators. The three main categories used here are *separated flow*, *dual continuous* and *dispersed flow*. In separated flow both liquids retain their continuity at the top and bottom of the pipe. It consists of *stratified flow* (ST), where the oil flows above the water and the interface between the two liquids is smooth; and *stratified wavy flow* (SW) where the flow is still stratified but the interface has large amplitude waves. Dual continuous flow is any flow pattern where both phases remain continuous, but there is a degree of dispersion of one phase into the other. This flow pattern is divided into a number of sub-categories. At the lowest mixture velocities, where there are few drops around the interface, the flow pattern is *stratified with mixing at the interface* (ST & MI). As the flowrates increase further this interfacial mixing increases giving a thick dispersed interface referred to as *three-layer flow* by Angeli (1996). The maximum limit of the dual continuous flow is when the dispersion is distributed throughout the opposite phase forming a *dispersion of oil in water and a dispersion of water in oil* (Dw/o & Do/w). Core-annular flow is also considered a dual continuous flow as both phases still retain continuity while there is entrainment of each phase in the other. In *dispersed flow* one phase is completely dispersed into the other, with either the water or the oil phase being continuous. In the water continuous flow patterns there can either be a complete oil in water dispersion (o/w), or a dispersion of oil in water with a layer of water flowing at the bottom of the pipe (Do/w & w). For the oil continuous flow the possible flow patterns are a complete dispersion of water in oil (w/o), or a dispersion of water in oil with an oil layer (Dw/o & o). Diagrams of the flow pattern identified by Trallero (1995) are shown in Fig. 2.1.

Flow pattern maps have been suggested by most researchers (Charles et al., 1961; Guzhov et al., 1973; Trallero, 1995; Angeli, 1996). The flow pattern boundaries tend to be quite specific for the liquids and test facilities used, and examples are shown in Fig. 2.2 (Charles et al., 1961) and Fig. 2.3 (Guzhov et al., 1973).

To date most investigations have concentrated on pressure gradient and in-situ hold-up measurements. In-situ hold-up is a result of the difference in the average velocities of the two phases and is expressed as the ratio of oil to water velocity, S . As a result of this velocity difference, input and in-situ phase fractions are different, and the velocity ratio, S , can be found by;

$$S = \frac{\text{input oil volume fraction/ input water volume fraction}}{\text{in - situ oil volume fraction/ in - situ water volume fraction}} = \frac{U_o}{U_w} \quad (2.1)$$

If the oil phase is flowing faster than the water phase, S is greater than 1, and if the water phase is flowing faster then S is less than 1. This difference in average velocity can be caused by differences in velocity profile resulting from viscosity differences, or differences in the wall contact area of each phase arising from interfacial and wall wettability phenomena.

2.1.1 Separated flow

Separated flow, when the two liquids flow in layers on top and below each other according to their densities, occurs at the lower flowrates. At these flowrates the flow is gravity dominated. At very low flowrates the interface is smooth and well defined. As the flowrates increase the interface develops long waves which are reported to be approximately twice the pipe diameter (Valle, 1998). As the flowrates increase further, droplets of either oil or water start to appear in the opposite liquid and the transition to the dual continuous flow pattern is initiated. Although it has not been quantified without other parameters changing, it has been qualitatively observed that as the density difference between the two liquids increases, the stratified flow region extends to increased flowrates (Valle, 2000).

Pressure gradient studies associated with this flow pattern are quite limited as most research has been carried out at mixture velocities where there is some degree of dispersion (ST & MI). Guzhov et al. (1973) found that the pressure gradient decreased steadily from the single phase oil value towards the single phase water

value. Valle and Kvandal (1995) and Trallero (1995) also found a similar trend for the pressure gradient.

The experimental data from the literature on hold-up and slip between the two phases is even more scarce. Only Trallero (1995) shows any data for ST or SW flow. The few points available show that S is less than 1 indicating that the water is the faster flowing phase, and that S increases with increasing oil fraction. The data available only goes up to 50% input oil concentration with all values of S being less than 1.

Despite the very few experimental data for stratified flow, some research has been carried out on the modelling of this pattern using Computational Fluid Dynamics (CFD). Due to the nature of the flow occurring at low mixture velocities, CFD simulations for laminar-laminar flow are relatively straightforward (Charles and Redberger, 1962; Kurban, 1997). Fig. 2.4 shows the velocity profile for a two-phase liquid-liquid system where the lower water phase is clearly travelling faster than the upper oil phase, resulting in an S value of 0.5 (Ng, 2002).

The interface shape is also an important factor of the flow behaviour. The interface can either curve up or down depending on the fluids used and the wall wetting properties. Valle and Kvandal (1995) have observed experimentally this phenomenon, and depending on the physical system involved the effect on the pressure gradient and hold-up can be substantial (Brauner et al., 1995, 1998; Ng, 2002).

2.1.2 Dual Continuous Flow

At intermediate mixture velocities a combination of both separated and dispersed flow patterns can appear, where both fluids maintain their continuity on top and bottom of the pipe respectively, but there is a dispersion of one phase into the other at various degrees. Investigators have identified different flow patterns depending on the degree of entrainment of one phase into the other, without, however, providing any qualitative criteria on how to differentiate between them. In order to avoid further ambiguity, the patterns where both phases are continuous while there is

entrainment of one phase into the other are classified in this work as *dual continuous flow*. Any further subdivisions would depend on detailed knowledge of the degree of dispersion and height of dispersion layer within each phase, which is difficult to obtain. Dual continuous flow appears to be very common for a wide range of mixture velocities and input oil volume fractions especially with low viscosity oils.

It was observed by Russell et al. (1959) and Guzhov et al. (1973) that the presence of a layer of water below the oil layer causes the oil layer to move into a turbulent flow regime at lower velocities than it would if it were flowing through the pipe alone. During the early stages of this transition from stratified flow the oil moves along the pipe above the water with a slightly wavy interface. As the velocities increase vortices develop at the interface due to shear forces causing small droplets of each phase to appear in the other phase. Droplets could be formed by the relative movement of the two phases which causes vortices that penetrate the interface boundary (Guzhov et al., 1973). Once a droplet has formed in the opposing phase it is subjected to inertial forces which try to disperse it evenly throughout the cross section of the pipe, and gravitational forces which tend to return it to its original phase. As the flowrates increase the inertial forces increase and the dispersion of droplets throughout the pipe increases. A generalised version of the Kelvin-Helmoltz instability equation may be able to predict the onset of droplet formation, with the instability arising from the different relative velocities caused by the waves or from large differences in viscosity across the interface. The instability can be great enough even for small shear velocities in laminar flow (Valle 1998). The degree of dispersion of either the oil in water or water in oil can be increased when the interface height is located near the top or bottom of the pipe respectively (Valle and Kvandal, 1995) due to the greater differences in velocities of the two phases resulting in higher shear forces. Oglesby (1979) and Arirachakaran et al. (1989) noted that at the lowest velocities for this type of flow, a thin film of water forms an annulus around the pipe wall with an oil continuous dispersion flowing in the middle. If the situation was reversed and the water was in low concentrations the oil would probably not form an annulus, due to the wetting properties of the transparent glass section used in the above experiments (Valle, 1998).

The defined interface has allowed experimental and theoretical investigations of stratified flows (Brauner and Moalem Maron, 1989; Kurban, 1997; Ng et al., 2001), while dispersed flow studies (Hinze, 1955; Karabelas, 1978; Angeli and Hewitt, 2000a) have benefited from the extensive work on liquid-liquid dispersions formed in stirred tanks, which offers insight on the mechanism of drop formation and emulsion viscosity. In contrast, little experimental information is available for the dual continuous flow pattern, documenting mainly its boundaries.

Table 2.1 summarises the previous experimental studies on dual continuous flow, along with the names given by the various investigators to patterns that can be classified as dual continuous flow. Guzhov et al. (1973) identified in their study an *emulsion of water/oil and oil/water (Do/w & Dw/o)*, a *separate flow with a thick layer of emulsion at the interface with a lower layer of water* and a *separate flow with a thick layer of emulsion at the interface with a lower layer of dilute emulsion*, which are understood to be dual continuous flow (Fig. 2.3). Cox (1985) and Scott (1985) found that departure from stratified wavy flow and onset of droplet formation at the interface, which signified the start of *stratified bubble* flow (equivalent to dual continuous flow), was marked by a decrease in the interfacial wave amplitude. Although the same flow system and fluids were used by both investigators, there were slight differences on the stratified/stratified bubble flow boundary at the lower oil fractions. This is a good example of the ambiguous nature of flow pattern classification by visual observation. In all cases of dual continuous flow these investigators found that the velocity ratio (defined as the ratio of the in-situ oil to water velocity) was less than 1, indicating that the water phase is flowing faster than the oil phase (Cox, 1985; Scott, 1985). Investigations at the University of Tulsa documented a *dispersion of water in oil and oil in water (Dw/o & Do/w)* at higher velocities as well as a *stratified with mixing at the interface (ST & MI)* pattern at lower velocities, both of which can be classified as dual continuous flow (Malinowski, 1975; Laflin and Oglesby, 1976; Oglesby, 1979; Trallero, 1995). Trallero (1995), from an extensive flow pattern study, reported that, within ST & MI flow, as the mixture velocity increased the amount of each phase dispersed into the other also increased and became more uniformly distributed into the opposite phase. Visual observations revealed drop sizes between 1-12mm in diameter for ST & MI, decreasing to 2-3mm for Dw/o & Do/w flow. With the addition of water during ST

& MI flow, pressure gradient was found to decrease, while during Dw/o & Do/w flow, apart from some initial fluctuations, pressure gradient did not vary significantly. In nearly all cases of dual continuous flows, velocity ratios were less than 1, with the value increasing with increasing input oil fractions. Valle and Kvandal (1995) studied flow patterns in detail with the use of wall mounted conductivity probes and a sampling tube and observed entrainment of one phase into the other and onset of the *stratified wavy-entrained* pattern at mixture velocity of about 0.85m/s. At high and low input oil fractions a *stratified wavy with highly dispersed water zone and moderate dispersed oil zone* pattern and a *stratified wavy with highly dispersed oil zone and moderate dispersed water zone* pattern were observed respectively. These patterns can be considered as dual continuous flow, since both phases retained their continuity. Pressure gradient decreased with the addition of water until it reached a minimum at about 60% input water concentration and then increased again. Valle and Utvik (1997) in subsequent studies observed that the velocity ratio was generally less than 1, and increased with increasing input oil fraction. From the flow patterns observed by Nädler and Mewes (1997) the *layers of water-in-oil dispersion and water* and the *layers of water in oil and oil in water dispersion and water* as well as a *stratified flow with mixing at the interface* at lower mixture velocities, can be considered as dual continuous flow (Figs. 2.5 and 2.6). The patterns identified by Vedapuri et al. (1997) can also be considered as dual continuous flow. These investigators divided them into two categories depending on the height of the dispersed layer between the clear oil and water phases, which they obtained with a sampling probe. As the thickness of the dispersed layer increased, flow changed from *semi-segregated* to *semi-mixed*. When a high viscosity oil (90mPa s) was used instead of a low viscosity one (2mPa s), mixing was less intense. Angeli and Hewitt (2000b) found that both a *three-layer* (with both phases continuous and entrainment of one phase into the other) and a *stratified wavy with drops* flow patterns appeared in a steel test section at lower mixture velocities than in an acrylic test section with the same internal diameter. In the steel test section, two-phase pressure gradient during dual continuous flow was higher than that of single phase oil or water, while in the acrylic test section it was lower than the single phase values (Angeli, 1996). Similar observations were also made by Soleimani (1999) who, in the same experimental set-up, found that velocity ratio during dual continuous flow remained above 1.

From Table 2.1 it appears that high viscosity oils cause the dual continuous pattern to extend to lower mixture velocities. There is not a systematic effect of the pipe diameter on the boundaries of dual continuous flow; this cannot be conclusive, however, given the small range of diameters used and the variation of the other flow parameters at the same time.

2.1.3 Dispersed Flow

The third type of flow pattern, dispersed flow, has been studied in greater depth. During dispersed flow either phase can be continuous with the other phase in the form of entrained drops. There is usually a vertical concentration gradient of droplets due to gravity, and only at very high velocities or in stable emulsions can this be overcome by the dynamic, inertial forces and the dispersion become homogeneous. Drop size distribution across the pipe is a function of fluid properties, superficial velocities, pipeline configuration, and pipe length (Hinze, 1955; Collins and Knudsen, 1970; Sevik et al., 1973; Karabelas, 1978; Hanzevack and Demetriou, 1989). Due to this vertical concentration gradient of the dispersed phase a number of sub-categories of dispersed flow have been reported (Guzhov, 1973; Trallero, 1995; Nädler and Mewes, 1995). At the highest mixture velocities the dispersed phase is uniformly distributed throughout the continuous phase giving rise to either a dispersion of oil in water, or a dispersion of water in oil. If the mixture velocity is insufficiently high a clear layer of water can form at the bottom of the pipe. This flow pattern has been described as a *dispersion of oil in water with a clear water layer* (Do/w & w) (Fig. 2.1) (Guzhov et al., 1973; Trallero, 1995).

Pressure gradient associated with dispersed flow is quite complicated due to the nature of dispersions. From rheological studies it has been shown that the relative viscosity increases as the fraction of the dispersed phase increases. For a particular mixture velocity a peak in the pressure gradient would appear at increasing dispersed phase fraction at the *phase inversion point*, defined as the phase fraction at which the phase that was continuous becomes the dispersed phase, and the dispersed phase becomes the continuous phase (Arirachakaran et al., 1989, Angeli and Hewitt, 1998). Pal (1986) experimented with stable emulsions in laminar flow and also found a

peak in pressure gradient at inversion point. In turbulent flow with unstable dispersions however, pressure gradient and viscosity was found to be lower in oil continuous dispersions compared to single phase oil, a phenomenon now referred to as *drag reduction* (Angeli, 1996). The degree of drag reduction increased with an increasing water concentration in the oil. Soleimani et al. (1997), also observed a decrease in pressure gradient when water was fully dispersed in oil, except for the phase fractions close to phase inversion where a large narrow peak appeared (Fig. 2.7). Turbulent, unstable, water continuous dispersions also show drag reduction with increasing oil volume fraction but to a lesser degree (Pal, 1993). However, results by Kvandal and Sønvedt (1995) and Valle and Utvik (1997) showed that pressure gradient in oil continuous stable emulsions increased with increasing dispersed water fraction, not only in laminar, but also in turbulent flow regimes.

Pressure gradient peaks have also been observed during other flow pattern transitions. Guzhov et al. (1973) found that at intermediate mixture velocities (0.9-7.6m/s) the pressure drop gives a small peak as the oil concentration is increased to approximately 40% of the mixture volume (Fig. 2.8). This pressure gradient peak marks the boundary of a dispersion of oil in water and water (Do/w & w) to a pattern of stratified flow with mixing at the interface (ST & MI). After a decrease in the pressure gradient back down to a level comparable to the single phase water, a second, much larger pressure gradient peak is observed at around 85% oil fraction. This peak corresponds to the flow pattern transition from ST & MI to a dispersion of water in oil, over oil in water (Do/w & Dw/o). For higher flowrates the transition between Do/w & Dw/o and fully dispersed flow (w/o) is marked by another pressure gradient peak. A similar increase in pressure gradient was also observed by Nädler and Mewes (1995) during the transition between the Do/w and Do/w & Dw/o, and between Do/w & Dw/o to Dw/o.

Slip ratio in dispersed flow can be different from that found in stratified and dual continuous flow. For Do/w & w flows the only data available are those by Trallero (1995) who suggested that the only differences in velocities between the two phases are due to the increase in interfacial drag, and drag from the continuous phase on the drops. The mean oil velocities were found to be slightly higher than the water velocities. For a fully dispersed flow pattern the data obtained by Angeli (1996)

indicate a higher mean velocity for the dispersed oil phase than the continuous water phase. However, local measurements of drop distribution show that there was a higher concentration of drops in the high velocity pipe core which may explain the findings. Valle and Utvik (1997) also found higher mean cross sectional velocities for dispersed water droplets than the continuous oil phase with the slip ratio indicated a greater difference in velocities at high flowrates. In contrast to the above findings, Charles et al. (1961) and Trallero (1995) presented some data where the dispersed phase was slightly slower than the continuous phase. However, no information on the drop distribution was given. Clearly more measurements need to be carried out before a general conclusion can be drawn.

It should be noted that the properties of the pipe material can have a dramatic effect on the observed flow patterns and pressure drop. Angeli and Hewitt (1998) conducted experiments comparing the flow behaviour of oil and water mixtures through stainless steel and acrylic resin pipes. Pressure gradient in the steel pipe was found to be higher than in the acrylic pipe, and that the difference was higher than pipe roughness could account for. Later work (Angeli and Hewitt, 2000) showed that flow patterns were also affected by the pipe wall material, with flow patterns in the steel pipe being more dispersed than in the acrylic pipe for similar flow conditions.

2.1.4 Phase Inversion

Phase inversion is characterised as the phenomenon where the continuous phase in a liquid-liquid dispersed system becomes the dispersed phase, while the phase that was previously dispersed becomes continuous. For the flow of immiscible liquids through a pipe, there is a range of volume fractions, the *ambivalent range*, where either phase can be continuous depending on the system configuration and the dispersion initialisation. The complexity of phase inversion has led to extensive research investigating the effect on it of physical and chemical parameters, with the majority of studies carried out in stirred vessels rather than in pipes. This work showed that the volume fraction of oil at inversion varies greatly with the agitation rate (Luhning and Sawistowski, 1971; McCleary and Mansoori, 1978). Viscosity also plays an important role, and according to Treybal (1951) the phase with the higher viscosity will tend to become the continuous phase. Selker and Sleicher

(1965) found the opposite, and it is now acknowledged that the more viscous phase is more likely to form the dispersed phase (Arirachakaran et al., 1989). Ethimiadu and Moore (1994) concluded that the wall material wetting characteristics could prevail over viscosity and the phase that preferentially wetted the wall could become the continuous phase. It was argued by Selker and Sleicher (1965) and McClarey Mansoori (1978) that the surface tension had no effect on the phase inversion. However work by Luning and Sawistowski (1971) and Efthamiadu and Moore (1994) showed that surface tension and surfactants exert an important influence on phase inversion.

Arirachakaran et al. (1989) carried out phase inversion experiments in horizontal pipes and found that the inversion of oil and water mixtures was affected by input water fraction, oil viscosity and mixture velocity. Increasing the oil viscosity led to a decrease in the required input water fraction necessary to cause inversion from a water in oil (w/o) to an oil in water (o/w) dispersion. Mixture velocity had little effect on the inversion point as long as there was no flow regime transition. A correlation was also suggested for predicting the water fraction at which phase inversion would occur based on results from previous investigators and their own data (Russell et al., 1959; Charles et al., 1961; Guzhov et al., 1973).

$$\epsilon_{w\text{ INV}}=0.5-0.1108 \log\mu_o \quad (2.2)$$

where $\epsilon_{w\text{ INV}}$ is the water fraction at inversion point.

The above model, however, cannot predict the hysteresis of phase inversion observed when the system starts from one phase as continuous. Brauner and Ullmann (2002) attributed this hysteresis to the time needed by the new continuous phase to wet the tube material after phase inversion or to the difference in surface tension in the new surfaces created after phase inversion compared to those existing before, where contaminants may have accumulated.

2.2 Drop Size and Distribution

In liquid-liquid dispersions the drop size and its distribution are important factors that determine the rheology and stability of a dispersion. Therefore many studies have been carried out to formulate models that predict these parameters. Drop size is a function of the break-up of large droplets into smaller ones, and the coalescence of small droplets to form large ones. Once a system has reached a pseudo-steady state, there is a break-up and coalescence of drops with a theoretical maximum and minimum drop size. Studies have mainly been carried out in stirred vessels, while information on drop size in pipe flows is almost entirely limited to low dispersed phase concentrations.

2.2.1 Drop Break-up

The first fundamental work in this area was conducted by Hinze (1955) who assumed drop break-up in a turbulent flow field. Hinze (1955) suggested that the force acting on a drop per unit area, τ , from the continuous phase could be either a viscous stress or a dynamic pressure force and would deform it. Surface tension forces, σ/d , where σ is the surface tension and d is the drop diameter, would counteract this force and tend to maintain the drop as a sphere. As the drop deforms internal flows are set up which can cause viscous stresses and dynamic pressure forces inside the drop. The dynamic pressure force will be of the order of τ , causing flow velocities of the order of $(\tau/\rho_d)^{0.5}$. Viscous stresses inside the drop will then be of the order of

$$\frac{\mu_d}{d} \sqrt{\frac{\tau}{\rho_d}} \quad (2.3)$$

From the three different forces that act upon the drop, two dimensionless groups can be formed. The first, a generalised Weber number (N_{We}), is the balance between

external forces trying to deform the drop, and the counteracting surface tension force.

$$N_{We} = \frac{\tau d}{\sigma} \quad (2.4)$$

The greater the value of N_{We} the greater the value of τ compared to σ/d and the greater the deformation of the drop. At a critical Weber number, N_{WeCrit} , the force acting on the drop becomes too great for the surface tension to counteract and the drop beaks. N_{WeCrit} gives the maximum drop size, d_{max} :

$$N_{WeCrit} = \frac{\tau d_{max}}{\sigma} \quad (2.5)$$

The second dimensionless group is the Viscosity number, N_{Vi} , that accounts for the dispersed phase viscosity that tends to stabilise the drop:

$$N_{vi} = \frac{\mu_d}{\sqrt{\rho_d \sigma d}} \quad (2.6)$$

where ρ_d is the dispersed phase density, and μ_d is the dispersed phase viscosity.

Hinze (1955) argued that since the deformation process can be described in terms of two dimensionless numbers, in general N_{WeCrit} will be a function of N_{Vi} , as follows:

$$N_{WeCrit} = C_1 [1 + \varphi(N_{vi})] \quad (2.7)$$

where the function φ decreases to zero as $N_{Vi} \rightarrow 0$ (as the drop viscosity decreases), and C_1 is a constant.

In more complicated flow fields there will be local variations in the flow patterns and varying flow velocities will occur. In these situations the value of N_{WeCrit} will not be

the same for all the drops in the system. What is required is a statistical mean value of N_{WeCrit} to determine the average largest drop size that can withstand the break-up forces of the flow field. To obtain this statistical mean a higher weight must be assigned to the more turbulent flow patterns that produce a lower value of N_{WeCrit} (Hinze, 1955).

Investigators have commonly believed that the splitting of drops in turbulent flow is a result of viscous shearing action, however Hinze (1955) suggested that this is only the case if the undeformed and elongated drops are small compared to the local regions of the viscous flow. For medium to high Reynolds numbers, the local dimensions of the viscous flow are small, and the drop is deformed by dynamic pressure forces caused by changes in the velocity over a distance equal to the drop size;

$$\tau = \rho_c \Delta v^2 \quad (2.8)$$

where ρ_c is the density of the continuous phase, and Δv is the velocity difference across the drop.

To estimate the value of this velocity difference, Δv , an understanding of the turbulent flow field of the continuous phase is required. The theory of length scales was first developed by Kolomogorov (1949) who divided turbulent flow into different regions, each one having a different energy pattern associated with it. The largest eddies with a size comparable to that of the system, l , have an eddy velocity approximately equal to the change of velocity over a distance l . Most energy is contained in these anisotropic large eddies, which depend on an external energy source for their existence. The energy dissipation rate per unit mass, ε , is a function of Δv and l , and therefore by dimensional analysis;

$$\varepsilon \propto \frac{(\Delta v)^3}{l} \quad (2.9)$$

where Δv is the change in velocity over a distance equal to l . In pipe flow a value of $l \approx 0.1D$ (where D is the pipe diameter) is used (Hutchison et al., 1971; Kubie and Gardener, 1977). The energy is eventually dissipated from the small scale eddies. In this region $Re \approx 1$ as the viscous forces become important and of the same order of magnitude as the inertial forces. The characteristic length, λ_o (Kolmogorov scale) and velocity, v_{λ_o} , are given by:

$$\lambda_o = \left(\frac{\mu_c^3}{\varepsilon} \right)^{0.25} \quad (2.10)$$

and

$$v_{\lambda_o} \propto (\mu\varepsilon)^{0.25} \quad (2.11)$$

where μ is the viscosity. The structure of these eddies is independent of the large scale geometry of the flow (Hinze, 1955).

In between these two scales exists the *inertial subrange* with a length scale λ ; $l \gg \lambda \gg \lambda_o$ where the turbulence is still isotropic. Velocity in this range is a function of ε and λ only and by dimensional analysis the eddy velocity, v_λ , is;

$$v_\lambda \propto (\varepsilon\lambda)^{1/3} \quad (2.12)$$

Hinze proposed that drop break up would occur in the inertial subrange of flow, a condition met for high Re numbers according to Kolmogorov. Assuming that the N_v group is small in turbulent flows, from equations (2.7), (2.8) and (2.12) Hinze obtained;

$$d_{\max} \left(\frac{\rho_c}{\sigma} \right)^{\frac{3}{5}} \varepsilon^{\frac{2}{5}} = C_2 \quad (2.13)$$

where C_2 is a constant. Hinze (1955) fitted this model to data from Clay (1940) and found a value of 0.725 for the constant C_2 . Sprow (1967) found that the above model fitted his d_{\max} data from stirred vessel experiments. The model can be used for pipeline flow as well, where ε is the rate of the mean energy dissipation per unit mass, ε_M , in the pipe:

$$\varepsilon_M = \frac{fU_c^3}{2D} \quad (2.14)$$

where f is the friction factor, U_c is the average axial velocity of the continuous phase and D is the pipe diameter. Kubie and Gardener (1977) and Karabelas (1978) combined equations (2.13) and (2.14) to get:

$$\left(\frac{d_{\max} \rho_c U_c^2}{\sigma} \right) \left(\frac{fd_{\max}}{4D} \right)^{2/3} = 0.369 \quad (2.15)$$

The value of 0.369 comes from the value that Hinze (1955) calculated for the constant C_2 after incorporating the energy dissipation term. This equation was able to predict d_{\max} for dilute turbulent pipeline flow dispersions well (Kubie and Gardner, 1977; Karabelas, 1978).

Karabelas (1978) argued that the drop break up in pipeline flow can appear in the inertial sub-layer, because at high Reynolds numbers the thickness of the buffer layer is greatly reduced so that the lower boundary of the inertial sub-layer is very close to the wall. In all practical cases the maximum stable drop size generated in the turbulent core is larger than the wall layer thickness. Karabelas also stated that the distribution law (equation (2.12)) that describes the eddies in the inertial sub-range for stirred vessels is also valid for the inertial sub-layer. In the inertial sub-layer in pipe flow the local energy dissipation rate per unit mass, ε_l , is inversely proportional to the distance, y_w , from the wall (Tennekes and Lumley, 1972):

$$\varepsilon_l \approx \frac{U_*^3}{Ky_w} \quad (2.16)$$

where U^* is the friction velocity, and K is the von Karman constant. There is a distance from the wall where $\varepsilon_M = \varepsilon_l$. Close to the wall ε_l will be larger than ε_M . Karabelas (1978) assumed that where break-up occurred in the inertial sub-layer, the d_{\max} would appear at a distance from the wall between the beginning of the inertial sub-layer and the distance at which $\varepsilon_M = \varepsilon_l$.

A model that considers the viscosity of the drop was proposed by Sleicher (1962):

$$\left(\frac{d_{\max}\rho_c U_c}{\sigma}\right)\left(\frac{\mu_c U_c}{\sigma}\right)^{0.5} = 38\left(1 + 0.7\left(\frac{\mu_d U_c}{\sigma}\right)^{0.7}\right) \quad (2.17)$$

where μ_d and μ_c are the dynamic viscosities for the dispersed and continuous phase respectively. This model does not account for the effect of pipe diameter; however later work by Paul and Sleicher (1965) showed a slight influence on pipe diameter on the maximum drop size.

For $d > l$, where $l = 0.1D$ for pipe flows, Kubie and Gardner (1977) argued that the fluctuating turbulent velocity, u_f , should be used for calculating the external shear force, τ , in equation (2.8), as suggested by Hughmark (1971). They derived the following equation for calculating d_{\max} :

$$\frac{fd_{\max}\rho_c U_c^2}{\sigma} = 5.53 \quad (2.18)$$

For pipe flow u_f is approximately $1.3U^*$.

Brauner and Ullmann (2002) suggested that the Hinze model was applicable for dilute dispersions, but cannot be used for high concentration dispersed systems because the turbulent kinetic energy flux of the continuous phase (required for drop break-up) may not be sufficient to provide the extra surface energy required by the

formation of new drops. A model for high concentration dispersions was therefore proposed:

$$d_{\max} = 2.22C_H \left(\frac{\rho_c U_c^2 D}{\sigma} \right)^{-0.6} \left[\frac{\rho_m}{\rho_c (1 - \phi_d)} f \right]^{-0.4} \left(\frac{\phi_d}{1 - \phi_d} \right)^{0.6} \quad (2.19)$$

where C_H is a tunable constant, $C_H = O(1)$,

$$\phi_d = \frac{U_{ds}}{U_{ds} + U_{cs}} \quad (2.20)$$

U_{ds} is the dispersed phase superficial velocity, and U_{cs} is the continuous phase superficial velocity.

2.2.2 Drop Coalescence

In a turbulent dispersion the drops are randomly moving around and continuously colliding with each other. These collisions may result in coalescence. As mentioned above, a drop in a turbulent dispersion is also experiencing shear forces which are acting to break the drop up, and so for any system an equilibrium between coalescence and break-up exists. For two drops to coalesce, first they must collide, and then stay together for sufficient time to allow the continuous phase film between them to drain to a critical thickness, where it ruptures and the drops join together. The rate of coalescence depends on the efficiency as well as the frequency of collisions, which increases with the dispersed phase concentration (Coulaloglou and Tavlarides, 1977). Coulaloglou and Tavlarides suggested that the collision efficiency, Λ , could be given by:

$$\Lambda = \exp\left(-\frac{t_{dr} n}{t_{contact}}\right) \quad (2.21)$$

where t_{drain} is the continuous film drainage time (sec), and $t_{contact}$ is the contact time between the colliding drops (sec). In stirred vessels the drainage time is given as a

function of the continuous phase viscosity and density, interfacial tension, drop size, agitation rate, and impeller size. The contact time is given as a function of drop size, and the agitation rate and impeller size. During their contact, but before the drops coalesce, they can be separated by turbulent eddies. Modelling of this process is difficult because the drainage of the film depends on many parameters such as temperature, vibrations, surfactants, and the fluid properties (Valentas et al., 1966; Thomas, 1981).

Coulaloglou and Tavlarides (1977) suggested an equation for the coalescence rate for equal sized drops and uniform energy dissipation:

$$N_c = K_1 V^{1/9} N D_i^{2/3} \Lambda_1 N_d^2 \quad (2.22)$$

where

$$\Lambda_1 = \exp \left[- \frac{K_2 \mu \rho_c D_1^2 N^3 \left(\frac{V_1^{1/3} V_2^{1/3}}{V_1^{1/3} + V_2^{1/3}} \right)^4}{\sigma^2} \right] \quad (2.23)$$

K_1 and K_2 are dimensional coalescence constants related to the collision frequency and efficiency (and particularly the film thickness at coalescence) respectively, V is the volume of the two drops, N is the agitation speed, D is the impeller diameter, and N_d is the number of drops.

Howarth (1964) considered the collision frequency and the coalescence frequency of uniformly sized drops in an isotropic turbulent flow. He suggested an equation for the collision frequency, f_{col} , for a single drop assuming that the density of the dispersed and continuous phases were identical, and using Taylor's theory of diffusion:

$$f_{col} = \left(24 \phi \sigma \bar{u}^2 / d^3 \right)^{0.5} \quad (2.24)$$

where ϕ is the dispersed phase concentration, and \bar{u}^2 is the mean squared turbulent velocity fluctuations. Howarth suggested that the cohesive forces between drops, which must be related to the molecular forces, are not strong enough to overcome the turbulent forces and cause coalescence. Instead it was suggested that the relative velocity between the two drops at the point of collision should therefore exceed a certain critical value, w^* , for coalescence to occur. However no relationship for calculating w^* was given.

Shinnar (1961) considered that drop coalescence, like drop break-up, occurred in the inertial sub-range of turbulence and assumed that drops which had collided exert an attraction force to each other which is dependent on drop size. The energy of adhesion, E_a , for two drops of equal diameter is:

$$E_a = A(h_o)d \quad (2.25)$$

where h_o is the film thickness, $A(h_o) = \frac{1}{2} \pi \int_{h_o}^{\infty} \int_h^{\infty} f(h)\delta(h)\delta$, and $f(h)$ is the attractive force per cm^2 between two finite surfaces h distance apart.

In the inertial sub-range the kinetic energy of two drops with equal diameters, d , in relative movement to each other is proportional to $\rho_c v^2 d^3$. To prevent coalescence this energy must be greater than E_a . From this a minimum drop diameter, d_{min} , for which separation after collision is still possible can be found (Shinnar, 1961):

$$\frac{\rho_c v^2 d_{\text{min}}^2}{A(h_o)} = C_3 \quad (2.26)$$

where C_3 is a constant. For drops that are larger than d_{min} coalescence is not possible.

Thomas (1981) considered the time that the drops were in contact and not the adhesion energy to be important in coalescence. It was suggested that the time required for the film between two drops to drain to the critical thickness, h_r , was given as:

$$t = \frac{3}{32\pi} \mu_c F \left(\frac{d}{\sigma h_r} \right)^2 \quad (2.27)$$

where F is the force pressing the drops together, and h_r is the critical film thickness. The force F is applied by the eddies in the inertial sub-range of turbulence and is proportional to $\rho_c v^2 d^2$. The time, T , that the drops are together is given by:

$$T \propto \left(\frac{d^2}{\varepsilon} \right)^{\frac{1}{3}} \quad (2.28)$$

For coalescence to occur T must be greater than t .

The above correlations give an understanding of the mechanism of coalescence but cannot be used in practical situations as there are no generalised equations for the prediction of important parameters such as h_r in eq. (2.27).

2.2.3 Drop Size Distribution

The majority of flow patterns observed during two-phase oil-water flows include the formation of droplets of one phase dispersed into the other. At high mixture velocities one phase is completely dispersed, while at lower mixture velocities both phases can be continuous, with droplets of one phase into the other forming around the interface to various degrees depending on the specific flow conditions (*dual continuous flow*). It is of interest to study the size and distribution of these droplets so that an improvement in modelling and design of dispersed systems can be made. At present all studies have looked at fully dispersed systems, and the dual continuous pattern has been ignored. The level of entrainment in the upper and lower phases will affect the pressure drop for that phase, and therefore potentially influence the interface height and the velocity ratio between the phases.

Mean diameters are often used to describe drop size distributions, which give an indication of the distribution's characteristics. The limiting d_{\max} and d_{\min} values of a

distribution have already been mentioned above, however in distributions with a long 'tail' in the large sizes the d_{\max} value may be very large. Instead the diameter that represents 95% of the volume (or number) in a cumulative volume (or number) distribution is often used. For systems where the interfacial area is important the Sauter mean diameter, d_{32} , is used, defined as the ratio of volume to surface area of the droplets:

$$d_{32} = \frac{\sum_{j=1}^n d_j^3}{\sum_{j=1}^n d_j^2} \quad (2.29)$$

where n is the number of drops measured (Pacek et al., 1998).

A number of standard functions have been used to describe the shape of drop size distributions in pipeline. Karabelas (1978) suggested that the Rosin-Rammler distribution (equation (2.30)) represented his data satisfactorily. The Rosin-Rammler distribution can be expressed by:

$$V_{cum} = \exp\left[-\left(\frac{d}{d^*}\right)^n\right] \quad (2.30)$$

where V_{cum} is the cumulative volume fraction, d is the particle diameter, and n and d^* are the slope of the curve and the diameter corresponding to $V_{cum} = 0.3679$ respectively. The distribution can be used for any characteristic diameter, and if used for d_{95} by volume then it becomes:

$$V_{cum} = \exp\left[-2.996\left(\frac{d}{d_{95}}\right)^n\right] \quad (2.31)$$

Simmons and Azzopardi (2001) found good comparison with experimental data from pipe flow and the upper limit log normal distribution for dispersed phase concentrations up to 42%. Other distributions from stirred tanks for distributions

with long tails have used the log normal distribution which is described by the following equation;

$$y(d) = \frac{\varphi}{\sqrt{2\pi\delta^2}} \exp\left[\frac{-1}{2\delta^2} (\ln(d - \xi))^2\right] \quad (2.32)$$

where d is the drop size and δ , φ and ξ are parameters of the log-normal distribution, with δ affecting the distribution height and ξ affecting the distribution width.

Drop size distributions in liquid-liquid dispersions have been studied extensively in stirred tanks, but relatively few studies exist for dispersions in pipeline flow. One of the earliest studies looked at both droplet size and velocity distributions in downward vertical liquid-liquid flow for dispersed oil fractions up to 47% (Ward and Knudsen, 1967). A dispersion was made in a stirred vessel which was then pumped to the test pipes, rather than the droplets being formed as a result of the turbulent flow process. Droplet size was measured using a photographic technique, while velocity was measured using a Pitot tube. The photographic technique employed was only able to measure droplet size for the entire pipe cross section. The results showed that the mean drop diameter (d_{32}) increased with increasing dispersed phase fraction. Sleicher (1962) investigated the stability of artificially formed drops via an inlet nozzle and concluded that the maximum drop size decreased as the velocity increased. Su and Hanzevack (1988) later showed that this relationship was linear. More recent studies by Angeli (1996) found that the effect of mixture velocity on drop size is less strong. This may be because Sleicher (1962) was measuring drop size close to the wall where there is greater shear, a theory supported by Ward and Knudsen (1967) who concluded that the maximum drop size also seems to increase with increasing distance from the wall.

Collins and Knudsen (1970) investigated the effect of flow turbulence on the drop diameter distribution for downward vertical flow, where the organic phase was injected into the flowing aqueous phase at dispersed phase fractions of 0.6-10%. The injection process caused a certain drop size distribution to be formed, but as the flow developed along the pipe, a second distribution began to appear as a result of the

turbulent flow. The distribution near the injector nozzle was found to fit a log-normal distribution, which deteriorated further away from the nozzle as the turbulence affected the distribution. The study suggested that as the viscosity of the drops increases, so does the time required for them to break up into their final distribution. Greater drop break-up seemed to occur near the walls of the pipe compared to the turbulent core region. The effect of changes in dispersed phase concentration on drop diameter were difficult to determine as the nozzle configuration was rarely kept constant for a changing dispersed phase concentration. It was found that the model proposed by Sleicher (1962) (eq. (2.17)) predicted well the maximum stable drop diameter;

Kubie and Gardner (1977) conducted experiments in horizontal pipes where the dispersed phase was injected into the flowing continuous phase. Four different injector types were tried, but with little effect on the final drop size distributions. Measurements, taken using photography through the pipe wall, showed that as the continuous phase velocity increased d_{\max} decreased at a greater rate than d_{\min} causing the distribution to become narrower. It was also stated that d_{\max} could be predicted by the Hinze model (equation (2.15)).

Karavelas (1978) also carried out studies for water dispersed in oil in a horizontal pipe. The drops were introduced via an injection tube at a concentration of 0.2%, however as the injected drops were far larger than the drops which were finally measured, it was assumed that the measured drop size distribution was a result of turbulence in the pipe rather than an effect of the injection process. Two techniques for measuring drop size were used; photography and dispersed phase sampling. The second technique involved the removal of the dispersed phase using a sample tube, and subsequent encapsulation of these droplets in a monomer to prevent coalescence. Once these encapsulated droplets had been sufficiently stabilised they were photographed and the results compared to the in-situ photography technique. It was found that the drop diameter distribution could be fitted to either a Rosin-Rammler distribution, or an upper limit log-normal distribution. It was also observed that the values for d_{\max} decreased with increasing mixture velocity and the data was predicted well by the Hinze (1955) model. Karabelas argued that the encapsulation technique gave more accurate, and more consistent data than the photography technique.

El-Hamouz and Stewart (1996) measured chord length distributions using a laser back-scatter technique for horizontal flow. The droplets were formed in a static mixer in the pipe before entering the 1.06m test section. The mean chord length increased with distance from the mixer, suggesting that the distributions were a result of coalescence in the test section, rather than turbulent break-up.

Drop size distributions generated in horizontal pipe flows were also measured by Angeli and Hewitt (2000) using video recording via an endoscope placed inside the flow. d_{\max} was found to decrease slightly with increasing continuous phase velocity. The continuous phase also affected the drop size and water drops in oil were smaller than oil drops in water. The pipe wall material, apart from the flow pattern (see Section 2.1.3) also affected the drop size distribution, with larger drops observed in the acrylic pipe than in the stainless steel pipe, probably due to the lower turbulence levels in the smooth acrylic pipe.

Simmons et al. (2000) carried out work in dispersed pipe flow comparing two different laser techniques; the first was a laser back-scatter device which can be used in high dispersed phase concentrations (>5%), while the second was a laser refractive technique that can only be used at low dispersed phase concentrations (<3%). These devices were placed into the test section, but due to their configuration were only able to give distribution data for the whole pipe. The few data presented show that the d_{32} value was found to decrease with increasing mixture velocity.

2.3 Chord Length / Drop Diameter Transformation

Measurements of drop size with techniques that are based on photo or video recording provide the actual drop diameter (Ward and Knudsen, 1967; Karabelas, 1978; Angeli, 1996). However techniques that are based on recording the length of the drop that passes through a certain location in the mixture (such as laser based techniques and local sensor techniques) measure chord length. An experiment using one of these techniques would therefore give a chord distribution rather than an actual diameter distribution. This chord length distribution would need to be converted into a diameter distribution for further data processing. The transformation

from chord length to drop diameter is complicated, and relies on probability density functions of the corresponding chord lengths and drop diameters. A number of investigators have opted to report chord length distribution data rather than drop diameters, assuming that the trends observed in chord length will also reflect those of the actual drop diameters (Chan et al., 1987; Lee et al., 1990).

A number of methods exist in the literature for the transformation of a chord length distribution to a drop diameter distribution (Clarke and Turton, 1988; Liu et al., 1996; Simmons et al., 1999; Langston et al., 2001). Weimer et al. (1985) suggested one of the earlier methods for the conversion of chord length distribution of bubbles in a fluidised bed to bubble size distribution. Spherical bubbles were assumed and the measured chord length was related to the actual bubble diameter using the Pythagorean Theorem:

$$x^2 + \left(\frac{y}{2}\right)^2 = \left(\frac{d}{2}\right)^2 \quad (2.33)$$

where d is the drop diameter, y is the chord length, and x is the length from the drop centre to the chord cut (see also Fig (2.9)). Solving for chord length, y , equation (2.33) becomes:

$$y = 2 \left[\left(\frac{d}{2}\right)^2 - x^2 \right]^{0.5} \quad (2.34)$$

Assuming that all values of x are possible, the mean bubble diameter, d , can be obtained from the mean chord length, \bar{y} , at a particular axial distance, x .

$$\bar{y} = \frac{2 \int_0^{d/2} \left[\left(\frac{d}{2}\right)^2 - x^2 \right]^{0.5} \delta y}{\int_0^{d/2} \delta y} = \frac{\pi}{4} d \quad (2.35)$$

which gives $d = \frac{4}{\pi} \bar{y}$

It should be noted that the mean chord length must underestimate the bubble size because the drops are not usually cut through their centre. However as larger bubbles are more likely to be measured, the method tends to overestimate the actual bubble diameter. The actual bubble diameter should be between the mean chord length \bar{y} and $(4/\pi) \bar{y}$.

2.3.1 Clarke and Turton (1988)

In a number of papers the group working at West Virginia University attempted to convert a chord length distribution to a drop diameter distribution. According to Clarke and Turton (1988) the size distribution of bubbles measured by a probe, $P(R)$, is not the same as the distribution of bubbles in the system, $P_s(R)$, because the larger bubbles are more likely to interact with the probe. There would therefore be a bias in the measured results proportional to the square of the bubble radius, R^2 . Considering the interaction of bubbles of radius R with the probe tip, and with the centres of the bubbles at distance r from the tip (Fig. 2.10), the bubbles will only touch the probe if r is less than R and greater than zero. The number of bubble centres passing through a small annulus dr wide and at a distance r from the probe tip increases proportionally as r increases. It can therefore be concluded that the probability density function for the distance between the bubble centres and the probe tip is in direct proportion to the distance r ,

$$P(r|R) = ar \quad 0 \leq r \leq R \quad (2.36)$$

where a takes the value $2/R^2$. The probability density function $P(y|R)$ of the chord lengths, y , for a specified bubble size R can be given by:

$$P(y|R) = P(r|R) \left| \frac{dr}{dy} \right| = \frac{2r}{R^2} \left| \frac{dr}{dy} \right| \quad (2.37)$$

where $P(y|R)$ is the probability of obtaining a chord y from a drop of size R . The probability of measuring a particular chord length, y , for any bubble size, R , in the system is:

$$P(y) = \int_0^{\infty} P(y, R) dR = \int_0^{\infty} P(R) P(y|R) dR \quad (2.38)$$

The upper limit can be replaced by the maximum drop radius, R_{max} , assuming it is known. If the diameter distribution $P(R)$ is known then the chord length distribution for a spherical bubble can be found. Clarke and Turton (1998) extended the work to different bubble shapes.

Since the experimental data are chord length distributions rather than drop size distributions, the reverse of the above procedure is of interest. Consider a chord length distribution, $P(y)$, that consists of n number of measurements. If the chord lengths are divided into m number of equal width 'bins', such that:

$$y_i = y_{max} - (i-1/2)\Delta y \quad 0 \leq i \leq m-1$$

where $\Delta y = \frac{y_{max}}{m}$ and y_{max} is the maximum measured chord length value;

an approximation of the probability of finding a chord length y between y_i and y_{i+1} is:

$$W(y_i < y < y_{i+1}) = \frac{\text{no. of chord lengths measured between } y_i \text{ and } y_{i+1}}{\text{total number of chord lengths measured. } n} \quad (2.39)$$

or:

$$W(y_i < y < y_{i+1}) = \int_{y_i}^{y_{i+1}} P(y) dy \quad (2.40)$$

Using equation (2.38):

$$W_i \equiv \sum_{j=0}^{m-1} C_{i,j} P(R_j) \Delta R \quad (2.41)$$

where $C_{i,j} = \int_{y_i}^{y_{i+1}} P(y|R_j) dy$

$$P(y|R_j) = \frac{y}{2R^2} \text{ when } 0 \leq y < 2R$$

is the probability of obtaining a chord y from a drop of size R_j

$$R_j = R_{max} - j\Delta R \quad 0 \leq j \leq m-1$$

and

$$\Delta R = \frac{R_{max}}{m} = \frac{y_{max}}{2m} \quad \text{for spherical bubbles}$$

A matrix can then be formed as follows:

$$\begin{bmatrix} C_{00}\Delta R & 0 & 0 & 0 \\ C_{10}\Delta R & C_{11}\Delta R & 0 & 0 \\ C_{20}\Delta R & C_{21}\Delta R & C_{22}\Delta R & 0 \\ C_{m-10}\Delta R & C_{m-11}\Delta R & C_{m-12}\Delta R & C_{m-13}\Delta R \end{bmatrix} \begin{bmatrix} P(R_0) \\ P(R_1) \\ P(R_2) \\ P(R_{m-1}) \end{bmatrix} = \begin{bmatrix} W_1 \\ W_2 \\ W_3 \\ W_{m-1} \end{bmatrix}$$

The W term can be calculated from the measured chord length data, and the $C_{i,j}$ term can also be found from the bubble shape. The solution, $P(R)$, can be found by solving the matrix for $P(R)$.

The model was found to have some instability problems, particularly with small data sets. It was later improved upon with the inclusion of a complicated Parzen window function (Clarke et al., 1996).

2.3.2 Probability Apportioning Method (PAM)

A number of techniques for transforming chord length distributions to drop diameter distributions have been proposed by Simmons et al. (1999) and co-workers (Langston et al. 2001). The simplest of them is the Probability Apportioning Method (PAM) (Simmons et al., 1999). The method assumes that the drop diameter bins are known prior to the calculation and back-calculates the diameter distribution from the chord length distribution using equation:

$$P(y_1, y_2) = \frac{\sqrt{d^2 - y_1^2} - \sqrt{d^2 - y_2^2}}{d} \quad (2.42)$$

where $P(y_1, y_2)$ is the probability of obtaining a chord length between y_1 and y_2 , from a drop diameter d . Since the drop diameter distribution is not known, a trial set of diameter bins has to be chosen. This can be the same as the chord length size bins.

To use the technique the chord length data have to be placed in chord length bins, while the largest chord length is set equal to the largest drop diameter. The chord bins have to be set at a width appropriate to the number of chord lengths measured, which can be determined by trial and error. Problems arise in the solution when there is insufficient chord length data in narrow bins. The resulting probabilities of each chord length for all bin sizes are summed and the distribution for each d_i collected. To account for the fact that the larger drops are more likely to be measured, the summed values, P_i , are divided through by the diameter, d_i , and then normalised. These values can be plotted against the diameter bands to give a distribution of drop diameters. The narrower the diameter bands chosen, the more precise the drop diameter distribution will be. However, narrow bands require more chord length data to prevent 'un-real' distributions. In the PAM method each set of data is used in isolation from the others, and does not benefit from the collective information that other methods benefit from. PAM, on the other hand, does not suffer from the stability problems associated with the method by Turton and Clark (1988).

2.3.3 Finite Element Method (FEM)

The FEM technique, was suggested by Simmons et al. (1999) as a more robust alternative to PAM because it uses the entire set of measured chord length data to produce the diameter distribution. It uses the Galerkin finite element method to simultaneously solve the equations relating the chord length to the drop diameter distribution. The model is based on equation (2.42) from PAM with the addition of a bandwidth, $2w$, in order to produce a continuous distribution from the discrete data available. It is therefore possible to assume that the probability of a chord with length y from a drop in the diameter bin k is,

$$P_k(y) = \frac{\sqrt{d_k^2 - (y-w)^2} - \sqrt{d_k^2 - (y+w)^2}}{d_k} \quad (2.43)$$

where d_k is a drop diameter in bin k , and w is half the width of the diameter bins. For a polydisperse system, the total number of chord lengths of size y , $\hat{n}(y)$, can be found by summing all the contributions from all the drops,

$$\hat{n}(y) = \sum_{k=1}^K n_k P_k(y) \quad (2.44)$$

where n_k is the number of drops in the system in the k th diameter bin. If experimental information is lacking, the diameter bins can be set equal to the chord length size bins. The quality of the discretised element, the residual at the point y , can be found from equation (2.45), where $n(y)$ is the true number of counts at chord size y ,

$$R(y) = n(y) - \hat{n}(y) = n(y) - \sum_{k=1}^k n_k P_k(y) \quad (2.45)$$

To obtain the total weighted residual of the discrete system the above equation can be integrated over all values of y . The solution will be the set of n_k that gives the minimum weighted residual. The weighting residual for the Galerkin finite element

method is shown in equation (2.46), ensuring that the total residual is minimised with respect to variations of n_k at all drop diameter bands.

$$R_i = \int_0^y \frac{\partial \hat{n}(y)}{\partial n_i(y)} (n(y) - \hat{n}(y)) dy \quad (2.46)$$

There are now the same number of equations as drop size bands.

By differentiating equation (2.44) and substituting it into equation (2.46) the following equation is obtained,

$$R_i = \int_0^y P_i(y) [n(y) - \hat{n}(y)] dy = 0 \quad (2.47)$$

Substituting equation (2.45) into the above equation yields,

$$R_i = \int_0^y P_i(y) \left[n(y) - \sum_{k=0}^K P_k(y) n_k(y) \right] dy = 0 \quad (2.48)$$

where $n(y)$ are the number of chord lengths of length y , and n_k are the estimates of the number of drops at the band k . This can be rearranged to give a linear system of equations for n_k

$$[A]\{y\} = \{b\}$$

where $[A]_{i,j} = \int_0^y P_i(y) P_j(y) dy$,

and $\{y\} = n_i$ (the solution vector)

$$\{b\}_i = \int_0^y P_i(y) n(y) dy$$

The FEM method was developed to overcome the problems associated with the PAM method. However while the FEM overcomes the problem of not knowing the diameter bands, it can be inaccurate with discontinuous chord distributions and therefore often predicts negative drop diameter frequencies.

2.3.4 Probability Apportioning Method 2 (PAM2)

A modified version of the original PAM that addresses some of the problems associated with it and the FEM has been suggested recently (Langston et al., 2001). PAM worked satisfactorily when the diameter ranges were known, but was inaccurate when they were not. The FEM worked well when the diameters were not known, but presented problems with near discontinuous chord length distributions.

PAM2 is an iterative method that uses Bayes' theorem to calculate the drop diameter distributions from a measured set of chord length data. The improvements of PAM2 over PAM are the inclusion of Bayes' theorem for conditional probabilities which states:

$$P(A_i|B) = \frac{P(B|A_i)P(A_i)}{\sum_{k=1}^N P(B|A_k)P(A_k)} \quad i=1,2,\dots,N \quad (2.49)$$

where N is the number of diameter bins; $P(A_i)$ is the probability of cutting a particle with a diameter in bin i ; $P(B_j)$ is the probability of cutting a chord length in bin j ; hence $P(A_i|B_j)$ is the probability that the measured particle is from bin i , and the chord length measured is from bin j ; $P(B_j|A_i)$ is the probability that given a particle from bin i a chord length from bin j will be obtained. Also f_i is the fraction of particles with diameters in bin i , d_i is the representative diameter in bin i , and N_{chord} which is the number of chord cuts.

The process by which the drop diameter distributions are found from the chord length distributions is as follows:

- 1) A uniform diameter distribution across all the diameter bins is assumed:

$$f_i = \frac{1}{N} \quad (2.50)$$

2) $P(A_i)$ for each diameter bin i is calculated:

$$P(A_i) = \frac{f_i d_i}{\sum_{k=1}^N f_k d_k} \quad (2.51)$$

3) For each measured chord Bayes' theorem is used to calculate $P(A_i|B_j)$ for each diameter bin, i , using equation (2.52) to calculate $P(B|A_i)$ This will give a matrix whose columns are the chord bins, j , and rows are the diameter bins, i .

$$P(x_1, x_2) = \frac{\sqrt{d_i^2 - x_1^2} - \sqrt{d_i^2 - x_2^2}}{d_i} \quad (2.52)$$

where $P(x_1, x_2)$ is the probability of obtaining a chord length between x_1 and x_2 from a drop of diameter d_i (equivalent to $P(B|A_i)$)

4) Each value of $P(A_i|B_j)$ is multiplied by the N_{chord} value for the appropriate j , and $P(A_i)$ is recalculated for each i :

$$P(A_i) = \frac{\left[\sum_1^{N_{chord}} P(A_i|B_j) \right]}{N_{chord}} \quad (2.53)$$

5) Using this new $P(A_i)$ value, f_i is recalculated for each i :

$$f_i = \frac{[P(A_i) d_i]}{\sum_{k=1}^N P(A_k) / d_k} \quad (2.54)$$

The procedure is repeated from step (2) if the new value of f_i has changed significantly from the previous value. The method is able to include all the chord

length data in a collective fashion because the calculated distribution is fed back into the algorithm in an iterative process.

2.4 Pressure Gradient and Hold-up Modelling

There is a significant drive to formulate models which are able to predict pressure gradient and hold-up in liquid-liquid flows. Unlike gas-liquid systems, where there is considerable literature on the development of models both general and flow-regime specific, comparatively few modelling attempts have been reported for liquid-liquid flows.

In an early effort, Charles and Lilleht (1965) showed that pressure gradient during stratified oil-water flows could be correlated in terms of the Lockhart and Martinelli parameters Φ and X , modified for liquid-liquid systems. The parameter X is defined as:

$$X^2 = \frac{\Delta P_o}{\Delta P_w} \quad (2.55)$$

where ΔP_o and ΔP_w are the single phase pressure gradients for oil and water respectively, if they were flowing in the pipe at the mixture flowrate. Parameter Φ is defined as:

$$\Phi^2 = \frac{\Delta P_T}{\Delta P_o} \quad (2.56)$$

where ΔP_T is the two-phase pressure gradient.

Theissing (1980) suggested a correlation between Φ and X that was not restricted to a specific flow pattern and accounted for the density ratio of the two phases:

$$\Delta P_T = \left[\Delta P_o^{1/ne} \left(\frac{G_o}{G_T} \right)^{1/e} + \Delta P_w^{1/ne} \left(\frac{G_w}{G_T} \right)^{1/e} \right]^{ne} \quad (2.57)$$

where:

$$e = 3 - 2 \left(\frac{2\sqrt{\rho_o / \rho_w}}{1 + \rho_o / \rho_w} \right)^{0.7/n} \quad (2.58)$$

$$n = \frac{n_1 + (1/X)^{0.2} n_2}{1 + (1/X)^{0.2}} \quad (2.59)$$

$$n_1 = \frac{\ln(\Delta P_{os} / \Delta P_o)}{\ln(G_o / G_T)} \quad (2.60)$$

$$n_2 = \frac{\ln(\Delta P_{ws} / \Delta P_w)}{\ln(G_w / G_T)} \quad (2.61)$$

and G_o , G_w , G_T are the mass flowrates for the oil, water, and mixture respectively, and ΔP_{os} and ΔP_{ws} are the pressure gradients for the oil and water phases flowing at their superficial velocities.

However, the experimental results by Stapelberg and Mewes (1994) suggested that a single correlation would not be able to account for all flow regimes.

Regime specific models have mainly concentrated on stratified and dispersed flows; developments of the two-fluid model, suggested originally by Taitel and Dukler (1976) for gas-liquid systems, have been used in the former case, while the homogeneous model is considered more appropriate for the latter case.

2.4.1 Homogeneous Model

In this model the two phases are considered as fully mixed to form a homogeneous mixture which is then regarded as one 'pseudo-fluid' with appropriately averaged properties. The pressure gradient is then calculated using single phase flow equations:

$$\frac{\Delta P}{l} = \frac{4f\rho_m U^2}{D} \quad (2.62)$$

where $\Delta P/l$ is the pressure gradient per unit length, f is the Darcy friction factor, ρ_m is the mixture density, U is the mixture velocity, and D is the pipe diameter. The mixture velocity can be found from $\frac{Q_o + Q_w}{A}$ where Q_o and Q_w are the oil and water volumetric flowrates respectively, and A is the pipe cross sectional area. The friction factor is related to the Reynolds number: $f = CRe^{-n}$, where Re is the mixture Reynolds number, and C and n are constants.

The above equations require the density of the homogeneous liquid which can be obtained from:

$$\rho_m = \epsilon_o \rho_o + \epsilon_w \rho_w \quad (2.63)$$

where ϵ_o and ϵ_w are the in-situ oil and water volume fraction respectively, and ρ_o and ρ_w are the oil and water densities respectively. The viscosity of the mixture is more difficult to find. A number of equations have been suggested mainly from emulsion studies and the more commonly used correlations are given below:

$$\mu_m = (1 + 2.5\phi)\mu_c \quad \text{Einstein (1906)} \quad (2.64)$$

where μ_m is the mixture viscosity, μ_c is the continuous phase viscosity, and ϕ is the dispersed phase volume fraction. This model was developed for monodispersed systems.

$$\mu_m = (1 + \phi)^{-2.5} \mu_c \quad \text{Brinkman (1952), Roscoe (1952)} \quad (2.65)$$

which was developed for polydispersed systems

$$\mu_m = \varepsilon_o \mu_o + (1 - \varepsilon_o) \mu_w \quad \text{Dukler et al. (1964)} \quad (2.66)$$

where ε_o is the volume fraction of the oil, and the subscripts o and w refer to the oil and water respectively.

$$\mu_m = \left[1 + \frac{\left(\frac{\phi}{(\phi)_{\mu_r=100}} \right)}{1.187 - \left(\frac{\phi}{(\phi)_{\mu_r=100}} \right)} \right]^{2.5} \mu_c \quad \text{Pal and Rhodes (1989)} \quad (2.67)$$

where $(\phi)_{\mu_r=100}$ is the dispersed phase concentration at which the relative viscosity of the mixture becomes 100. The relative viscosity is defined as the viscosity of the mixture divided by the viscosity of the continuous phase. It is possible to obtain this value in stable emulsions, but for pipeline flows it has to be extrapolated. This is done by calculating the friction factor from pressure gradient data, and from it the Reynolds number and the mixture viscosity can be obtained.

The Einstein (1906), Roscoe (1952), and Pal and Rhodes (1989) models assume that as the dispersed phase volume fraction increases, so does the mixture viscosity due to closer packing of the dispersed droplets, until a maximum is reached at phase inversion. Trallero (1995) found that the Pal and Rhodes model predicted his experimental data satisfactorily, but it does not predict the drag reduction phenomenon that has been shown to exist in two-phase liquid-liquid systems (Pal, 1993; Angeli and Hewitt, 1998).

2.4.2 Two-fluid Model

In the two-fluid model the momentum equations for each phase are written and appropriate wall and interfacial shear stresses are implemented (Brauner and Moalem Maron, 1989; Kurban, 1997). The hydraulic diameters assigned to each phase, as well as the sign of the interfacial shear stress term, would depend on which phase flows faster within the pipe (Brauner and Moalem Maron, 1989). In most cases the interface between the two fluids is considered flat, but Brauner et al. (1998) and Ng et al. (2001) have calculated the curvature of the interface which can then be used in conjunction with the two-fluid model for a more accurate prediction of pressure gradient and in-situ phase volume fraction (Brauner et al., 1998). For no slip between the two phases and smooth interface Arirachakaran et al. (1989) suggested that pressure gradient could be found from the sum of the single phase oil and water wall shear stresses averaged over the wall perimeter wetted by each phase. Comparisons with experimental data showed that this model gave better pressure gradient predictions at low mixture velocities, where the interface during separated flow was smooth.

The difficulty in measuring the interfacial shear stress has resulted in a number of suggested correlations. For liquid-liquid annular flow where the core is the faster flowing phase, Brauner (1991) suggested the following equation:

$$f_i = BC_4 \left(\frac{D_c U_c \rho_c}{\mu_c} \right)^{-n} \quad (2.68)$$

which is used to calculate the shear stress by

$$\tau_i = f_i \left(\frac{\rho_c U_c^2}{2} \right) \quad (2.69)$$

where f_i is the interfacial friction factor, D_c is the diameter of the core phase, U_c is the core phase average velocity, ρ_c is the core density, μ_c is the core viscosity, C_4 and n are constants which depend on the flow regime and B is an augmentation factor

which accounts for interfacial waviness. Brauner (1991) suggested that in liquid-liquid flows the waviness at the interface would be very slight and B should take the value of 1. Neogi et al. (1994), however, used the same approach to model oil-water interfacial shear stress in three-phase, gas-oil-water flows and found from experimental data that the value of B could vary from 0.8 to 1. It has also been suggested (Taitel et al., 1995) that a constant value of 0.014 can be used for the interfacial friction factor except when the wall friction factor of the faster phase is greater than 0.014; in this case this wall friction factor value should be used.

According to Hall (1992):

$$\tau_i = \gamma \tau_o \quad (2.70)$$

where τ_o is the oil wall shear stress and γ is a proportionality factor which must be less than 1. The term γ was calculated from the analytical solution of one-dimensional momentum equations for oil-water laminar stratified flow between parallel plates and was found to be closely related to the water/oil viscosity ratio. In his three-fluid model, Roberts (1996) actually used γ equal to this viscosity ratio.

The above correlations by Hall (1992) and Taitel et al. (1995) and a correlation by Baker et al. (1988), (developed for gas-oil interfacial shear stress) were used in a three-fluid model by Khor et al. (1997) and were compared against experimental data from gas-oil-water flows. Although both correlations by Baker et al. (1988) and Taitel et al. (1995) predicted well the experimental data, the suggestion by Taitel et al. was recommended due to its simplicity.

Analytical solutions were developed by Russell and Charles (1959) and Kurban (1997) for laminar annular and stratified flows respectively. Numerical techniques have also been used for stratified systems provided that the interface height is known (Charles and Redberger, 1962; Kurban, 1997; Ng et al., 2001)

Modelling of the dual continuous flow presents difficulties since this regime combines characteristics of both stratified and dispersed flows. A first attempt to

model this pattern was presented by Guzhov and Medvedev (1971), who considered the mixture of the two phases concentrated around the liquid-liquid interface and treated the system as three-phase flow, with clear oil and water phases at the top and bottom of the pipe respectively and an emulsion phase in the middle (Fig. 2.11). An extension of the two-fluid model for three-phase systems was applied and momentum equations were written for each phase. The relative velocities of each phase were considered similar and as a result the interfacial shear stress terms were eliminated while the interfacial lengths were not included in the hydraulic diameters needed for the calculation of the wall shear stresses. The oil and emulsion volume fractions and the dispersed phase concentration in the emulsion were the required input parameters in this model. The authors, however, did not present any comparisons with experimental data. The model was extended by Vedapuri et al. (1997) to include interfacial shear stresses. Apart from the flowrates of the two phases, this model also required two more input parameters, namely the water fraction and the in-situ velocity of the emulsion layer, which were found from experimental data on in-situ oil-water distribution and on velocity profile respectively. The predicted emulsion and water layer thickness compared reasonably well with experimental data both for horizontal and inclined flows.

Jayawardena et al. (2000) modelled their dual continuous flow as two separate layers, where the lower water phase did not contain any oil dispersed in it and the top oil-continuous layer formed a water-in-oil dispersion. For each layer momentum equations were written using average densities and viscosities. The three parameters needed for the solution of the model were the inlet oil and water flowrates and the height of the free water layer, which was found experimentally from photographs of the flow pattern. The model compared well against experimental data and showed an improvement over the standard two-fluid model.

Based on the above literature it is clear that the current information on liquid-liquid flows is limited, and that the data on the dual continuous flow pattern is even more sparse. In this work the dual continuous pattern will be studied in more detail. Apart from the overall parameters such as pressure gradient and average in-situ hold-up, local parameters such as phase and drop size distribution will also be investigated. The use of local probes will allow the study of these parameters and the clear

limitation of the flow pattern boundaries even at high flow velocities where visual observation is not possible.

The experimental data will be used to develop a two-fluid model for dual continuous flow that takes into account entrainment of one phase into the other.

Authors	Pipe ID (mm)	Pipe Material	Oil Properties			Dual C. boundaries			Observed dual cont. flow patterns	Flow pattern identification method	Other measured parameters
			μ (mPa s)	ρ (kg/m ³)	σ (mN/m)	Min Mixt. vel. Oil %	Max Mixt. vel. Oil %				
Guzhov et al. (1973)	39.4	Steel	21.8	896	44.8	0.3m/s 30-90%	1.6m/s 70-90%	Sep. flow with disp. at int. and water or oil/water bottom layer, emulsion of water/oil & oil/water	Visual observation	ΔP	
Malinoswky (1975)	38.4	Steel	4.6	850	22.3	0.6m/s 55%	2m/s 55%	Do/w & w/o	Visual observation		
Lafin & Oglesby (1976)	38.4	Steel	4.94	828	22.3	0.5m/s 43-64%	1.2m/s 58%	Segregated, Do/w & w/o	Visual observation		
Oglesby (1979)	41		32	868	30.1		1.4m/s 74%	Semi segregated, Semi mixed			
Cox (1985), Scott (1985)	50.1	Acrylic	1.38	754		0.7m/s 30-76%	1m/s 30-76%	Stratified bubble	Visual observation	Hold-up	
Trallero (1995)	50.1	Acrylic	29.6	850	36	0.25m/s, 5-95%	>3m/s 50-62%	ST & MI, Do/w & Dw/o	Visual observation	ΔP	
Valle & Kvandal (1995)	37.5	Glass	2.3	794	37.3	0.85-0.9m/s 24-68%	1.7m/s >64%	Stratified wavy-entrain. Stratified wavy with oil and water dispersed zones	Conductivity and sample probes	Dispersed layer ΔP	
Nadler & Mewes (1997)	59	Perspex	22-35	841		0.3m/s 20-95%	1.6m/s 60%	Stratified with mixing at int., Layers of w/o & w or w/o, o/w & w	Conductivity probe	ΔP	
Vedapuri et al. (1997)	101.2	Plexi-glass	2.0			0.4m/s 20-80%	1.4m/s 20-80%	Semi-segregated, Semi-mixed	Isokinetic probe	Dispersed layer height	
Angeli (1996)	24.3	St. Steel	1.6	801	17.0	0.3m/s 32-77%	1.3m/s 66%	Stratified wavy/drops, Three-layer	Mainly visual observation-Impedance probe	ΔP Phase distribution	
Angeli & Hewitt (2000a)	24	Acrylic	1.6	801		0.3m/s 33%	1.6m/s 50%				
Soleimani (1999)	24.3	St. Steel	1.6	801	17.0	0.5m/s 20-85%	1.5m/s 62-66%	Stratified wavy/drops, Three-layer	Visual obs. Impedance probe-Gamma densitometer	ΔP Hold-up Phase distribution	

Table 2.1. Summary of studies carried out at the dual continuous flow pattern

Image removed due to third party copyright

Image removed due to third pa

Fig. 2.1. Flow patterns as described by Trallero (1995)

Image removed due to third party copyright

Fig. 2.2. Flow pattern map by Charles et al. (1961)

Image removed due to third party copyright

Fig. 2.3. Flow pattern map by Guzhov et al. (1973)

Image removed due to third party copyright

Fig. 2.4. Velocity profile of oil-water flow showing water flowing faster than oil
($S=0.5$) (Ng, 2002)

Image removed due to third party copyright

Fig. 2.5. Flow pattern map by Nädler and Mewes (1995)

Image removed due to third party copyright

Fig. 2.6. Pressure gradient data by Nädler and Mewes (1995), where j_f is the mixture velocity

Image removed due to third party copyright

Fig. 2.7. Pressure gradient data by Soleimani (1997) showing peak at phase inversion

Image removed due to third party copyright

Fig. 2.8. Pressure gradient against input oil concentration by Guzhov et al. (1973)

Image removed due to third party copyright

Fig. 2.9. Relevant geometric parameters when a sensor tip is cutting a drop (Weimer et al., 1985)

Image removed due to third party copyright

Fig. 2.10. Relevant dimensions in Probe-droplet interaction (Clarke and Turton, 1988)

Image removed due to third party copyright

Fig. 2.11. Geometry used for modelling the dual continuous flow pattern (Guzhov and Medvedev, 1971)

3. INSTRUMENTATION AND EXPERIMENTAL METHODS

In order to study oil-water flows in horizontal pipes, an experimental pilot scale flow facility was designed, built and commissioned in the Department of Chemical Engineering at UCL. To allow accurate identification and measurement of the flow parameters, various measuring instruments were used. Standard equipment, such as pressure transducers and flowmeters, was purchased from external suppliers, while the more specialised measuring devices were designed and manufactured as part of the project within the Department. The experimental oil-water flow facility is described in Section 3.1 and a schematic diagram is shown in Fig. 3.1a. Pressure gradient and hold-up measurements are described in Sections 3.2 and 3.3 respectively. The local electrical probes used for continuous phase identification, phase distribution and drop size distribution are described in Section 3.4. The oil used (Exxsol D140) was supplied by Exxon Chemicals. Its viscosity was measured for a range of temperatures using a Contraves 155 rheometer. Surface tension and interfacial tension were measured using a Kruss Processor Tensiometer K-12 (oil properties are shown in Table 3.1). Tap water was used as the second phase.

Product Name	EXXSOL D140
Density	828 kg/m ³
Viscosity	6cP @ 25°C
Surface tension	27.6mN/m @ 25°C
Oil-water interfacial tension	39.6mN/m @ 25°C

Table 3.1. Properties of oil used in the study.

3.1 Experimental Flow Facility

The experimental facility consists of (see also Figs. 3.1a-c):

- Two fibreglass storage tanks with a total volume of approximately 880 litres, one for each of the oil and water phases. These contain baffles to reduce any vortices in the tank which could introduce air into the liquid exiting to the pumps. The baffles also aid separation of any contaminating phases in the tanks. The oil tank is fitted with a cooling coil to maintain a constant temperature. The coil is

attached to a refrigeration unit which is set to a temperature of about 5°C. The coil pipe has an internal diameter of 8mm, and a wall thickness of 1.5mm. The coil diameter is 145mm, its length is 680mm and the pitch is 60mm. The cooling fluid is ethylene glycol and has a flowrate of about 200ml/min, which is sufficient to maintain the temperature of oil in the tank below 31°C even during extensive experimentation and hot ambient air temperatures. The normal operational temperature was approximately 25°C. The water temperature is maintained at 25°C by continuously draining and re-filling the water tank. This process also helps to remove any excess heat from the oil during the mixing of the two phases in the pipe.

- Two centrifugal pumps (Ingersoll-Dresser CPX200) capable of generating a flowrate of $4 \times 10^{-3} \text{ m}^3/\text{s}$ at 450kPa. As the pumps have a fixed flowrate, recycle pipes have been installed to allow fluid return back to the storage tanks to help regulate the flow. The flow of each fluid to the recycle pipe and the test section is controlled by gate valves. Care must be taken not to have these valves too closed as this can cause large pressure drop across the valves resulting in excessive heat generation.
- Two armoured variable area flowmeters (ABB Instrumentation 10A5400) are employed which are connected to a computer for data logging. They have a range of 0-240 l/min, with an accuracy of 1% full scale and are calibrated to be specific to the fluid used. Two smaller flowmeters (also ABB Instrumentation 10A5400) with 2% full scale accuracy are used for the lower flowrates. The oil flowmeter has a range of 0-20 l/min, while the water flowmeter has a range of 0-6.5l/min. All flowmeters have been calibrated specifically to the fluid used. Depending on the experimental conditions, either the large or small flowmeter for each phase is inserted into the facility after the pumps to ensure accuracy at a wide range of flowrates.
- A stainless steel test pipe with an internal diameter of 38mm, which consists of two, eight metre sections. Each section is made from two-metre and one-metre lengths connected with tri-clamp fittings which provide a near seam-free connection. This provides the ability to rapidly alter the total length of the test pipe and to move instrumentation to different positions along each of the sections. The two sections are connected with a 180° turn. The whole test pipe can be

inclined from the horizontal to approximately 10° . The inlet configuration of the two fluids is a modified T-junction (Fig. 3.2), with the water phase entering beneath the oil phase. There is a 90° elbow prior to the first test section, after the T-junction.

- Two one-metre long transparent acrylic pipes. These can be placed between any two steel lengths and allow visualisation of the flow. They are also equipped with Quick Closing Valves (QCV) at both ends. The QCV are used to trap the oil-water mixture between them, which can then be drained to a graduated cylinder to measure the in-situ volume fraction.
- One separator vessel of approximately 800 litres that contains a KnitMesh coalescer (DC9201, KnitMesh Ltd.) to aid the separation of the oil-water mixture after the test section. The mesh has a large surface area and is made from two materials with different free surface energies. These different materials aid the coalescence of the two phases as each material (one plastic and one metal) is wetted by only one of the phases. The mesh is located 0.97m from the fluid inlet pipe in the separator tank. It also reduces the turbulence inside the separator and further aids separation by gravity. The size of the vessel has been calculated to give a residence time that is sufficiently long to allow separation of the smallest dispersed drops (approximately $50\mu\text{m}$) expected at the high mixture velocities that were planned to be used in this work. The separator tank has exit pipes to each of the two storage tanks. The exit flow is controlled by ball valves which allow the interface level within the separator to be maintained approximately in the middle. This prevents the flow of one phase into the storage tank of the other.
- One computer with HPVee software for data logging allowing data from the flow meters, pressure transducers and the conductivity probe to be recorded at 10Hz simultaneously.
- One computer with custom made software in MS-DOS for the logging of the data from the impedance and the dual impedance probes. The logging frequency varies and is the same as the sampling frequency.

The above configuration allows continuous operation of the flow facility.

At the beginning of each experimental run the water storage tank was filled with fresh water via a hose straight from the mains supply. Fresh water was used as growth of micro-organism was observed in water that was left for a period of time after an experiment. During hot weather, and periods of extensive use, the storage tank was continuously filled with fresh water and drained at the same time as this helped to maintain both the water and oil temperatures.

3.2 Pressure Gradient Measurements – Pressure Transducers

A Validyne DP103 differential pressure transducer coupled with a CD223 digital transducer indicator were used for pressure gradient measurements. The pressure transducer has a maximum pressure rating of 22kPa and an accuracy of 0.25% full scale. The indicator is attached to the PC which can log pressure gradient data at a rate of 10Hz. Each of the 8 meter pipe sections has two 2 meter pipe lengths with pressure tapping ports. The transducer is connected to the stainless steel pipes of the test section by hard walled, flexible Dekabon tubing. A system comprising of quick connect couplings was devised for easy changing of the measuring locations. The male adapters of the quick connect couplings are fitted to the test section and the female adapters are fitted to one end of the Dekabon tubing from the pressure transducer. These are special auto shut-off, flat face connectors that prevent any air entering the tapping line during connection and disconnection. The dimensions of the pressure ports were carefully designed so that the port openings in the test section have a bore size $1/8^{\text{th}}$ of the total pipe diameter. This bore size was maintained for 3 bore sizes (Perry and Green, 1984) (Fig. 3.3).

The pressure tapping lines are fitted with pressure ‘snuffers’ between the transducer and the pressure ports which are designed to reduce pressure shock waves which had been observed during initial pressure gradient measurements. The snuffers consist of a metal tube (2.5cm diameter, 8.5cm long) considerably larger than the tapping line diameter. Inside the snuffer are 3 evenly spaced randomly perforated discs which are designed to break up shock waves so that their energy is dissipated prior to reaching the transducer diaphragm. The snuffers are incorporated into a valve assembly which allows easy change to a manometer when the pressure gradient falls below the range of the transducer (Fig. 3.4). An inverted manometer was used at the lowest mixture

velocity (0.7m/s) using water as the measuring fluid. The experimental data from the manometer and the pressure transducer at higher mixture velocities compared well (approximately +/- 3% max.).

3.3 Average In-situ Phase Fraction and Slip Ratio - Quick Closing Valves (QCV)

The transparent sections in the test pipe are fitted with quick closing valves (QCV) at each end allowing a volume of the oil-water mixture (800ml) to be captured and in-situ average phase fraction to be measured. The transparent sections were fitted with two holes, one for draining at the bottom of the pipe, and one to let in air at top of the pipe. As with the pressure ports, the holes have a diameter $1/8^{\text{th}}$ of the pipe diameter. Any disturbance to the flow was greatly minimised by use of a plug which seals the holes flush with the internal pipe wall. For each measurement the desired flowrates were set and the mixture left to run for a few minutes to obtain steady state. The pumps were then shut off and the QCV simultaneously closed. The bottom hole was then opened and the trapped mixture drained into a graduated cylinder with increments of 10ml while the top hole was also opened to let air in. The volume of each phase was then measured using the graduated cylinder. The accuracy of the measuring cylinder was 5ml giving an error of approximately 0.6%. There was always a small volume of liquid remaining inside the pipe (approximately 5ml), which was assumed to be oil as this was the last phase to flow out of the pipe. This 'missing' oil was added to the amount collected in the cylinder to bring the total mixture volume to 800ml.

3.4 In-situ Flow Behaviour - Local Probes

The above measurements and relevant instrumentation provide information on overall flow properties. Flow pattern identification, apart from at very low mixture velocities, cannot be achieved through visual observation and more detailed information on local volume fraction and continuity in the pipe cross-section is required. In addition other local parameters such as drop size and drop velocity in dispersed flows would help to better understand these systems and explain the trends observed in pressure gradient and hold-up. For these detailed measurements local

probes were used that can detect the different phases at a specific point inside the pipe. Their small size ensured minimum disturbance of the flow. Local probes are sensors with a tip that is sensitive to a property of the phase that surrounds it. Placed in a two-phase mixture, these sensors can differentiate between the phases flowing past the tip. The properties used to distinguish between phases can be electrochemical, thermal, optical, and electrical (Cartellier and Achard, 1991). Electrochemical probes exploit the different diffusivities of ions in liquids. Thermal probes are based on the differences in thermal conductivity between the fluids and have been developed from hot wire anemometry for applications in two-phase flows. In these probes a current crosses a thin resistance and the resulting heat flux dissipates through the surrounding fluid. The magnitude of this flux depends on the liquid velocity and properties around the probe. Optical probes emit light along an optical guide and the reflected light, sensed by a detector, depends on the refractive index of the surrounding phase (Cheremisinoff and Cheremisinoff, 1988). Electrical probes use the differences in electrical resistance or impedance of the two phases. In the current study, where the two fluids used have very different electrical properties, local probes based on the electrical conductivity and impedance were chosen. Compared to the others, electrical probes have the advantage that they are relatively simple and cheap to manufacture.

3.4.1 High Frequency Impedance Probe – Phase Distribution

Impedance probes measure the capacitance and/or resistivity of the phase present at the probe tip. The probe consists of two electrodes connected to an electrical circuit. They have been used extensively in research in various configurations in both gas-liquid and liquid-liquid flows (Das and Pattanayak, 1993; Lang and Auracher, 1996; Angeli, 1996; Soleimani, 1999). The most common configuration for local measurements is to have both electrodes on a single coaxial wire. The shape of the probe tip is important because it is this that will pierce the interface. A sharp pointed tip will be able to pierce the interface more easily without significant deformation. It would also increase the chances of recording small droplets that a blunt tip may not pierce. The tip geometry, however, affects the electrical field around the probe and can be important when the tip is close to the pipe wall. A blunt tip has a non-

spreading electrical field and is therefore less prone to errors caused by the pipe wall compared to a pointed tip (see Fig. 3.5).

Direct current (DC) and alternating current (AC) can both be used in impedance probes. With direct current the probes are easy and cheap to set up, but polarisation effects can occur resulting in electro-chemical attack on the probe tip. This can affect the probe sensitivity during a set of experiments as the tip degrades. Measurements with DC are based on the resistivity of the two liquids which depends on the liquid temperature and purity. As these change during an experiment, some uncertainty is introduced into the measurements. Alternating current is able to overcome some of these problems. With frequencies in the range of a few kilo-Hertz the measurements are primarily still dependent on resistivity and are therefore prone to the uncertainties of changes in liquid properties. However electro-chemical attack on the tip is greatly reduced. With electrical frequencies at the mega-Hertz level the measurements rely on capacitance which is independent on liquid temperature. The disadvantage of using alternating current is that the electronics needed tend to be expensive and can have a limited lifetime.

An impedance probe based on the work of Das and Pattanayak (1993) was designed for this project and constructed by the Electronic Workshop in the Department. The probe is able to detect the difference in electrical impedance between the oil and water phases. The electronics use a variable AC frequency with measurements made when the current is flowing in one direction only. Das and Pattanayak (1993) advised measurements in one direction as this eliminates the risk of obtaining different results from each direction. For each alternating current cycle a count is given representing the amount of time in which the probe is in oil. As the duration of the total cycle is known the percentage of oil for that cycle can be calculated. At the beginning of each cycle the value of impedance that exists in the electronic circuitry and wires is measured. During pre-experimental calibration in single phase water, this value, together with the value of water, is set to zero using a compensation potentiometer (Fig. 3.6). The time counter is turned on and off depending on the state of a capacitor rather than by a predetermined value of impedance. The capacitor is charged quickly when the probe tip is in a low impedance water environment, and slowly when it is in a high impedance, oil environment. When the probe is in oil the

capacitor is not charged and the time counter is initiated (Fig. 3.6). This count continues until the probe is surrounded by water which causes the capacitor to be charged and the time counter to stop. If the probe is in oil for the entire duration of the cycle the counter will continue until the end of the cycle giving a maximum count; the capacitor will not be sufficiently charged to stop the counting. If the probe is in water for the whole cycle then the capacitor will be charged quickly and the counter will not be triggered. The counter can only be triggered once in each cycle, meaning that if two oil drops are present during one cycle, only the first drop will be measured (Fig. 3.7). To eliminate this problem the alternating current frequency (equal to the sample rate) has to be set high enough so that even the smallest drop is present at the tip for more than one cycle (Fig. 3.8).

The current frequency, and therefore the sampling rate, and the number of samples can be set using the software that accompanies the probe. High sampling frequencies require a large amount of data to be collected and stored for a set sampling time. Conversely low sampling frequencies require less storage space, but could allow more than one drop to be present at the tip during each cycle. The electronic hardware used allowed sampling frequencies ranging from 2 to 45kHz. For the local volume fraction measurements that are used to obtain phase distribution plots, a frequency of 3.5kHz was chosen. At this frequency each sample cycle lasts 285 μ sec, which corresponds to a drop size of 200 μ m at a mixture velocity of 2.5m/s. At the maximum mixture velocities used the average drop size expected is of the order of 0.5mm (Brauner and Ullman, 2002). Average in-situ volume fractions obtained at this frequency were compared to those at higher frequencies where smaller drops are able to be detected and very little difference was found. This indicates that small drops do not contribute significantly to the volume fraction. At 3.5kHz frequency 21,000 samples were collected resulting in a total sampling time of 3sec. Experiments with longer sampling times (8sec) showed no difference in the measured local volume fraction.

For drop size measurements the frequency was increased to 35kHz so that drops in the range of 50-100 μ m could be detected. By increasing the frequency the number of cycles per drop increases resulting in more accurate measurements of larger drops.

Experiments performed at higher frequencies showed no significant difference in the drop size distributions obtained. At 35kHz the number of samples taken at each location was 120,000 resulting in a sample time of 3.4sec. At these conditions the resulting file size for 50 locations was over 100MB. A Fortran code was written which uses all samples from each location, and calculates the total count (see Appendix A1). The percentage oil present was estimated by comparing the total measured count with the values obtained for a 100% oil and water count.

The wire used for the probe was a semi-rigid coaxial wire (EZ34 Huber – Suhner) with a solid copper outer conductor and a silver-coated copper inner conductor separated by an insulator (Fig. 3.9). The inner electrode has a diameter of 0.2mm and the outer electrode has a diameter of 0.9mm. The wire was coated with a heat shrink insulator which makes the total outside diameter equal to 1.4mm. For phase fraction measurements the tip was cut short with the inner conductor protruding approximately 0.5mm so that the distance between the two conductors was kept to a minimum. This configuration allowed measurements to be made close to the pipe wall.

The probe mounting is shown in Fig. 3.10a and 3.10b. The mechanism allows the probe to scan across a pipe diameter to an accuracy of 0.5mm using the thumbscrew on the mounting. The whole mounting is located on a separate short stainless steel pipe section, approximately 15cm long, with the same internal diameter as the test section. It can therefore be rotated to different angles to allow sampling at any location in the pipe cross section. The probe mounting section can also be placed in between two pipe lengths of the test section and can therefore sample at any distance from the inlet. Measurements were made in the horizontal, vertical and 45° diagonal plane, at 2mm intervals (Fig. 3.11). The measurements at 135° are assumed to be the same as those at 45° due to vertical plane symmetry. At lower velocities where the interface between the two phases was more distinct, different angles were also used to obtain an accurate interface shape. On average 50 locations were sampled, giving 80 measurement positions. By interpolating the measurements over the pipe cross section, the in-situ average volume fraction of the two phases could be found. These results are compared to the Quick Closing Valve results in Section 4.4. Phase

distribution contour plots were also created using Matlab (version 5.0.0.4073 The MathWorks, Inc.) Using these phase distribution plots in conjunction with the conductivity probe results on phase continuity (see Section 3.4.3), entrainment of water in the upper oil continuous phase and oil in the lower water continuous phase can also be found for the dual continuous flow pattern.

3.4.2 High Frequency Dual Sensor Impedance Probe – Drop Size Distribution

A dual sensor impedance probe, with two coaxial wires instead of one, was used for measuring drop velocity and drop size distribution in the two-phase mixture. The electronic hardware is very similar to the single sensor impedance probe described above (Section 3.4.1), but with the addition of a second timing/counting device for the second sensor. The frequencies of the two probes are both controlled by the same device ensuring that the measuring cycles coincide. The frequency used was 35kHz, with 120,000 samples taken at each location. This frequency gives cycles with a 28.5 μ sec duration, which correspond to a drop size of 70 μ m for a mixture velocity of 2.5m/s and to a drop size of 42 μ m for a velocity of 1.5m/s. At this frequency it was found that even at the highest mixture velocity used, where the flow is dispersed, each drop which passed the probe caused a succession of pure water or oil values which indicated that the drop extended to more than one measuring cycle. The two probes are set at the same height inside the pipe, in-line with the flow direction. It is therefore assumed that the mixture detected by the first, upstream probe, will then flow on and be detected by the second probe after a certain time. This time can be found by cross-correlating the signals of the two probes as described in Section 3.4.2.1. From the time and the distance between the probes the drop velocity can be estimated. The velocity can then be used, together with the time duration that the drop was present at the probe tip, to calculate the chord length of the drop that has been intercepted by the probes (see Section 3.4.2.2). The probes are set at a distance 10mm apart, as visual observations at low mixture velocities showed that this distance is greater than the largest drops expected. It is also sufficiently close to ensure cross-correlation is possible. The mounting is designed to allow the sensors to move together at the same height (Fig. 3.12). It can also be rotated at any angle to

allow sampling at any location in the pipe cross section. Measurements were taken every 2mm in the vertical direction to give a total of 20 sample locations.

3.4.2.1 Drop Velocity Measurement - Cross-correlation

The time delay between the two sensors can be found from cross-correlating the two signals. This technique has been used in previous research for calculating interface velocities in pipe flows (Auracher and Lang, 1996) and bubble rise velocities in fluidised beds (Brown et al., 1983; Hasiba and Kojima, 1996), but with different probe configurations. The cross-correlation function, R_{xy} , is calculated as follows:

$$R_{xy}(r\Delta T) = \frac{1}{N-r} \sum_{n=1}^{N-r} x_n y_{n+r} \quad \text{Unbiased} \quad (3.1)$$

$$R_{xy}(r\Delta T) = \frac{1}{N} \sum_{n=1}^{N-r} x_n y_{n+r} \quad \text{Biased}$$

where x and y are the two sets of data, N is the total number of samples, n is the sample number ranging from 1 to N , and r is the lag time interval between the two probes ranging from 0 to m . The summations for each r value are divided by either N or $N-r$. The number of data which have been used to calculate the summed values is $N-r$, however if N is much greater than m then the biased approach can be used (Bendat and Piersol, 2000). The correlation proposed by Hasiba and Kojima (1996) calculates the cross-correlation coefficient function, R_c , by dividing the covariance function with the autocorrelations of the two sets of data (eq. (3.2)). This also has the effect of normalising the data as it gives values from -1 to 1 .

$$R_c(r\Delta T) = \frac{\frac{1}{N} \sum (x_n - \bar{x})(y_{n-r} - \bar{y})}{\sqrt{\frac{1}{N} \sum (x_n - \bar{x})^2} \sqrt{\frac{1}{N} \sum (y_{n-r} - \bar{y})^2}} \quad (3.2)$$

where \bar{x} and \bar{y} are the mean values of x and y respectively. There are no lag times included so there is only one solution. The autocorrelations are special cases when $x_n = y_n$.

A Fortran code has been written to implement equation (3.1) for the data from the dual impedance probe which is able to calculate either the biased or unbiased cross-correlations (see Appendix A2). The output from this program is the cross-correlation function, which reaches a maximum when r is the same as the actual time delay between the two probes. Fig. 3.13 shows a plot of the cross-correlation function against lag time, r , where a clear maximum value can be seen indicating the time delay to be approximately $6000\mu\text{s}$. Since the distance between the two sensors is known (10mm), the local drop velocity can be calculated by dividing this distance with the time delay.

3.4.2.2 Chord length measurement

From the signal of either sensor of the dual impedance probe, the time duration that each dispersed phase drop was in contact with that sensor can be found. Combined with the drop velocity (see Section 3.4.2.1) the chord length of the drop that was intersected by the sensor can be deduced. In a two-phase flow the signal from each probe is expected to take two values, with the oil value being higher than the water value, and resemble a square wave. However in many cases the signal departs from the ideal square wave configuration due to the piercing process of the probe through the liquid-liquid interface. Cartellier and Achard (1991) suggested that this process takes part in three stages (Fig. 3.14). As the probe approaches the second phase, a local pressure surge is imposed causing a thin film of phase 1 to be entrained in phase 2 around the probe tip. As the tip further approaches the second phase, this film begins to drain at a rate dependent on the liquid properties. Finally the film ruptures (stage 2) and in stage 3 the second phase starts to wet the probe tip. This stage causes the rise and fall of the output signal. For a wetting liquid, such as water, where the contact angle θ is less than $\pi/2$ a thin layer of water remains on the probe and the time taken for the water to leave increases.

Another cause of the signal departing from the ideal square wave is the electronics associated with impedance probes. When the probe is wetted by the other phase it will take some time for the signal to reach its final value depending on the capacitance of the circuitry inside the probe hardware. In addition, at high mixture

velocities very small drops might not be present at the probe tip for the whole duration of a sample and in this circumstance the signal would not reach the maximum value for these drops.

To process the signal more easily the output from the sensor needs to be converted to a square wave. This can be done using different methods. The most common and simple is the *single threshold technique*, where the raw signal is compared to a pre-set threshold value. If a data point is below the threshold value it is assigned the value of the water phase (in this case), and if it is greater than the threshold value it is assigned the value of the oil phase. However, errors can occur using this method which arise from the different time delay in the raw signal when the probe is moving from oil to water and from water to oil. Also if the threshold value is not set close enough to the continuous phase value, small peaks in the raw data that could indicate a small drop of the other phase may go undetected. Furthermore, if the liquid mixture has a high dispersed phase concentration, or changes continuous phase, the threshold value cannot be easily set. Teyssedou et al. (1988) found that the optimal threshold value in a gas-liquid system depended on the mean volume fraction of the dispersed phase. A second threshold associated with the second phase can also be used to eliminate some of the problems associated with the single threshold method. However, small drops that do not cause a sufficient increase in the value of the signal above the thresholds can still go undetected.

A further improvement can be made by using the method proposed by van der Welle (1985), where the changes in the signal slope are considered to indicate a change in phase. This is similar to the signal differentiation method proposed by Koribi and Terrada (1978). Using the signal slope rather than its actual value ensures that very small drops, which give rise to very small peaks, can be measured, while the problems associated with lag of the electronic circuitry are eliminated. The method by van de Welle (1985) is used in the current work, and is based on the comparison of each sample to the previous one and to two self adjusting trigger values. The n^{th} sample from the raw data is compared to the $n-1^{\text{th}}$ sample and with two variable maximum and minimum values, n_{max} , n_{min} . At the beginning n_{min} and n_{max} are given the values of pure water and oil respectively that have been measured at the start of the experiment. Where the n^{th} sample is greater than the $n-1^{\text{th}}$, n_{max} is taken equal to

the n^{th} value. If the n^{th} sample is less than the $n-1^{\text{th}}$, then n_{min} is taken equal to the n^{th} value. If the n^{th} value is equal to the $n-1^{\text{th}}$ then n_{max} and n_{min} remain the same. The n^{th} value is then compared to the new maximum and minimum values, which are modified with a threshold value, ν , to account for any noise in the system. If the n^{th} sample is greater than the $n_{\text{min}}+\nu$, then the n^{th} value is set equal to that of oil, and if the n^{th} sample is less than $n_{\text{max}}-\nu$ then the n^{th} value is set equal to that of water. If neither of these statements is true then the n^{th} value is set the same as the $n-1^{\text{th}}$ value. As a result of this procedure the raw data is converted into a series of oil or water values (see Fig. 3.15).

From the square wave signal the time each drop interacted with one of the sensors can easily be calculated (see Fig. 3.15). The chord length of this drop intersected by the probe is then calculated as follows.

$$\text{Chord length} = \text{time that drop is present at sensor tip} \times \text{drop velocity}$$

The change of the raw signal to the square wave form and the calculation of the chord length were implemented in a Fortran code (see Appendix A3) allowing large number of drops can then be sampled easily.

3.4.2.3 Chord Length to Drop Size Conversion

As mentioned in Section 2.3 there are a number of methods available to convert measured chord length distributions to drop diameter distributions. The methods for their use are also described in Section 2.3 and will not be mentioned further here. The methods are compared in Section 5.

3.4.3 Conductivity Probes – Phase Continuity

A conductivity probe was developed for determining the continuous phase in dispersed flows and the interface height in stratified and dual continuous flows. The identification of the two phases still relies on their different electrical properties, but in this case electrical conductance is used and as a result the electronics associated with the conductivity probe are simpler than those of the impedance probe. In the

conductivity probe, when the sensor is in a water continuous phase there is a signal, while when it is in an oil continuous phase there is no signal. The actual value of the signal for water continuous flow depends on the water quality and the configuration of the sensor. In this work the conductivity was measured using an Alpha 800 conductivity meter (Courtcloud Ltd.).

The conductivity probe consists of two single wire probes a certain distance apart, greater than the largest expected drop size. If the gap between the two electrodes is less than this distance, then as the droplets come into contact with both electrodes simultaneously the wrong phase could be interpreted as the continuous one. A distance of 10mm was chosen, which is larger than the largest drop expected in the conditions used in this work. The same probe mounting as that for the dual impedance was used which allows the two electrodes to be moved across the pipe diameter together (Fig. 3.12). Because both wires can move at the same height from the bottom of the pipe, the interface height in stratified and dual continuous flows can be detected with great accuracy. As the probe mounting is on a short length of pipe the assembly can be rotated and phase continuity can be detected at every location in the pipe cross section. This can be useful for the identification of the interface shape.

By measuring local phase distributions and phase continuity with the high frequency impedance probe and the conductivity probe, identification of the flow patterns was possible for the whole range of conditions used in this study.

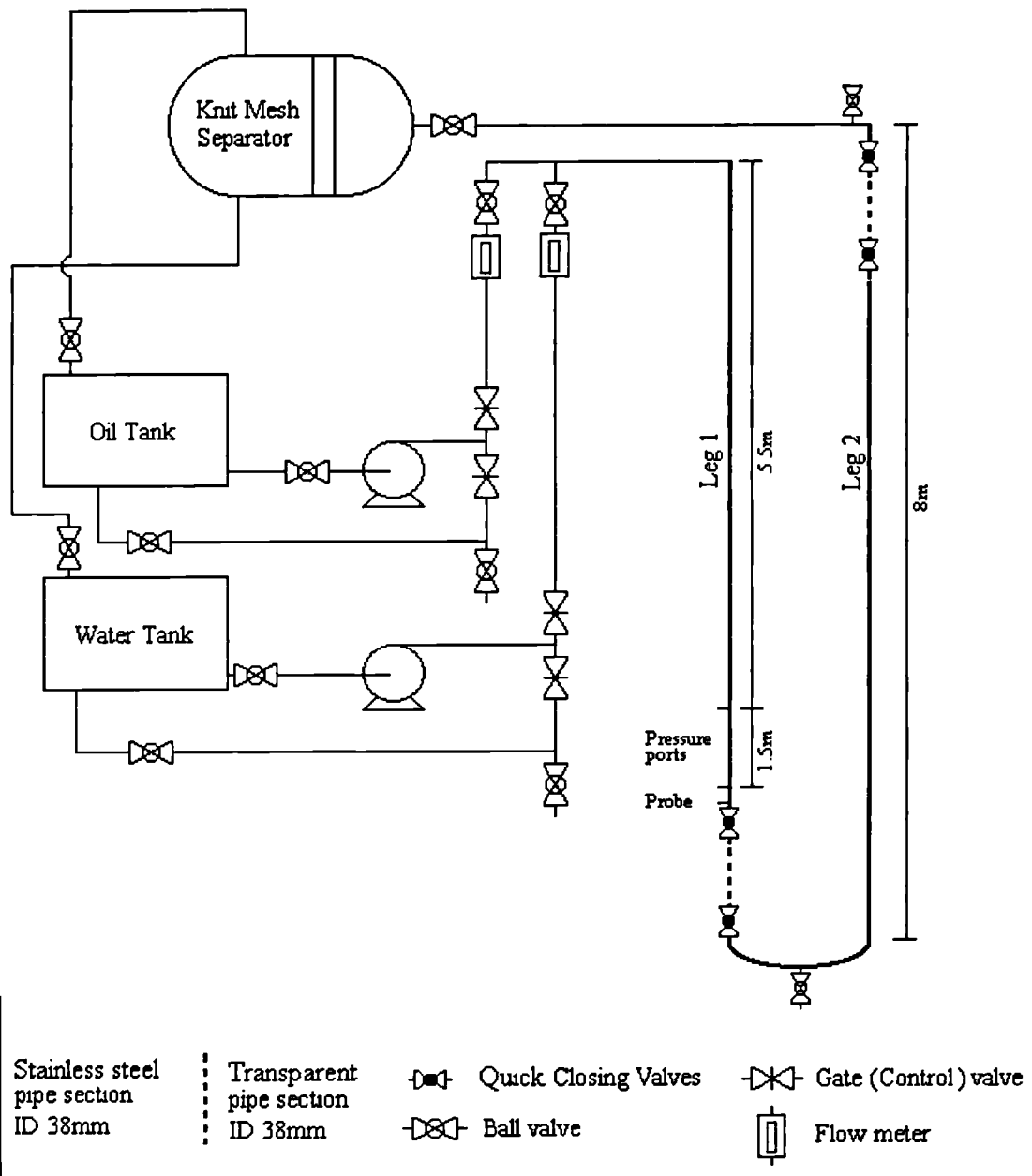


Fig. 3.1a. Experimental liquid-liquid flow facility

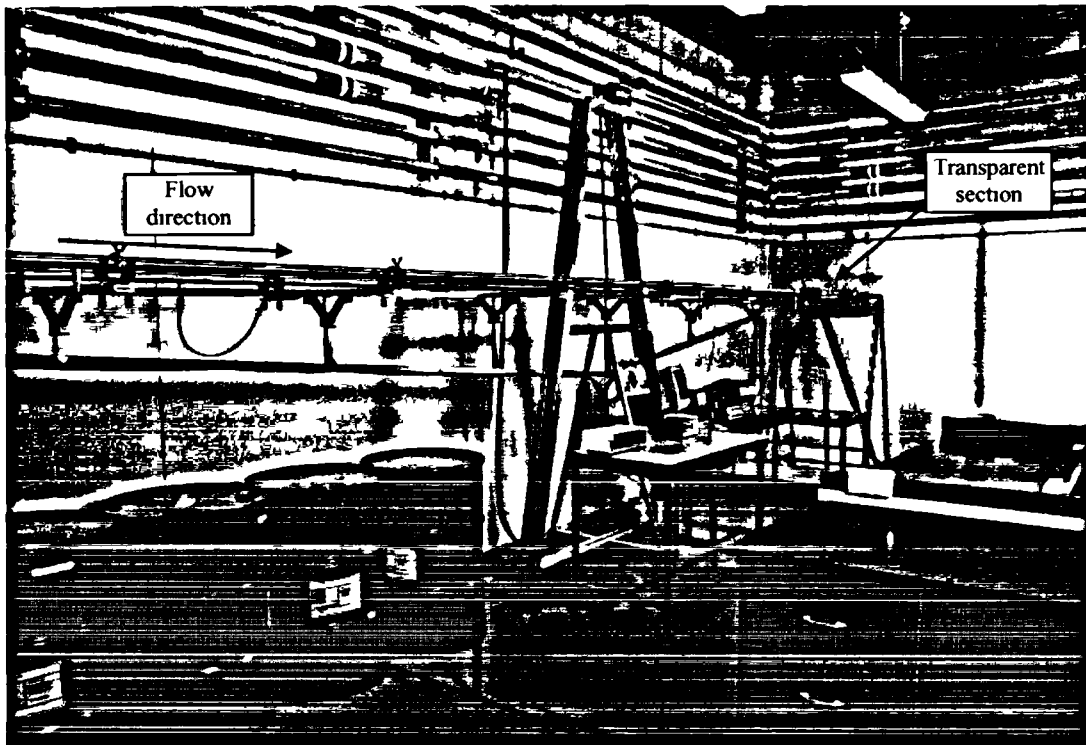


Fig. 3.1b. Photograph of measurement of test section. Measurement location at far end above PC. Inlet to the left of picture



Fig. 3.1c. Photograph of experimental facility showing storage tanks, separator, and inlet to test section. Measurement location to the right of picture

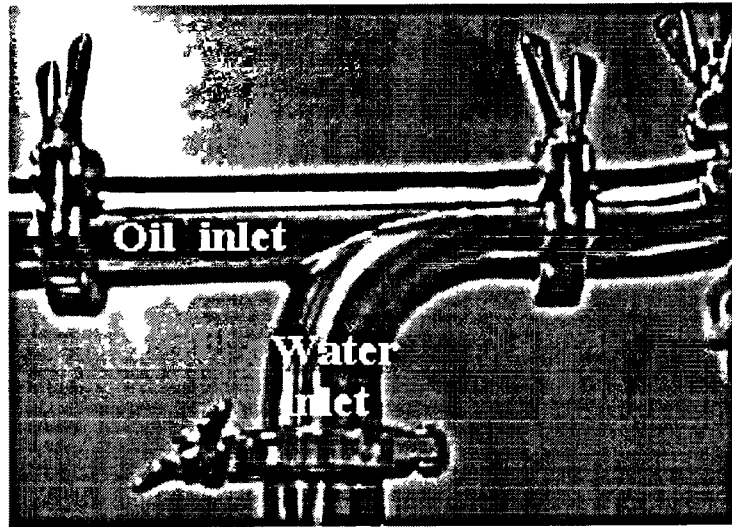


Fig. 3.2. Photograph of modified 'T-junction' where the oil and water phases come together

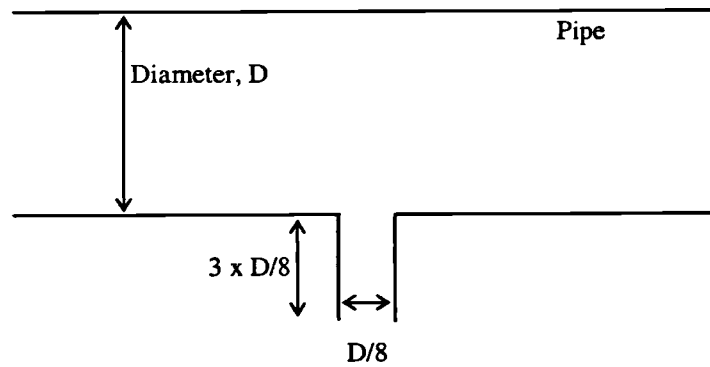


Fig. 3.3. Pressure tapping port

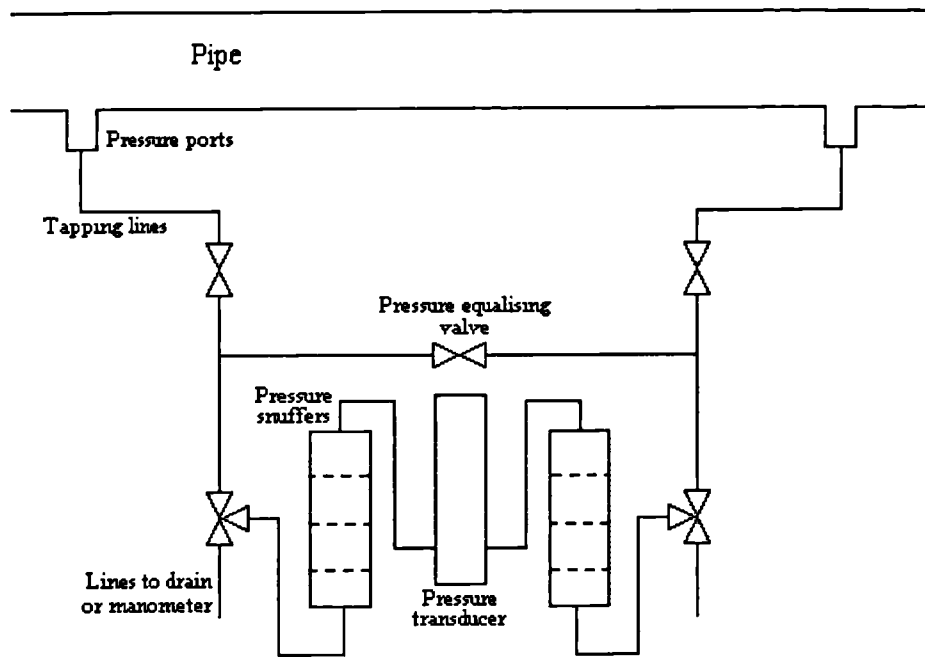


Fig. 3.4. Assembly for pressure gradient measurements

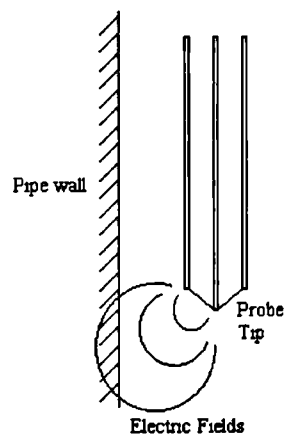


Fig. 3.5. Electrical field around sharp impedance probe tip

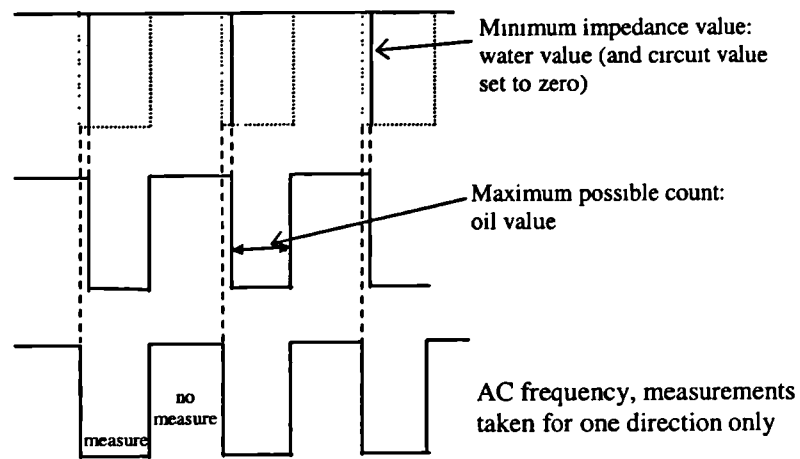


Fig. 3.6. Measuring cycles of impedance probe

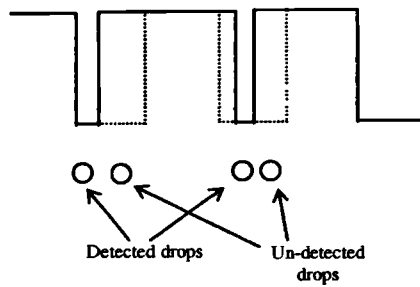


Fig. 3.7. Low sample frequency allowing drops to go undetected

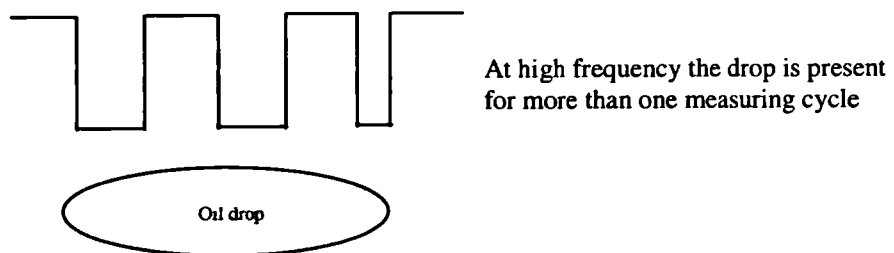


Fig. 3.8. High sample frequency with many cycles per drop

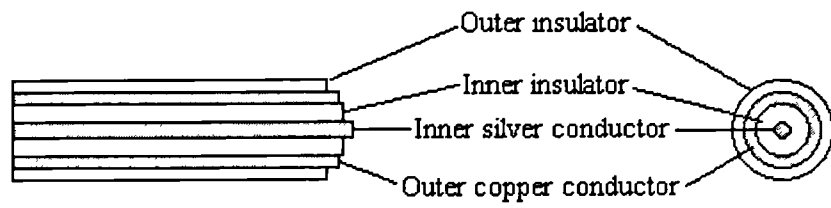


Fig. 3.9. Wire used for high frequency impedance probe

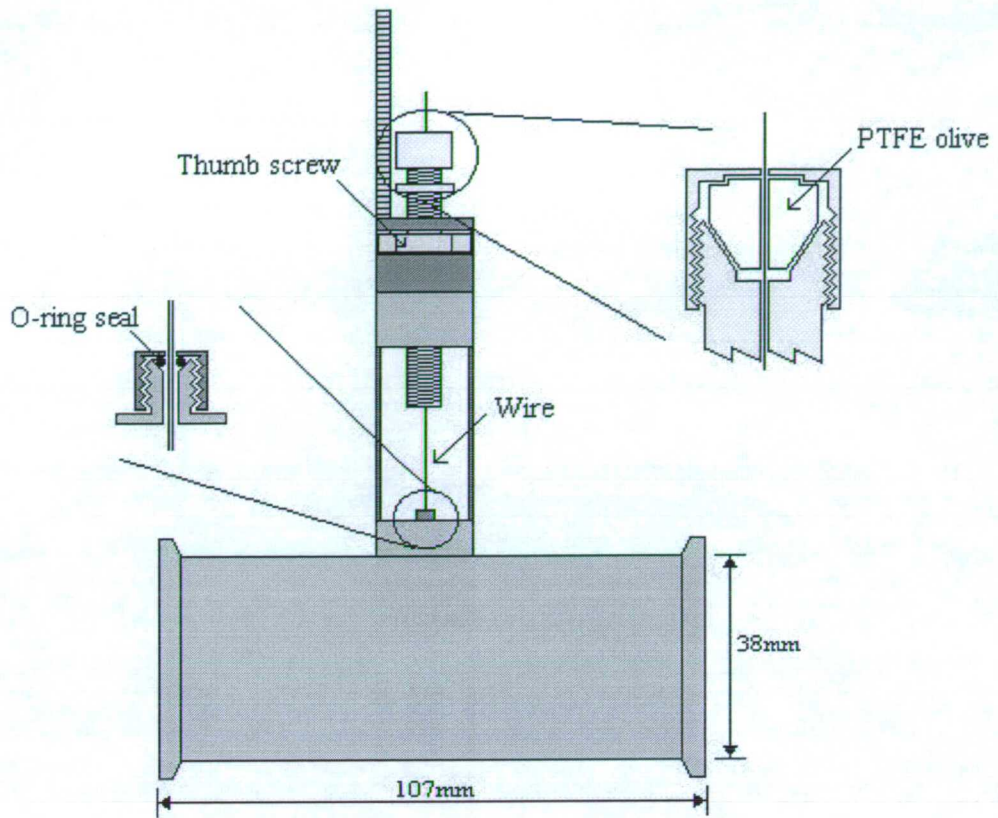


Fig. 3.10a. Impedance probe mounting

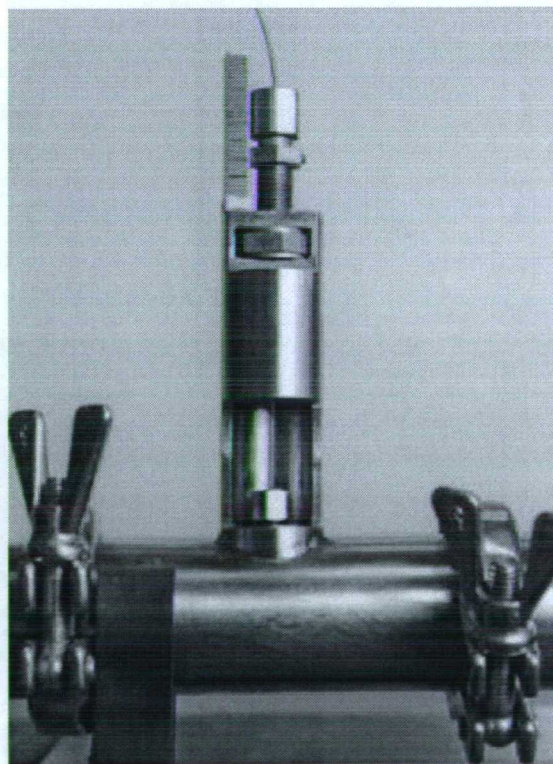


Fig. 3.10b. Photograph of impedance probe mounting between two sections of pipe

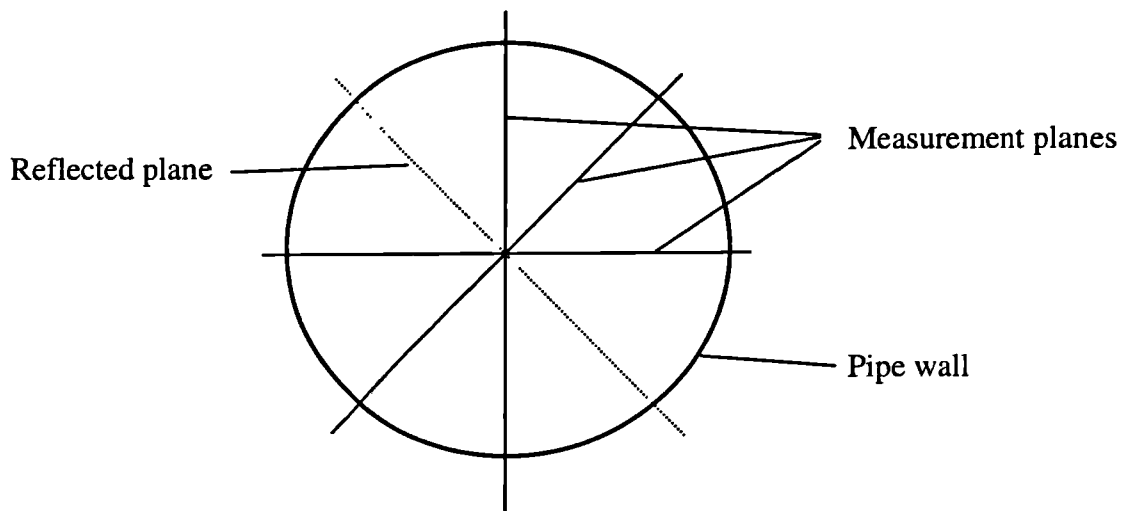


Fig. 3.11. Measurement planes for impedance probe

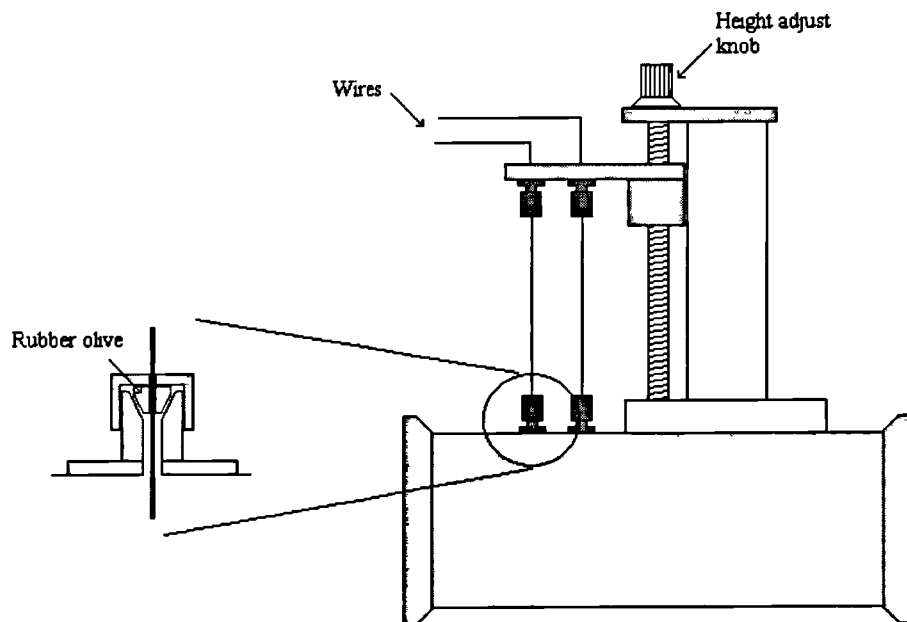


Fig. 3.12. Dual impedance and conductivity probe mounting

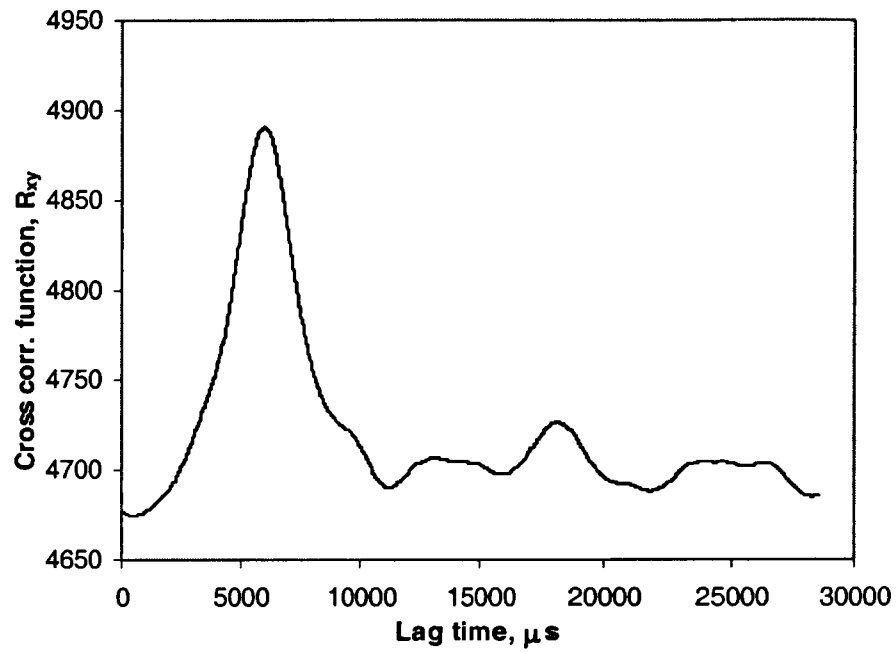


Fig. 3.13. Cross-correlation function against lag time, with time delay between sensors at $6000\mu\text{s}$.

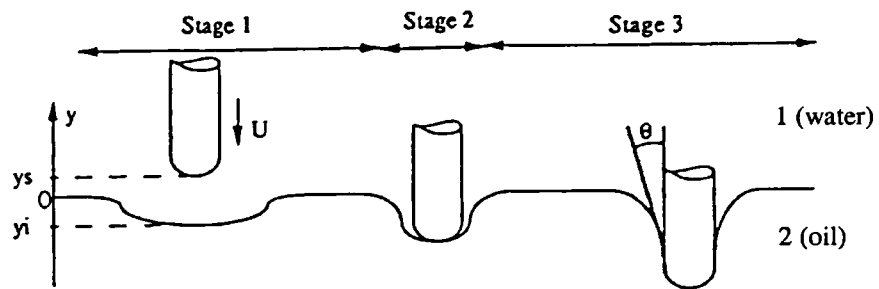


Fig. 3.14. Probe tip interaction with interface (Cartellier and Achard, 1991)

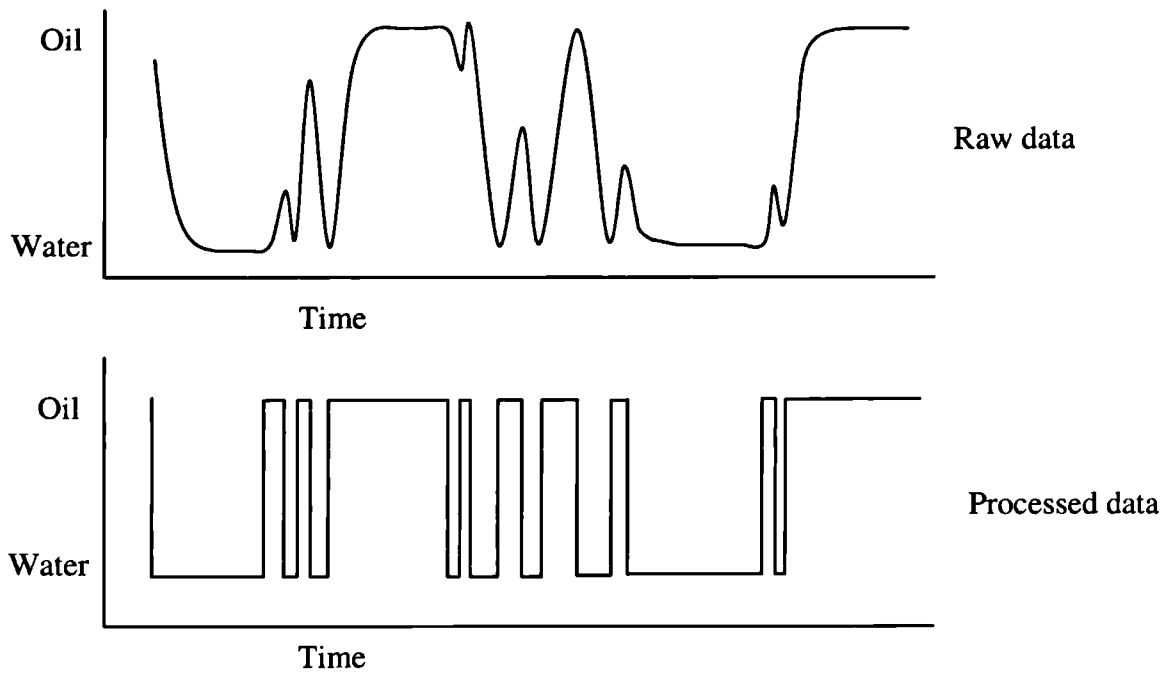


Fig. 3.15. Signal from the impedance probe in the raw and processed square wave form

4. FLOW PATTERN, PRESSURE GRADIENT AND HOLD-UP RESULTS

Preliminary investigations into flow patterns allowed the limits of the dual continuous flow pattern to be established for the flow facility described in Section 3 and the oil shown in Table 3.1. All the experiments were carried out in the first section of the test pipe unless otherwise stated. Pressure gradient readings were taken between 5.5m and 7m, and the local probes were situated at 7m from the entrance of the test section (see Fig. 3.1). Before each experiment single phase oil was run through the pipe.

Experiments were performed for input oil fractions from 0 – 100% with increments of 10% at the extremes, but up to 2% at the intermediate range of volume fractions where variations in pressure gradient were observed (68-80%). The mixture velocities used were 0.7 – 3.5m/s.

4.1 Flow Development

All flow measurements were taken at a distance of 7m from the inlet of the test section. At the inlet the two liquids are combined in a modified 'T' piece (see Fig. 3.2) and then pass through a 90° elbow before entering into the straight test pipe. It was therefore necessary to ensure that the flow had become fully developed by the time it had reached the measurement location. The development of the flow was studied using phase distribution diagrams along the test pipe at 2m intervals using the high frequency impedance probe. The probe was moved from the bottom to the top of the pipe along the vertical and the two 45° diagonal axes, and also all along the horizontal axis, at 2mm increments. This provided 80 measured locations. From these diagrams the flow pattern can be further identified, and the interfacial curvature observed.

Figs. 4.1 a-d show the flow development at 1m/s mixture velocity, 50% input oil fraction at locations 1m, 3m, 5m and 7m from the inlet of the test section respectively. It can be seen that at this low velocity where there is low dispersion

around the interface, the flow pattern develops very quickly. At a higher mixture velocity (2m/s 72% input oil fraction) where the flow is more dispersed the flow pattern again becomes fully developed before 7m (Figs 4.2a-d). It can be seen that the flow pattern is in a transient state after the pipe inlet, however by 5m from the inlet its final form has been established.

Based on the above diagrams the flow was considered fully developed at 7m where measurements were taken.

4.2 Flow Patterns

As mentioned in Chapter 2, during the simultaneous flow of two immiscible liquids a number of different flow patterns can form depending on the flow velocity, the input phase fraction, and to some degree the pipe material. As mentioned there has been some discrepancy in the names assigned to different flow patterns, particularly those occurring between stratified and fully dispersed flow. For this work, flow patterns where both the oil and water phases retain their continuity at the top and bottom of the pipe respectively, with a degree of dispersion of one phase into the other are classified as *dual continuous* flow.

The flow patterns were identified using a number of techniques. Visual observation and high speed video recording were used through the short transparent section. Although it has been shown that the pipe material can effect the flow pattern (Angeli, 1996) it can be assumed that for such a short section of transparent, acrylic pipe, the flow patterns remained the same as in the preceding 7m of stainless steel pipe. These two 'visual' techniques could only be used at the lower mixture velocities where dispersed phase fraction was low. At high mixture velocities the dispersed phase fraction was too high and the flow pattern unable to be identified.

The second method was the use of the conductivity probe. The two sensors were placed at the same height (see Fig 3.12), and moved together from the bottom to the top of the pipe at 1mm intervals while the data was logged for 10sec at each location. Averaged values were then taken at each location and these results plotted to give a 'conductivity profile' along the vertical pipe diameter where high conductivity

values represent water and low values represent oil. There was a 'wall effect' which resulted in the conductivity value decreasing as the probe approached the wall even in pure water flow. The problem was partially overcome by measuring the conductivity in pure water at all vertical locations inside the pipe, and using these values as a reference point for the two-phase flow. An example of a conductivity profile is shown in Fig. 4.3 for dual continuous flow. The values for continuous oil appear constant, however at the lower part of the pipe where water is continuous the conductivity values are high, but not constant despite taking into account the wall effect. This is because the conductivity values are also affected by the dispersed oil fraction. For this reason the sensor was used to find out whether an interface existed or not that would indicate the presence of dual continuous flow or fully dispersed flow. In fully dispersed flows it also indicated the continuous phase. The results of the conductivity probe were used in conjunction with the phase distribution diagrams from the impedance probe which confirmed that low or high conductivity values corresponded to high or low oil fractions.

The high frequency impedance probe (as described in Section 3.4.1) can also give the extent of interfacial dispersion. The probe was moved in the same way as for the flow development studies. Measurements were taken from the bottom to the top of the pipe, along one diagonal axis, and half the horizontal axis. This provided 50 measured locations, which becomes 80 when the data is reflected in the vertical axis. At mixture velocities below 1.5m/s where dispersion was concentrated around the interface the diagonal axis was often altered to ensure that the small amount of dispersion was measured. Integrating the volume fraction data at each location over the whole pipe cross section allows the average in-situ phase fractions to be found.

Using the above methods three main patterns were identified which are shown in the flow pattern map in Fig. 4.4, plotted in terms of mixture velocity against input oil volume fraction. At mixture velocities lower than 0.8m/s *stratified wavy* (SW) (Fig. 4.8a) flow was observed. There was a clear interface between the two phases with no entrainment. The wave amplitude was approximately half the pipe diameter, and the wave length approximately one pipe diameter for the mixture velocities studied. Drops of one phase into the other and the onset of *dual continuous* flow appeared at 0.8m/s mixture velocity, with initially only few drops existing at the interface. At the

lower mixture velocities, during the dual continuous regime, the dispersions were mainly concentrated around the interface; as the mixture velocity increased the amount of the dispersed phase within the continuum of the other increased and extended towards the pipe wall. At 0.8m/s the dispersion was located around the interface, a flow pattern identified as *stratified with mixing at the interface* (ST & MI) flow by Trallero (1995). Fig. 4.5 shows the phase distribution for 0.8m/s, 80% input oil fraction, where it can be seen that the dispersion extends to a 'thickness' of approximately 2-3mm around the interface. The transition between SW and dual continuous flow coincided with a decrease in the interface wave amplitude of the SW flow. As mentioned above, the dual continuous flow pattern includes any pattern where both the oil and the water phases remain continuous while there is a degree of dispersion of one phase into the other. There has been no attempt to try and subdivide the dual continuous flow pattern into other flow patterns, as further subdivision would require knowledge of the extent and height of dispersion in each continuous phase. Apart from at the lowest velocity, this would be difficult to identify as some drops do seem to reach the top or bottom the pipe for nearly all cases. Furthermore, it would be difficult to compare these subcategories with literature, as most reported patterns have been classified based on visual observations and not on quantitative criteria such as dispersion height.

Up to a mixture velocity of 1.5m/s, dual continuous flow was observed for all input oil fractions studied (10% - 90%). Fig. 4.6 shows the phase distribution diagram for 1.5m/s, 68% input oil fraction where it can be seen that the dispersion is more spread into each continuous phase when compared to 0.8m/s mixture velocity (Fig. 4.5). Further increase of the mixture velocity decreased the range of input oil fractions where this pattern appeared, and limited it at intermediate fractions. At greater or lesser oil fractions the flow pattern was *dispersed with oil* (Dw/o) or *water* (Do/w) as the continuous phase respectively. Fig. 4.7 shows the phase distribution for 2m/s, 90% input oil fraction where the flow pattern is oil continuous, with the water completely dispersed. However it is clear from the diagram that there is still a vertical concentration gradient, with a higher water fraction at the bottom of the pipe. At 3m/s and 72% input oil fraction, the flow pattern was dual continuous, however visual observations suggested that there were waves or slugs of oil continuous and water continuous flow with a wavelength of approximately 1-2m. These were seen

as a colour difference between the two continuous phases. Above 3m/s, dual continuous flow did not appear at any oil fraction. At 3.5m/s the change from a water continuous dispersion to an oil continuous dispersed occurred between 68% and 72% input oil fraction.

Photographs taken of the flow structure at low mixture velocities help illustrate the different patterns that make up the dual continuous flow pattern. Fig. 4.8b shows the pattern at low mixture velocities where the dispersion is very slight, with few drops located around the interface. This flow pattern has been identified as *Stratified with mixing at the interface* (ST & MI). As the mixture velocity increases to 1.5m/s the dispersion increases, but generally remains around the interface (Fig. 4.8c). It can be seen, however, that there are oil drops dispersed throughout the water continuous phase, with occasional drops at the very bottom of the pipe. Finally at 2m/s mixture velocity, and 68% input oil fraction, the dispersion is spread throughout the continuous phase and drops reach the opposite pipe wall (Fig. 4.8d). All three of these flow structures are considered dual continuous in this study.

The data on entrainment of one phase into the other during oil-water, dual continuous flow, obtained by the impedance probe is shown in Fig. 4.9, as dispersed phase fraction in the upper (oil continuous) and lower (water continuous) phases. In general, as the mixture velocity increases the dispersed phase fraction in the upper and lower phases also increases. The degree of entrainment of one phase into the opposite also increases as the input volume fraction of this phase increases. For the same input fractions and mixture velocities, it appears that the oil has a greater tendency to disperse into the lower water continuous phase, than the water has to disperse into the upper oil-continuous phase. Due to the limited amount of data, it would be difficult at this stage to formulate a predictive model for the entrainment of one phase into the other; the experimental entrainment values will therefore be used for the solution of the two-fluid model with entrainment, developed in Section 6.

From the existing flow pattern maps only those by Malinowski (1975) and Laflin and Oglesby (1976) have been obtained in conditions close to those of the current work (Table 2.1). In general, Laflin and Oglesby reported a limited range of conditions where dual continuous flow appeared. It can be seen that the onset of dual

continuous flow (ST & MI is their case) occurred at lower mixture velocities than the current study (Figs. 4.10). The onset of fully dispersed flow also occurred in general at lower mixture velocities. Malinowski's data (Fig. 4.11) showed dual continuous flow, (ST & MI), started at mixture velocities as low as 0.53m/s which is also lower than the current work. Dispersed flows also started at lower mixture velocities for oil continuous flows, and for similar velocities for water continuous flows. This start of the dispersed patterns at lower mixture velocities than in the current work could be attributed to the lower oil-water interfacial tension (22.3mN/m in the work by Malinowski, and Laflin and Oglesby compared to 39.6mN/m in the current work). Valle and Kvandal (1995) carried out experiments at similar conditions, i.e oil viscosity and pipe diameter, but used a different pipe material (glass) and mixture velocities only up to 1.7m/s. Dual continuous flow started at approximately 0.8m/s for high and low input oil fractions, and at approximately 1.2m/s for the intermediate ones. This suggests that it is probably the increased energy dissipation close to the wall, when the interface is at the bottom or top of the pipe for high and low oil fractions, that increases drop entrainment in the continuous phases and causes dual continuous flow to occur at lower mixture velocities at these oil fractions.

4.3 Pressure Gradient Experiments

Various initial experiments were carried out in order to understand the characteristics of the experimental rig. Single phase pressure gradient experiments were carried out to find the pipe roughness, and pre-wetting experiments to ascertain if this had an effect on the pressure gradient results. Pressure gradient was measured using a differential pressure transducer as described in Section 3.2, except at the lowest mixture velocities where measurements were taken using an inverted manometer for better accuracy. The experiments were repeated at least twice and the average value from each flow condition taken. The values shown below are the average values.

4.3.1 Single phase pressure gradient

Single phase pressure gradient experiments for both oil and water were carried out to determine pipe roughness. The velocities used were from 0.29m/s to 2.9m/s which

gave Reynolds numbers ranging from 1750 to 18000 for oil, and from 11170 to 111700 for water.

Pressure gradient, ΔP , was used to calculate the friction according to:

$$f = \frac{2D\Delta P}{U^2\rho} \quad (4.1)$$

where U is average velocity, ρ is density, D is pipe diameter, and f is the Darcy friction factor.

Once the friction factor has been found it is possible to calculate the pipe roughness using the Colebrook equation (Colebrook, 1939):

$$\frac{1}{\sqrt{f}} = -2 \log \left[\frac{e/D}{3.7} + \frac{2.51}{\text{Re}\sqrt{f}} \right] \quad (4.2)$$

where e is the pipe roughness, Re is the Reynolds number, and D is the pipe diameter.

A plot of friction factor against Reynolds number is shown in Fig. 4.12 for both the oil and the water, along with the theoretical plot for a smooth pipe. Only those points which have a Reynolds number greater than 4000 have been plotted to ensure that the flow is fully turbulent. The average calculated dimensionless roughness (e/D) for the stainless steel test section is 0.0009, with an actual roughness, e , of 0.032mm.

4.3.2 Initial Pre-wetting comparisons

To determine the effect of initial conditions on pressure gradient, experiments were carried with each phase flowing through the pipe at high flowrate for approximately 5min, before adding the second phase to give the desired mixture velocity and oil fraction. The mixture was then left to flow for about 1min before the pressure gradient data and flow pattern were recorded. It should be noted at this point that the

pipe was always left overnight with water inside. Pressure gradient results obtained with the two initial conditions are compared in Figs 4.13 and 4.14 for mixture velocities 2m/s and 3m/s respectively. The results are fairly similar for the two types of experiments. At the higher mixture velocity the flow pattern is oil continuous above 72% input oil fraction, and water continuous below 68% input oil fraction. There appears to be a trend for the water pre-wetted system to give a lower pressure gradient for water continuous flow. During the dual continuous flow the water pre-wetted system then give higher pressure gradient than the oil pre-wetted system. At the lower mixture velocities, where the dual continuous pattern appears and both phases are continuous, there is less of a trend between the two systems. Flow pattern boundaries determined with the conductivity probe appeared to be similar for the two types of initial conditions. As the results of the effect of the initial phase are inconclusive it was decided for consistency between different data sets to have all experiments starting with single phase oil.

Angeli and Hewitt (1997) carried out similar experiments and found that pre-wetting a stainless steel and an acrylic pipe with either oil or water did have an effect on subsequent pressure gradient. The experimental technique used was slightly different to the current work and involved overnight contacting of the pipe with the appropriate initial phase, before running the initial phase for 30mins through the pipe. The second phase was then introduced for the two-phase experiment. Differences between pressure gradient data obtained from oil and water pre-wetted pipes ranged from 3.6% to 5.8% for high and low mixture velocities respectively.

4.3.3 Mixture velocity comparisons

Two-phase pressure gradient experiments were carried out at different mixture velocities and input oil fractions. The same input conditions as those used for the flow pattern map were used, with mixture velocities ranging from 0.8-3.5m/s, and input oil fractions from 10-90%. The results are shown in Figs. 4.15 and 4.16, where the dotted lines indicate regions where the flow is dual continuous. At high mixture velocities the continuous lines to the left of the dotted lines indicate water continuous flow ($D_{o/w}$), and to the right of the dotted lines indicate oil continuous flow ($D_{w/o}$).

At the lowest mixture velocity (0.8m/s) there is no definite trend in the pressure gradient data, with the slight variations possibly related to the exact nature of the dual continuous flow pattern that exists as explained below. At the slightly higher mixture velocities (1m/s and 1.5m/s) small pressure gradient fluctuations are also observed, but again there is no change in flow pattern occurring. One possible explanation to these fluctuations is the change in interface shape. This can be illustrated by the phase distribution diagrams for 1.5m/s 50%, 68%, and 80% input oil fractions (Figs. 4.17a, b, and c respectively). At 50% input oil fraction the interfacial is strongly curved upwards giving a small oil wall contact area compared to its cross sectional area which results in a low pressure gradient. As the input oil fraction increase to 68% the interface becomes more flat so that the oil wall contact area increases at a greater rate than its cross sectional area resulting in an increase in the pressure gradient. Finally at 80% input oil fraction the water maintains a thin layer at the bottom of the pipe which curves upwards resulting in a large lubricating effect and therefore a low pressure gradient.

At the high mixture velocities (2m/s, 2.5m/s, 3m/s, and 3.5m/s) there are relatively large pressure gradient fluctuations between 60-90% input oil fraction (Figs 4.15 and 4.16). For mixture velocities 2-3m/s these changes appear in the region where the flow pattern changes from Dw/o to Do/w via dual continuous flow. The addition of water in single phase oil results in a decrease in pressure gradient. This reduction in pressure gradient has been observed in previous research and has been attributed to a 'drag reduction' phenomenon (Pal, 1993; Angeli and Hewitt, 1998, Soleimani, 1999). Pal (1993) suggested that the turbulence intensity is modified in the presence of dynamic coalescence and break-up of drops and that the transition from laminar to turbulent flow occurs at higher Reynolds numbers for dispersed systems. It is this decrease in the turbulence that may account for the decrease in pressure gradient. Drag reduction has been found to be stronger in oil than water continuous mixtures and seems to increase with increasing dispersed phase volume fraction.

From Fig 4.16 it seems that as the amount of dispersed water increases the pressure gradient decreases until a water layer separates and dual continuous flow starts (Fig 4.18). At this point the initial thin water film would not have a large amount of dispersed oil drops and may exert a lubrication effect. As the thickness of the water

layer increases, and at the same time as the amount of oil dispersed in it increases, drag reduction will also appear in the water continuous layer (Fig 4.19). Since drag reduction is less strong in water than in oil continuous flows, the relative increase of the water layer compared to the oil layer would result in an overall pressure gradient increase with increasing water fraction. With increasing water fraction the oil layer is finally reduced to dispersed drops in the water phase (Fig 4.20). The drag reduction effect is diminishing and pressure gradient slowly increases to the single phase water value.

At the highest mixture velocity used the increase in pressure gradient at 68% oil is at the point of phase inversion.

There has been little reported pressure gradient data in the literature for dual continuous flow. Trallero (1995) for most of the cases studied, Valle and Kvandal (1995) and Nädler and Mewes (1997) also observed a reduction in pressure gradient compared to that of single phase oil during dual continuous flow, similar to the current work. Guzhov et al. (1973), on the other hand, reported that the two-phase mixture pressure gradient, compared to that of single phase oil, increased with the addition of water during 'water/oil and oil/water emulsion' flow at high oil fractions, and reached a peak, but decreased during 'stratified flow with mixing at the interface and a lower layer of oil/water emulsions' flow, at medium oil fractions. Angeli (1996) found that pressure gradient depended on the pipe material used; in the steel pipe dual continuous flow resulted in higher pressure gradient, while in the acrylic pipe it resulted in slightly lower pressure gradient than that of single phase oil flow. Pressure gradient fluctuations during flow pattern transitions have also been reported by other investigators. Nädler and Mewes (1997) observed pressure gradient peaks at the boundaries of dual continuous flow and fully dispersed flows, while Guzhov et al. (1973) also observed a peak at the transition from water continuous dispersed flow to dual continuous flow.

Comparisons with standard models and a model with entrainment are considered in Chapter 6.

4.4 Velocity Ratio

Average in-situ phase fraction data were obtained using the Quick Closing Valves (QCVs). The experiments were run in the same way as those for pressure gradient. In this case the two-phase mixture was left to run for approximately 3min before simultaneously stopping the pumps and closing the QCVs. The measurement technique and the way to calculate the velocity ratio was described in Section 3.3 using equation (2.1).

Although average in-situ volume fractions could also be obtained from the phase distribution graphs, all the velocity ratio data shown here is from the QCVs. However, the results from the two techniques were compared and this can be seen in Fig. 4.21. It can be seen that all the data falls within the $\pm 15\%$ error lines (dotted) while the average value is 5.8%.

The velocity ratios are plotted against the input oil volume fraction for all mixture velocities studied in Figs. 4.22, 4.23, and 4.24 where dotted lines indicate the dual continuous flow pattern. It can be seen that, in general, as the mixture velocity increases the velocity ratio, S , becomes closer to 1. At mixture velocities greater than 1.5 m/s, S tends to be greater than 1 for low input oil fractions (where the flow is oil dispersed in water), and less than 1 for high input oil fractions (where the flow is water dispersed in oil). This suggests that the dispersed phase is flowing faster than the continuous phase. However, this trend is reversed at a mixture velocities of 1.5m/s and below (Fig. 4.22), where at low input oil fractions S is less than 1, and increases above 1 with increasing oil fractions. At these lower mixture velocities the flow pattern is dual continuous for all input oil fractions.

The trends in velocity ratio were explained with the results from the phase distribution diagrams which indicate the flow pattern formed. Some of these diagrams have already been shown, but are repeated here to facilitate comparisons. As can be seen in Fig. 4.25a for mixture velocity 1.5m/s, at 20% input oil fraction, the oil forms a thin continuous layer at the top of the pipe with a downward curved interface. This means that the oil has a large wall contact perimeter compared to its cross sectional area. The oil therefore experiences large frictional drag, which

reduces its velocity compared to that of water and results in S being less than 1. Fig. 4.25c, shows the phase distribution for 1.5m/s at high oil fraction (80%) where the water forms a thin continuous layer at the bottom of the pipe with an upward curving interface. This means that it is the water in this case which has a large wall contact perimeter compared to its cross sectional area and therefore causes it to flow slower, resulting in S values greater than 1. The transition from S less than 1 to greater than 1 appears at oil fractions below 40% rather than at intermediate input fractions (as would be expected from the two-fluid model (see Section 6)) because the interface curves upwards at intermediate input oil fractions and causes the water to have a higher wall perimeter than the oil and S to be greater than 1 (Fig 4.25b).

At the intermediate mixture velocities during dual continuous flow pattern S is less than 1 for a mixture velocity of 2m/s and greater than 1 for 2.5m/s (see Fig. 4.23). In order to explain this change in S values at similar flow patterns the phase distributions at 68% input oil fraction for mixture velocities 2m/s and 2.5m/s are shown in Figs. 4.26a and 4.26b respectively. At 2m/s the water is forming a semi-annulus at the lower part of the pipe and has a large contact perimeter with the wall. It is, therefore, experiencing higher frictional drag than the oil which is able to flow faster resulting in S being greater than 1. However at 2.5m/s the water fraction has increased in the faster flowing central region of the pipe, while the oil is now forming a semi-annulus at the top part of the pipe. The oil, therefore, has a large contact perimeter with the wall and experiences high frictional drag, resulting in an S value less than 1.

Another interesting phenomenon which occurs between 2m/s and 2.5m/s is the appearance of a high water fraction flowing in the core at high input oil fractions (80%). At 2m/s the flow is dual continuous, with entrainment either side of the interface (Fig. 4.27a). At 2.5m/s the flow is still dual continuous, but there now exists a high water fraction in the core of the pipe (Fig. 4.27b). Data from the conductivity probe suggests that the water core is oil continuous with a high water droplet fraction. Looking at the velocity ratios of these flow conditions, S is greater than 1 for 2m/s while S is less than 1 for 2.5m/s. Using the phase distribution diagrams this can clearly be explained. At the lower mixture velocity the water is generally flowing near the wall in the low velocity region of the pipe and is therefore

being held back giving an S value greater than 1, while at the higher mixture velocity the water is flowing in the centre of the pipe at the place where the highest mixture velocity would be expected. This therefore means that it is flowing faster than the oil giving an S value less than 1.

As with the pressure gradient data there are few velocity ratio data available in the literature for the dual continuous regime. The current results are compared with the available literature data in Fig. 4.28. Comparisons are made for the same (dual continuous) flow pattern at similar mixture velocities, since hold-up depends mainly on flow pattern. Both Cox (1985) and Scott (1985) (mixture velocities used are 0.88m/s to 1.08m/s) and Trallero (1995) (mixture velocities used are 0.9m/s to 1.3m/s) reported a similar trend to the current work for dual continuous flow, with S values increasing with increasing input oil fractions. Their S values, however, did not exceed 1 (apart from few exceptions in the data by Trallero), which could be due to the different pipe material (acrylic) they used compared to the pipe material in the current work (steel). It has been shown (Angeli and Hewitt, 1997) that acrylic is preferentially wetted by oil, which could affect the interface shape and the contact area of the phases with the pipe wall, resulting in higher in-situ oil fractions and lower velocity ratios. Of course the different properties of the fluids used in all these investigations would also have affected the distribution of the phases in a pipe cross section and subsequently the velocity ratio. Soleimani (1999) reported hold-up data at a high mixture velocity (1.25m/s) where dual continuous flow pattern existed at the intermediate input oil fractions (50-74%). For these conditions, his S values were above 1 during dual continuous flow in agreement with the current results.

Little information is also available on phase distribution in a pipe cross section. Soleimani (1999) provides the most complete set of diagrams obtained using an impedance probe and also a Gamma Densitometry System (GDS). The results obtained from the two systems showed that the flow was dual continuous for all conditions studied with the GDS. The interface for nearly all the input fractions was found to curve downwards even at high input oil fractions where the interface is near the bottom of the pipe. This might have been a result of using an acrylic pipe that is preferentially wetted by oil. The lower viscosity of the oil (1.6×10^{-3} Pa s) used by Soleimani (1999) could explain the differences between the results presented here.

Comparisons of the velocity ratio data with a two-fluid model with entrainment developed in this are shown in Chapter 6.

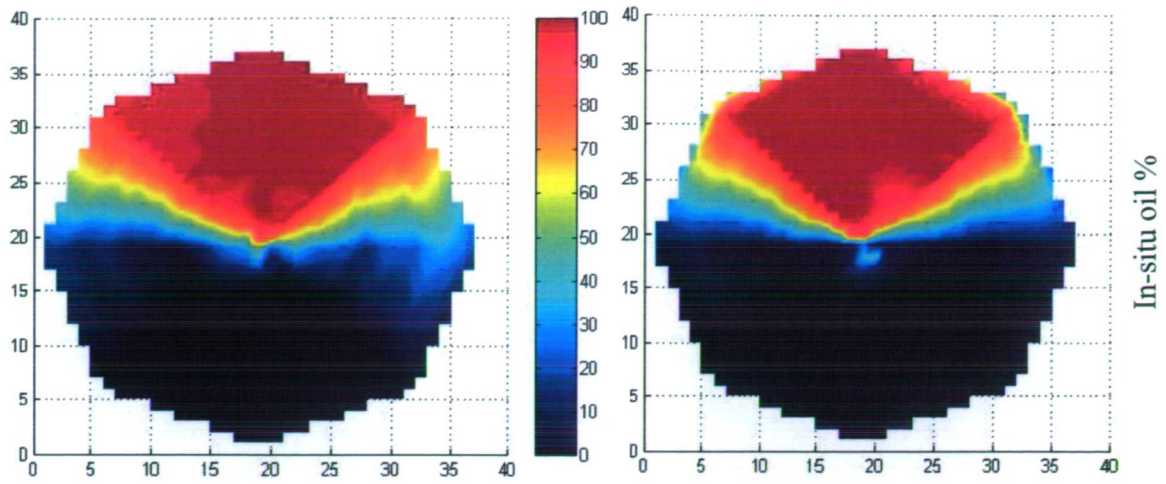
4.5 Conclusions

From the above data it can be concluded that the dual continuous flow exists at the intermediate mixture velocities, with the range of input oil fraction decreasing with increasing mixture velocity. At all except the highest mixture velocity the transition from an oil continuous to water continuous dispersion passed through a region of dual continuous flow.

The pressure gradient results showed evidence of the drag reduction phenomenon seen previously by other researches (Pal, 1993; Soleimani, 1999), especially for oil continuous dispersions. The difference in the magnitude of drag reduction in oil compared to water continuous dispersions confirmed with the phase distribution in dual continuous flow could explain the trends in the pressure gradient observed.

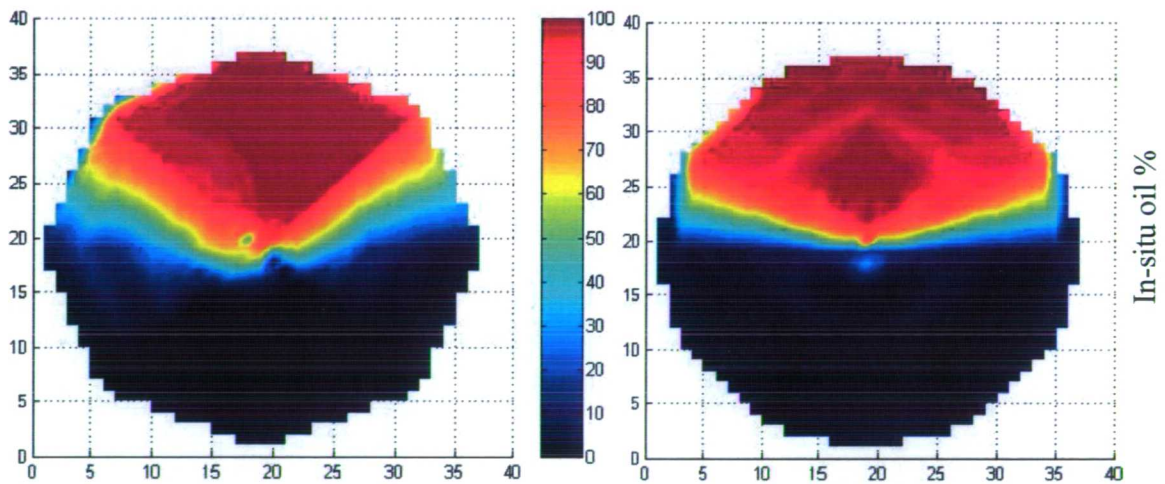
The phase distribution was also shown to have a large effect on the velocity ratio. The increase in S at low mixture velocities from below 1 to above 1 could be explained by the change in interface curvature. Likewise the decrease in S at high mixture velocities could again be related to the distribution of the phases.

The distribution of the drop size in the dispersed regimes in analysed is Section 5, while the comparison of pressure gradient and velocity ratio with the model developed in this study is analysed in Chapter 6.



a. 1m from test section inlet

b. 3m from test section inlet



c. 5m from test section inlet

d. 7m from test section inlet

Fig. 4.1. Phase distribution diagram at mixture velocity 1m/s and input oil fraction 50%, at different distances from test section inlet

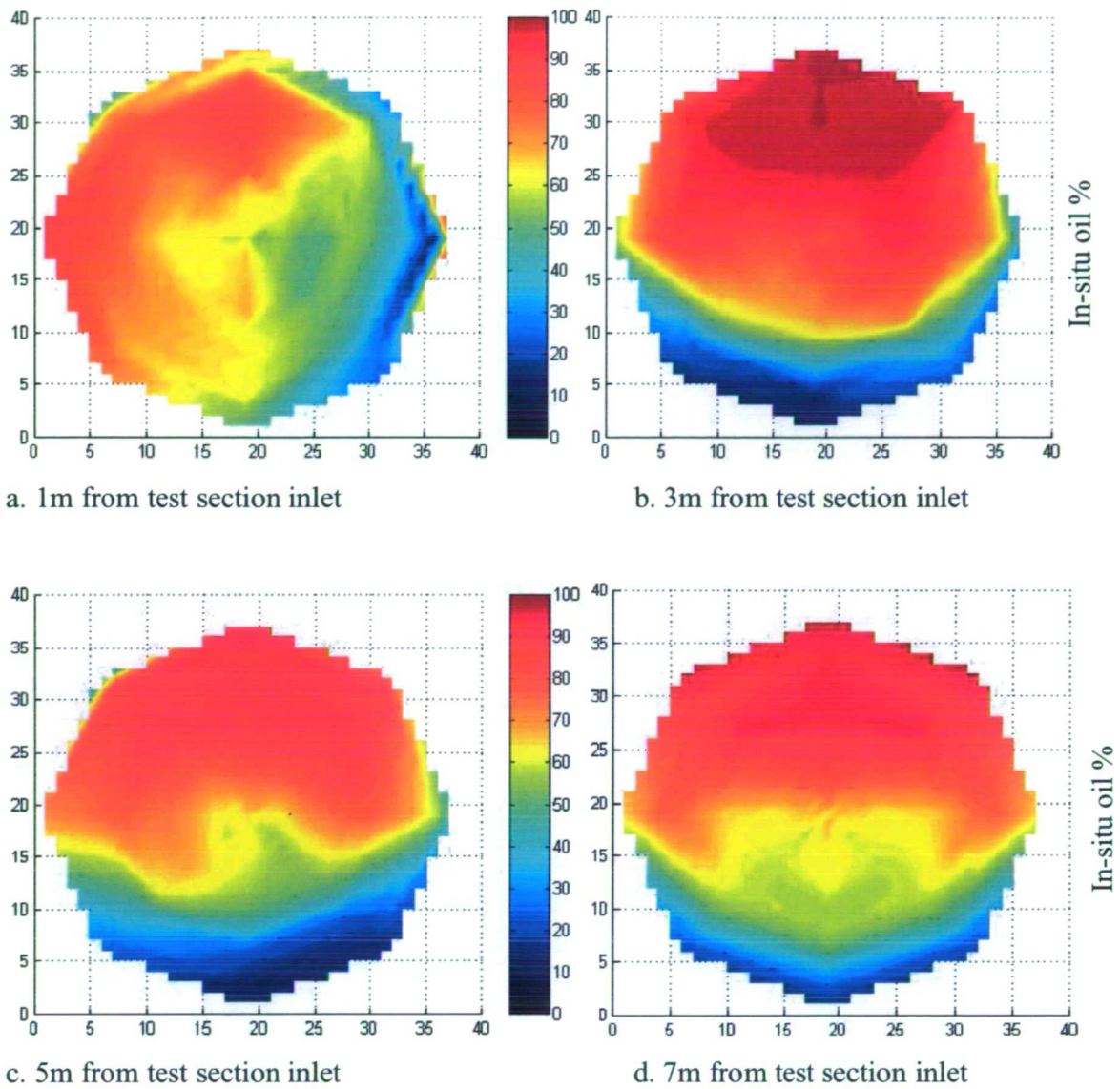


Fig. 4.2. Phase distribution diagram at mixture velocity 2m/s and input oil fraction 72%, at different distances from test section inlet

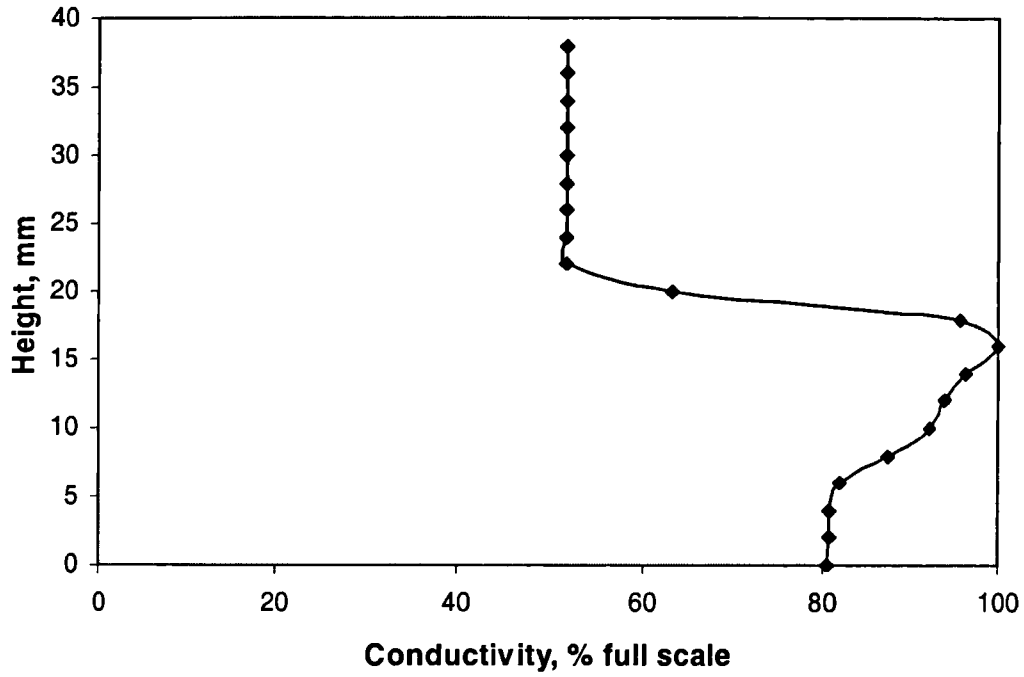


Fig. 4.3. Profile of conductivity probe data for 60% input oil fraction, 0.8m/s mixture velocity

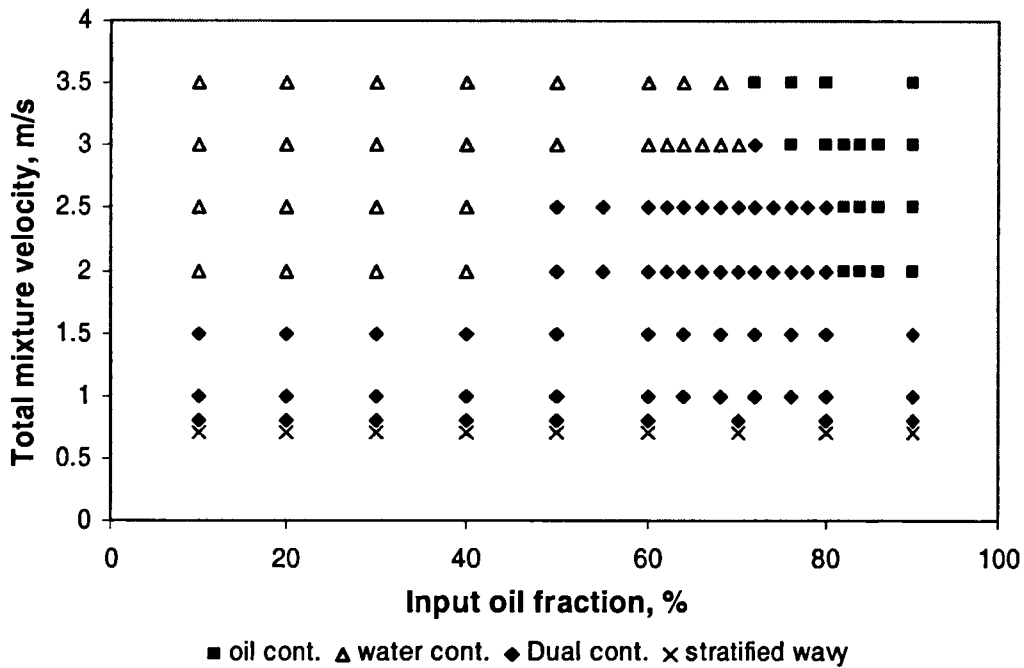


Fig. 4.4. Flow pattern map for current study

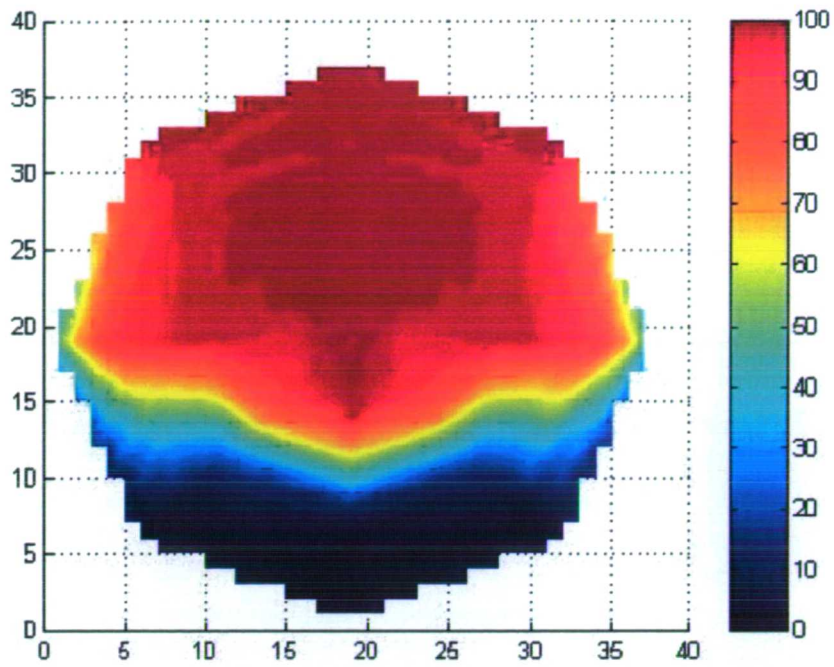


Fig. 4.5. Phase distribution diagram at mixture velocity 0.8m/s and input oil fraction 80%

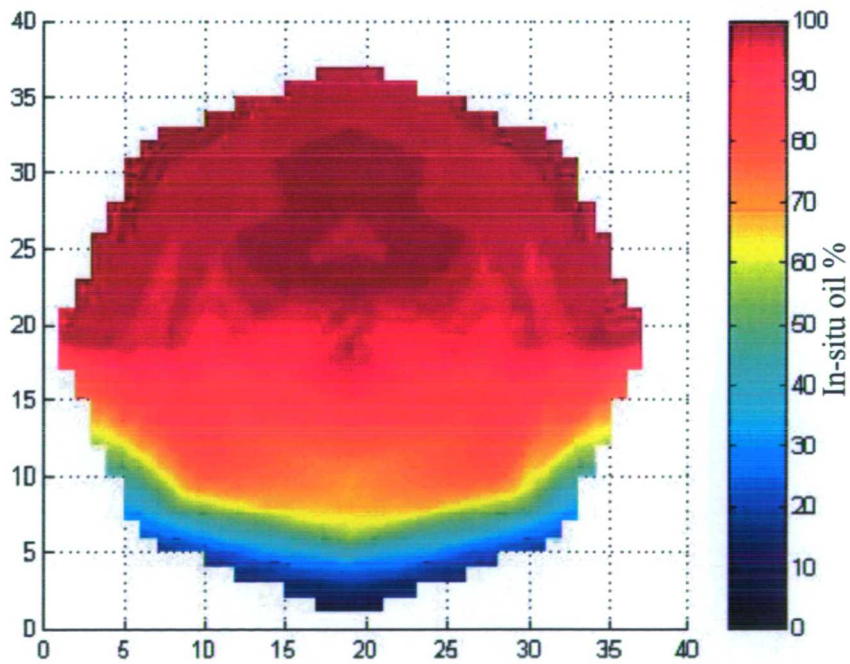


Fig. 4.6. Phase distribution diagram at mixture velocity 1.5m/s and input oil fraction 68%

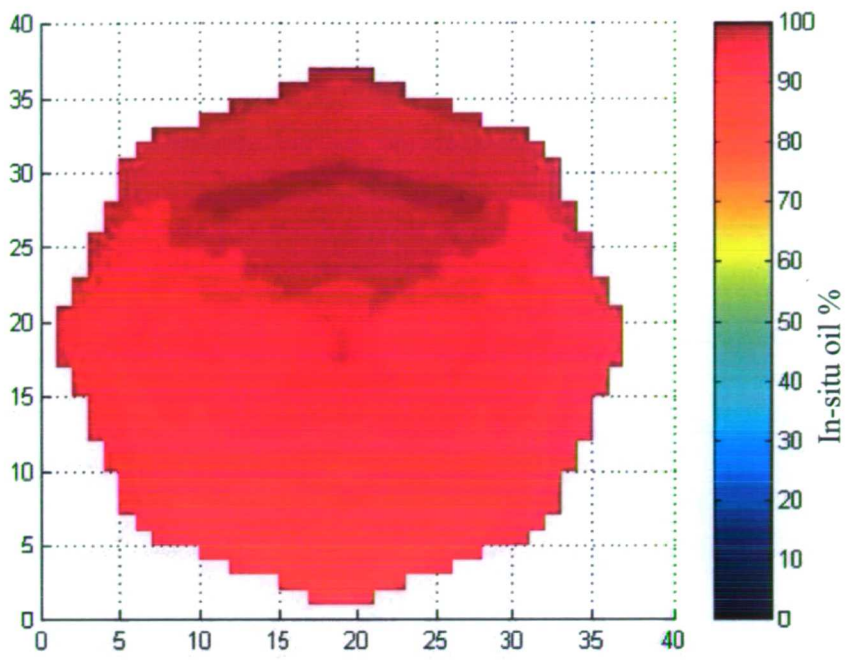


Fig. 4.7. Phase distribution diagram at mixture velocity 2m/s and input oil fraction 90%

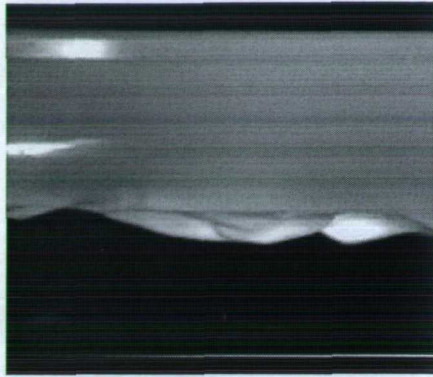


Fig. 4.8a Photograph of Stratified Wavy flow



Fig. 4.8b. Photograph of Dual Continuous flow pattern with low entrainment



Fig. 4.8c. Photograph of Dual Continuous flow pattern with increased entrainment

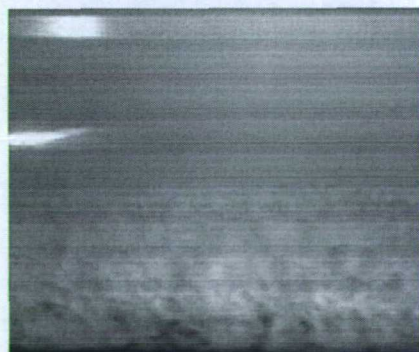


Fig. 4.8d. Photograph of Dual continuous flow pattern, referred to in previous studies as a Dispersion of oil in water and water in oil

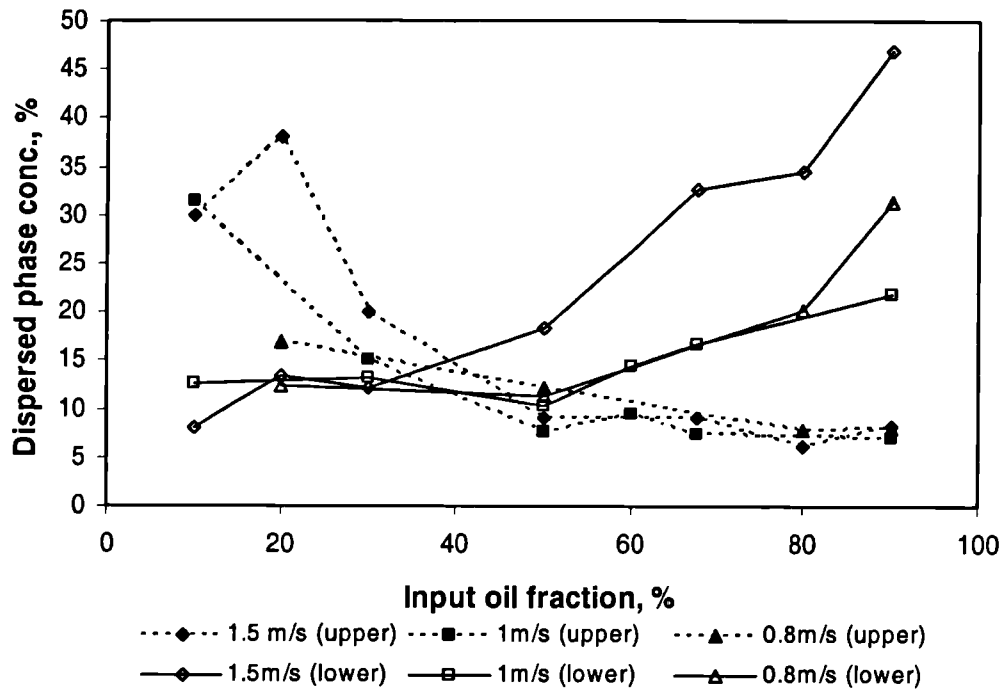


Fig. 4.9. Entrainment concentration in the upper (oil continuous) and lower (water continuous) phases during dual continuous flow at different mixture velocities

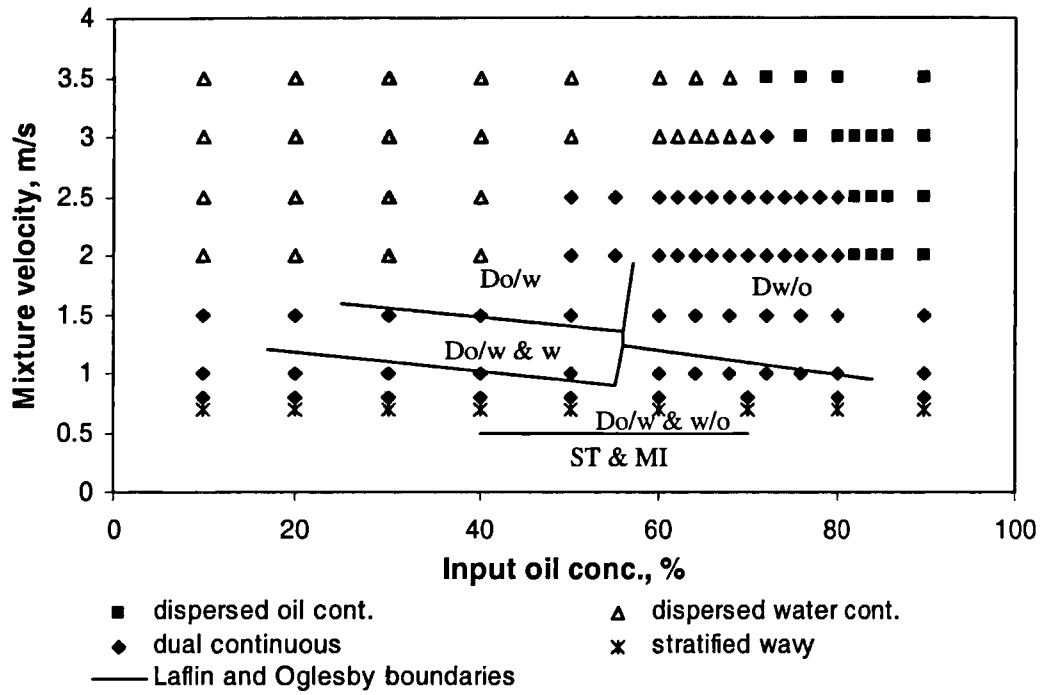


Fig. 4.10. Comparison of flow pattern map from current study, with that of Laflin & Oglesby (1976)

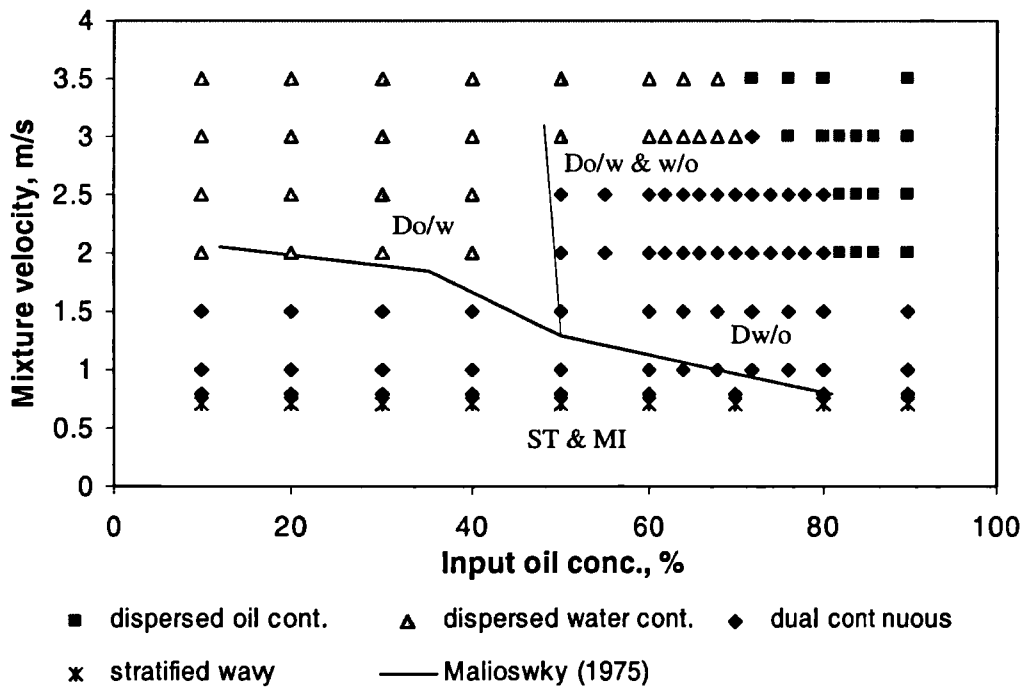


Fig. 4.11. Comparison of flow pattern map from current study, with that of Malinowsky (1975)

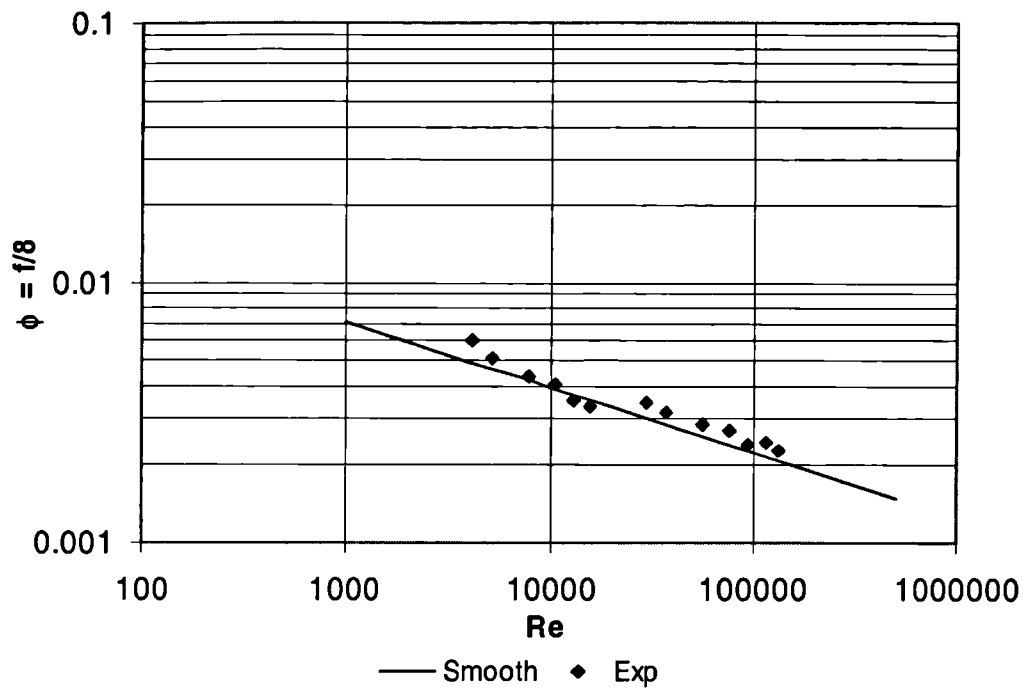


Fig. 4.12. Friction factor vs. Reynolds number for single phase flows

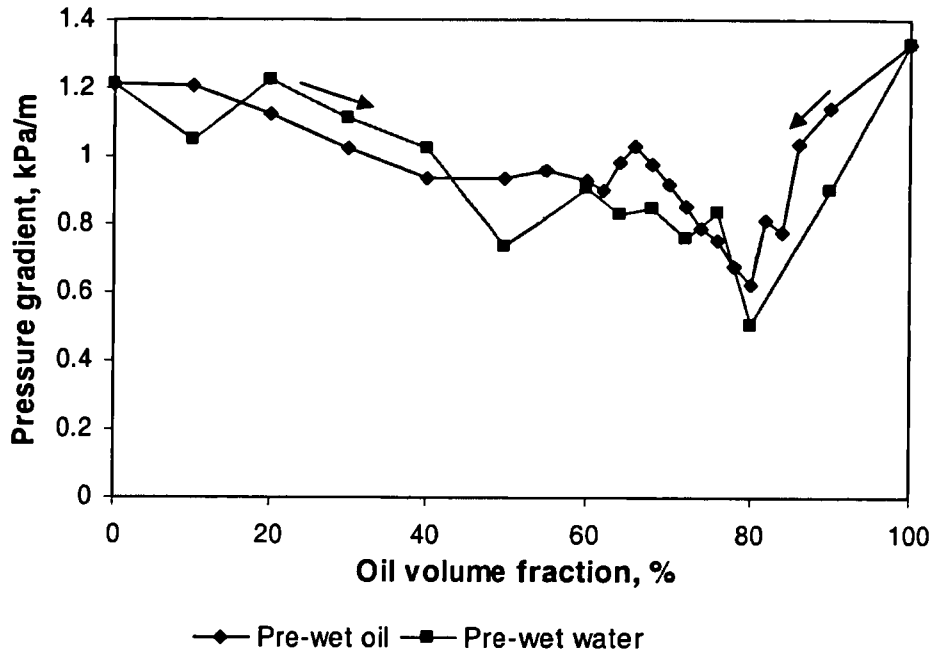


Fig. 4.13. Pressure gradient comparison for oil and water pre-wetted pipes at mixture velocity 2m/s

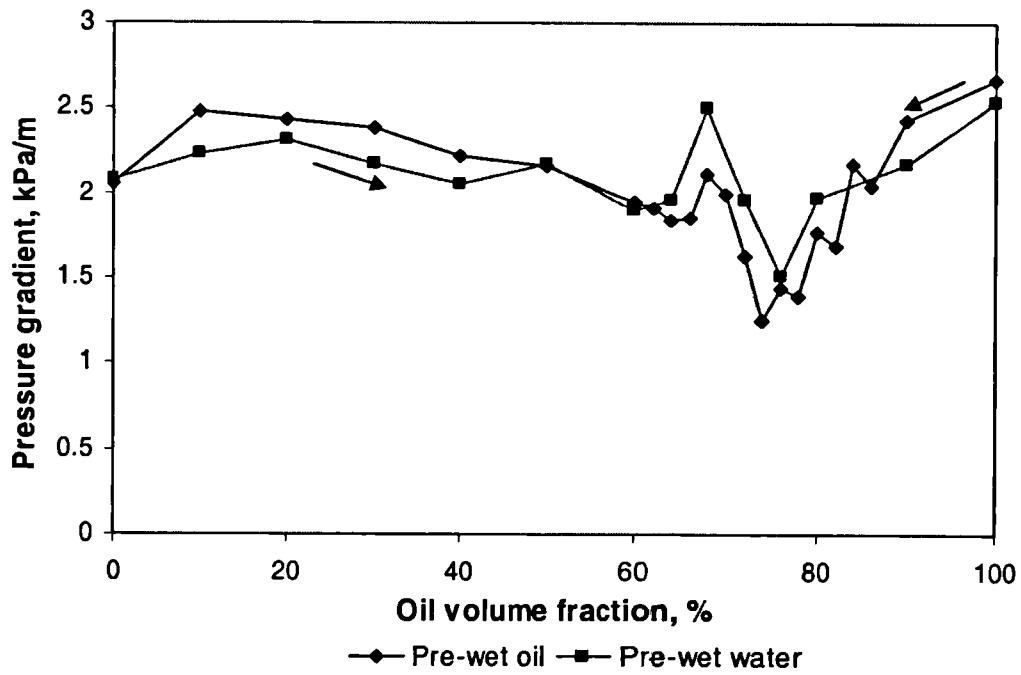


Fig. 4.14. Pressure gradient comparison for oil and water pre-wetted pipes at mixture velocity 3m/s

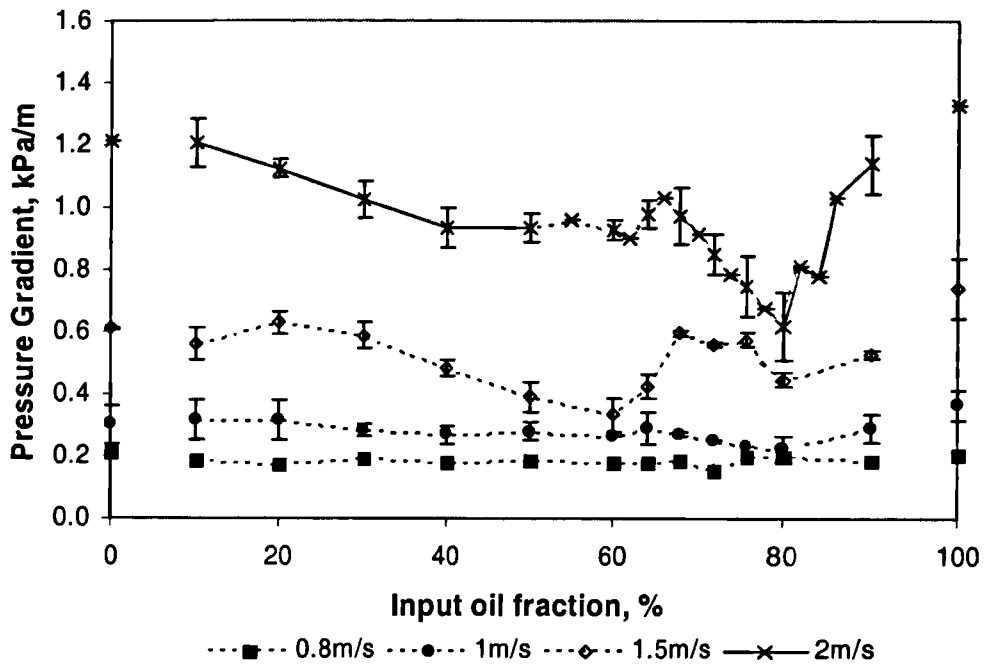


Fig. 4.15. Pressure gradient comparisons for low mixture velocities

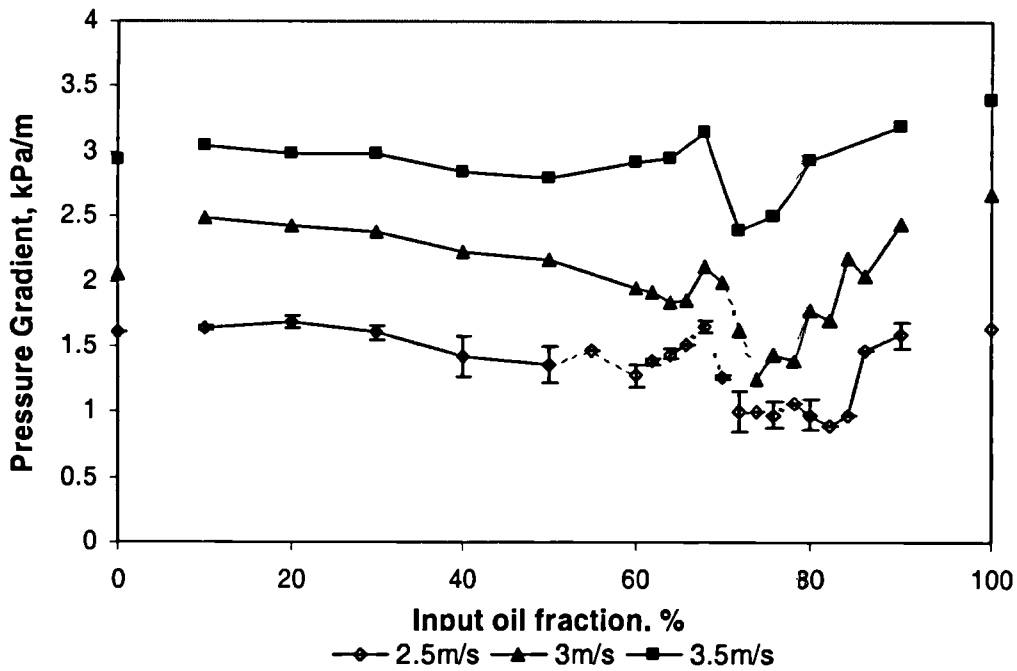


Fig. 4.16. Pressure gradient comparisons for high mixture velocities

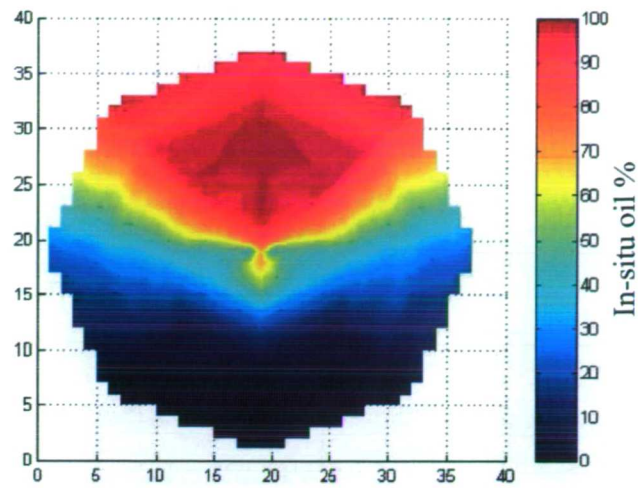


Fig. 4.17a. Phase distribution diagram at mixture velocity 1.5m/s and input oil fraction 50%

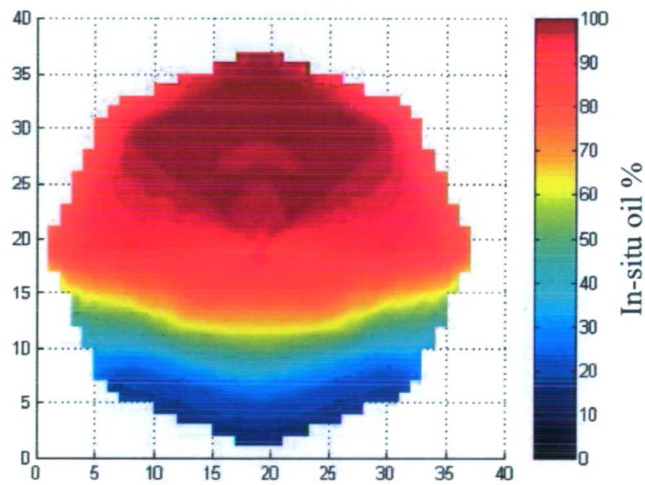


Fig. 4.17b. Phase distribution diagram at mixture velocity 1.5m/s and input oil fraction 68%

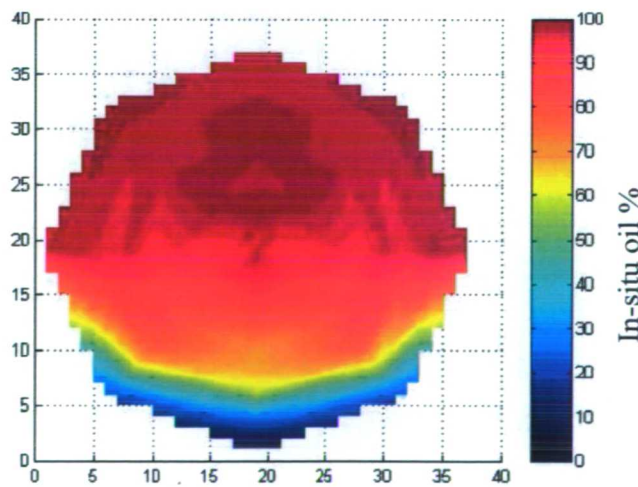


Fig. 4.17c. Phase distribution diagram at mixture velocity 1.5m/s and input oil fraction 80%

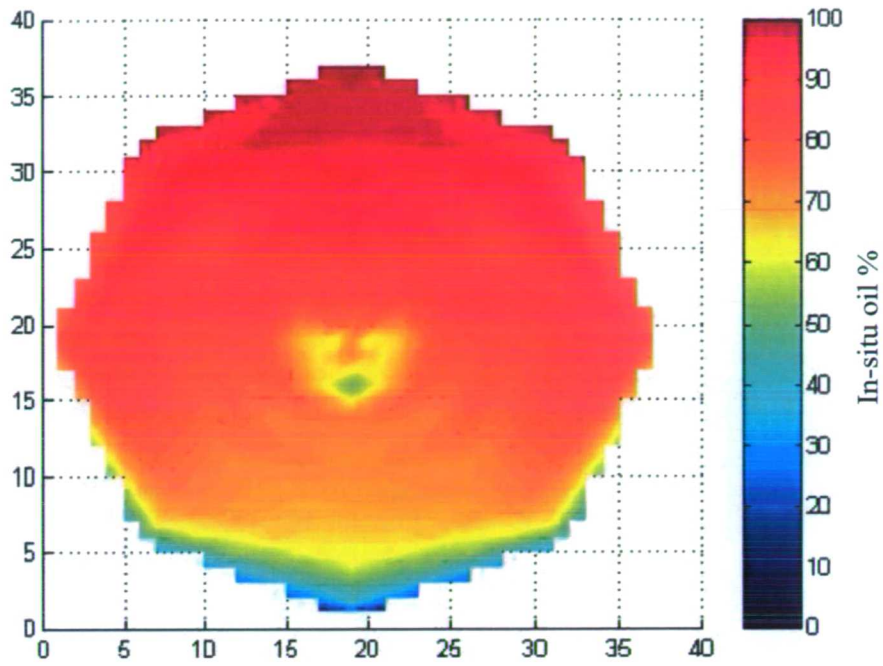


Fig. 4.18. Phase distribution diagram at mixture velocity 2.5m/s and input oil fraction 80%

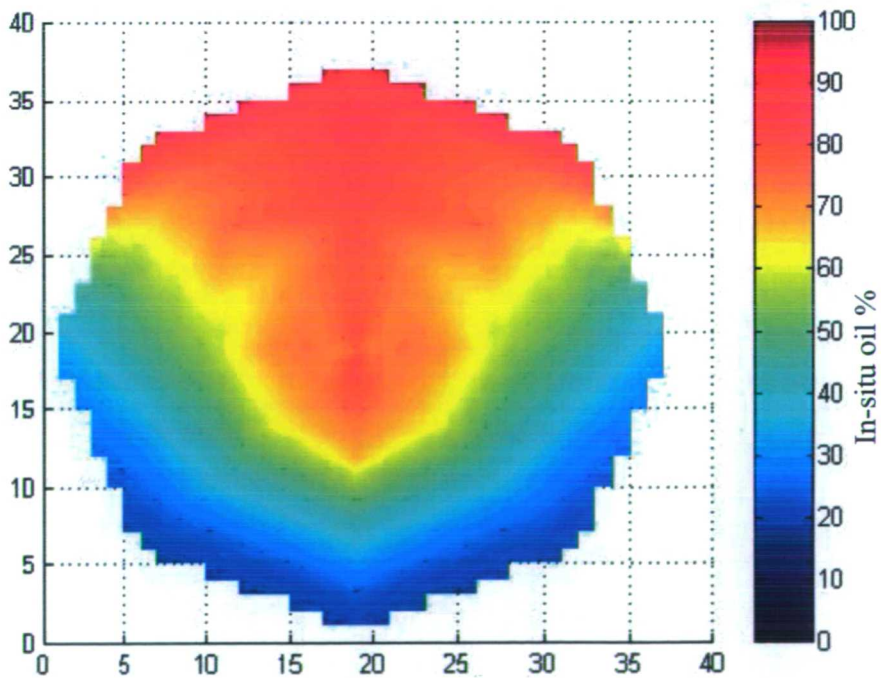


Fig. 4.19. Phase distribution diagram at mixture velocity 2.5m/s and input oil fraction 50%

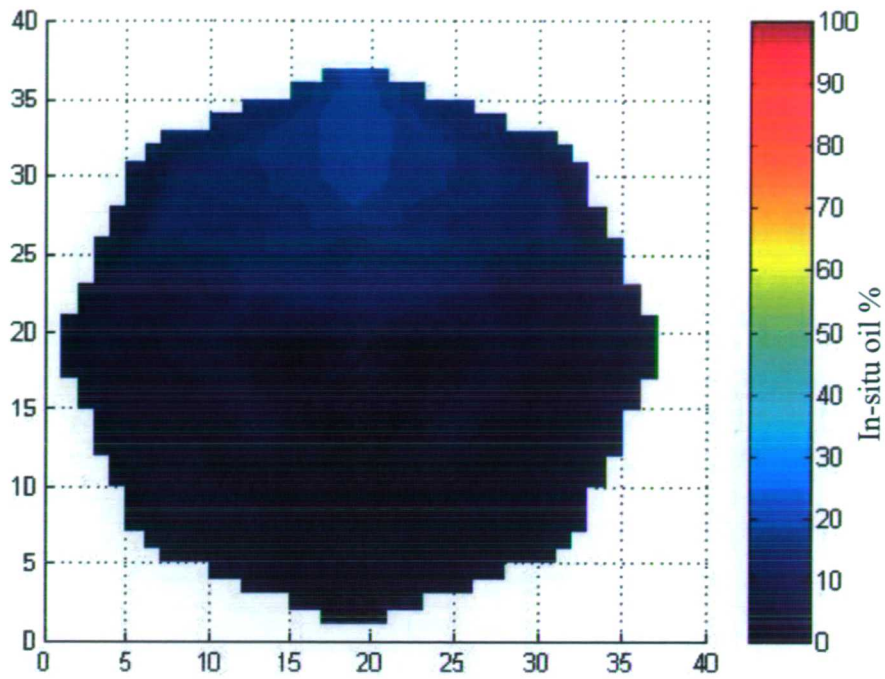


Fig. 4.20. Phase distribution diagram at mixture velocity 2m/s and input oil fraction 10%

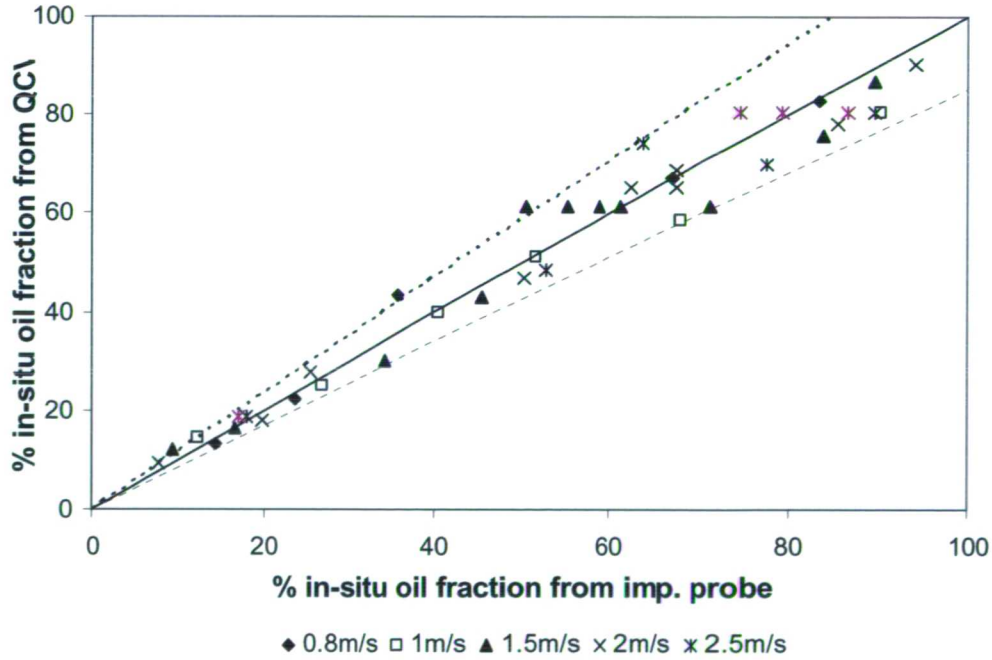


Fig. 4.21. Comparison of in-situ oil fraction measured by the QCVs and the impedance probe diagrams for different mixture velocities. Dotted lined indicate +/- 15% difference

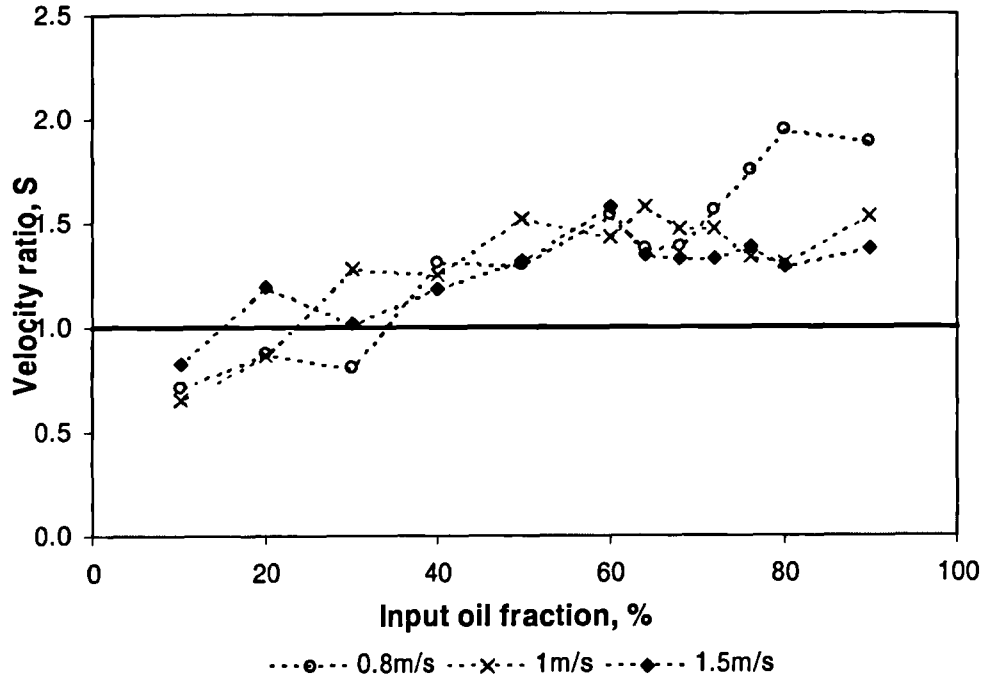


Fig. 4.22. Velocity ratio for low mixture velocities. $S > 1$ indicates oil flowing faster than water; $S < 1$ indicates oil flowing slower than water

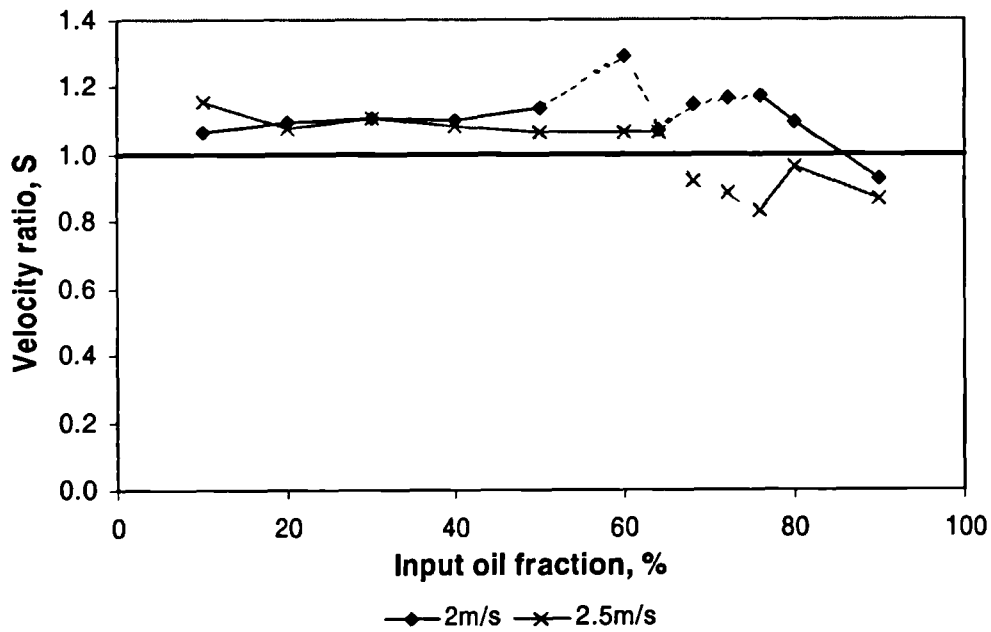


Fig. 4.23. Velocity ratio for intermediate mixture velocities. $S > 1$ indicates oil flowing faster than water; $S < 1$ indicates oil flowing slower than water

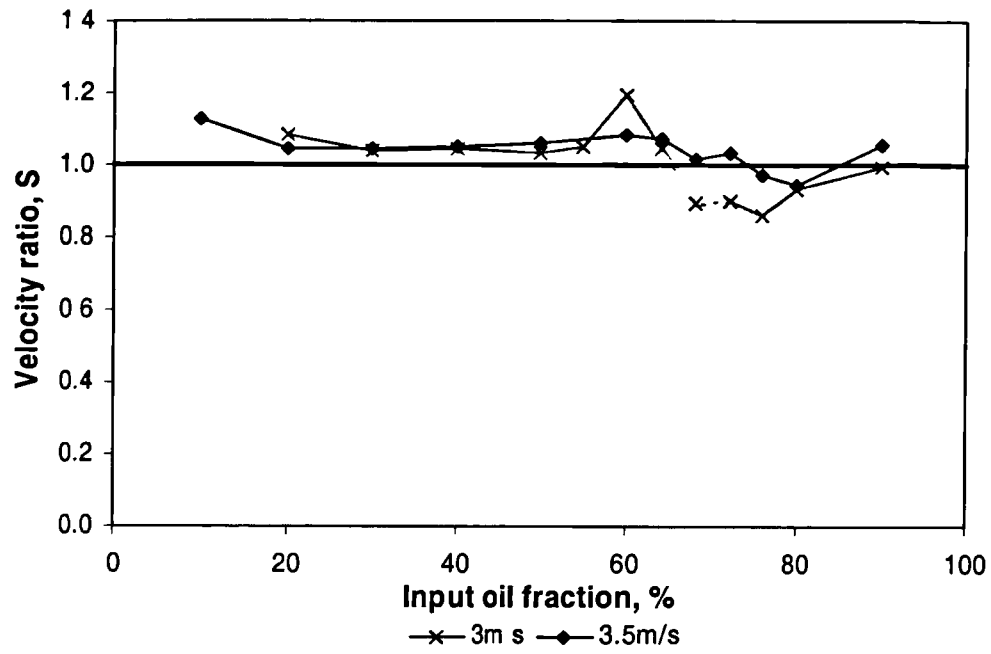


Fig. 4.24. Velocity ratio for high mixture velocities. $S > 1$ indicates oil flowing faster than water; $S < 1$ indicates oil flowing slower than water

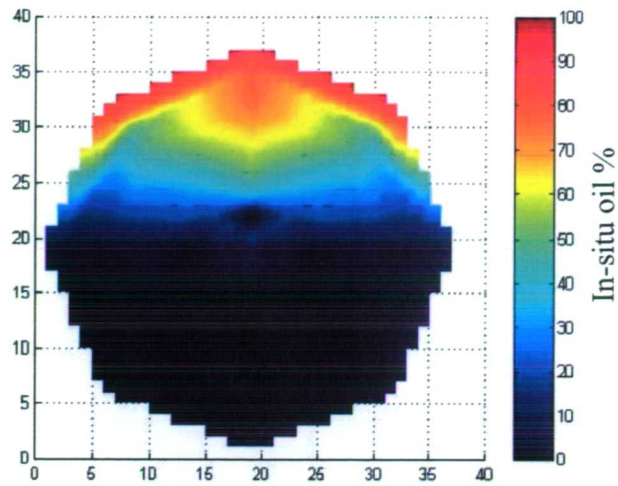


Fig. 4.25a. Phase distribution diagram at mixture velocity 1.5m/s and input oil fraction 20%

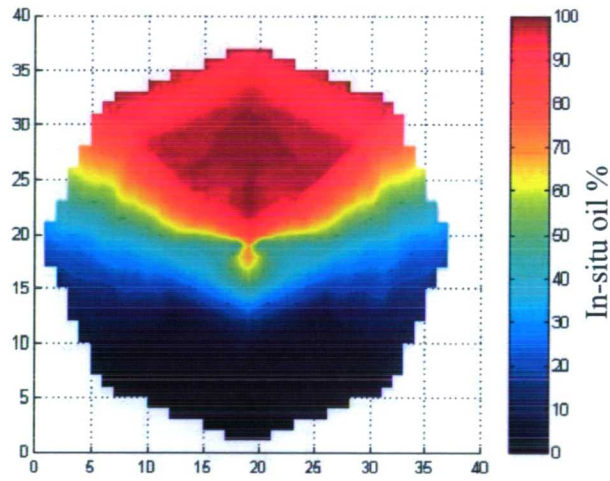


Fig. 4.25b. Phase distribution diagram at mixture velocity 1.5m/s and input oil fraction 50%

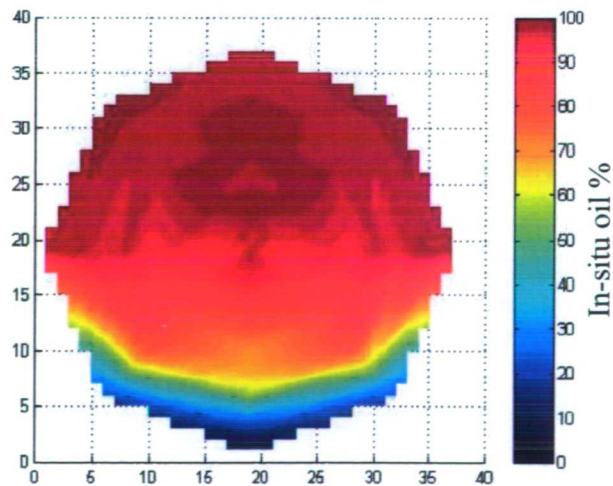


Fig. 4.25c. Phase distribution diagram at mixture velocity 1.5m/s and input oil fraction 80%

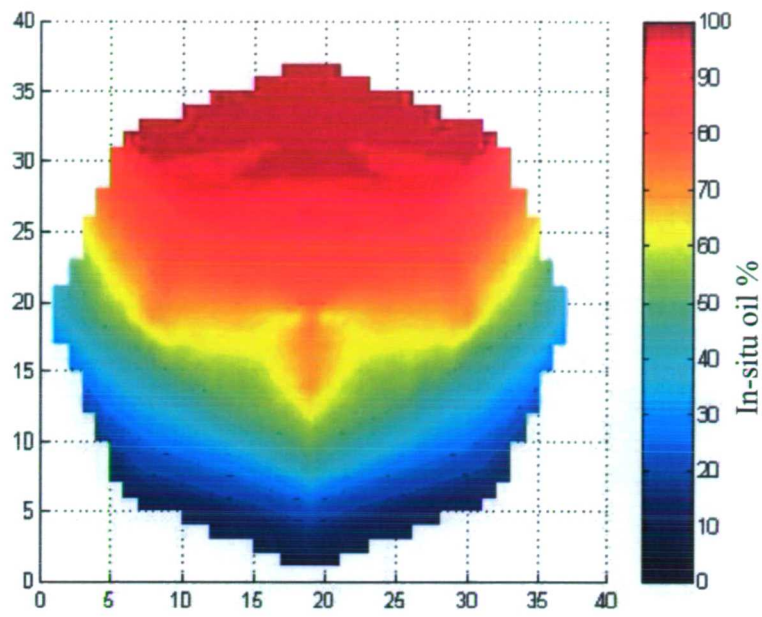


Fig. 4.26a. Phase distribution diagram at mixture velocity 2m/s and input oil fraction 68%

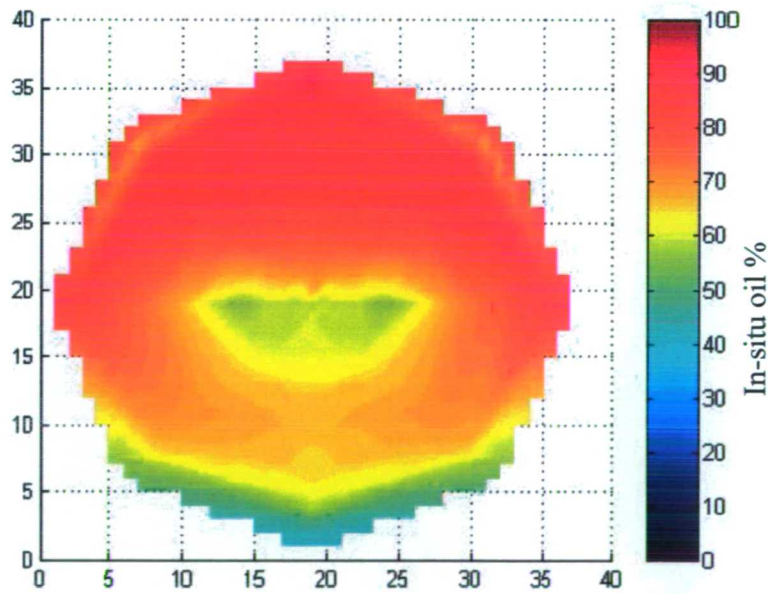


Fig. 4.26b. Phase distribution diagram at mixture velocity 2.5m/s and input oil fraction 68%

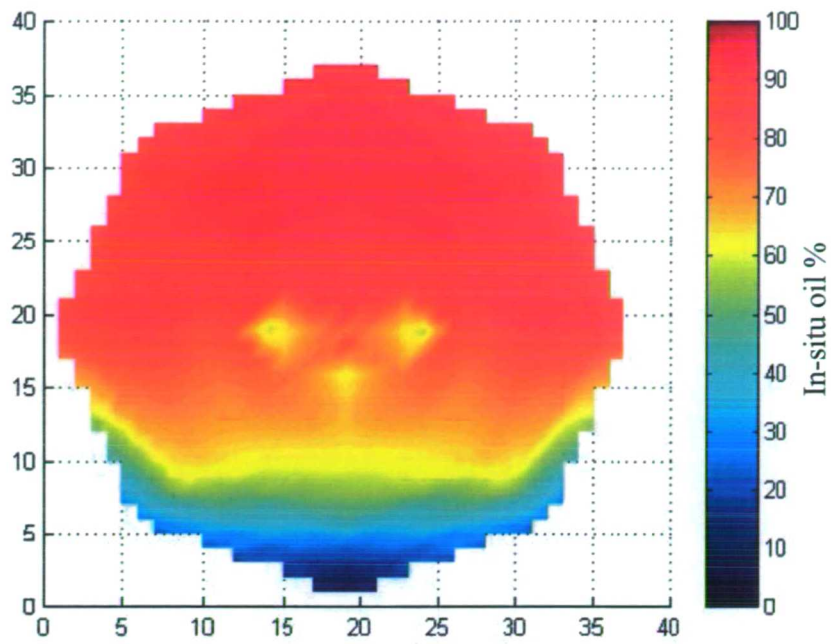


Fig. 4.27a. Phase distribution diagram at mixture velocity 2m/s and input oil fraction 80%

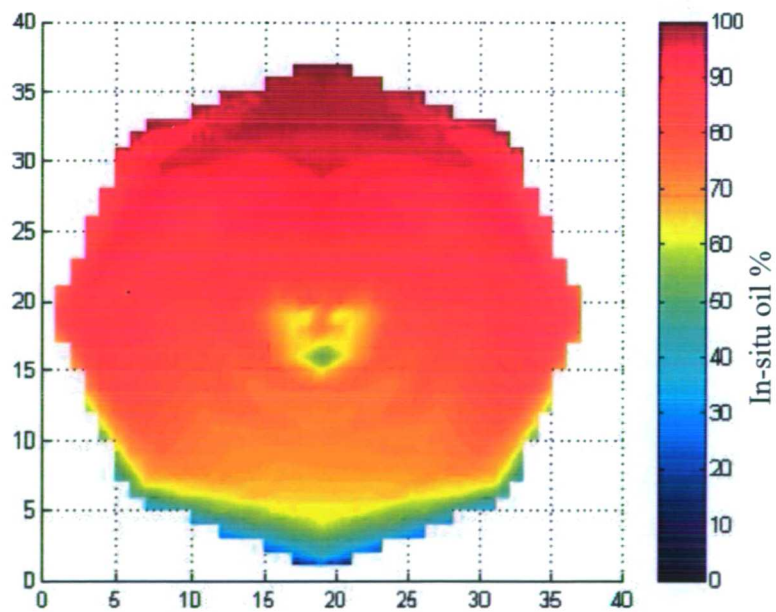


Fig. 4.27b. Phase distribution diagram at mixture velocity 2.5m/s and input oil fraction 80%

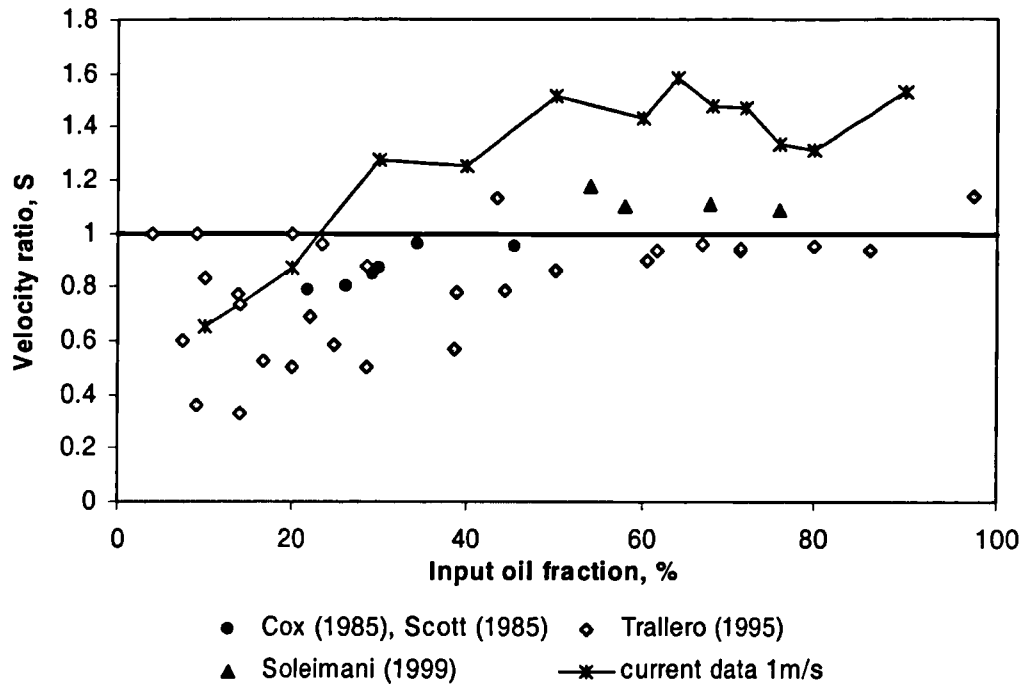


Fig. 4.28. Velocity ratio at 1m/s mixture velocity compared to data from literature for dual continuous flow

5. CHORD LENGTH/DROP SIZE AND DISTRIBUTION RESULTS

Drop size distributions in pipe flow have been previously studied using a number of different techniques (see Section 2.2.3) (Kubie and Gardner, 1977; Karabelas, 1978; Angeli and Hewitt, 2000; Simmons et al., 2000). Using the dual impedance probe as described in Section 3.4.2, chord length measurements were taken from drops flowing at different locations inside the pipe. Experiments were performed for mixture velocities ranging from 1.5m/s to 2.5m/s for input oil fractions from 20%, 50%, 68%, and 80%. At these conditions the flow pattern is either dual continuous or fully dispersed. At lower mixture velocities the flow pattern is also dual continuous, but there are too few drops in each continuous phase to enable cross-correlation of the signals from the two sensors. It was found that when the dispersed phase fraction was less than approximately 3% there were insufficient drops for the cross-correlation and no clear peak was seen. An example of the cross-correlation function against lag time interval between the two impedance sensors was shown in Fig. 3.13.

5.1 Velocity Profiles

Application of cross-correlation to the data obtained from the dual impedance probe yields velocity profiles. It should be noted here that the velocity measured is the dispersed phase velocity.

Fig. 5.1 shows the drop velocity profile for 2.5m/s mixture velocity, 80% input oil fraction against the single phase turbulent flow profile along a vertical pipe diameter. The corresponding phase distribution diagram is also presented. It can be seen that the velocity profile follows the turbulent profile quite well, apart from near the centre of the pipe. This location corresponds to an increase in the water droplet concentration. The velocity profile suggests that as the oil concentration increases towards the top of the pipe the velocity decreases. For input conditions of 2.5m/s mixture velocity and 20% input oil fraction the flow is a water continuous dispersion throughout the pipe cross-section. At the top of the pipe where the dispersed phase concentration is highest (oil

drops) the drop velocity becomes less than that of the turbulent profile, while for all other locations the drop velocity is higher than the turbulent profile (Fig. 5.2). In general the oil drops appear to be faster than the average mixture velocity, suggesting that the dispersed oil is flowing faster than the water phase. The results from the QCV also show that at these conditions S is greater than 1.

As the mixture velocity decreases the concentration of each dispersed phase into the other decreases due to the reduction of inertial forces. From the drop velocity profile for 2m/s, 50% input oil fraction (Fig. 5.3) it appears that the oil drops in the water continuous phase flow slightly faster than the water drops in the oil phase. In all cases, however, the velocity of the dispersed phase seems to be quite close to the single phase profile. It can be said that the presence of drops makes the profile flatter in the middle of the pipe. From these results (apart from the water continuous dispersion in Fig. 5.2) it can not be concluded whether the dispersed phase travels faster than the continuous phase or not since the continuous phase velocity profile is not known.

The drop velocities can however be compared with the average velocities of the respective upper/lower layers and this is shown in Fig. 5.4. The upper and lower layer velocities are found from the two-fluid model (see Chapter 6) that includes the experimentally measured entrainment of one phase into the other and takes into account the interfacial curvature. In this case the interface was assumed to be part of a circle with radius equal to 0.038m (equal to the pipe diameter). When the flow pattern was fully dispersed the mixture velocity was used. It can be seen that in all cases water drops are faster than the layer velocity while oil drops can be either faster or slower than the layer velocity. This could be due to the distribution of the drops in the opposite phase. As will be seen later, water drops are located closer to the interface where the velocities are higher, while oil drops tend to spread more uniformly in the opposite phase (see Fig 5.11 and 5.12).

Once the drop velocity is known, the chord lengths can be calculated. This was done after the raw data had been transformed to a square wave form following the procedure

described in Section. 3.4.2.2. An example of the raw data and the transformed square wave form is shown in Fig. 5.5, where the high values correspond to oil, and the low values correspond to water. The threshold value was normally set to a value of 2, which was sufficiently large to remove any electrical noise effects, whilst still allowing the detection of small drops that give small peaks. From the square wave signal the time duration that each phase was present at the tip could be found and, depending on the dispersed phase, the number and intercepted chord length of the drops could be calculated.

5.2 Chord Length to Drop Diameter Transformations

Once the drop chord length distribution is known a number of statistical techniques (detailed in Section 2.3) can be used to calculate the drop diameter distribution. Depending on the type of transformation process used, the diameter bins may need to be known or assumed for the transformation to work successfully. The Probability Apportioning Method (PAM) is one such procedure where prior knowledge of the diameter bands is important for obtaining a meaningful diameter distribution. In total four different chord length/drop diameter distribution transformations were tried; the Clarke and Turton method (Clarke and Turton, 1988), PAM (Simmons et al., 1999), FEM (Simmons et al., 1999), and PAM2 (Langston et al., 2001). The transformation methods were initially applied to chord size distributions derived from uni- and bi-modal diameter distributions to check whether these could be retrieved. They were then used on real chord length data.

Fig. 5.6 shows the comparison of the drop number frequency distribution between the four methods for a uni-modal system where all the particles have a diameter equal to 10. The chord distribution used was generated using equation (2.42) as suggested by Simmons et al. (1999). The results from PAM2 show only the 1st and 10th iterations, after which the differences between distributions became negligible. It can be seen that the PAM and PAM2 methods both give predictions which remain positive for all diameter bins, with PAM2 giving a greater peak at iteration 10 than at iteration 1. The

FEM and Clarke method both give negative frequencies prior to the frequency peak. Similar trends are observed for a bi-modal system with a 50:50 particle split between sizes 5 and 10 (Fig. 5.7). The PAM and PAM2 methods give positive results for all diameter bins, but both methods over estimate the fraction of particles at size 5. The FEM and Clarke method again give negative values for diameter bins just before the frequency peaks.

The PAM2 and Clarke method were used to transform an experimental chord size distribution to a drop diameter distribution. The results are shown in Fig. 5.8, where the PAM2 results are shown for the 1st and the 10th iteration. Again no significant change in the distribution was found after this iteration. The Clarke method predicts a drop diameter number frequency distribution that is similar to the experimental chord distribution apart from the lower sizes. This is likely to be due to instabilities in the method. The PAM2 method follows the chord distribution data at the 1st iteration, but at subsequent iterations a narrow peak appears at the maximum of the chord distribution.

Since none of the techniques were found to satisfactorily transform a chord length distribution to a drop size distribution, in the results and discussion that follow the measured chord lengths rather than drop diameters are used in the comparisons between different conditions.

5.3 Chord Length Distributions

Once the velocity had been found, the chord lengths could be measured. This was done after the raw data had been transformed to a square wave form following the process described in Section. 3.4.2.2. An example of the raw data and the transformed square wave form is shown in Fig. 5.5, where the high values correspond to oil, and the low values correspond to water. The threshold value was normally set to a value of 2, which was sufficiently large to remove any electrical noise effects, whilst still allowing the program to detect even the smallest drop giving rise to a small peak. Once the square wave form was available, the time duration that each phase was present at the tip could

be found and, depending on the dispersed phase, the number and length of chord established.

To characterise the distributions three different chord lengths, namely l_{99} , l_{32} and l_{50} have been chosen. l_{99} is found from the chord length cumulative volume distribution and corresponds to the size that is equal or larger than 99% of the drops by volume. This size can be considered as an indication of the maximum chord length and subsequently maximum drop size (Karabelas, 1978). In a distribution of 3000 drops only 4 will have size between l_{99} and l_{\max} which is statistically very small to obtain experimentally especially when the size distributions have long tails. The commonly used Sauter mean size, l_{32} , defined as the ratio of the third to the second momentum of the drop size distribution, can be biased towards large drops and in case of distributions with long tails, unrealistically high. The median chord length, l_{50} , represents the middle value in the series of chord lengths arranged in ascending or descending order.

The variation of drop size in a pipe cross section can be seen in Fig. 5.9 for 50% input oil fraction and 2.5m/s mixture velocity, for dual continuous flow. The interface between the oil and water continuous phases is shown as a solid line and was identified with the use of the conductivity probe. In general, as the distance from the interface increases the number of drops dispersed in the respective continuous phase decreases. Phase distribution diagrams also show that the volume fraction of each phase entrained into the other decreases with distance from the interface. From the distributions it is not clear whether the oil or the water drops are larger. In addition, the characteristic dimensions l_{99} and l_{32} are smaller for oil than for water drops but the opposite is true for l_{50} . For both phases chord lengths tend to be larger close to the interface.

At 2m/s mixture velocity and the same input oil fraction (see Fig. 5.10) there is again a decrease in the size and number of dispersed drops with distance from the interface for both phases. At this lower velocity the number of drops, particularly away from the interface is not always sufficient to produce smooth distributions. Again there does not seem to be a clear effect of the continuous phase on drop size. Compared to 2.5 m/s

(Fig. 5.9), it can be seen that a decrease in mixture velocity decreases the number of drops entrained from one phase into the opposite and causes greater vertical concentration gradient. This is expected since at lower velocities turbulent forces may not be large enough to overcome gravitational forces that tend to accumulate drops around the interface. Velocity, however, does not have a clear effect on drop size. Lower velocities would favour larger drops, but at the same time turbulent diffusive forces would be smaller and perhaps not able to disperse the drops with large sizes away from the interface. A decrease in velocity would also lead in a decrease in entrainment of one phase into the other and a reduction of dispersed phase fraction, which would favour smaller drops.

In the following l_{50} and l_{99} are used to represent average and largest drop size; l_{32} was not used as it can be biased towards large sizes. The effect of distance from the interface on chord length can be seen in Figs. 5.11 and 5.12 for the l_{50} and l_{99} sizes respectively. In the dual continuous flow pattern where there is an oil-water interface, the distances are either positive (water drops in oil) or negative (oil drops in water). In the fully dispersed water continuous flows distances are taken from the top of the pipe. No fully dispersed oil continuous flows were encountered in this study. It can be seen from Fig. 5.11 that l_{50} tends to increase near the interface which shows that gravity forces have a strong effect. Also drops at 1.5m/s are less dispersed in the pipe cross section compared to those at higher mixture velocities (2m/s and 2.5m/s). Drops at 1.5 m/s would be expected to be larger than at the other two higher velocities. As mentioned above, however, during dual continuous flow lower mixture velocities reduce the entrainment of one phase into the other, as well as the turbulent dispersive forces that prevent large drops from settling towards the interface. Both these phenomena can cause a reduction in the drop size at a location. Velocity does not therefore cause a monotonic change to drop size, and it can be seen that in many distances from the interface the higher velocities also produce the largest drop sizes. Small chord length medians were observed both close and away from the interface. It has been suggested (Karabelas, 1978) that drop break up will take place in the inertial sub-layer near the pipe wall.

The variation of l_{99} with distance from the interface can be seen in Fig. 5.12, where similar trends are observed.

The effect of velocity on l_{50} can be seen in Fig. 5.13, both for oil and water drops. The velocity used is the upper/lower phase velocity, as explained in Section 5.1. It can be seen that there is no obvious difference in sizes between oil and water drops, probably due to the small differences in the properties of the two phases. It would be expected that with an increase in the phase velocity the drop size would decrease. This does not appear to be the case, probably as a result of two competing phenomena. An increase in velocity would affect drop break up and coalescence and lead to a decrease in drop size. On the other hand, during dual continuous flow increase in velocity is associated with a higher degree of entrainment of one phase into the other and consequently a higher dispersed phase fraction which would favour larger drop sizes. Fig. 5.14 also shows a possible increase in l_{99} with increasing velocity, which again could be explained by the increase in dispersed phase fraction resulting in larger drop sizes.

5.4 Comparisons with Models

The Rosin-Rammler distribution was found to fit the experimental data well in almost all cases (see for example Fig. 5.15). The distribution is given by the following equation:

$$1 - V_{\text{cum}} = \exp\left(-\left(\frac{l}{\alpha}\right)^\delta\right) \quad (5.1)$$

where V_{cum} is the cumulative volume for particles with size less than l , α is the size corresponding to $(1 - V_{\text{cum}}) = 0.3679$ and δ is the slope of the line. The value of δ ranged from 2.62 to 4.22 which is wider than that reported by Karabelas (1978) and Angeli and Hewitt (2000) possibly because a wider range of volume fractions has been used in the current work. There was no obvious trend of δ with mixture velocity, dispersed phase or distance from the interface. The log-normal function found by:

$$y(l) = \frac{\varphi}{\sqrt{2\pi\delta^2}} \exp^{-\frac{1}{2\delta^2}(\ln(l/\xi))^2} \quad (5.2)$$

where d is the drop size and δ , φ and ξ are parameters of the log-normal distribution, with δ affecting the distribution height and ξ affecting the distribution width, was also fitted to the experimental distributions for 2.5m/s 68% and 50% input oil concentration respectively. Again the fit was quite good in some cases, and the examples of the best fits are shown in Figs. 5.16 and 5.17. Despite these relatively good fits, the Rosin-Rammler distribution gave the better fit in more cases than the log-normal distribution. Several models exist in the literature for predicting maximum drop size during dispersed flow. These can be compared with the results from fully dispersed systems. For drops smaller than the length scale of turbulence the model proposed by Hinze (1955) can be used, which in the case of pipe flow is given by Karabelas (1978) and Kubie and Gardner (1977) (equations 2.13 and 2.14)

Kubie and Gardner (1977) suggested an extension to the Hinze model for drops larger than the length scale of turbulence where the fluctuating turbulent velocity instead of the velocity difference was used to calculate the shear rate across the drop. However, maximum sizes calculated by this model were found to greatly over predict the experimental values.

To extend the Hinze model to dense dispersions Tsouris and Tavlrides (1994) proposed that a modified energy dissipation rate, ε^* should be used, where

$$\varepsilon^* = \varepsilon \left(\frac{\nu}{\nu^*} \right)^3$$

and ν^* and ν_c are the mixture and the continuous phase kinematic viscosities respectively.

At high dispersed phase concentrations the model suggested by Brauner and Ullmann (2002) can also be considered:

$$d_{\max} = 2.22C_H \left(\frac{\rho_c U_c^2 D}{\sigma} \right)^{-0.6} \left[\frac{\rho_m}{\rho_c (1 - \phi_d)} f \right]^{-0.4} \left(\frac{\phi_d}{1 - \phi_d} \right)^{0.6} \quad (5.3)$$

where C_H is a tunable constant, $C_H = O(1)$,

$$\phi_d = \frac{U_{ds}}{U_{ds} + U_{cs}} \quad (5.4)$$

U_{ds} is the dispersed phase superficial velocity, and U_{cs} is the continuous phase superficial velocity. A model that considers the viscosity of the drop was proposed by Sleicher (1962) (equation 2.17) and is also used as a comparison.

In the present work fully dispersed flows occurred only at 20% oil volume fraction at 2m/s and 2.5m/s mixture velocities, where water was the continuous phase. Experimental l_{99} data for these conditions are compared with the models predictions in Fig. 5.18. It can be seen that all models underpredict the experimental values, with the Hinze model, developed for dilute dispersions, performing the least well.

In dual continuous flow apart from turbulent forces the mechanism of drop entrainment will also define drop size. It was found that the above correlations developed for fully dispersed systems underpredicted the maximum drop sizes found experimentally. This is probably due to the continuous entrainment of drops that do not have time to reach their final size before they deposit again at the interface. For liquid-liquid systems Valle (2000) attempted to estimate the size of drops that entrain from one phase to the other. In his model he assumed that the entrained drop size is governed by surface and turbulent dynamic forces and can be found by combining the d_{50} value from a Rosin-Rammler distribution with the d_{95} value calculated using the Hinze (1955) model. Using this method gave an estimated entrained drop size 0.8-0.4mm for oil drops in water with

smaller drops being estimated for higher velocities, and 0.9-0.45mm for water drops in oil, again with smaller drops estimated for higher mixture velocities. Nigmatulin et al. (1996) also suggested a correlation for maximum entrained liquid drop sizes in gas-liquid systems. When used in the current work it predicted maximum drop sizes of 0.6mm for oil drops in water, and 0.4 for water drops in oil. Both methods give a 10 fold underestimation of the experimental drop diameters.

From the experimental data the vertical concentration gradient of the dispersed phase and of the different drop sizes can also be found. These can be compared with the predictions of the model suggested by Karabelas (1977) for dispersion of solid particles in liquid in two dimensional pipe flow. The overall input droplet concentration for each size, as well as the diffusivity of the dispersed drops in the continuous phase are required. The latter parameter was set equal to 0.4 which gave the best fit to the experimental data for fully dispersed flow (see Fig. 5.19); it also compares well to the range 0.3 to 0.46 reported in the literature for particle-liquid flows (Binnie and Phillips 1958; Sharp and O'Neill 1971). To account for the high dispersed phase concentration the hindered settling velocity correlation (Perry and Green, 1984) was used to calculate particle settling velocity, also required in the model.

The comparison between model predictions and experimental data for fully dispersed flow can be seen in Fig. 5.19 for a water continuous dispersion (mixture velocity 2m/s and input oil volume fraction 20%). The results are presented in terms of relative concentration defined as concentration of dispersed drops in a particular height over the total concentration of that dispersed phase. The distribution of oil drops is shown at two different heights from the top of the pipe. According to the model there is a greater concentration of oil drops at a height 6mm from the top of the pipe than at 32mm, a difference that is more pronounced for the smaller drops. Although the same trend is seen in the experimental data, there is a larger vertical concentration gradient than predicted by the model.

The model was also applied to the dual continuous flow pattern and results can be seen in Fig. 5.20 for the upper oil continuous layer at mixture velocity 2m/s and input oil fraction 50%. It can be seen that the model predicts a greater concentration of drops close to the interface, which is also seen in the experimental data. The extent of the experimentally found vertical concentration gradient is underpredicted by the model. Similar trends were obtained for the lower water continuous layer (Fig. 5.21) but in this case the underprediction of the vertical concentration gradient is even larger.

5 Conclusions

The size and vertical distribution of drops was studied in detail during horizontal liquid-liquid dispersed pipe flows. Emphasis was given on the dual continuous pattern where both phases retain their continuity but there is interdispersion of one phase into the other. Drop velocities and chord lengths were measured at different locations in a pipe cross section with a double sensor impedance probe. The following summarises the conclusions:

- In dual continuous flows drop concentration and size decreased with increasing distance from the interface.
- There was only a slight effect of velocity on l_{99} and median drop sizes. This was attributed to the competing phenomena of decreasing drop size and increasing drop entrainment of one phase into the opposite with velocity.
- Water drops were in general faster than the velocity of their respective (upper) layer while oil drops could be either faster or slower.
- The Rosin-Rammler function was found to fit satisfactorily the experimental chord length distributions. However, the available correlations on maximum drop size underpredicted the sizes found experimentally.

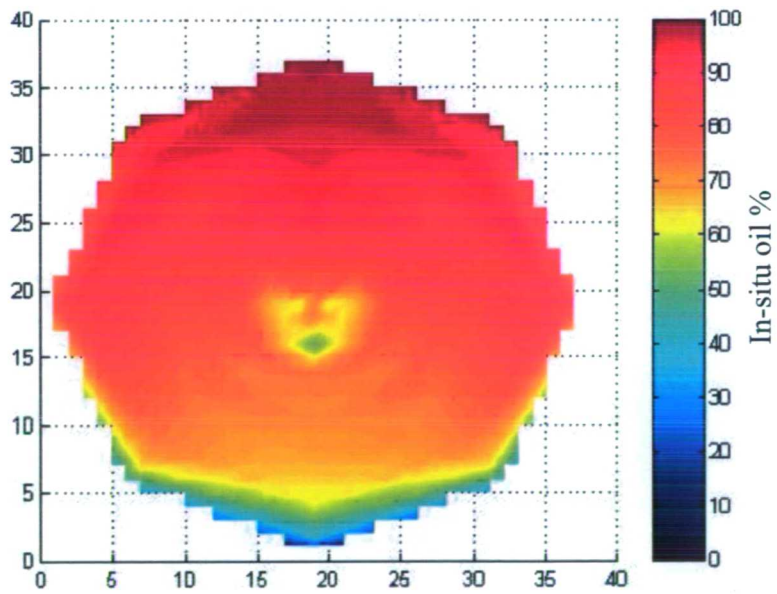
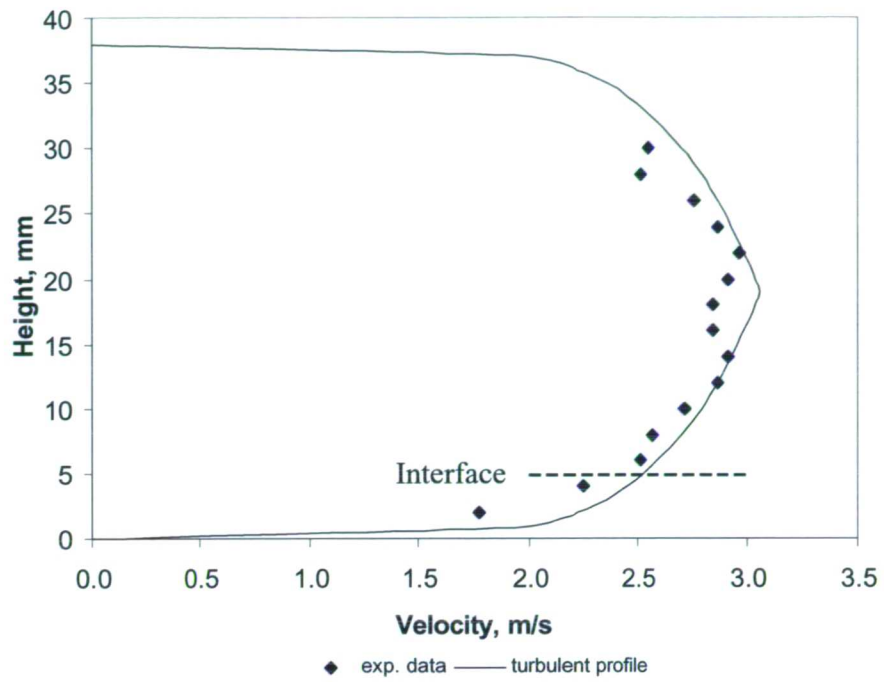


Fig. 5.1. Velocity profile and phase distribution diagram for mixture velocity 2.5m/s, input oil concentration 80%

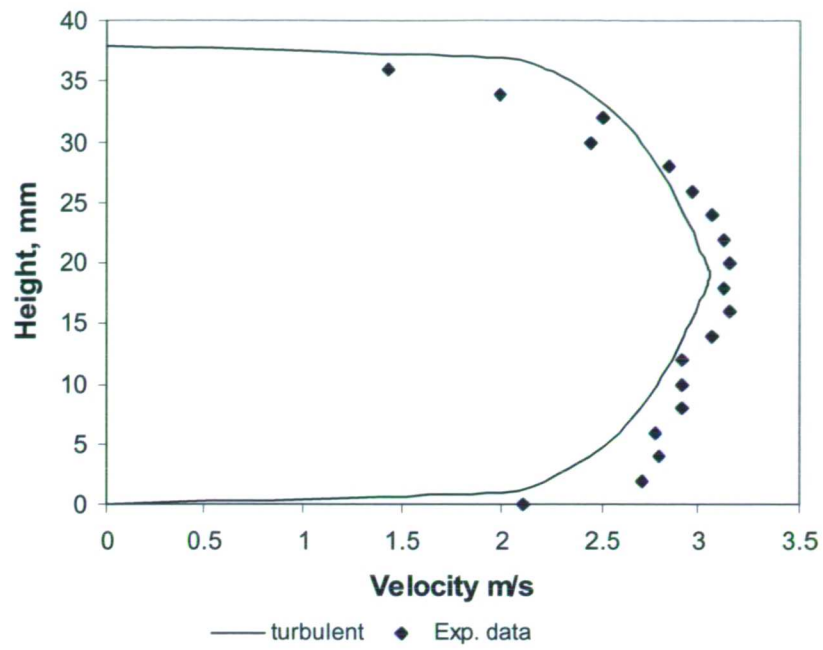


Fig. 5.2. Velocity profile and phase distribution diagram for mixture velocity 2.5m/s, input oil concentration 20%

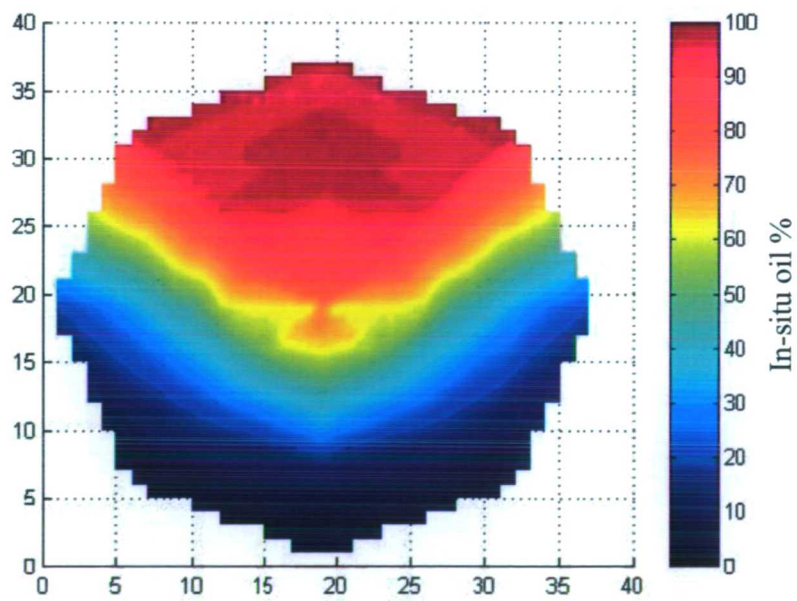
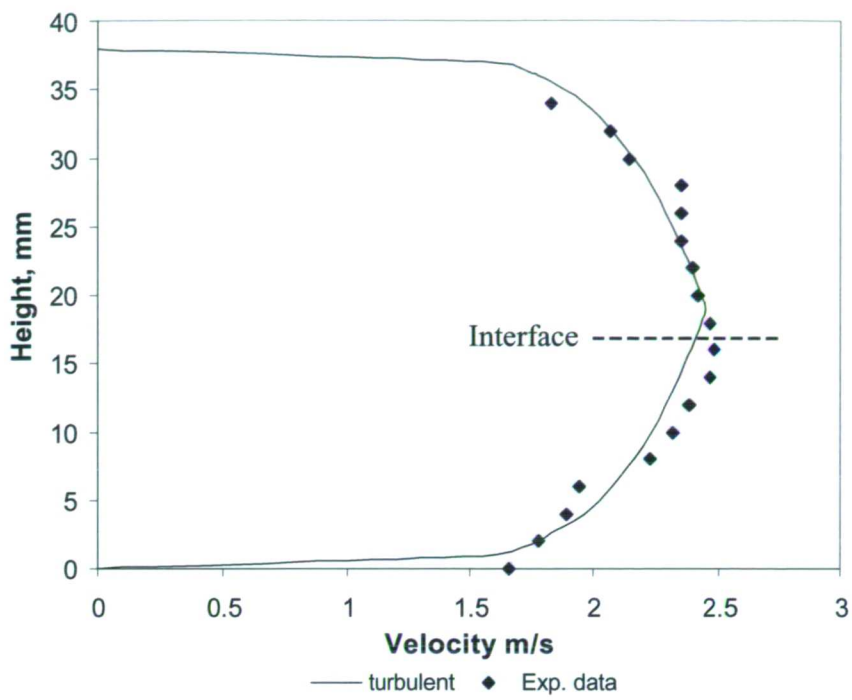


Fig. 5.3. Velocity profile and phase distribution diagram for mixture velocity 2m/s, input oil concentration 50%

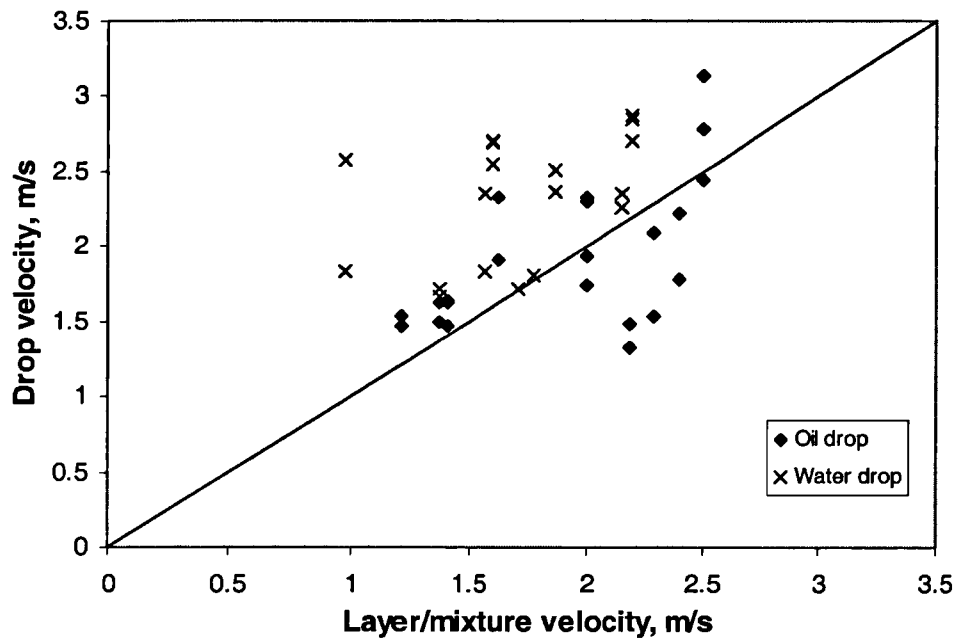


Fig. 5.4. Graph of drop velocity against continuous phase velocity for oil and water drops

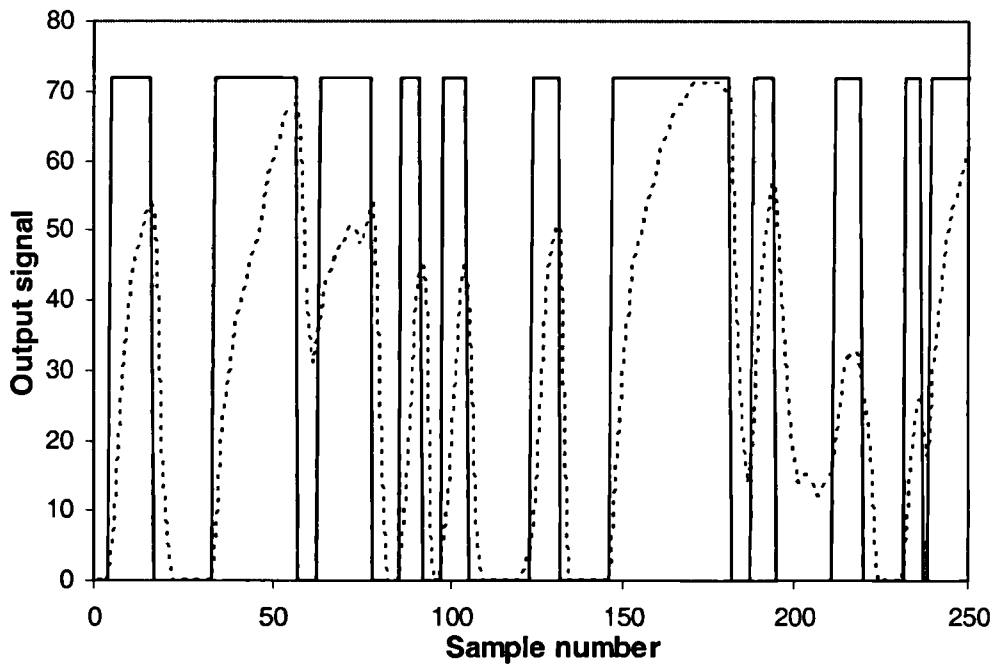


Fig. 5.5. Raw data and data transformed to a square wave

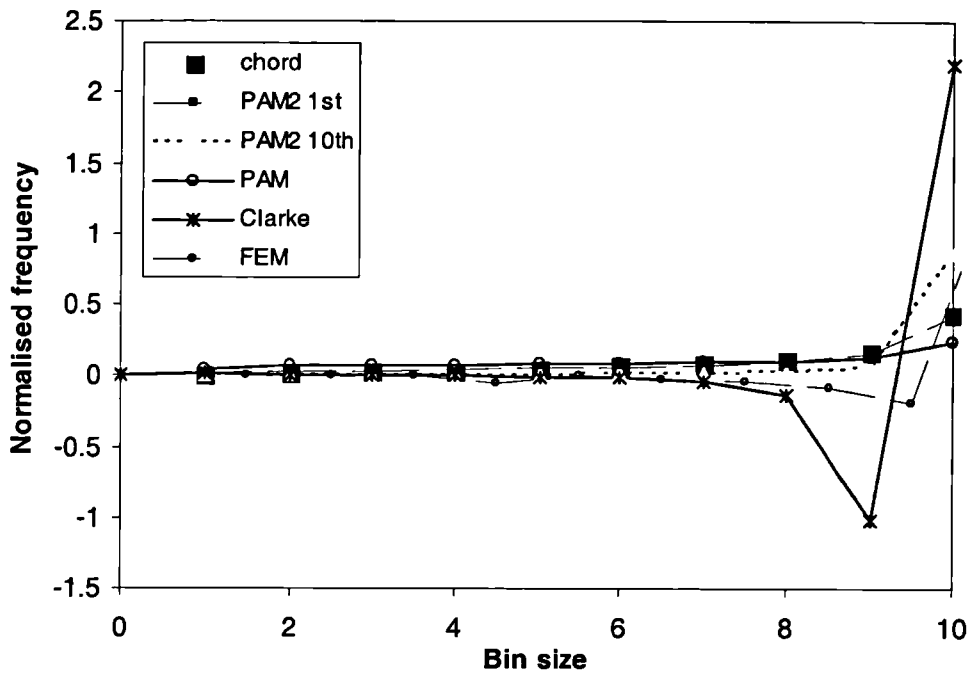


Fig. 5.6. Chord and derived diameter distributions for a system with initial unimodal particle size distribution at size 10

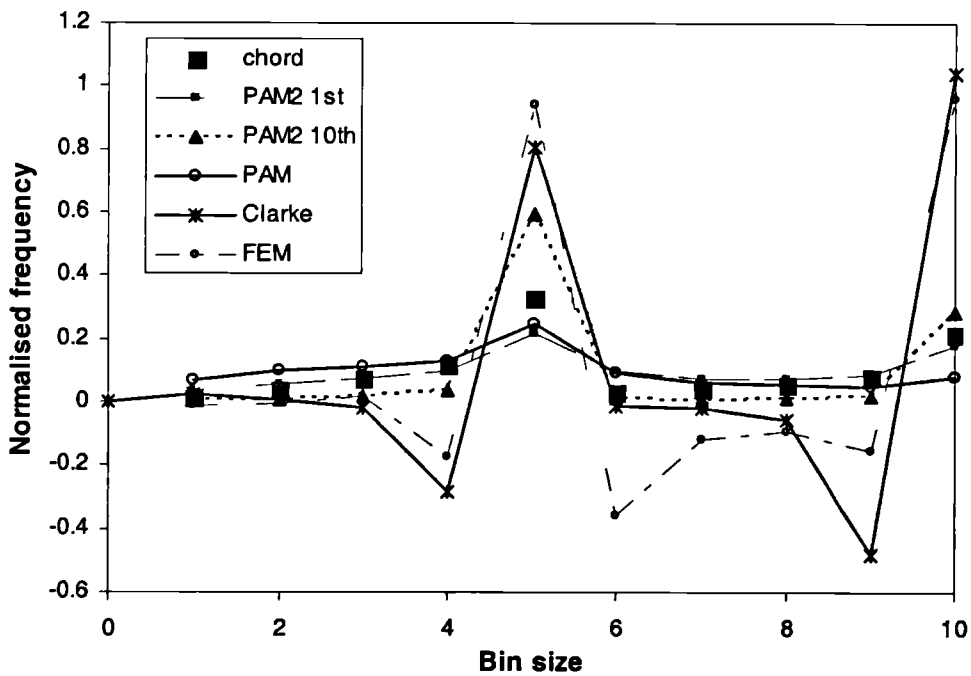


Fig. 5.7. Chord and derived diameter distributions for a system with initial bimodal particle size distribution at sizes 5 and 10

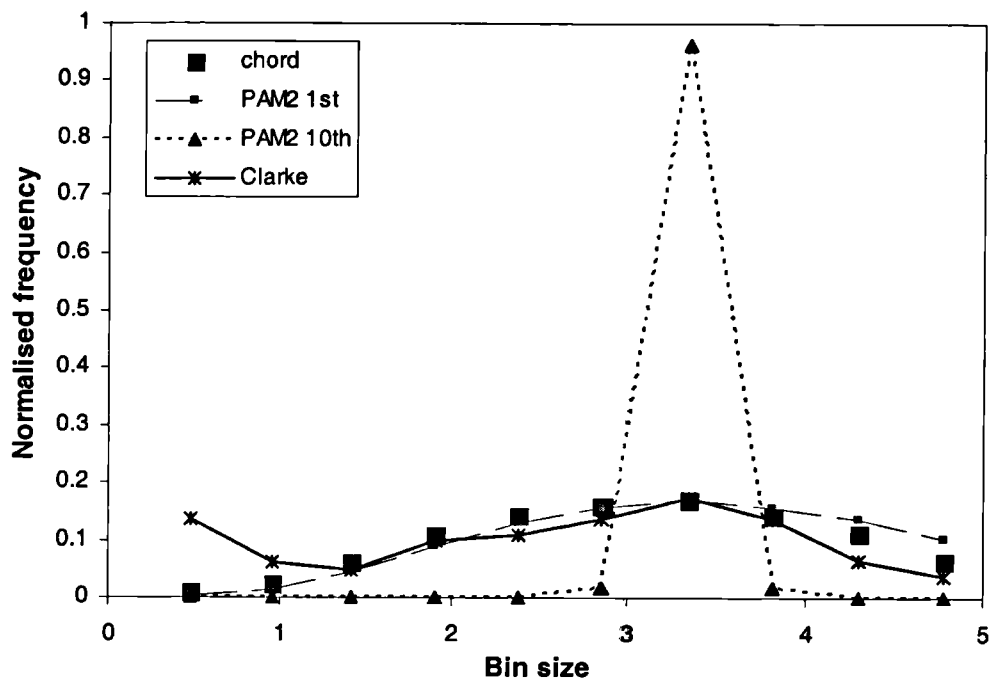


Fig. 5.8. Chord and derived diameter distributions for an experimental chord distribution

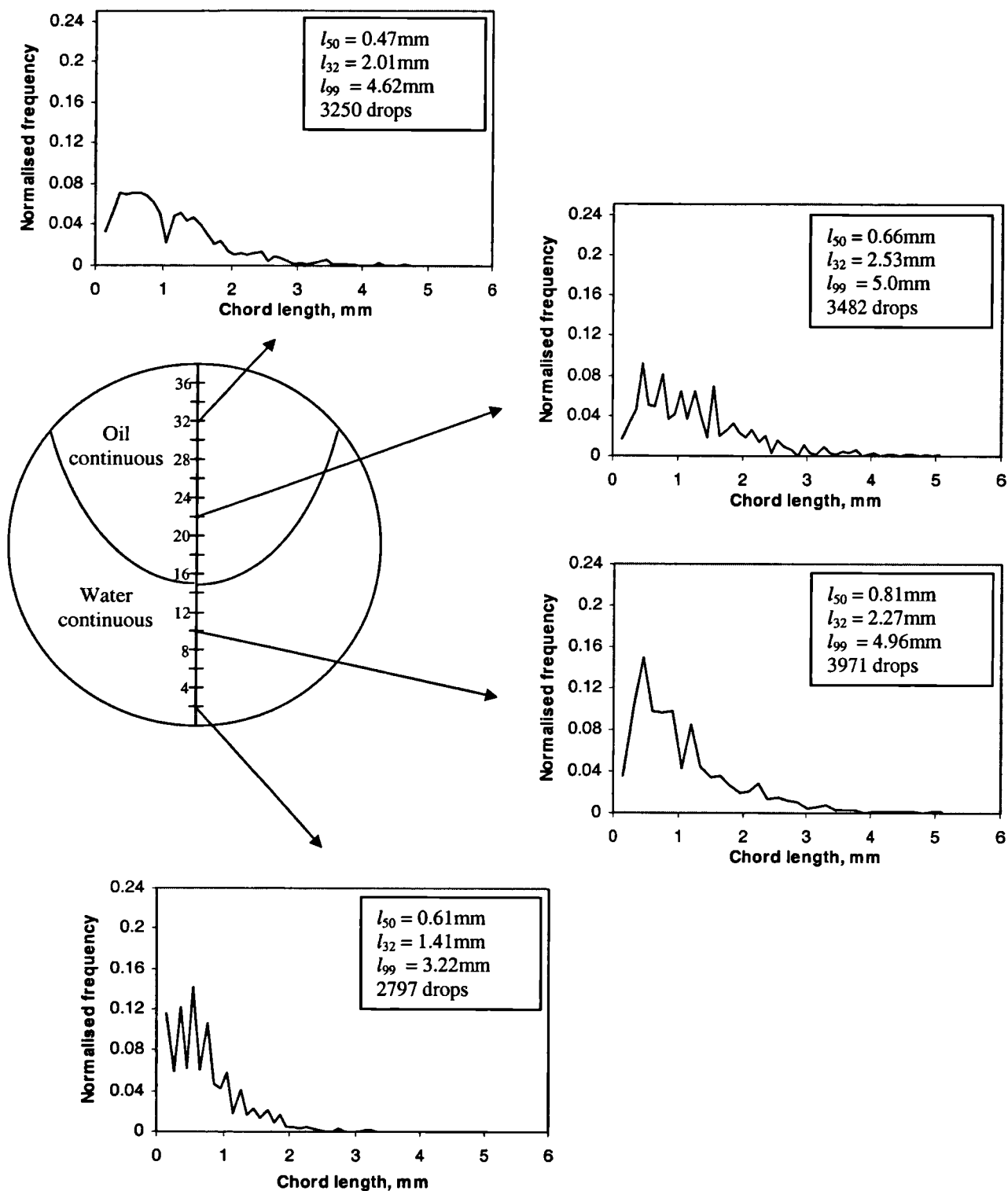


Fig. 5.9. Chord length distribution for mixture velocity 2.5m/s, input oil concentration 50 and heights 2mm, 14mm, 22mm, 32mm from the bottom of the pipe

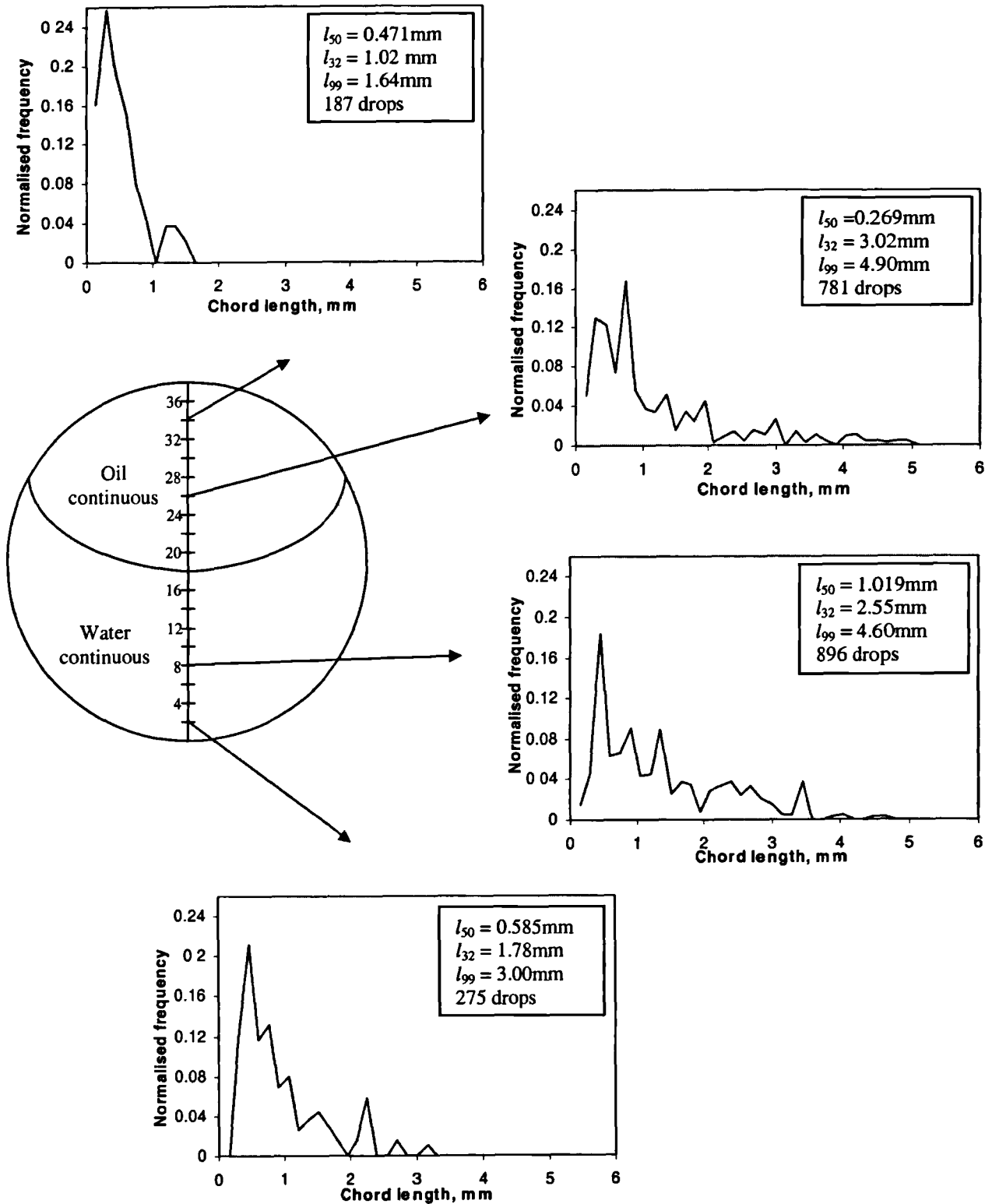


Fig. 5.10. Chord length distribution for mixture velocity 2 m/s, input oil concentration 50 %, and heights 2 mm, 16 mm, 26 mm, and 34 mm from the bottom of the pipe

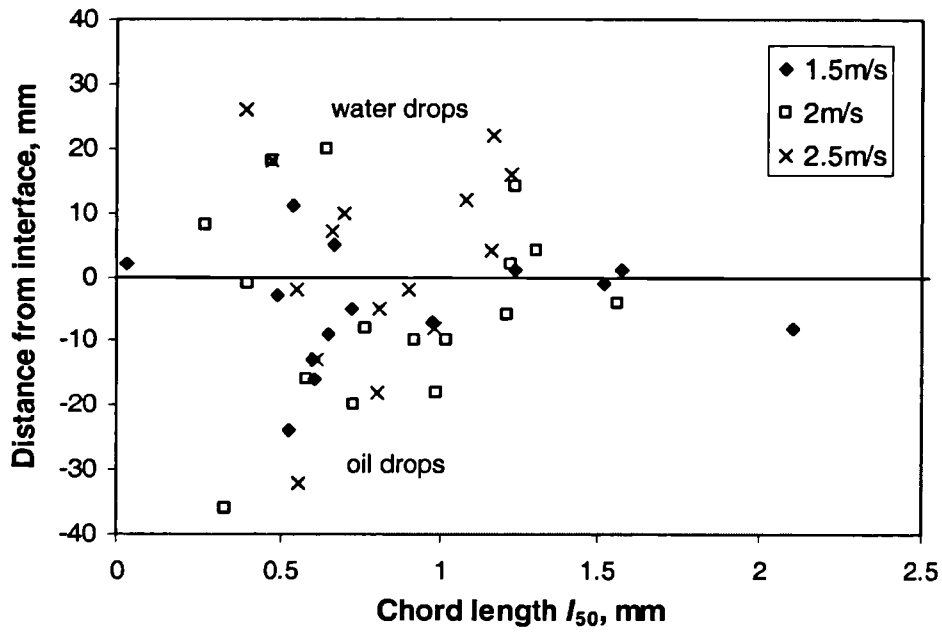


Fig. 5.11. The effect of the distance from the interface on chord length medians for all mixture velocities and input oil concentrations

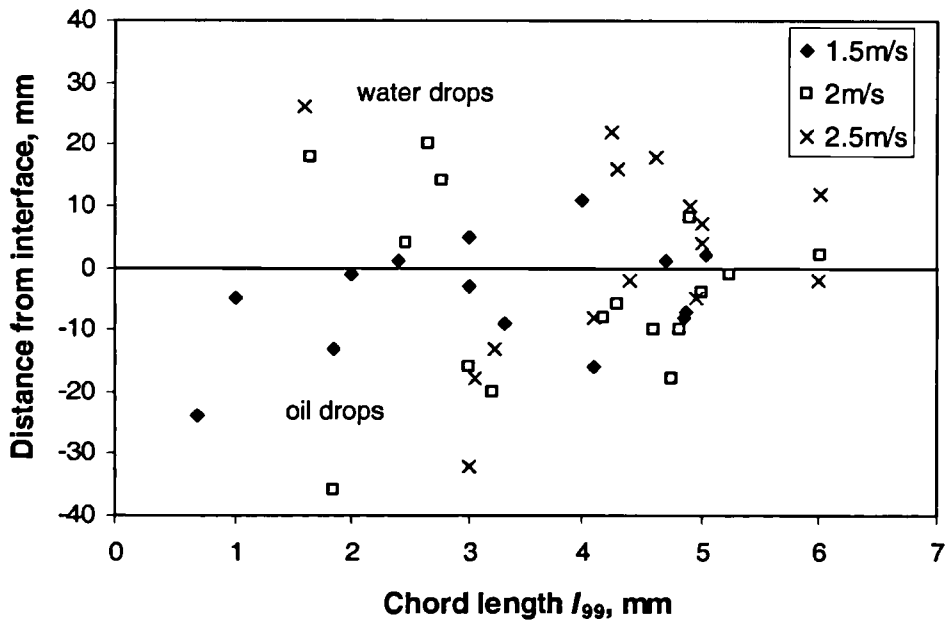


Fig. 5.12. The effect of the distance from the interface on chord length d_{95} values for all mixture velocities and input oil concentrations

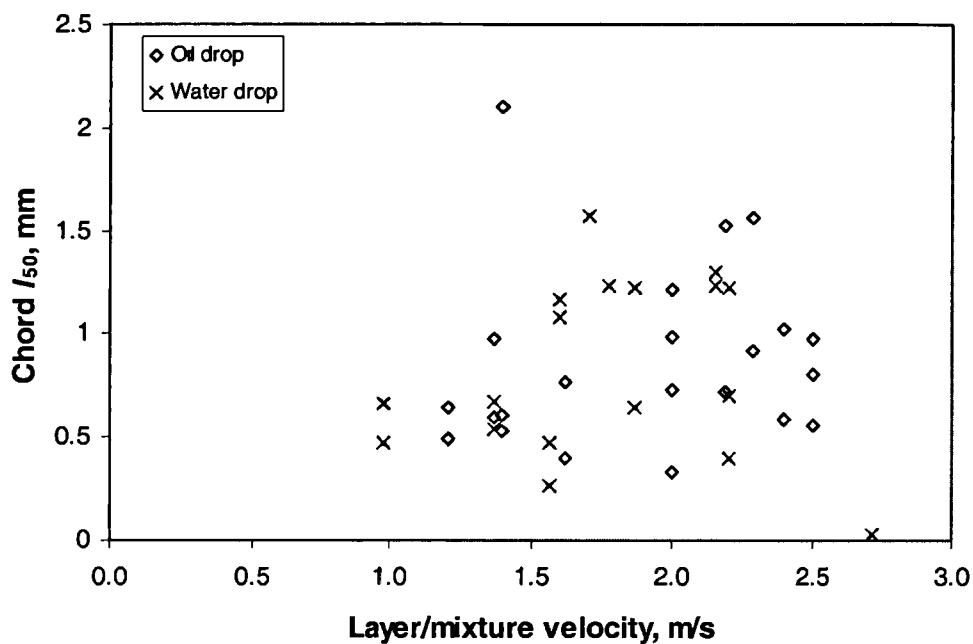


Fig. 5.13. The effect of continuous phase velocity on the chord distribution median for all mixture velocities and input oil concentrations

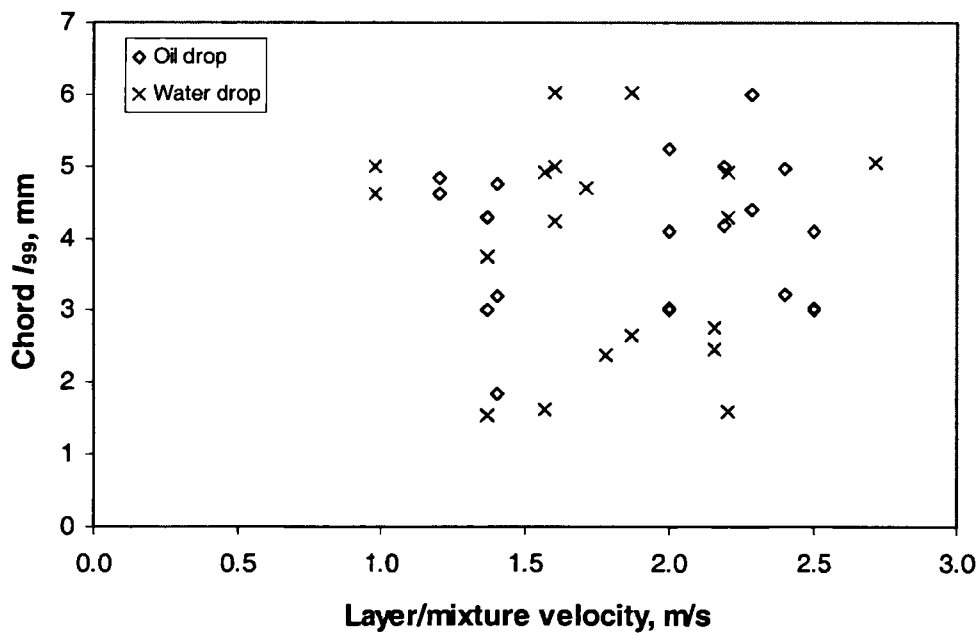


Fig. 5.14. The effect of continuous phase velocity on the chord distribution d_{95} values for all mixture velocities and input oil concentrations

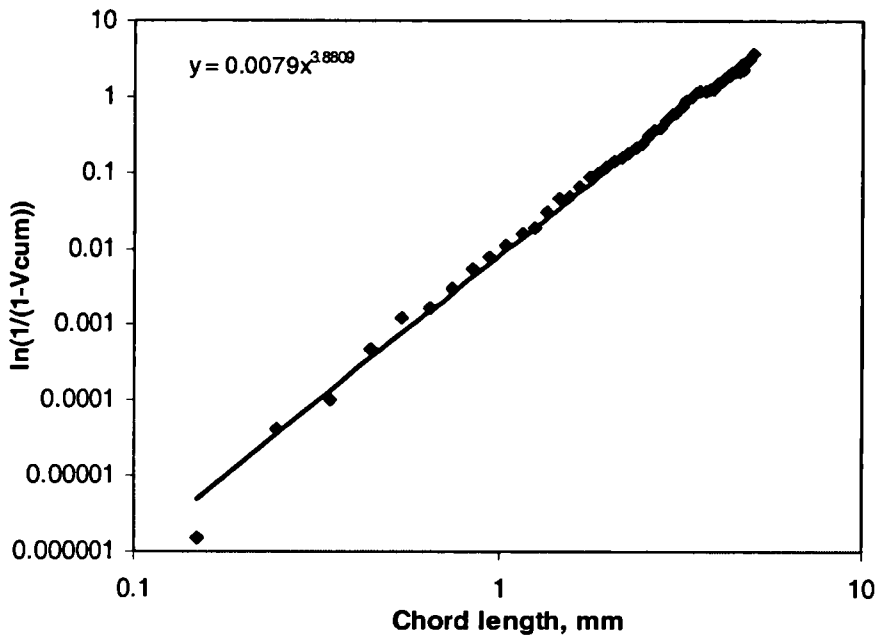


Fig. 5.15. Rosin-Rammler distribution fit to 2m/s mixture velocity, 68% input oil concentration, 8mm from the bottom of the pipe

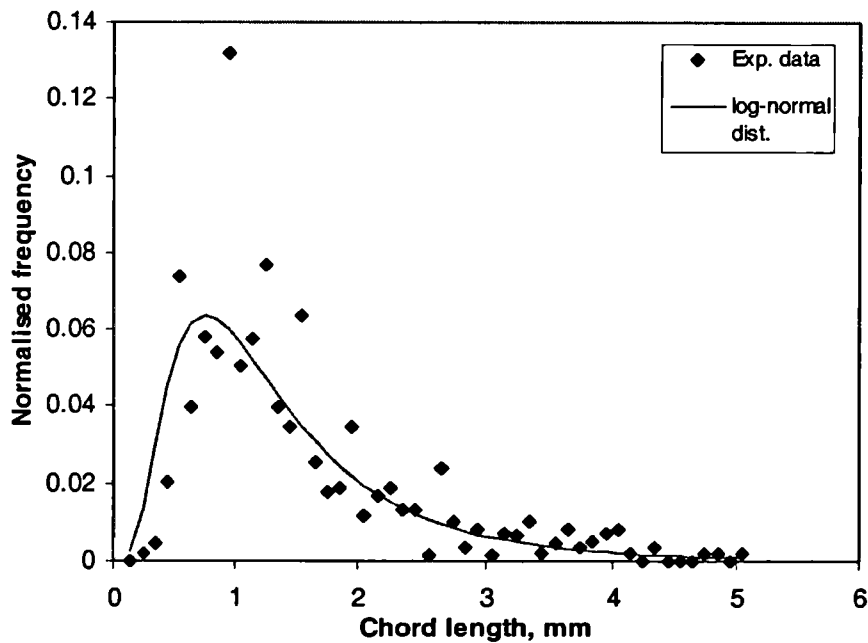


Fig. 5.16. Log-normal distribution fit to 2.5m/s mixture velocity, 68% input oil concentration, 10mm from the bottom of the pipe

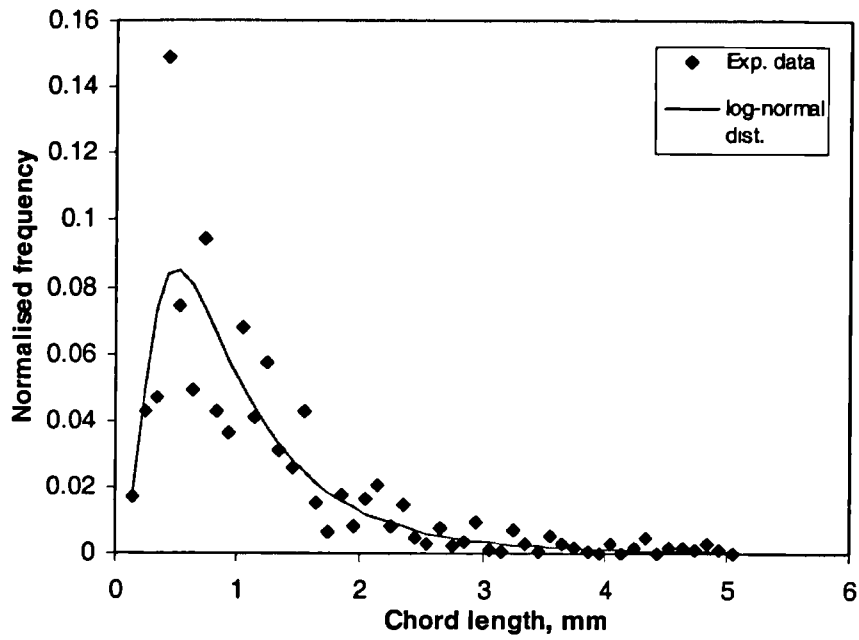


Fig. 5.17. Log-normal distribution fit to 2.5m/s mixture velocity, 50% input oil concentration, 32mm from the bottom of the pipe

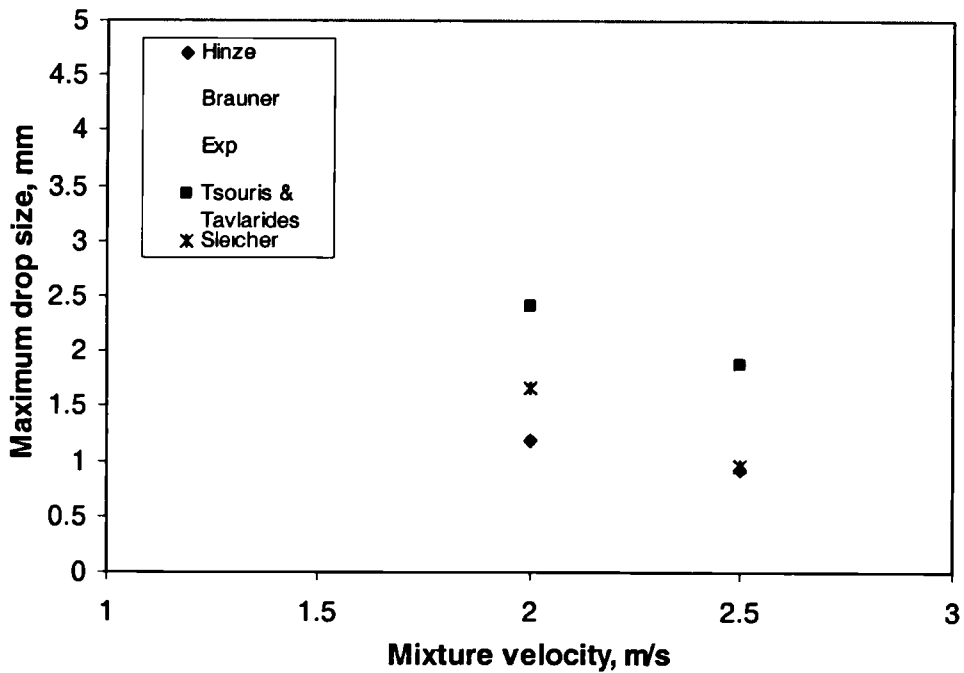


Fig. 5.18. Comparisons of the experimental maximum drop sizes with predictions of literature models for fully dispersed flow at 2m/s and 2.5m/s mixture velocities and 20% input oil fraction

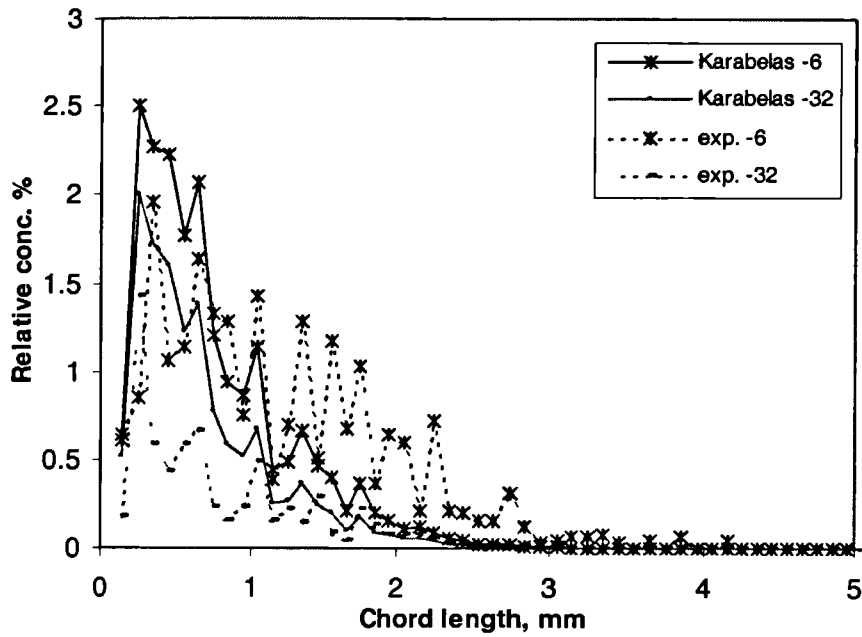


Fig. 5.19. Vertical concentration gradient of chord distribution for the Karabelas (1977) model and experimental data for 2m/s mixture velocity and 20% input oil concentration

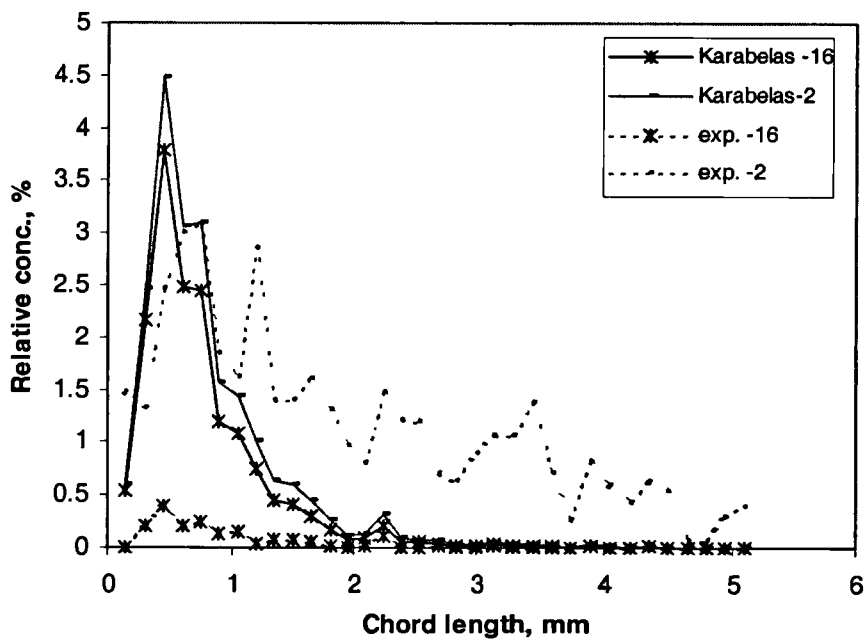


Fig. 5.20. Vertical concentration gradient of chord distribution for water drops in oil for the Karabelas (1977) model and experimental data for 2m/s mixture velocity and 50% input oil concentration

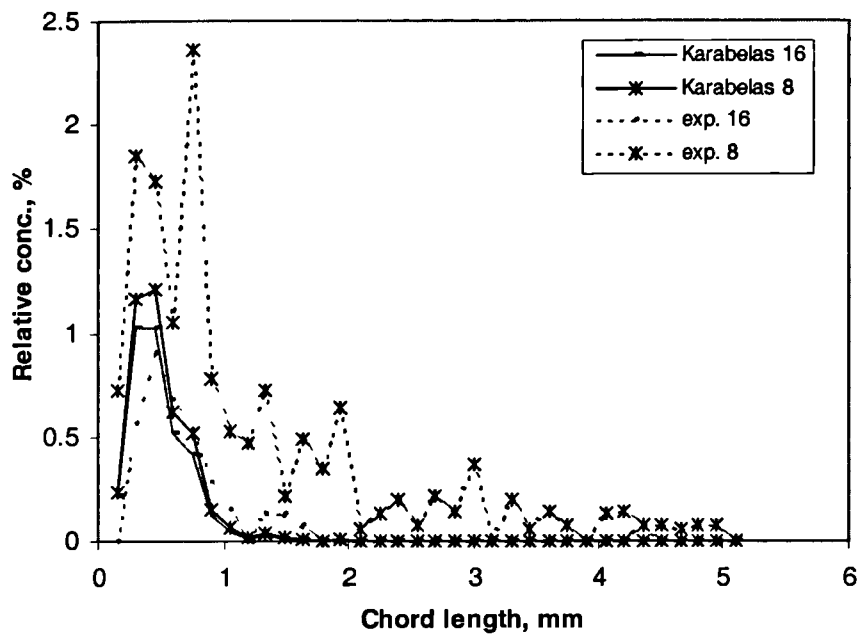


Fig. 5.21. Vertical concentration gradient of chord distribution for oil drops in water for the Karabelas (1977) model for 2m/s mixture velocity and 50% input oil concentration

6. PREDICTIVE MODEL FOR DUAL CONTINUOUS FLOW

Dual continuous flow combines characteristics of both stratified and dispersed systems. A development of the two fluid model (Taitel and Dukler, 1976) that takes into account the existence of two continuous layers and the entrainment of one phase into the other (*two-fluid model with entrainment*) is presented in this chapter. The model development is described in Section 6.1 while the comparisons of the model predictions with experimental pressure gradient and velocity ratio are presented in Sections 6.2 and 6.3 respectively. Pressure gradient comparisons are also made between the existing homogeneous model (Arirachakaran et al., 1989), and the Theissing (1980) correlation.

6.1 Model Development

According to the two-fluid model (Taitel and Dukler, 1976) the two phases are assumed to flow separately in the pipe, and one-dimensional momentum balance equations are written for each one. Appropriate wall and interfacial shear stress terms are used for closure. A development of the two-fluid model is used in this current work for the dual continuous flow pattern where entrainment of one phase into the other is introduced. The two-fluid model with entrainment assumes that dual continuous flow consists of two dispersed phases; an oil continuous phase with entrained water which flows at the top of the pipe (*upper phase*) and a water continuous phase with entrained oil which flows at the bottom of the pipe (*lower phase*). A flat interface was assumed initially, while curved interfaces, as found experimentally, were also considered. The one dimensional momentum balances in the flow direction for the upper and lower phases in a horizontal system are as follows (see also Fig. 6.1);

$$\left(\frac{dP}{dx}\right)_u = -\tau_w \left(\frac{S_u}{A_u}\right) \mp \tau_i \left(\frac{S_i}{A_u}\right) \quad (6.1)$$

$$\left(\frac{dP}{dx}\right)_l = -\tau_w \left(\frac{S_l}{A_l}\right) \pm \tau_i \left(\frac{S_i}{A_l}\right) \quad (6.2)$$

where (dP/dx) is the pressure gradient, τ is the shear stress, S is the perimeter, A is the cross sectional area and the subscripts u , l , and i , refer to the upper phase, the lower phase and the interface respectively. The sign of the interfacial shear stress term in these equations depends on the relative velocities between the two phases; the upper sign corresponds to the upper phase flowing faster than the lower, while the lower sign corresponds to the lower phase flowing faster. However, when the ratio of the two phase velocities is between 0.98 and 1.05 (Brauner and Moalem Maron, 1989), it can be assumed that the interfacial stress is equal to zero.

Wall shear stresses are calculated as follows:

$$\tau_u = f_u \left(\frac{\rho_u U_u^2}{2} \right) \quad \tau_l = f_l \left(\frac{\rho_l U_l^2}{2} \right) \quad (6.3)$$

where

$$f_u = C \left(\frac{D_u U_u \rho_u}{\mu_u} \right)^{-n} \quad f_l = C \left(\frac{D_l U_l \rho_l}{\mu_l} \right)^{-n} \quad (6.4)$$

f is the friction factor, U is the average velocity of the phase, D is the hydraulic diameter, μ is the viscosity and ρ is the density of the respective phase. The values 0.046 and 0.2 are used for the constants C and n respectively for turbulent flows.

Average in-situ phase velocities are calculated from the upper and lower phase flowrates divided by the respective areas, as follows:

$$U_u = \frac{Q_u}{A_u} \quad (6.5)$$

$$U_l = \frac{Q_l}{A_l} \quad (6.6)$$

where

$$Q_o = Q_u \varepsilon_u + Q_l \varepsilon_l \quad (6.7)$$

$$Q_w = Q_u (1 - \varepsilon_u) + Q_l (1 - \varepsilon_l) \quad (6.8)$$

Q_o and Q_w are the known input oil and water flowrates, Q_u and Q_l are the flowrates of the upper and lower phases, and ε_u and ε_l are the fractions of oil in the upper and lower phases respectively, which in this work are found experimentally. The hydraulic diameters can be found from:

$$D_u = \frac{4A_u}{S_u + S_l} \quad D_l = \frac{4A_l}{S_l} \quad \text{where } U_u > U_l \quad (6.9a)$$

$$D_u = \frac{4A_u}{S_u} \quad D_l = \frac{4A_l}{S_l + S_u} \quad \text{where } U_u < U_l \quad (6.9b)$$

$$D_u = \frac{4A_u}{S_u} \quad D_l = \frac{4A_l}{S_l} \quad \text{where } 0.98 < U_u : U_l < 1.05 \quad (6.9c)$$

The above are based on the assumption that the phase with the highest average velocity is flowing within a closed conduit, in which case the interface length, S_i , is used in the calculation of its hydraulic diameter. When the ratio of the two phase velocities is between 0.98 and 1.05 (Brauner and Moalem Maron, 1989) there is no interfacial shear stress and both phases are assumed to flow in an open channel (equation (6.9c)).

Since both the upper and lower phases are dispersions, appropriate equations are needed for the calculation of their density and viscosity. One approach is to assume that the dispersed phase is uniformly distributed within the continuum of the other and one density and viscosity can be used for the whole phase. Density can then be found as follows:

$$\rho_u = \varepsilon_u \rho_o + (1 - \varepsilon_u) \rho_w, \quad \rho_l = \varepsilon_l \rho_o + (1 - \varepsilon_l) \rho_w \quad (6.10)$$

where the subscripts o and w refer to oil and water respectively. These equations are similar to those used for the homogeneous model (equation (2.63)).

Various correlations have been suggested for the viscosity of liquid-liquid dispersions which take into account the dispersed phase concentration (see Section 2.4.1). A comparison has been made between the different viscosity correlations using the homogeneous model and experimental pressure gradient data at a mixture velocity of 3.5m/s where the flow pattern is fully dispersed. The results are shown in Fig. 6.2, and it can be seen that at low dispersed phase fractions the Brinkman (1952) and Roscoe (1952) correlation (equation (2.65)) predicts well the experimental pressure gradient.

The equations for emulsion viscosity predict increased viscosity, and consequently the pressure gradient, as the dispersed phase concentration increases (see Fig. 6.2). In many liquid-liquid dispersed flows, however, the opposite has been observed (Pal, 1993; Angeli and Hewitt, 1998) with pressure gradient decreasing with increasing dispersed phase fraction from the single phase values (*drag reduction phenomenon*). According to Rozentsvaig (1982) drag reduction can be accounted for by modifying the friction factor in dispersed systems, f_d , as follows:

$$f_d = \frac{f_e}{1 + n\phi} \quad (6.11)$$

where f_e is the friction factor of a finely dispersed emulsion with the same dispersed phase concentration as the two-phase mixture, and n is a concentration function constant, ranging from 0.5 to 1.125 in pipe flows. In this work, f_e was calculated using the Brinkman and Roscoe correlation for viscosity for the reasons stated above.

The interfacial stress term can be found from:

$$\tau_i = f \left(\frac{\rho (U_f - U)^2}{2} \right) \quad (6.12)$$

The density used in the interfacial stress term, ρ_f , is the density of the faster flowing phase (Brauner and Moalem Maron, 1989) and the velocity component is the difference between the faster (U_f) and the slower (U_s) phase velocities. In contrast to

gas-liquid stratified flows, where a number of correlations have been suggested for the interfacial friction factor, f_i , only a few exist for oil-water flows (Brauner, 1991; Hall, 1992; Neogi et al., 1994; Taitel et al., 1995).

For liquid-liquid annular flow where the core is the faster flowing phase, Brauner (1991) suggested the following equation

$$f_i = BC \left(\frac{D_c U_c \rho_c}{\mu_c} \right)^{-n} \quad (6.13)$$

where D_c is the diameter of the core phase, U_c and U_w are the core phase and the wall phase average velocities respectively, ρ_c is the core density, μ_c is the core viscosity, C and n are constants which depend on the flow regime and B is an augmentation factor which accounts for interfacial waviness. Brauner (1991) suggested that in liquid-liquid flows the waviness at the interface would be very slight and B should take the value of 1. Neogi et al. (1994), however, used the same approach to model oil-water interfacial shear stress in three-phase, gas-oil-water flows and found from experimental data that the value of B could vary from 0.8 to 1.

Hall (1992) suggested that

$$\tau_i = \gamma \tau_o \quad (6.14)$$

where τ_o is the oil wall shear stress and γ is a proportionality factor which must be less than 1. The term γ was calculated from the analytical solution of one-dimensional momentum equations for oil-water laminar stratified flow between parallel plates and was found to be closely related to the water/oil viscosity ratio. In his three-fluid model, Roberts (1996) actually used γ equal to this viscosity ratio (Khor et al. 1997).

Taitel et al. (1995) suggested that a constant value of 0.014 can be used for the interfacial friction factor except when the wall friction factor of the faster phase is greater than 0.014; in this case this wall friction factor value is used.

In the above model the interface is assumed to be flat. The results of the current work on phase continuity and distribution actually showed that the interface generally curves upwards, with the water forming a semi-annulus around the oil phase (see Fig. 6.3a and b), with the exception of input oil fractions below 25% where the interface curves downwards (Fig. 6.3c). It was also found that in most cases the radius of this curvature is approximately twice the pipe radius apart from the high and low oil fractions where it is approximately equal to the pipe radius. The assumption in the model is that the interface is curved, and that this curvature is circular is supported by the work of Brauner et al. (1998) and Ng et al. (2001). Interface curvature changes the areas and perimeters needed in the two-fluid model with entrainment. Table 6.1 shows the geometric parameters for flat and curved interfaces, all of which are dependent on the interface height, h . For the curved interfaces h is the distance between the interface apex and the wall (Figs. 6.3a, b, and c). These geometric parameters will change slightly, in the case of curved interfaces, where X is greater than the pipe radius, r (see Fig. 6.3b), and where the interface curves downwards at high input oil fractions (see Fig. 6.3c).

The proposed two-fluid model with entrainment requires the oil and water input flowrates and the entrainment values of water in oil in the upper phase, $(1-\varepsilon_u)$, and oil in water in the lower phase, ε_l . Assuming an interface height, h , the geometric parameters can be found from Table 1 for flat and curved interfaces. These can then be used to calculate the wall and interfacial shear stresses which, when substituted in the momentum equations (6.1) and (6.2) will give the pressure gradient, dP/dx , of the upper and lower phases respectively. An iterative method is followed, where the interface height is varied in intervals of 1×10^{-4} m, and the pressure gradient is calculated at each height for both the upper and lower phases. The height at which the pressure gradient difference between the upper and lower phases is at its minimum is the solution. From the interface height, the area occupied by each phase and its in-situ average volume fraction can be found which allow the velocity ratio to be estimated.

Fortran codes have been written which implement this procedure for different interfacial stress models (see Appendices A6).

6.2 Comparisons of Experimental Pressure Gradient Data with the Predictions of the Two-Fluid Model with Entrainment

Comparisons between the experimental values and the two-fluid model with entrainment were performed for mixture velocities 0.8-2.5m/s where dual continuous flow appears. Results will be shown for mixture velocities up to 1.5m/s where the flow pattern is dual continuous for all input oil fractions.

The model requires the entrainment of oil in the water continuous layer, and water in the oil continuous layer as input parameters. At present there is no predictive model for entrainment, and the experimental values obtained from the impedance and conductivity probes (see Section 4.2 and Fig. 4.9) were used instead.

6.2.1 Pressure gradient predictions

Pressure gradient predictions were performed for the three basic models; the Theissing (1980) correlation, the homogeneous model, and the two-fluid model with the modifications described above.

The homogeneous model assumes that the two phases are flowing as a mixture within the pipe, using correlations to calculate the density and viscosity. The density is calculated using equation (6.10), while the viscosity can be found from a number of different correlations outlined in Section 2.4.1. At low mixture velocities the flow pattern is either stratified or dual continuous, and therefore does not conform to the models assumptions. The model predictions for pressure gradient at a mixture velocity of 1.5m/s are shown in Fig. 6.4 for the different viscosity correlations. It can be seen that the predictions are greater than the experimental results. As the mixture velocity increases the flow pattern becomes more dispersed giving predictions closer to the assumptions of the model. The predictions at 3.5m/s have been shown in Fig. 6.2, where it can be seen that the model still overpredicts the pressure gradient because the viscosity correlations predict an increase in viscosity as the dispersed

phase concentration increases. However the model does not account for the drag reduction phenomenon as observed by Pal (1993) and Angeli and Hewitt (1998).

The correlation by Theissing (1980) that uses the Lockhart-Martinelli parameters, X and Φ , was also considered. The model was described in Section 2.4 with equations (2.53) to (2.57). The predictions are shown in Fig. 6.5 which combines data from mixture velocities 1.5m/s and 2m/s. At X values greater than 1, where the single phase oil pressure gradient is greater than the single phase water pressure gradient the Theissing correlation over predicts the experimental data. For the test fluids used in the current work, this range is associated with an oil concentration greater than the water where the pressure gradient fluctuations are observed. At X values less than 1 the Theissing correlation predicts the experimental data well.

6.2.1.1 Flat interface

The experimental pressure gradient data were first compared with the predictions of the two-fluid model with entrainment and flat interface (Fig. 6.6) for different interfacial friction factors. These included the suggestions by Taitel et al. (1995) (*entrainment*), Neogi et al. (1994) (*Neogi*), and Roberts (1996) (*Roberts*). According to Taitel et al. (1995), f_i is equal to 0.014; except when the wall friction factor of the faster flowing phase is greater than 0.014 in which case this value is used instead. In the Neogi et al. correlation (based on equation (6.13) suggested by Brauner, 1991), the interfacial friction factor is the same as the wall friction factor of the faster flowing phase multiplied by a factor B ; B was taken equal to 0.8, as suggested by Neogi et al., which gave the closest to experimental data predictions in this study. The viscosities used to calculate the proportionality factor, γ , in the correlation by Roberts (equation (6.14)) are found by considering that both the upper and lower phases are dispersions. In the same graph the predictions of the standard two-fluid model (no entrainment and flat interface) are also shown with interfacial friction factor calculated as suggested by Taitel et al. (1995) (*no entrainment*).

It can be seen that all models predict higher pressure gradients than the experimental data, especially at the medium input oil volume fractions. Including the entrainment

resulted in higher pressure gradients than those given by the two-fluid model without entrainment; this is attributed to the higher viscosities of the two phases when entrainment is included, which are now treated as emulsions. The different models for interfacial shear stress had little effect on the predictions. Therefore, in the following, unless otherwise specified, the simpler method for calculating the interfacial friction factor as suggested by Taitel et al. (1995) will be used.

The experimental data actually shows that the two-phase pressure gradient was in most cases below the single phase oil values, indicating the appearance of a drag reduction phenomenon. To account for this, modified friction factors, as suggested by Rozentsvaig (1982) (see equation (6.11)) were used for the friction factor calculations in the upper and lower dispersed phases. The value 1 was used for the parameter n , which gave the best fit compared to the experimental data. Also, experimental friction factors, found from oil and water continuous dispersed flow experiments that had the same dispersed phase concentrations as those in the upper and lower phases in dual continuous flow respectively, were implemented in the model. These factors typically ranged from 0.0025 to 0.0053 (the f values in the model with entrainment calculated from equation (6.4) and averaged phase properties ranged from 0.005 to 0.01), and were higher in the water than in the oil continuous dispersions; in general they decreased with increasing dispersed phase volume fraction. Both the predictions of the model with friction factors calculated as suggested by Rozentsvaig (f by *Rozentsvaig*) and of the model with experimental friction factors (*experimental f values*) are compared with the experimental pressure gradient data for a mixture velocity of 1.5m/s in Fig. 6.7. The predictions of the two-fluid model without (*no entrainment*) and with entrainment (*entrainment*) are also included.

Accounting for turbulence damping with the Rozentsvaig correlation improved the predictions of the two-fluid model except at very high and very low input oil fractions. The experimentally derived friction factors have a large effect and result in predicted pressure gradients significantly lower than those of the previous models. Both models were, however, unable to predict the trend in the pressure gradient data observed experimentally.

At the two lower mixture velocities used, the degree of entrainment of one phase into the other decreased (see Fig. 4.9) and the models gave predictions closer to the experimental data (see Fig. 6.8 for mixture velocity 1m/s). In this case, the use of the experimental friction factors to account for turbulence damping underpredicted the pressure gradient. These friction factors were obtained at similar dispersed phase concentrations, but higher mixture velocities, which would have resulted in different drop sizes. Turbulence modification in dispersed systems has been related to the size of the dispersed particles but results are still inconclusive as to how variation of particle size affects the magnitude of modification (Kenning and Crowe, 1997). The experimentally derived friction factors may, therefore, not be suitable when used at different mixture velocities.

6.2.1.2 Curved interface

The interface in dual continuous flow is not expected to be flat as the phase distribution diagrams show (see Chapter 4). To account for this, interface curvature was introduced in the two-fluid model with entrainment. Two curvatures with different radii were used in this work; 0.038m (twice the pipe radius) and 0.019m (the same as the pipe radius) and the results are shown in Fig. 6.9 and 6.10 respectively. It was found experimentally that the interface curved upwards at oil concentrations greater than 25%, while it curved downwards at lower oil concentrations (see Figs. 6.3a, b and c).

Experimental data on pressure gradient were compared in Fig. 6.9 and 6.10 with the predictions of the standard two-fluid model with flat interface and no entrainment (*no entrainment-flat*) and of the same model with curved interface (*no entrainment-curved*). The predictions of the model with entrainment and curved interface (*entrainment-curved*) were also included as well as the predictions of the same model with modified phase friction factors obtained from experimental data (*experimental f values-curved*). Considering a curved interface in the two-fluid model without entrainment results in little effect on the pressure gradient predicted. This could be due to the small viscosity difference between the two phases, meaning that any changes in the contact area of each phase with the wall is balanced by changes in the in-situ area it occupies, and consequently its average velocity. Only at

high input oil fractions when interface curvature is included are the pressure gradients predicted less than those with flat interface, a difference which became more significant as the interface curvature increased (the radius decreased, Fig. 6.10). The formation of a water semi-annulus layer at the bottom of the pipe around the oil phase resulted in this case in an overall reduction in pressure drop.

When entrainment was included in the model with curved interface then, as expected, higher pressure gradients were predicted. At the smaller interface radius, however, and at high and low input oil fractions, inclusion of entrainment resulted in lower pressure gradients than the *no-entrainment* case (Fig. 6.10). This is probably due to a combination of entrainment and interface curvature which affect the phase flowrates (and consequently friction factors) and wall contact area respectively. Again, the model with turbulence damping gave reduced predicted pressure gradients. It appears that inclusion of the experimental f values has a more dramatic effect on the predicted pressure gradient than interface curvature. Similar observations were made at the other mixture velocities used.

6.3 Comparisons of Experimental Velocity Ratio Data with the Predictions of the Two-Fluid Model with Entrainment

Comparisons between model predictions and experimental data were carried out for similar conditions to those used for pressure gradient comparisons in Section 6.2. Predicted velocity ratios from the models described can be found, according to equation (2.1), from the cross sectional areas of the upper and lower layers and the experimentally measured entrainment of the phases in each of these layers.

6.3.1 Flat interface

The velocity ratio predictions for models that assume a flat interface, are compared in Fig. 6.11 with experimental data obtained with the QCVs. It can be seen from Fig. 6.11 that all models give the same trend as the experimental data of increasing S with input oil fraction. They do, however, underpredict S , particularly at the medium oil volume fractions. Inclusion of entrainment (*entrainment*) improves the predictions of the two-fluid model without entrainment (*no entrainment*) at the lower input oil

fractions but performs worse at the higher fractions. One possible reason for this is the phase distribution inside the pipe. The interface is curved upwards at the intermediate input oil fractions meaning that the oil has a low wall contact area in comparison to its cross sectional area. It therefore experiences less drag and is able to flow faster than the water resulting in an S value greater than 1. Because the model assumes a flat interface this phenomenon is not taken into account.

The different models for interfacial shear stress and Rozentsvaig's turbulence damping correlation gave similar predictions. Only the use of the experimentally derived friction factors (*experimental f values*) for the calculation of the upper and lower phase wall shear stresses improved the predictions significantly, apart from at the highest input oil fraction where the S value is underpredicted. The same trends were observed for other mixture velocities used.

6.3.2 Curved interface

Interface curvature would be expected to affect the velocity ratio, as it changes the wall perimeter wetted by the continuous phase. The model predictions when interface curvature of radius 0.038m was included were compared with experimental data in Fig. 6.12. Including interface curvature on the two-fluid model without entrainment (*no entrainment-curved*) gave slightly higher velocity ratios, closer to experimental data, compared to the results of the same model with flat interface (*no entrainment-flat*), with the exception of the low input oil fractions. This is expected, as a model with curved interface compared to the same model with flat interface, would give lower S values at low oil concentrations (where the interface curves downwards the oil would be expected to have a larger wall wetted perimeter and be held back more than in the case of flat interface) and higher S values for the high oil fractions (where the water has now larger wall contact area than in the case of flat interface). The reason that this difference is not very pronounced may be the small difference in viscosities between the two phases. The two graphs showing flat and curved interface cross at the input oil volume fraction (25%) where the interface shape changed from a downward curvature to an upward one.

From the models with entrainment only the model with experimental f values and curved interface (*experimental f values-curved*) is shown in Fig. 6.12 since it gave the best predictions in the case of flat interface (Fig. 6.12); this model again gave S values closest to experimental data apart from the highest oil fractions used.

Using the smaller (0.019m) radius for the interface curvature did not affect significantly the velocity ratio predictions while the same trends were also observed at the other mixture velocities.

6.4 Conclusions

From the comparisons between the model predictions and experimental data on pressure gradient and in-situ hold-up or velocity ratio, the following conclusions can be drawn:

- The models which included entrainment and drag reduction gave predictions closest to the experimental data both for pressure gradient and velocity ratio.
- The use of entrainment in the two-fluid model without accounting for drag reduction did not improve the predictions of pressure gradient or velocity ratio compared to the standard two-fluid model without entrainment.
- Including the interface curvature did not seem to affect the models' predictions significantly, which may be due to the small viscosity difference between the two phases. However, including the drag reduction phenomenon, particularly by using experimentally measured dispersed phase friction factors, affected the model predictions significantly.
- The different interfacial shear stress correlations used gave similar predictions. The drag reduction phenomenon and the way that friction factors change with mixture velocity and drop size distribution during unstable dispersed liquid-liquid flows needs to be further investigated. Furthermore, a model which predicts distribution of one phase into the other during dual continuous flow would allow the above model to be used in different oil-water systems.

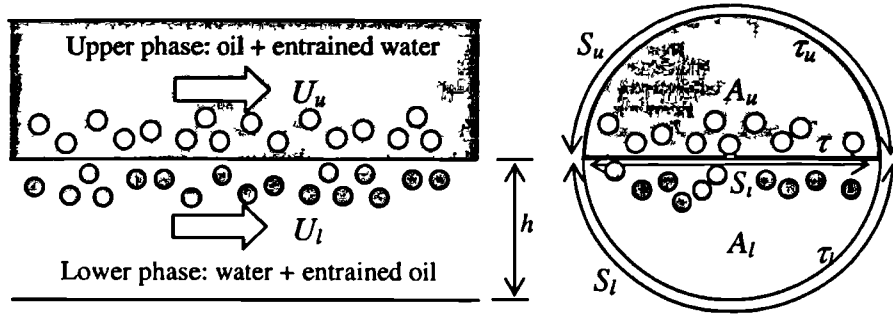


Fig. 6.1. Diagram of dual continuous flow and key for symbols used in equations (6.1) & (6.2)

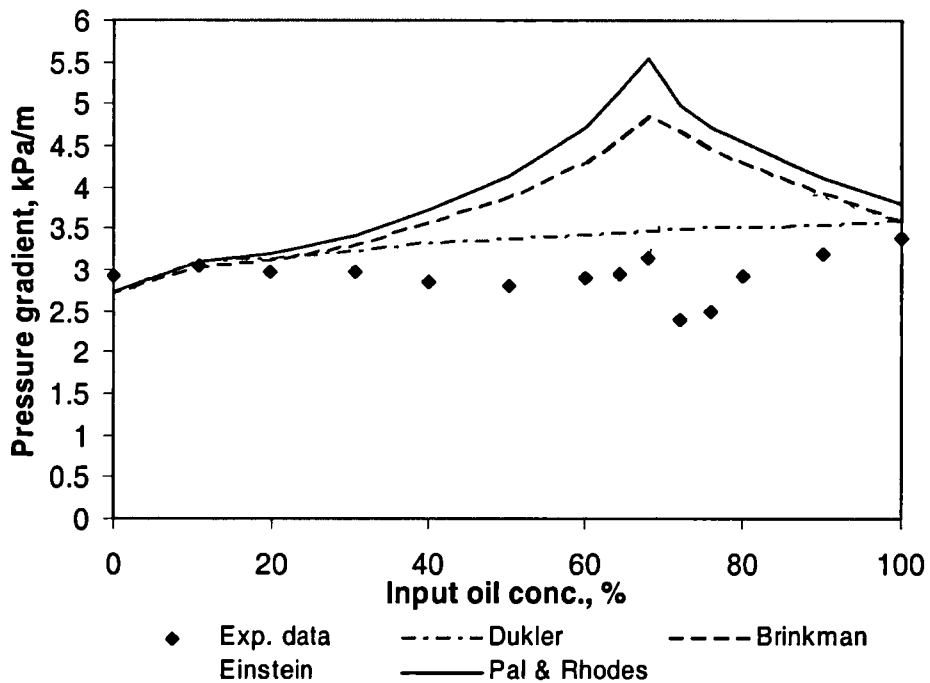
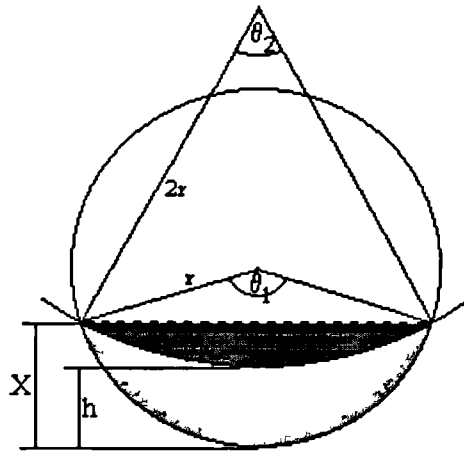
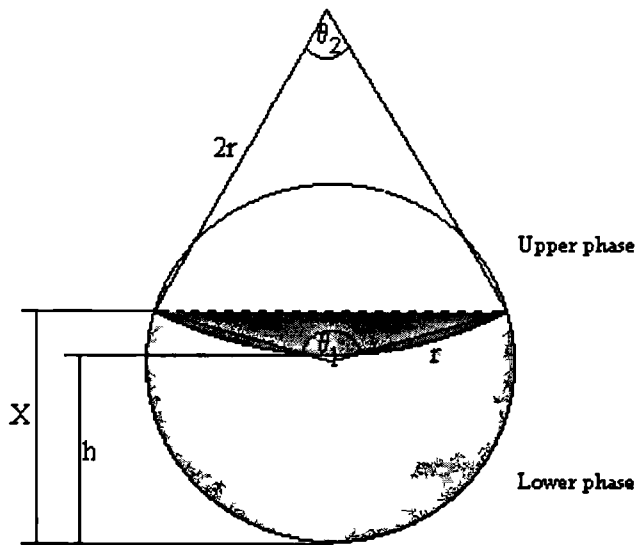


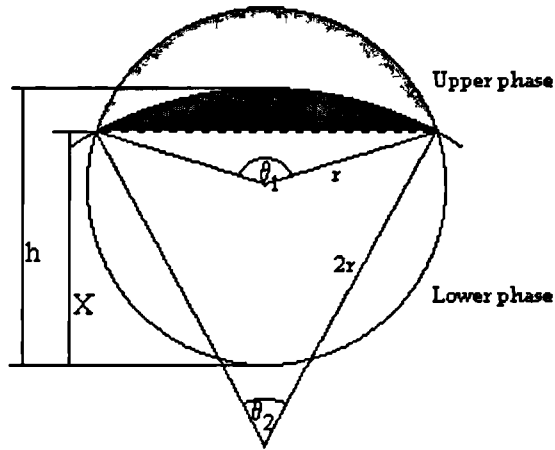
Fig. 6.2. Comparison of experimental pressure gradient data and predictions of the homogeneous model using different dispersed phase viscosity correlations at a mixture velocity of 3.5m/s



Figs 6.3a. Geometric parameters for the two-fluid model with entrainment and interfacial curvature (curved up) with $X < r$



Figs 6.3b. Geometric parameters for the two-fluid model with entrainment and interfacial curvature (curved up) with $X > r$



Figs 6.3c. Geometric parameters for the two-fluid model with entrainment and interfacial curvature (curved down)

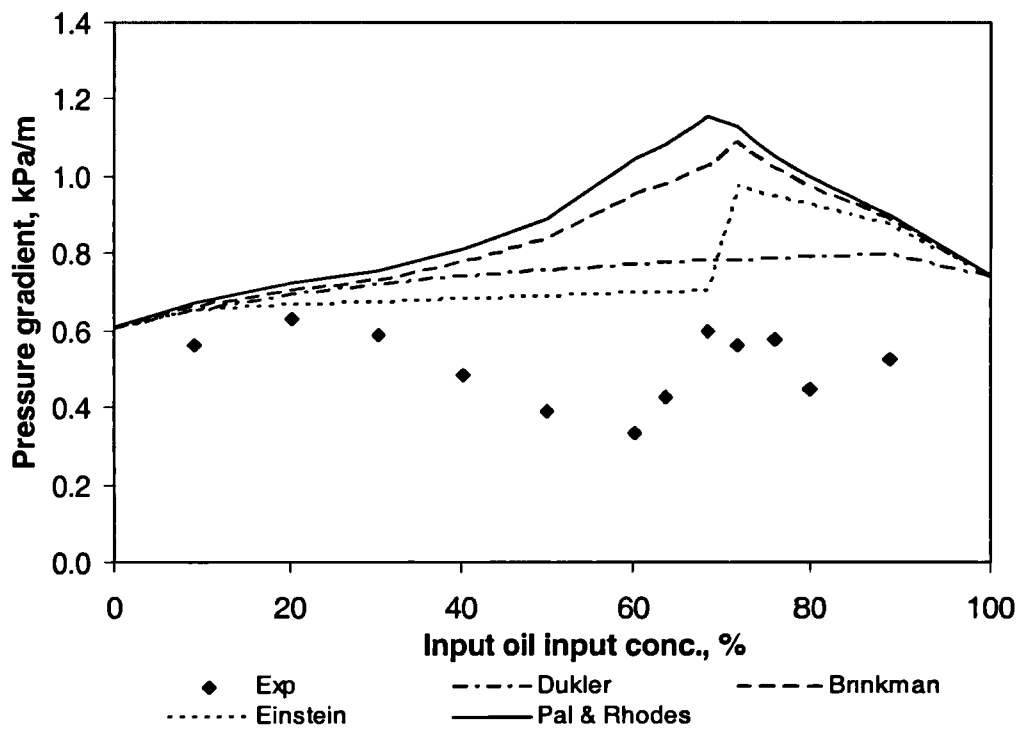


Fig. 6.4. Comparison of experimental pressure gradient data and predictions of the homogeneous model using different dispersed phase viscosity correlations at a mixture velocity of 1.5m/s

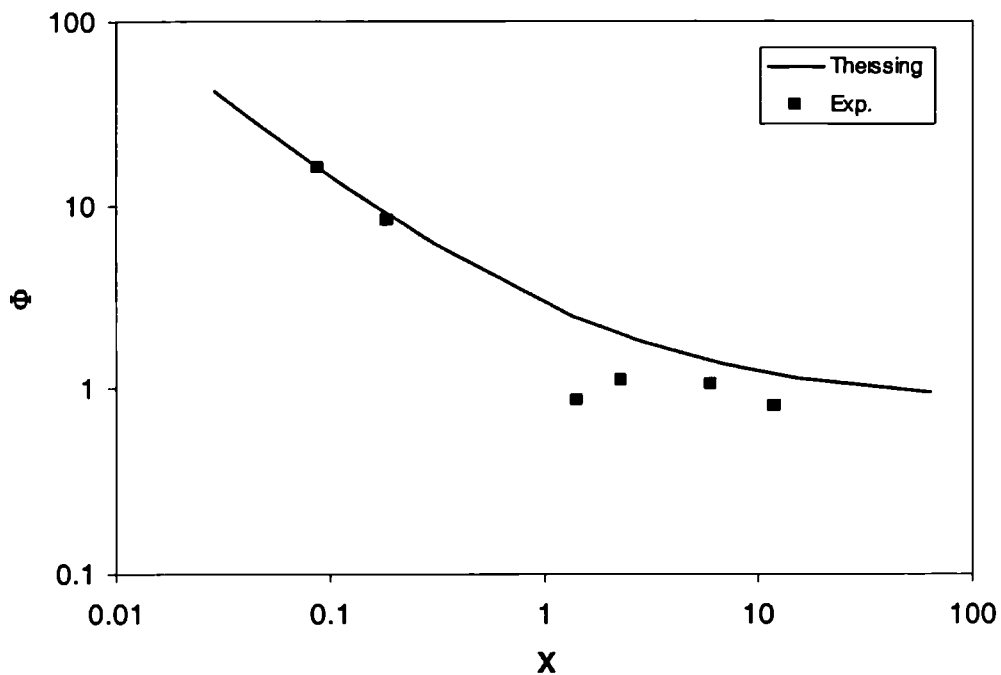


Fig. 6.5. Pressure gradient predictions for the Theissing (1980) correlation

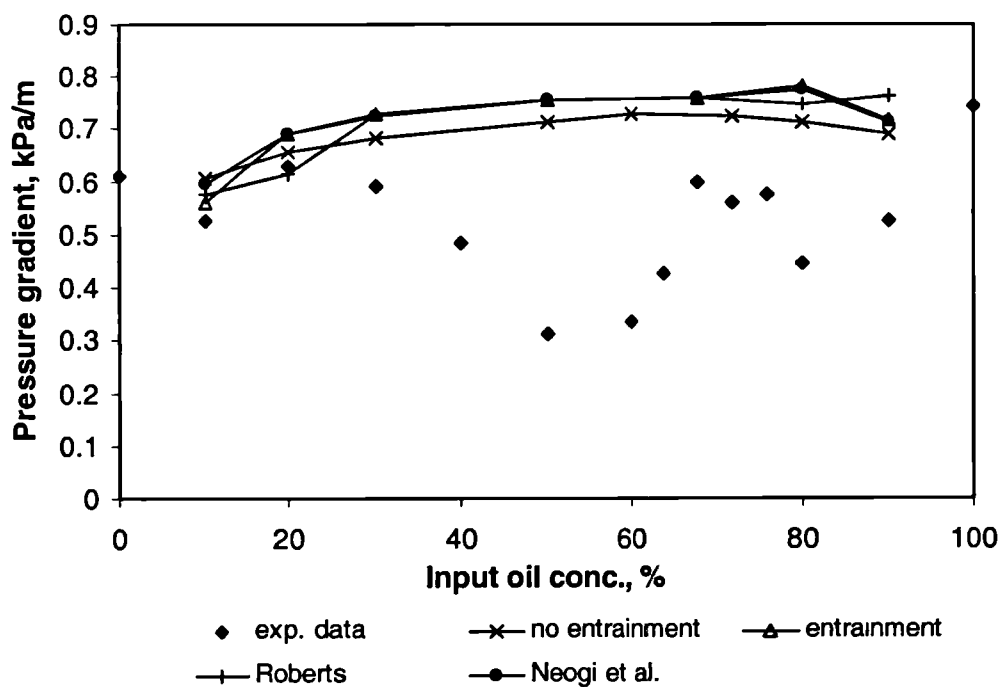


Fig. 6.6 Comparison of experimental presure gradient data with the model predictions for different interfacial shear stress terms at 1.5m/s mixture velocity

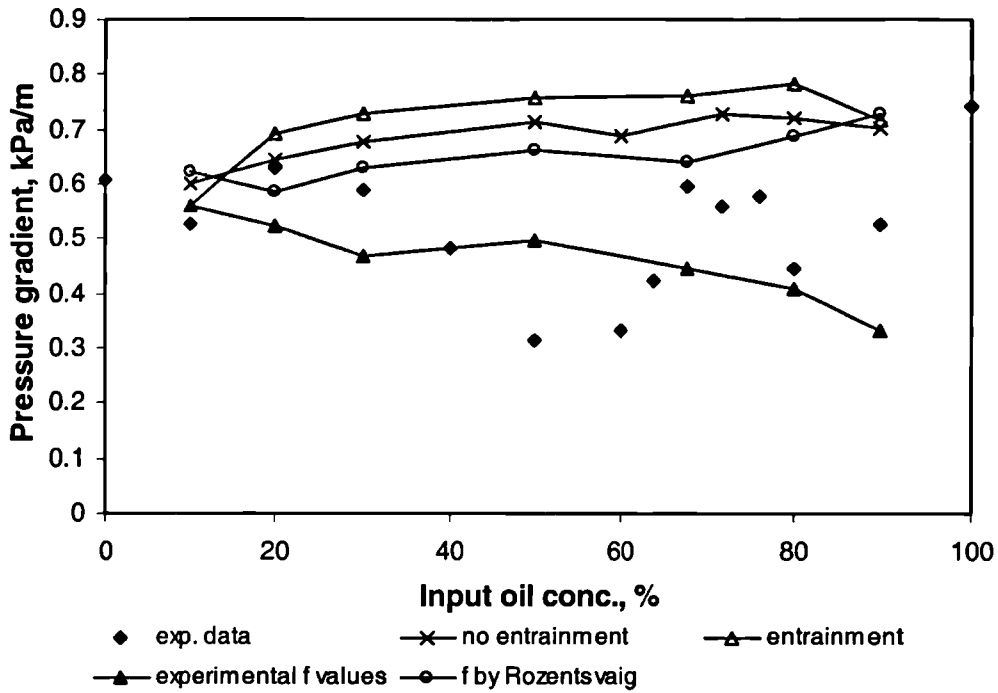


Fig. 6.7. Comparison of experimental pressure gradient data with the model predictions for different phase friction factors at 1.5m/s mixture velocity

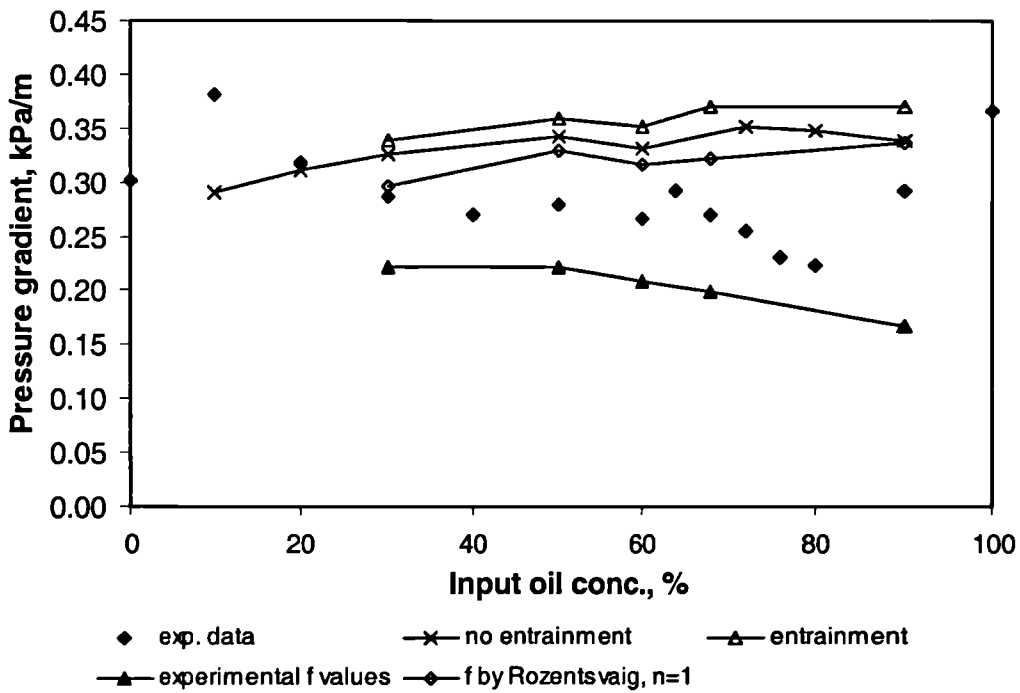


Fig. 6.8. Comparison of experimental pressure gradient with the model predictions for different phase friction factors at 1m/s mixture velocity

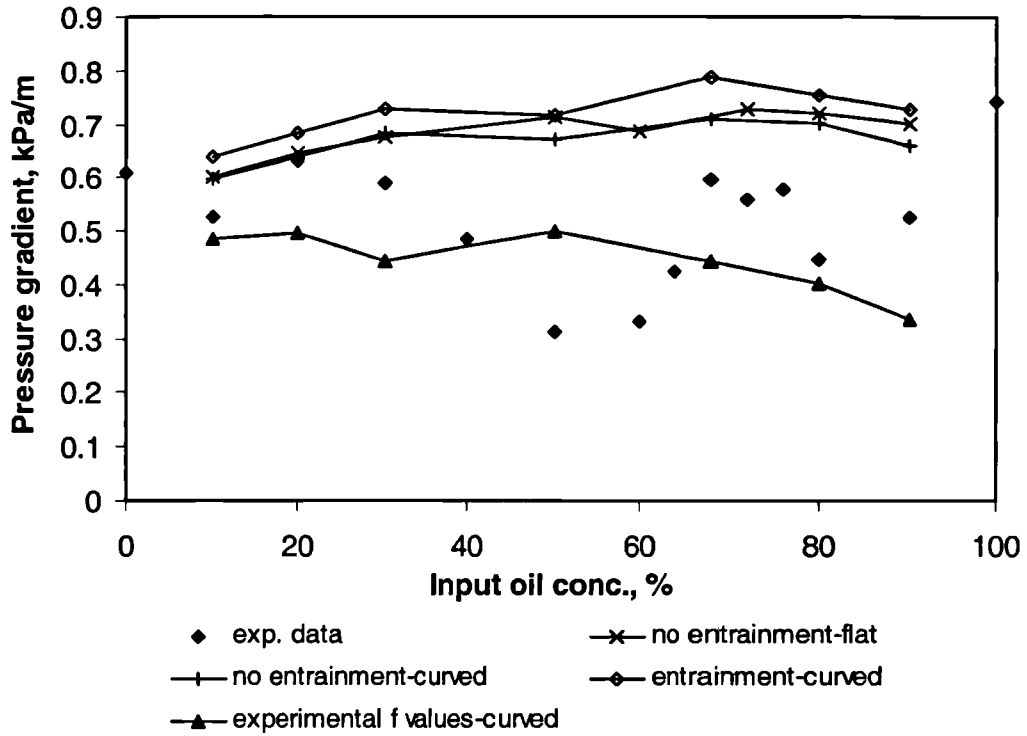


Fig. 6.9. Comparison of experimental pressure gradient data with the model predictions for curved interface with 0.038m radius at 1.5m/s mixture velocity

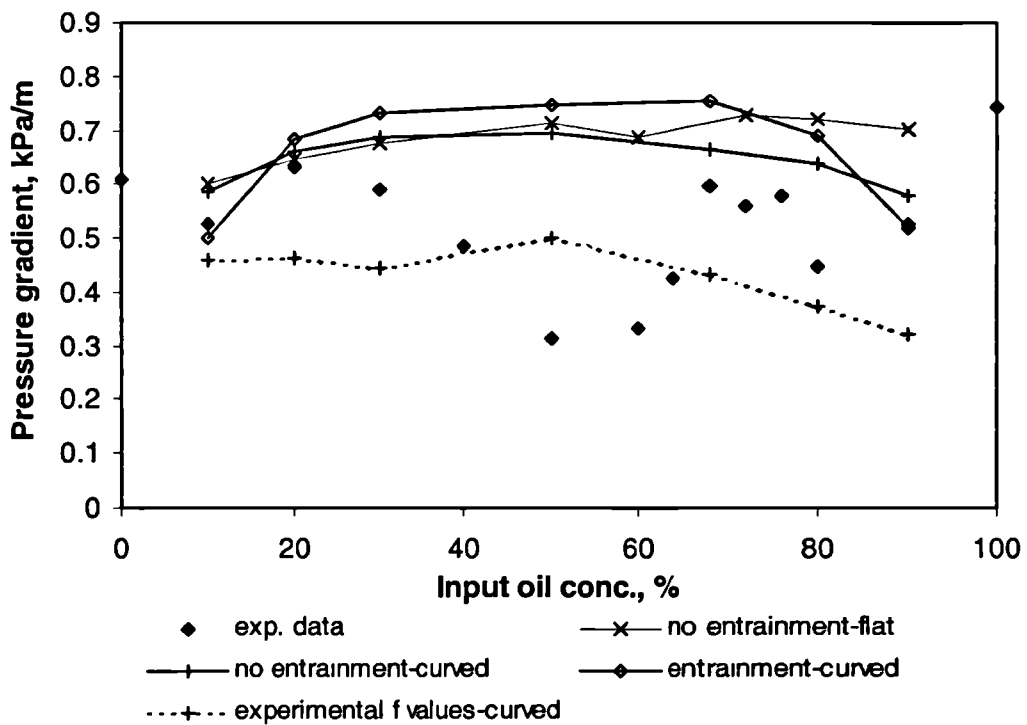


Fig. 6.10. Comparison of experimental pressure gradient data with the model predictions for curved interface with 0.019m radius at 1.5m/s mixture velocity

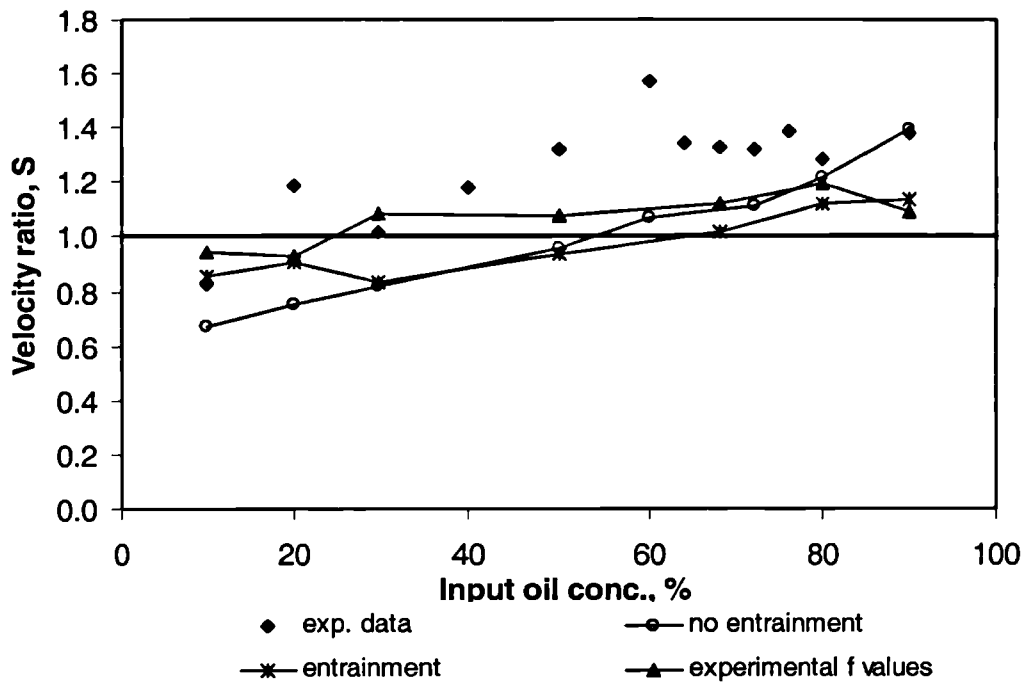


Fig. 6.11. Comparison of experimental velocity ratio data with the model predictions at 1.5m/s mixture velocity

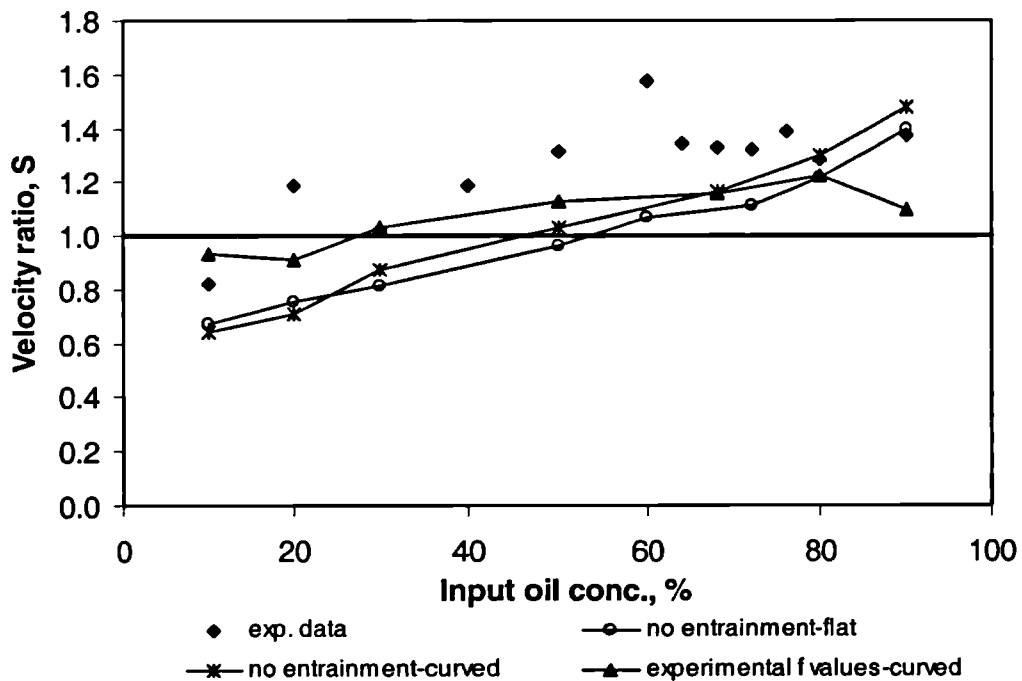


Fig. 6.12. Comparison of experimental velocity ratio data with the model predictions for curved interface with 0.038m radius at 1.5m/s mixture velocity

Flat interface	
θ_1	$2\cos^{-1}((r-h)/r)$
Area lower phase (A_l)	$0.5r^2(\theta_1-\sin\theta_1)$
Area upper phase (A_u)	$0.001134-A_l$
Wall perimeter of lower phase (S_l)	$r\theta_1$
Wall perimeter of upper phase (S_u)	$0.1194-S_l$
Interfacial length (S_i)	$2r \sin(\theta_1/2)$
Curved interface with radius $\frac{1}{2}$ pipe diameter	
X (height that interface touches the pipe wall)	$(2rh+h^2)/2h$
$\theta_1=\theta_2$	$2\cos^{-1}(r-(2r-X))/r$
A_l	$[0.001134-0.5r^2(\theta_1-\sin\theta_1)]- [0.5r^2(\theta_1-\sin\theta_1)]$
A_u	$0.001134-A_l$
S_u	$r\theta_1$
S_l	$0.1194-S_u$
S_i	S_u
Curved interface with radius equal to pipe diameter	
X	$(h^2+4rh)/(2r+2h)$
θ_1	$2\cos^{-1}((r-X)/r)$
θ_2	$2\cos^{-1}((2r-(X-h))/2r)$
A_l	$[0.5r^2(\theta_1-\sin\theta_1)]- [0.5(2r^2)(\theta_2-\sin\theta_2)]$
A_u	$0.001134-A_l$
S_l	$r\theta_2$
S_u	$0.1194-S_l$
S_i	$2r\theta_2$

Table 6.1. Geometric parameters used in the model to account for curved interface.

7. CONCLUSIONS

In this work, liquid-liquid horizontal pipeline flows have been studied in detail and overall, as well as local flow parameters have been measured. New data on pressure gradient and flow pattern boundaries as well as phase distribution, and drop size and concentration distribution are presented. The emphasis was on dual continuous flow, which combines characteristics of both stratified and dispersed flow patterns. Compared to stratified flow and dispersed flows, which lend themselves better to the development of predictive models, dual continuous flow is the least understood and studied.

As part of the project a number of local probes were developed which enabled local flow parameters, such as phase fraction, continuity and drop size, to be measured.

A model was also developed for predicting pressure gradient and hold-up in dual continuous flow. It is based on the two-fluid model where the entrainment of each phase into the other is included. The interface curvature was also considered.

The following summarises the findings of the work.

7.1 Experimental Results

The experiments were performed in an experimental flow facility made as part of this project. The test section was an 8m long stainless steel pipe with an internal diameter of 38mm. The local probe measurements were taken at a distance 7m from the inlet. Flow development experiments showed that this distance was sufficient for the flow pattern to develop. The test fluids used were a kerosene ($\rho = 828\text{kg/m}^3$, $\mu = 6\text{mPa s}$), and tap water. The experimental conditions varied from 0.7 to 3.5m/s and 10 to 90% input oil fraction.

7.1.1 Flow patterns

At low mixture velocities the flow pattern was separated with no interfacial mixing. As the mixture velocity increased to 0.8m/s droplets of each phase started to form in the opposite phase close to the interface for all input oil fractions. This mixing increased with increasing mixture velocity until 2m/s mixture velocity where the dual continuous flow pattern only existed at intermediate input oil fractions. At high input oil fractions the flow pattern was an oil continuous dispersion, while at low input oil fractions the flow pattern was a water continuous dispersion. As the mixture velocity increased further the range of oil fractions where the dual continuous flow existed decreased, until at 3.5m/s the flow pattern changes from a water continuous dispersion to an oil continuous dispersion (phase inversion) without passing through the dual continuous pattern. Results on phase distribution from the impedance probe showed that the interface was generally curved upwards except at low input oil fractions when the interface was curved downwards. The significance of the interfacial curvature became apparent when compared to the pressure gradient and hold-up data.

7.1.2 Pressure gradient

Pressure gradient during two-phase flow was found to be lower than that of the single phase oil in nearly all cases. This suggests the existence of a drag reduction phenomenon, noted also by previous researchers. Using the phase distribution data to help explain the pressure gradient results a clearer understanding can be achieved. It seems that as the amount of dispersed water increases the pressure gradient decreases until a water layer separates and dual continuous flow starts. At this point the initial thin water film would not have a large amount of dispersed oil drops and may exert a lubrication effect. As the size of the water layer increases, and at the same time as the amount of oil dispersed in it increases, drag reduction will also appear in the water continuous layer. Since drag reduction is less strong in water than in oil continuous flows, the relative increase of the water layer compared to the oil layer would result in an overall pressure gradient increase with increasing water fraction. With increasing

water fraction the oil layer is finally reduced to dispersed drops in the water phase. The drag reduction effect is diminishing and pressure gradient slowly increases to the single phase water value.

7.1.3 Velocity Ratio and Phase Distribution

Phase distribution in a pipe cross section helped to explain the trends observed in the velocity ratio data. In general as the mixture velocity increased the velocity ratio became closer to 1. At mixture velocities up to 1.5m/s, S increased with increasing oil fraction. At these mixture velocities flow is dual continuous for the whole range of oil fractions and the interface shape, which in the majority of cases is curved upwards, and the resulting wall contact areas for each phase justify this behaviour.

At intermediate mixture velocities during dispersed flow the dispersed phase was found to travel faster than the continuous phase ($S > 1$ for low oil fractions and water continuous mixtures, and $S < 1$ for high oil fractions and oil continuous mixtures). During dual continuous flow at high velocities S was above 1. As the mixture velocity increased, however, the interface shape changes from curving upwards to curving downwards and S is reduced to below 1.

7.1.4 Drop size distributions

To measure drop size a dual sensor impedance probe was used that gave drop velocity from the cross-correlation of the signal of the two sensors, and chord length from combining the signal of either sensor with the drop velocity. Although common in gas-liquid flows this technique has not been used in liquid-liquid systems before to measure drop size. The results presented here are unique as they show drop size distributions at different vertical locations in a pipe cross section, rather than averages over a whole cross section, of distributions at one particular point. Velocity can only be calculated when there is a sufficiently large number of drops interacting with the sensors for the

cross-correlation to work. It was therefore not possible to get drop velocities in all locations for the whole set of experimental conditions.

The drop velocities were compared with the mixture velocity in fully dispersed flow or with the upper and lower velocities in dual continuous flow. Water drops were found to be faster than the upper layer, or mixture velocity in all cases, while oil drops would be either faster or slower than the lower layer or mixture velocity. This was attributed to the distribution of drops in the opposite phase. Water drops are located usually close to the interface, where velocities are higher, while the oil drops are more uniformly distributed and are present in areas of both high (centre) and low (wall) velocities.

Statistical techniques from the literature were used to transform the measured chord lengths to drop diameter distributions, but the results were not satisfactory. For this reason chord lengths were used in the discussion of the experimental data. Two characteristic chord lengths, the median l_{50} and l_{99} were used to describe the distributions the median represents the average size, while the l_{99} represents the maximum chord length, which should be similar to the maximum drop diameter. It was found that in dual continuous flow, velocity only had a slight effect on l_{50} and l_{99} . This was attributed to the competing phenomena of decreasing drop size with increasing turbulence, and increasing drop entrainment of one phase into the other with increasing velocity. the drop concentration and size also decreased with distance from the interface and at low velocities drops tended to be concentrated around the interface.

From the distributions the Rosin-Rammler and in some cases the Upper Limit Log Normal were found to fit the experimental data satisfactorily. However correlations for maximum drop size underpredicted the sizes found experimentally.

The vertical drop concentration gradient and size distributions were compared to the model by Karabelas (1977). Similarly to the model, the experimental results showed that the dispersed phase concentration is affected by vertical height, but this effect was underpredicted by the model.

7.1.5 Modified two-fluid model

A two-fluid model with entrainment for the prediction of pressure gradient and in-situ hold-up was developed for dual continuous, oil-water horizontal flows. The model required information on the degree of entrainment of one phase into the other, which due to lack of literature information or predictive correlations was found experimentally. Different correlations for the interfacial shear stress term were used, while the experimentally found drag reduction during dispersed flow was accounted for by using modified friction factors in the upper oil continuous and lower water continuous phases. The oil-water interface curvature, experimentally observed in such systems, was also taken into account. The predictions of the various forms of the model tried here showed that the models which included entrainment and drag reduction gave predictions closest to the experimental data both for pressure gradient and velocity ratio. In fact, drag reduction with experimentally derived dispersed phase friction factors had the largest influence on model predictions. The use of entrainment only in the two-fluid model without accounting for drag reduction did not improve the predictions compared to the standard two-fluid model without entrainment. Including the interface curvature did not seem to affect the models' predictions significantly, probably due to the small viscosity difference between the two phases. The literature gave a number of different interfacial shear stress correlations, however when used in the model they gave similar predictions.

The model predictions for the velocity ratio were better, with the trend being predicted, but the values slightly underpredicted. The inclusion of the entrainment failed to significantly improve the model, as did the inclusion of the interfacial curvature. Again the biggest improvement was seen when the experimental wall friction factors were included.

7.2 Future Work

The initial experiments on pressure gradient, hold-up, and phase distribution have provided an important contribution to the limited data available on liquid-liquid horizontal flows. However further work, and improvements to the experimental rig would allow a greater understanding of dual continuous flow, and more consistent results to be possible.

The main improvements to the experimental rig would be a dedicated temperature control system. During this research the temperature was controlled using a constant replenishment of cold tap water, however this fluctuated on a seasonal basis. These slight temperature differences would have had an effect on the fluid properties. Smaller sensor wires for the single and dual impedance probes would possibly have allowed measurement of very small drops which may have been ignored in the current study. While in the majority of cases this has not been a problem (the chord length distributions show frequencies decreasing at low chord lengths) it would allow these drops to be included in these distributions and also phase fraction calculations. Having the computational capacity to take dual impedance probe measurements for very long periods of time (up to 1 min) could potentially negate the problems seen with cross-correlation where there are a few drops present. By measuring for a long period of time, a sufficient number of drops would be detected by the two sensors, and therefore allow the drop velocity to be found.

One characteristic of liquid-liquid flow that has not been fully explained, is drag reduction. An extensive investigation into this phenomenon, that considers pressure gradient, turbulence, and drop size, would be of great significance. The use of hot film anemometry would allow the measurement of the turbulence, while further experiments using the existing dual impedance probe would provide the drop size data.

Experiments using the same experimental rig, but with a different oil would allow direct comparisons to be made, and allow trends to be found for different fluid properties. It

would also be of interest to see how the different models used for this research predict the experimental data.

Another area of research that would allow improvements in the predictive model to be made would be into the onset of entrainment and the dispersed phase concentration. This would not only have implications for the pressure gradient / hold-up model, but also for drop diameter predictions.

As shown in the model results, the wall friction factor for the two phases has a large effect on the ability of the model to predict both the pressure gradient and the velocity ratio. Measuring the wall shear stress with the electrochemical technique would provide some actual experimental data and allow future models to be able to predict this key parameter with greater accuracy.

NOMENCLATURE

Roman symbols

A	cross sectional area	m^2
A_i	diameter bin for PAM2 method	-
B	factor accounting for interfacial waviness, eq. (2.64)	-
B_j	chord bin for PAM2 method	-
C_1	constant in eq. (2.7)	-
C_2	constant in eq. (2.14)	-
C_3	constant in eq. (2.21)	-
C_4	constant in eq. (2.64)	-
C_H	tunable constant, eq. (2.18)	-
C_{ij}	parameter in eq. (2.39)	-
c_i	in-situ droplet concentration, eq. (2.29)	-
(dP/dx)	pressure drop	Pa/m
D	hydraulic diameter	m
d	drop diameter	m
d_{max}	maximum drop diameter	m
d_{min}	minimum drop diameter	m
d_{32}	Sauter drop diameter, eq (2.24)	m
d_{95}	mean drop diameter	m
E_a	adhesion energy between two drops	Joule
e	parameter in eq. (2.53), defined in eq. (2.54)	-
e	pipe roughness	m
F	force holding two drops together	N/m^2
f	friction factor	-
f_{col}	collision frequency, eq. (2.24)	-
f_i	fraction of diameters in diameter bin i	-
G	mass flow rate	kg/s
h	distance between two drops	m
h_o	film thickness between two drops	m

K	Von Karman constant	-
K	coalescence constants, eq. (2.22) and (2.23)	-
K_j	ratio of settling velocity to diffusivity, eq. (2.29)	-
l	length scale	m
N_{We}	Weber number, eq. (2.4)	-
$N_{We\text{ Crit}}$	critical Weber number giving d_{max} , eq. (2.5)	-
N_{Vi}	viscosity number, eq. (2.6)	-
n	constant in eq. (2.64)	-
n	number of samples	-
n	parameter in eq. (2.53), defined in eq. (2.55)	-
n_1	parameter in eq. (2.53), defined in eq. (2.56)	-
n_2	parameter in eq. (2.53), defined in eq. (2.57)	-
P	probability	-
ΔP	pressure gradient	Pa/m
Q	volumetric flowrate	m ³ /s
Q	shape defining term for drops (equals 1 for spheres)	-
R	drop radius	m
R_i	Galerkin weighting residual, eq. (2.48)	-
R_{xy}	cross correlation function	-
R_c	cross-correlation coefficient function	-
Re	Reynolds number	-
r	distance between drop centre and probe tip	m
r	lag time associated with cross correlation	-
S	perimeter	m
S	velocity ratio	-
T	time two drops are held together	s
t	time taken for two drops to coalesce	s
H	velocity ratio	-
U	average velocity	m/s
U^*	fiction velocity	m/s
u'_f	fluctuation turbulent velocity	m/s

V_{cum}	cumulative volume fraction of drops	-
v	velocity in the inertial subrange of turbulence	m/s
v_j	input droplet concentration, eq. (2.29)	-
W	approximate probability of finding chord, eq. (2.37)	-
w	half the diameter band width, eq. (2.41)	-
X	Lockhart Martinelli parameter, eq. (2.51)	-
x	length of drop centre to chord cut	m
y	chord length	m
y_w	distance from the pipe wall	m

Greek symbols

α	shape defining term for drops (equals 1 for spheres)	-
γ	viscosity ratio / proportionality factor	-
δ	parameter in log-normal distribution, eq. (2.27)	-
ϵ_u	oil fraction in upper phase	-
ϵ_l	oil fraction in lower phase	-
ϵ_o	oil fraction	-
ϵ_w	water fraction	-
ϵ	energy dissipation rate per unit mass	m^2/s^3
ϵ_M	mean energy dissipation rate per unit mass	m^2/s^3
ϵ_i	local energy dissipation rate per unit mass	m^2/s^3
Λ	collision efficiency, eq. (2.21)	-
λ	inertial subrange length scale	m
λ_o	Kolmogoroff length scale	m
λ'	viscous dissipation length scale	m
μ	viscosity	Pa s
π	pi	-
ρ	density	kg/m^3
τ	force acting on a drop per unit area	
τ	shear stress	N/m^2

σ	interfacial tension	N/m
φ	function in eq. (2.7)	-
φ	parameter in log-normal distribution, eq. (2.27)	-
ξ	parameter in log-normal distribution, eq. (2.27)	-
ζ	dimensionless diffusivity	-
Φ	Lockhart Martinelli parameter, eq. (2.52)	-
ϕ	dispersed phase concentration	-

Subscripts

c	continuous phase
d	dispersed phase
e	emulsion
i	interfacial
l	lower
o	oil
s	superficial
u	upper
w	water

REFERENCES

Andritsos, P., and Hanratty, T.J., Influence of interfacial waves in stratified gas-liquid flow. *AIChE J.* Vol. 33, pp. 444-454, 1987

Angeli P., Liquid-Liquid dispersed flows in horizontal pipes, *PhD-Thesis, Imperial College London*, 1996

Angeli, P., and Hewitt, G., Pressure gradient in horizontal liquid-liquid flows, *Int. J. Multiphase Flow*, Vol. 24, pp. 1183-1203, 1998

Angeli, P., and Hewitt, G., Drop size distributions in horizontal oil-water dispersed flows. *Chemical Engineering Science* Vol. 55, pp. 3133-3143, 2000a

Angeli, P., and Hewitt, G., Flow structure in horizontal oil-water flow. *Int. J. Multiphase Flow*, Vol. 26, pp. 1117-1140, 2000b

Arirachakaran, S., Oglesby, K.D., Shoulam, O., and Brill, J.P., An investigation of oil water flow phenomena in horizontal pipes, *SPE Proc. Prod. Operation Symp.*, SPE 18836, pp. 155-167, 1989

Baker, A., Nielsen, K., and Gabb, A., Pressure loss, liquid hold-up calculations developed. *Oil & Gas J.*, pp. 55-59, 1988

Bendat, J.S., and Piersol, A.G., Engineering applications of correlation and spectral analysis, 3rd edition. *Wiley-Interscience, New-York*, 2000

Binnie A.M. and Phillips O.M., The mean velocity of slightly buoyant and heavy particles in turbulent flow in a pipe, *J. Fluid. Mech.*, Vol. 4, pp. 87-96, 1958

Brauner N., and Maron D., Two phase liquid-liquid stratified flow. *PhysicoChemical Hydrodynamics* Vol. 11, pp. 487-506, 1989

Brauner N., Two phase liquid-liquid annular flow, *Int. J. Multiphase Flow*, Vol. 17, pp. 59-76, 1991

Brauner N., and Maron D., Pattern transition in 2-phase liquid liquid flow in horizontal tubes, *Int. J. Multiphase Flow*, Vol. 18, pp. 123-140, 1992

Brauner, N., Moalem Maron, D., and Rovinsky, J., A two-fluid model for stratified flows with curved interfaces, *Int. J. Multiphase Flow*, Vol. 24, pp. 975-1004, 1998

Brauner, N., and Ullmann, A., Modelling of phase inversion phenomenon in two-phase pipe flows, *Int. J. Multiphase Flow*, Vol. 28, pp. 117-1204, 2002

Brinkman H.C., The Viscosity of Concentrated Solutions and suspensions, *J. Chem. Physics*, Vol. 20, pp. 571, 1952

Brown, NP., Shook, CA., Peters, J., and Eyre, D., A probe for point velocities in slurries, *Canadian J. of Chem. Eng.*, Vol. 61, pp. 597-602, 1983

Cartellier, A., and Achard, JL., Local phase detection probes in fluid/fluid two-phase flows, *Rev. Sci. Instruments.*, Vol. 62, pp. 279-303, 1991

Chan, IH., Sishla, C., and Knowlton, TM., The effect of pressure on bubble parameters in gas-fluidised beds, *Powder Tech.*, Vol. 53, pp. 217-235, 1987

Charles, ME., Govier, GW., and Hodgson, GW., The horizontal pipeline flow of equal density oil-water mixture, *Can. J. Chem. Eng.*, Vol. 39, pp.27-36, 1961

Charles, ME., and Lilleleht, LU., Correlation of pressure gradients for the stratified laminar-turbulent pipeline flow of two immiscible liquids, *Can. J. Chem. Eng.*, Vol. 44, pp. 47-49, 1966

Charles, ME., and Redberger, PJ., The reduction of pressure gradients in oil pipelines by the addition of water: numerical analysis of stratified flow, *Chem. Eng.*, Vol. 40, pp. 70-75, 1962

Cheremisinoff, NP., and Davies, EJ., Stratified turbulent-turbulent gas-liquid flow, *AIChE J.*, Vol. 25 pp. 48-56, 1979

Cheremisinoff, NP., and Cheremisinoff, PN., Flow measurement for engineers and scientists, *New York : M. Dekker* , c1988

Clarke, NN., and Turton, R., Chord length distributions related to bubble size distributions in multiphase flows, *Int. J. Multiphase Flow*, Vol. 14, pp. 413-424, 1988

Clay P.H., The mechanism of emulsion formation in turbulent flow, *Proceedings, Akademie van Wetenschappen, Amsterdam*, Vol. 43, pp. 852-965, 1940

Collins, SB., and Knudsen, JG., Drop size distribution produced by turbulent pipe flow of immiscible liquids, *AIChE J.*, Vol. 6, pp. 1072-1080, 1970

Colaloglou, CA., and Tavlarides, LL., Description of interactions processes in agitated liquid-liquid dispersions, *Chem. Eng. Sci.*, Vol. 32, pp. 1289-1297, 1977

Cox, AL., A study of horizontal and downhill two-phase oil-water flow, *M.S. Thesis. The University of Texas*, 1985

Dukler, AE., Wicks, M., and Cleveland, RG., Pressure drop and hold-up in two-phase flow, *AIChE J.*, Vol. 10, pp. 35-51, 1964

Efthimiadu, I., and Moore, IPT., Phase inversion of liquid-liquid dispersions produced between parallel shearing plates, *Chem. Eng. Sci.*, Vol. 49, pp. 1439-1449, 1994

El-Hamouz, AM. and Stewart, AC., On-line drop size distribution measurements of oil-water dispersions using a Par tec M300 laser backscatter instrument, *Proceedings of. SPE annual technical conf. and exhibition*, SPE 36672, pp. 785-796, 1996

Godfrey, J.C. and Grilc, V., Drop size and drop size distributions for liquid-liquid dispersions in agitated tanks of square cross-section, *Proc. 2nd European Conference on Mixing, BHRA Fluid Engineering, Cranfield, C1*, pp. 1-20, 1977.

Guzhov, AI., Grishan, AL., Medredev, VF., and Medredeva, OP., Emulsion formation during the flow of two immiscible liquids in a pipe, *Neft Khoz*, Vol. 8, pp. 58-61, 1973 (in Russian)

Guzhov, AI., and Medvedev, OP., Pressure losses in flow of two mutually immiscible liquids, *Int. Chem. Eng.*, Vol. 11, pp. 104-106, 1971

Hall, ARW., Multiphase flow of oil, water and gas in horizontal pipes. *Ph.D. Thesis*, Imperial College, University of London, UK, 1992

Hashiba, N., and Kojima, E., Simultaneous measurement of two-dimensional velocity and direction of liquid flow by cross-correlation method, *J. of Chem. Eng. of Japan*, Vol. 29, pp. 577-581, 1996

Hashiba, N., and Kojima, E., Measurement of liquid circulation in concentric airlift reactors by cross-correlation, *J. of Chem. Eng. of Japan*, Vol. 30, pp. 23-29, 1997

Hanzevack, EL., and Demetriou, GD., Effect of velocity and pipeline configuration on dispersion in turbulent hydrocarbon-water flow using laser image processing, *Int. J. Multiphase Flow*, Vol. 15, pp. 985-996, 1989

Hinze, JO., Fundamentals of the hydrodynamic mechanism of splitting in dispersion processes, *AIChE J.*, Vol. 1, pp. 289-295, 1955

Howarth, WJ., Coalescence of drops in turbulent flow field, *Chem. Eng. Sci.* Vol. 19, pp. 33-38, 1964

Hughmark, GA., Drop breakup in turbulent pipe flow, *AIChE J.*, Vol. 17, pp. 1000, 1971

Hutchinson, P., Hewitt, GF., and Dukler, AE., Deposition of liquid or solid dispersions flow turbulent gas streams: a stochastic model, *Chem. Eng. Sci.*, Vol. 26, pp. 419-439, 1971

Jayawardena, SS., Alkaya, B., Redus, CL., and Brill, JP., A new model for dispersed multi-layer oil-water flow, *Proceedings of BHR 2000 Multiphase Technology, Banff, Canada*, pp.77-89, 2000

Karabelas, AJ., Vertical distribution of dilute suspensions in turbulent pipe flow, *AIChE J.*, Vol. 23, pp. 426-434, 1977

Karabelas, AJ., Droplet size spectra generated in turbulent pipe flow of dilute liquid-liquid dispersions, *AIChE J.*, Vol. 24, pp. 170-180, 1978

Kenning, VM., and Crowe, CT., On the effect of particles on carrier phase turbulence in gas-particle flows, *Int. J. Multiphase Flow*, Vol. 23, pp. 403-408, 1997

Khor S., Mendes-Tatsis MA., and Hewitt GF., One-dimensional modelling of phase holdups in three-phase stratified flow, *Int. J. Multiphase Flow*, Vol. 23, pp. 885-897, 1997

Kolmogorov, AN., On the breaking of drops in turbulent pipe flow of dilute liquid-liquid dispersions, *AIChE J.*, Vol. 24, pp. 170-180, 1949

Kobori, T., and Terada, M., Application of the needle type void meter to blow down test. *Proc. Second CSNI Specialists meeting on Transient Two-Phase Flow. Paris*, pp. 699-714, 1978

Kubie, J., and Gardner, GC., Drop sizes and drop dispersion in straight horizontal tubes and helical coils, *Chem. Eng. Sci.*, Vol. 32, pp. 195-202, 1977

Kurban, APA., Stratified liquid-liquid flow. *Ph.D Thesis. Imperial College, University of London, UK*, 1997

Laflin, GC., and Oglesby, KD., An experimental study on the effects of flow rate, water fraction and gas-liquid ratio on air-oil-water flow in horizontal pipes, *B.S. Thesis. The University of Tulsa*, 1976

Langston, PA., Burbidge, AS., Jones., TF., and Simmons, MJH., Particle and droplet size analysis from chord measurements using Bayes' theorem, *Powder Tech.*, Vol. 116, pp. 33-42, 2001

Lang, P., and Auracher, H., Heat transfer to nonmiscible liquid-liquid mixture flowing in a vertical tube, *Exp. Thermal Fluid Sci.*, Vol. 12, pp. 364-372, 1996

Lee, SLP., Soria, A., and de Lasa, HI., Evolution of bubble length distributions in three-phase fluidised beds, *AIChE J.*, Vol. 36, pp. 1763-1767, 1990

Luhning, RW., and Sawistowski, H., Phase inversion in stirred liquid-liquid systems, *Proc. Int. Solvent Extr. Conf., The Hague, Society of Chemical Industry, London*, pp. 873-887, 1971

Liu, W., Clarke, NN., and Karamavruc, AI., General method for the transformation of chord length data to a local bubble size distribution, *AIChE J.*, Vol. 42, pp. 2713-2720, 1996

Liu, W., Clarke, NN., and Karamavruc, AI., Relationship between bubble size distributions and chord length distributions in heterogeneously mixed bubbling systems, *Chem. Eng. Sci.*, Vol. 6, pp. 1267-1276, 1998

Malinowsky, MS., An experimental study oil water and air-water flowing mixtures in horizontal pipes, *MS Thesis, The University of Tulsa*, 1975

McClarey, MJ., and Mansoori, GA., Factors affecting the phase inversion of dispersed immiscible liquid-liquid mixtures, *AIChE Symposium Series*, Vol. 4, pp.134-139, 1978

Nädler, M., and Mewes, D., Flow induced emulsification in the flow of two immiscible liquids in horizontal pipes, *Int. J. Multiphase Flow.*, Vol. 23, pp. 55-68, 1997

Neogi, S., Lee, A., and Jepson, WP., A model for multiphase (gas-water-oil) stratified flow in horizontal pipes, *Soc. of Petroleum Engineers Asia Pacific Oil & Gas Conf., Melbourne, 7-10 Nov, SPE 28799, 1994*

Nigmatulin, RI., Nigmatulin, BI., Khodzhaev, YD. and Kroshilin, VE., Entrainment and deposition rates in a dispersed-film flow, *Int. J. Multiphase Flow*, Vol. 22, pp. 19-30, 1996

Ng, TS., Lawrence, CJ., and Hewitt, GF., Two-phase stratified flow in and inclined circular pipe, *Proceedings of the 4th Int. Conf. On Multiphase Flow. New Orleans, USA, 2001*

Ng, TS., *Ph.D Thesis. Imperial College, University of London, 2002*

Oglesby, KD., An experimental study on the effects of oil viscosity, mixture velocity, and water fractions on horizontal oil-water flow, *MS Thesis, The University of Tulsa, 1979*

Pacek, AW., Man, CC. and Nienow, AW., On the Sauter mean diameter and size distributions in turbulent liquid-liquid dispersions in a stirred vessel, *Chem. Eng. Sci.*, Vol. 53, pp. 2005-2011, 1998

Pal, R., Bhattacharya, SN., and Rhodes, E., Flow behaviours of oil-in-water emulsions, *Canadian J. Chem. Eng.*, Vol. 64, pp. 3-10, 1986

Pal, R. and Rhodes, E., Viscosity/Concentration Relationships for Emulsions, *Journal of Rheology*, Vol. 33, pp. 1021-1045, 1989

Pal, R., Pipeline flow of unstable and surfactant-stabilized emulsions, *AIChE J.*, Vol. 39, pp. 1754-1764, 1993

Perry, R.H., and Green, D., *Perry's chemical engineering handbook 6th edition, McGraw Hill, New York, 1985*

- Roberts, I., Modelling and experimental studies of transient stratified multiphase flows, *Ph.D. Thesis, Imperial College, University of London, UK*, 1996
- Roscoe, R., The viscosity of suspensions of rigid spheres, *British J. of Applied Physics*, Vol. 3, pp. 267-269, 1952
- Rozentsvaig, AK., Turbulent pipe flow of concentrated emulsions with a nonequilibrium disperse phase, *Inzhenerno-Fizicheskii Zhurnal*, Vol. 42, pp. 336-372, 1982
- Russell, TWF., and Charles, ME., The effect of the less viscous liquid in the laminar flow of two immiscible liquids, *Canadian J. Chem. Eng.*, Vol. 37, pp. 18-34, 1959
- Russell, TWF., Hodgson, GW., and Govier, GW., Horizontal pipeline flow of mixtures of oil and water, *Can. J. Chem. Eng.*, 1959
- Scott, GM., A study of two-phase liquid-liquid flow at variable inclinations. *M.Sc. Thesis. The University of Texas*, 1985
- Selker, AH., and Sleicher, CA. Jr., Factors affecting which phase will disperse when immiscible liquids are stirred together, *Can. J. Chem. Eng.*, Vol. 43, pp. 298-301, 1965
- Sevik, M., and Park, SH., The splitting of drops and bubbles by turbulent fluid flow, *J. Fluid Eng., Transactions of the ASME*, March, pp. 54-59, 1973
- Sharp, BB. and O'Neill, IC., Lateral diffusion of large particles in turbulent pipe flow, *J. Fluid Mech.*, Vol. 45, pp. 575-584, 1971
- Shinnar R., On the behaviour of liquid dispersions in mixing vessels, *J. Fluid Mechanics*, Vol. 10, pp. 259-275 1961

Simmons, MJH., Langston, PA., and Burbidge, AS., Particle and droplet size analysis from chord distributions, *Powder Tech.*, Vol. 102, pp. 75-83, 1999

Simmons, MJH., Zaidi, SH., and Azzopardi, BJ., Comparison of laser-base drop size measurement techniques and their application to dispersed liquid-liquid pipe flow, *Opt. Eng.*, Vol. 32, pp. 505-509, 2000

Sleicher, CA. Jr., Maximum stable drop size in turbulent flow, *AIChE J.*, Vol. 8, pp. 471-477, 1962

Soleimani, A., Lawrence, CJ., and Hewitt, GF., Effect of mixers on flow pattern and pressure drop on horizontal oil-water pipe flow, *Int. Symp. on Liquid-Liquid Two Phase Flow and Transportation Phenomena, Turkey*, 1997

Soleimani, A., Phase Distribution and Associated Phenomena in Oil-Water Flows in Horizontal Tubes, *PhD Thesis, Imperial College London, UK*, 1999

Sprow F.B., Distribution of drop sizes produced in turbulent liquid-liquid dispersions, *Chem. Eng. Sci.*, Vol. 22, pp. 435-442, 1967

Stapleberg, HH, and Mewes, D., The pressure loss and slug frequency of liquid-liquid-gas slug flow in horizontal pipes, *Int. J. Multiphase Flow*, Vol. 20, pp. 285-303, 1994

Su, HT., and Hanzevack, EL., A model of drop size distribution and maximum drop size in two phase liquid-liquid flow, *AIChE Annual Meeting Washington DC*, 1998

Taitel Y., Barnea D., and Brill JP., Stratified three-phase flow in pipes, *Int. J. Multiphase Flow*, Vol. 21, pp. 53-60, 1995

Taitel Y., and Dukler AE., A model for predicting flow regime transitions in horizontal and near horizontal gas-liquid flow, *AIChE*. Vol. 22, pp. 47-55, 1976

Tayebi, D., Lunde, K., Nuland, S., and Fuchs, P., Droplet transport in oil-gas flow, *7th International Conference Multiphase 95, BHR Group Conference Series*, 1995

Tennekes H., and Lumley JL., A first course in turbulence, *The MIT Press, Cambridge, Mass.*, 1972

Teysseidou, A., Tapucu, A., and Lortie, M., Impedance probe to measure local void fraction profiles, *Rev. Sci. Instruments*, Vol. 59, pp. 631-638, 1988

Theissing, P., A generally valid method for calculating frictional pressure drop in multiphase flow, *Chem. Ing. Technik*, Vol. 59, pp. 344-345, 1980 (in German)

Thomas RM., Bubble coalescence in turbulent flows, *Int. J. Multiphase Flow*, Vol. 7, pp. 709-717, 1981

Trallero, JL., Oil water flow patterns in horizontal pipes, *PhD Thesis, the University of Tulsa*, 1995

Treybal, RE., Liquid Extraction, *1st Edition, McGraw Hill, New York*, 1951

Tsouris, C. and Tavlarides, LL., Breakage and coalescence models for drops in turbulent dispersions, *AIChE J.*, Vol. 40, pp. 395-406, 1994

Valentas KJ., Bilous O., and Amundson NR., Breakage and coalescence in dispersed phase systems, *Ind. Eng. Chem. Fundamentals*, Vol. 5, pp. 533-542, 1966

Valle, A., and Kvandal, HK., Pressure drop and dispersion characteristics of separated oil-water flows, *Int. Symp. on Two Phase Flow Modelling and Experimentation, Rome*, 1995

Valle, A., and Utvik, OH., Pressure drop, flow pattern and slip for two phase crude oil-water flow: Experiments and model predictions, *Int. Symp. on Liquid-Liquid two Phase flow and Transportation Phenomena, Turkey*, 1997

Valle, A., Multiphase pipeline flows in hydrocarbon recovery, *Multiphase Sci & Tech.*, Vol. 10, pp.1-139, 1998

Van de Welle, R., Void fraction, bubble velocity and bubble size in two-phase flow, *Int. J. Multiphase Flow*, Vol. 11, pp. 317-345, 1985

Vedapuri, D., Bessette, D., and Jepson, WP., A segregated flow model to predict water layer thickness in oil-water flows in horizontal and slightly inclined pipelines, *Proceedings of the 8th International Conference on Multiphase Flow. June 18-20, Cannes France, 1997*

Ward JP., and Knudsen, JG., Turbulent flow of unstable liquid-liquid dispersions: drop sizes and velocity distributions, *AIChE J.*, Vol. 13, pp. 356-365, 1967

Weimer, A., Application of a gamma radiation density gauge for determining hydrodynamic properties of fluidized beds, *Powder Tech.*, Vol. 44, pp. 179-194. 1985

Zhou, G. and Kresta, SM., Correlation of mean drop size and minimum drop size with the turbulence energy dissipation and the flow in an agitated tank, *Chem. Eng. Sci.*, Vol. 53, pp. 2063-2079, 1998

APPENDIX A1

Fortran 90 code for processing data from high frequency impedance probe and outputting in-situ oil concentration.

```
PROGRAM IMPREAD_CONTINUOUS
Character:: filestart1*1,filestart2*2,fileend*4, filename*6
integer:: nvals=0,j,i,k
integer::status, oilvalue, watervalue, alloil, allwater,
filenumber
real::value, mysum=0, oilpercent
real, dimension (120000)::mycount

Print*, 'Enter count for 100% oil'
read*, oilvalue
Print*, 'Enter count for 100% water'
read*, watervalue
Print*, 'Enter number of files to be read'
read*, filenumber
Print*, 'Enter number of samples in each file'
read*, samplenumber

open (unit=2, file='output.txt', status='replace')

do j=1,filenumber
open (unit=3, file='bin.txt', status='replace')
write(3,99) j
99 format (I2)
close(3)

open (unit=3, file='bin.txt', status='old')
if (j<=9) then
read(3,*) filestart1
else
read(3,*) filestart2
endif
close (3)

fileend='.csv'

if (j<=9) then
filename=filestart1//fileend
else
filename=filestart2//fileend
```

```

endif

print*, filename
  OPEN (UNIT=1, FILE=filename, STATUS='old')
  rewind (1)
  nvals=0
  readloop: DO k=1,samplenumbr
    read(1,*) time, count, probe1
    if (status/=0)exit
    mycount(nvals+1)=count
    nvals=nvals+1
  end do readloop

  mysum=0
  sumloop: do i=1,nvals
    mysum=mycount(i)+mysum
  end do sumloop

  allwater=nvals*watervalue
  alloil=nvals*oilvalue
  oilpercent=((mysum-allwater)/(alloil-allwater))*100
  write(2,*) filename, oilpercent

close (1)

end do
close (2)

END PROGRAM IMPREAD_CONTINUOUS

```

APPENDIX A2

Fortran 90 code for performing the cross-correlation on the two data sets from the dual impedance probe.

```
PROGRAM XCORR
Character::filestart1*1,filestart2*2,fileend*4,
fileendxcorr*9, fileread*6, filewrite*11
integer:: nvals,i, j,k
integer, parameter::max=120000
integer::status, oilvalue, count1, count2, r, m, sum,
multiply, answer, filenumber, samplenumbr
real::value,mysum=0, oilpercent
real, dimension (max)::mycount1
real, dimension (max)::mycount2

real, dimension (max)::timing

print*, 'Continuous cross-correlation'
Print*, 'Enter count for 100% oil'
read*, oilvalue
Print*, 'Enter value for m'
read*, m
Print*, 'Results biased (1) or unbiased(2)'
read*, bias
Print*, 'Enter number of files to be read'
read*, filenumber
Print*, 'Enter number of samples in each file'
read*, samplenumbr

do j=1,filenumber
  open (unit=3, file='bin.txt', status='replace')
  write(3,77) j
  77 format (I2)
  close(3)

  open (unit=3, file='bin.txt', status='old')
  if (j<=9) then
  read(3,*) filestart1
  else
  read(3,*) filestart2
  endif
  close (3)

  fileend='.csv'
  fileendxcorr='xcorr.csv'
```

```

    if (j<=9) then
    fileread=filestart1//fileend
    filewrite=filestart1//fileendxcorr
    else
    fileread=filestart2//fileend
    filewrite=filestart2//fileendxcorr
    endif

    print*, fileread, filewrite
    OPEN (UNIT=1, FILE=fileread, STATUS='old')
    open (unit=2, file=filewrite)
    rewind (1)

openif: IF(status==0)then
nvals=0
readloop: DO k=1,samplenumbr
        read(1,*,IOSTAT=status) time, count1, count2
        if (status/=0)exit

        mycount1(nvals+1)=count1
        mycount2(nvals+1)=count2
        nvals=nvals+1

        end do readloop

else openif
        write (*,1040) status
1040 format ('Error opening file: IOSTAT=',I6)
end if openif

DO r=0,m !do from r=0 to m
        sum=0

        DO i=1,nvals-r
                multiply=mycount1(i)*mycount2(i+r) !multiply each of
the values
                sum=sum+multiply !sum all the multiply values for one
r value
        end do

        if (bias==1) then
        answer=sum/nvals
        else if (bias==2)then

```

```
        answer=sum/(nvals-r)
        end if

        write (2,99) r, answer
        99 format (I6 ',' I6)

    end do

    CLOSE (1)
    close (2)

end do

END PROGRAM XCORR
```

APPENDIX A3

Fortran 90 code for the transformation of raw data from the first probe of the dual impedance probe into a square wave form. The code can easily be changed to perform the transformation on the second probe.

```
Program SQUAREWAVE
Integer:: oilvalue, watervalue, t_hold, ival=0, nval=0,
amax, amin, &
& oildrop, waterdrop, kval=0, jval=0
Character::filestart1*1, filestart2*2, fileend*4,
filename*6, filesquare*10, fileoil*11,&
&filewater*13, squarefile*12, oilfile*13, waterfile*15
Real::time, timestep
!Integer, parameter:: max
Real, dimension (120000)::mycount1
Real, dimension (120000)::timing
Real, dimension (120000)::sqwave
real, dimension (120000)::oilbub
real, dimension (120000)::waterbub

fileend='.csv'
filesquare='square.csv'
fileoil='oildrop.csv'
filewater='waterdrop.csv'

Print*, 'Is the filename greater than 9? 1:yes, 0:no'
Read*, filelength

If (filelength==0) then
  Print*, 'Enter filename'
  Read*, filestart1
  filename=filestart1//fileend
  squarefile=filestart1//filesquare
  waterfile=filestart1//filewater
  oilfile=filestart1//fileoil
else
  Print*, 'Enter filename'
  Read*, filestart2
  filename=filestart2//fileend
  squarefile=filestart2//filesquare
  waterfile=filestart2//filewater
  oilfile=filestart2//fileoil
end if
```

```

Print*, 'Enter value for 100% oil'
Read*, oilvalue
Print*, 'Enter value for 100% water'
Read*, watervalue
Print*, 'Enter threshold value'
Read*, t_hold

print*,filename, squarefile, waterfile, oilfile

Open (Unit=1, FILE=filename, STATUS='OLD', ACTION='READ')
Open (Unit=2, File=squarefile, status='replace')
Open (Unit=3, File=waterfile, status='replace')
open (unit=4, File=oilfile, status='replace')

openif: IF(status==0)then
Do j=1,120000
    read(1,*,IOSTAT=status) time, count1, count2

    if (count1>90) then
        count1=oilvalue
    end if

    timing(nvals+1)=time
    mycount1(nvals+1)=count1

    nvals=nvals+1

end do

else openif
    write (*,1040) status
1040 format ('Error opening file: IOSTAT=',I6)
end if openif

timestep=timing(2)-timing(1)
write(*, 99)timestep
99 format ('the time steps are', F10.5,'microseconds')

amax=oilvalue; amin=watervalue
Do i=1,nvals-1

    if (mycount1(i+1)>mycount1(i)) then
        amax=mycount1(i+1)

```

```

else if (mycount1(i+1)<mycount1(i)) then
    amin=mycount1(i+1)
endif

if (mycount1(i+1)>(amin+t_hold)) then
    D=oilvalue
    write(2,*)oilvalue
else if (mycount1(i+1)<(amax-t_hold)) then
    D=watervalue
    write(2,*)watervalue
else
    D=D
    write(2,*)D
endif

sqwave(ivals+1)=D
ivals=(ivals+1)

end do

oildrop=0
waterdrop=0

do i=2, ivals

    if (sqwave(i)==oilvalue .and. sqwave(i-1)==watervalue)
then
        oildrop=oildrop+1
        write(3,66)waterdrop
        66 format (I6)
        waterdrop=0
    else if (sqwave(i)==watervalue .and.
sqwave(i-1)==oilvalue) then
        waterdrop=waterdrop+1
        write(4,77)oildrop
        77 format(I6)
        oildrop=0
    else if (sqwave(i)==sqwave(i-1) .and.
sqwave(i)==oilvalue) then
        oildrop=oildrop+1
    else if (sqwave(i)==sqwave(i-1) .and.
sqwave(i)==watervalue) then
        waterdrop=waterdrop+1
    end if
end if

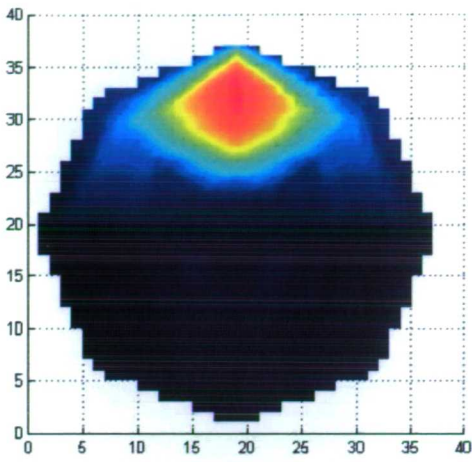
end do

```

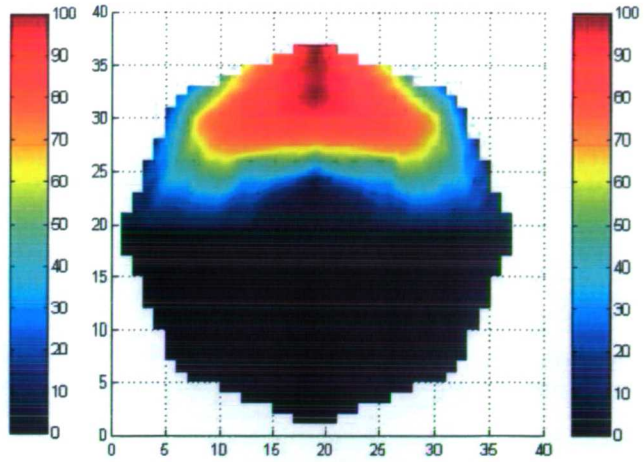
```
close (1)
close (2)
close (3)

end program SQUAREWAVE
```

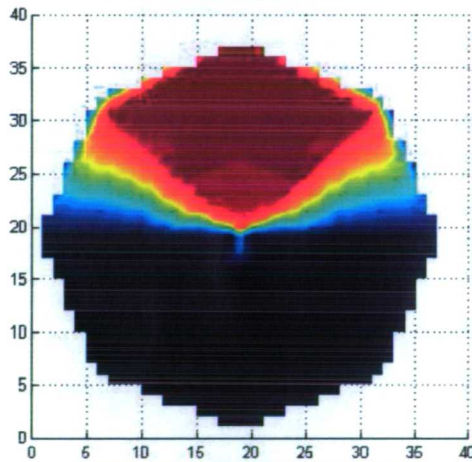
APPENDIX A4



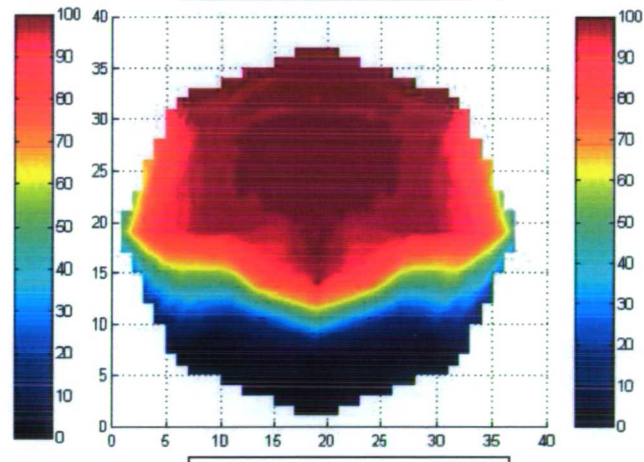
0.8m/s 10% input oil



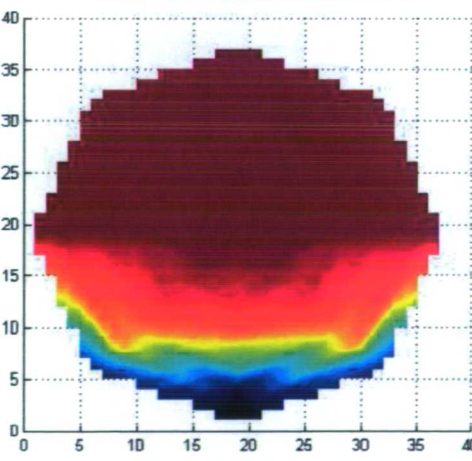
0.8m/s 20% input oil



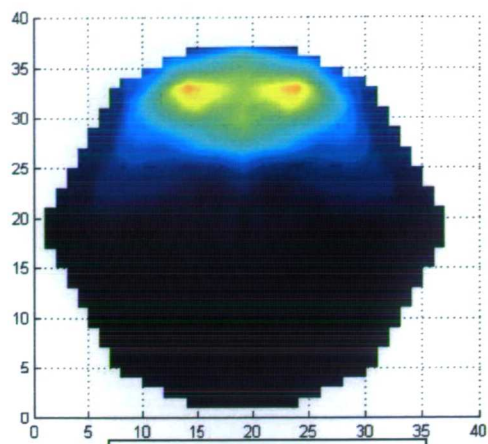
0.8m/s 50% input oil



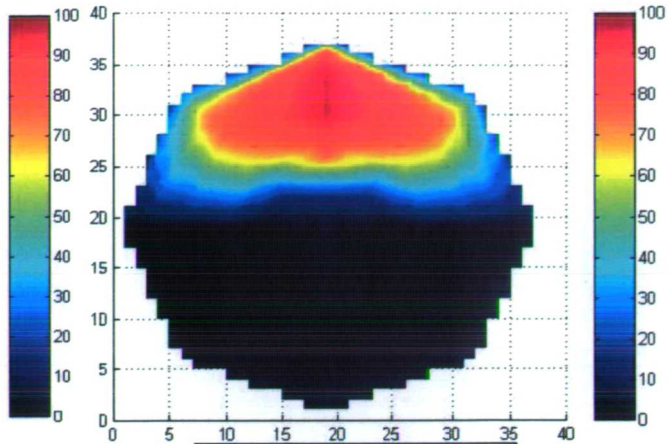
0.8m/s 80% input oil



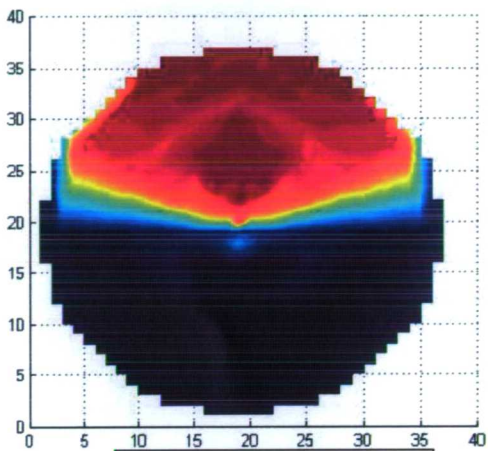
0.8m/s 90% input oil



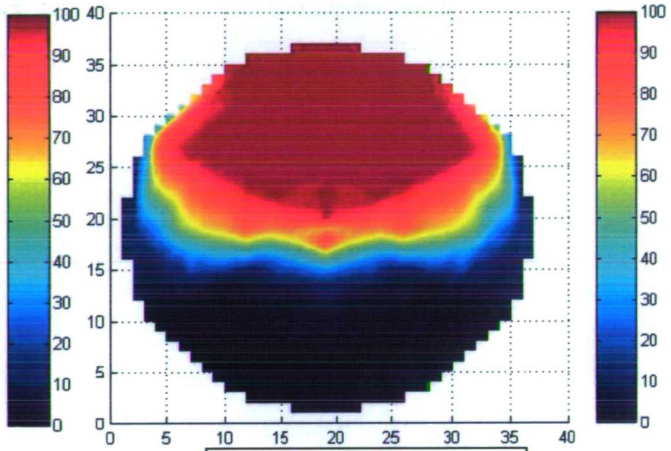
1m/s 10% input oil



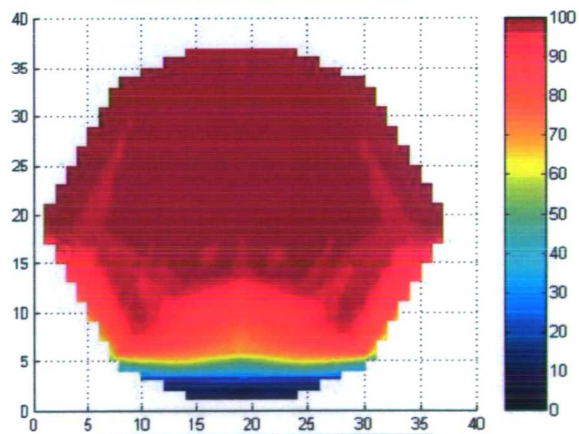
1m/s 30% input oil



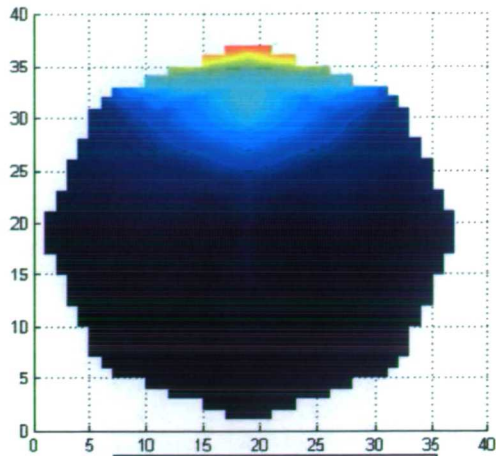
1m/s 60% input oil



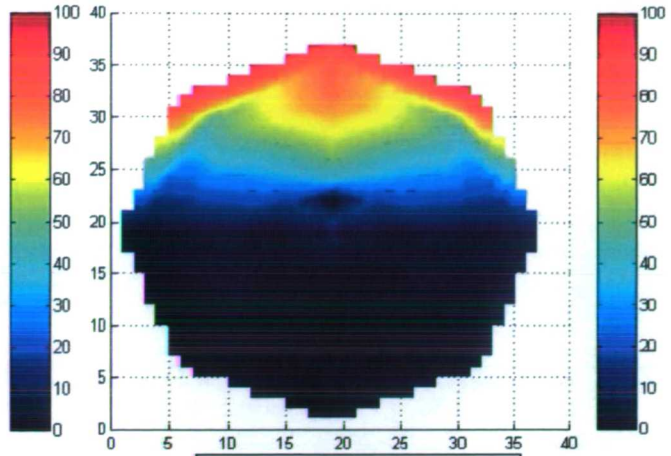
1m/s 68% input oil



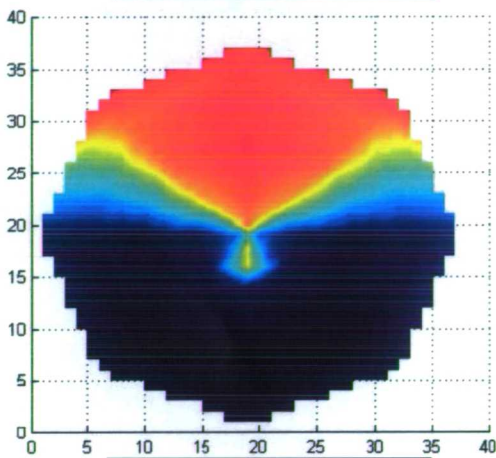
1m/s 90% input oil



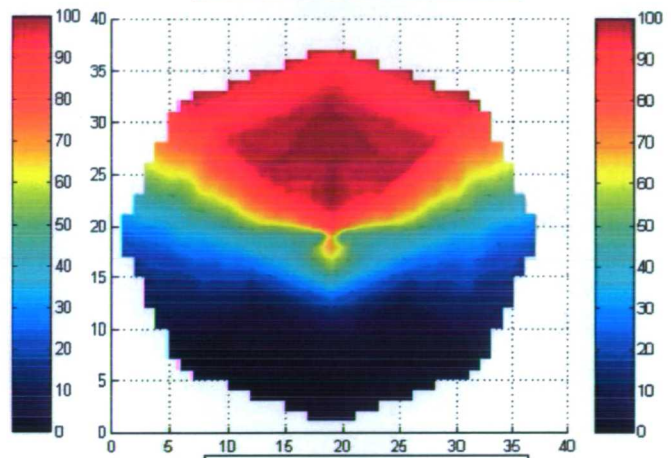
1.5m/s 10% input oil



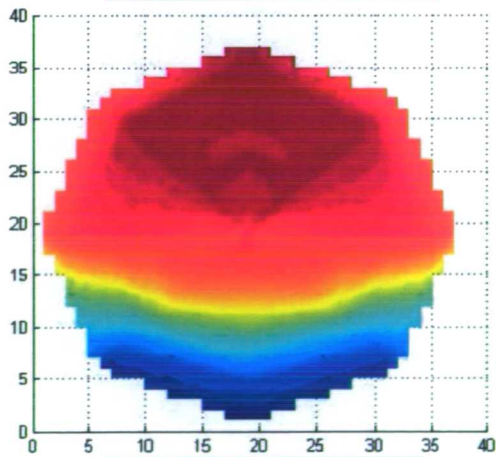
1.5m/s 20% input oil



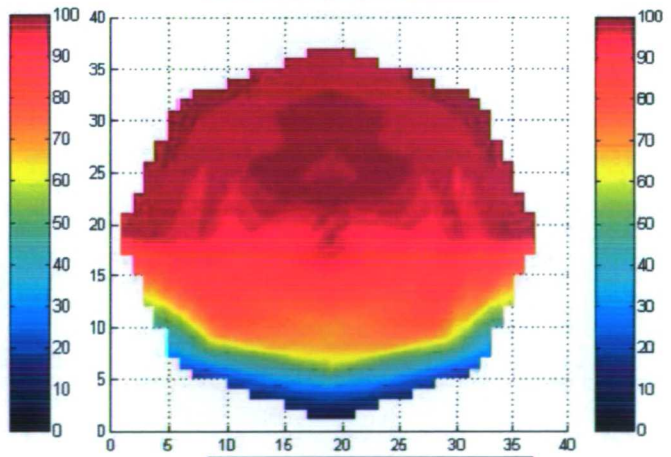
1.5m/s 30% input oil



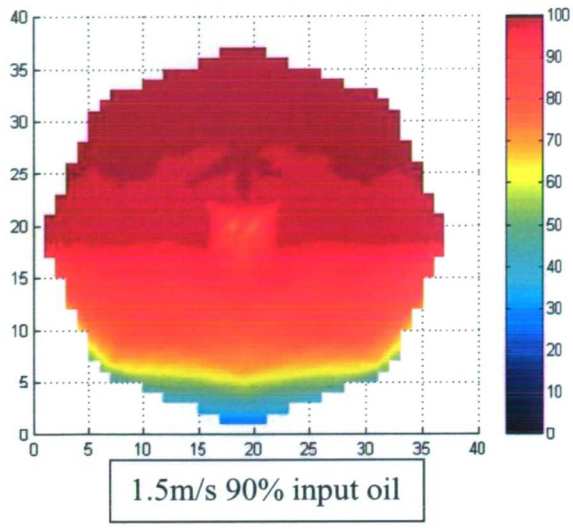
1.5m/s 50% input oil

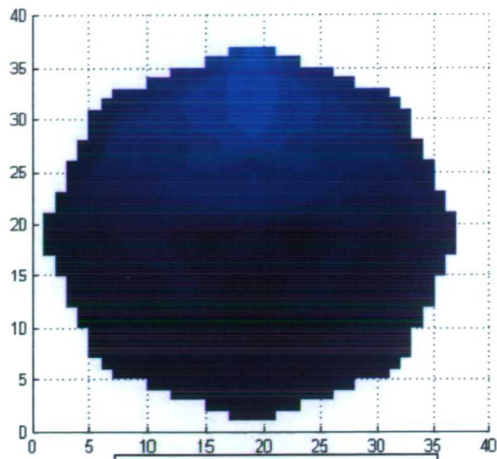


1.5m/s 680% input

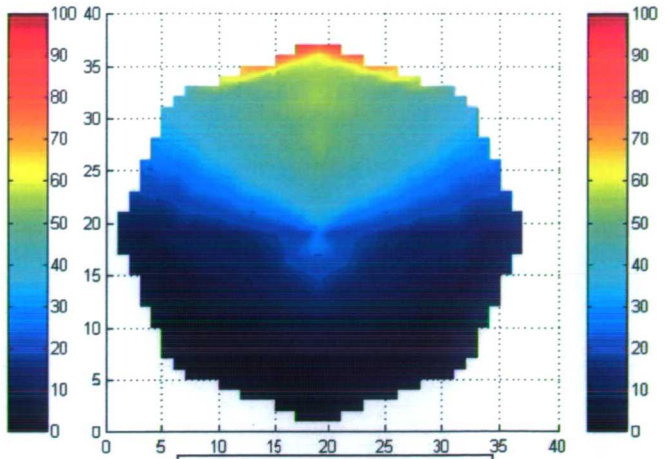


1.5m/s 80% input oil

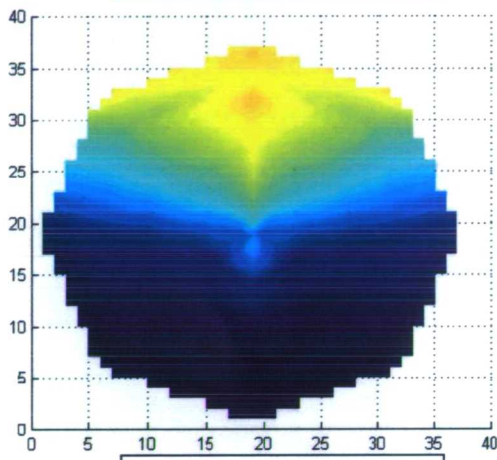




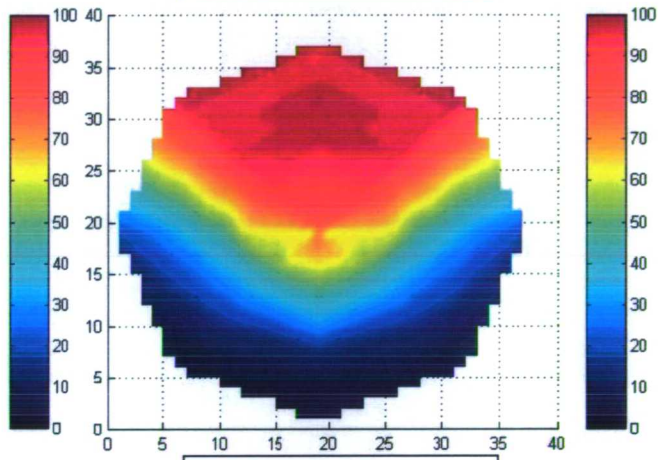
2m/s 10% input oil



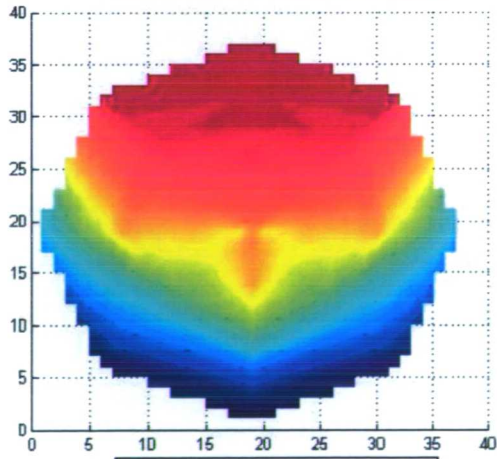
2m/s 20% input oil



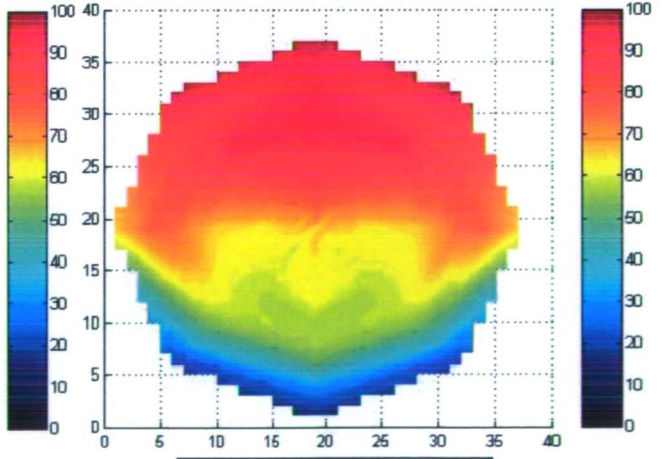
2m/s 30% input oil



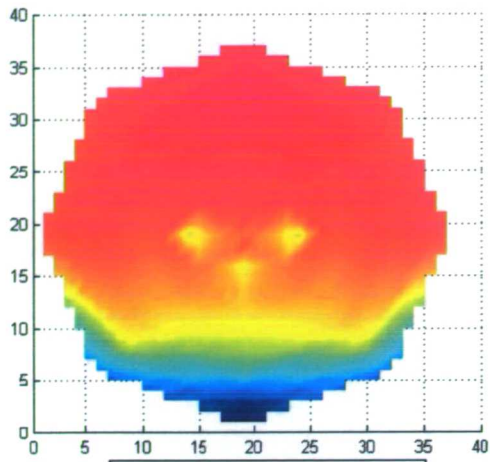
2m/s 50% input oil



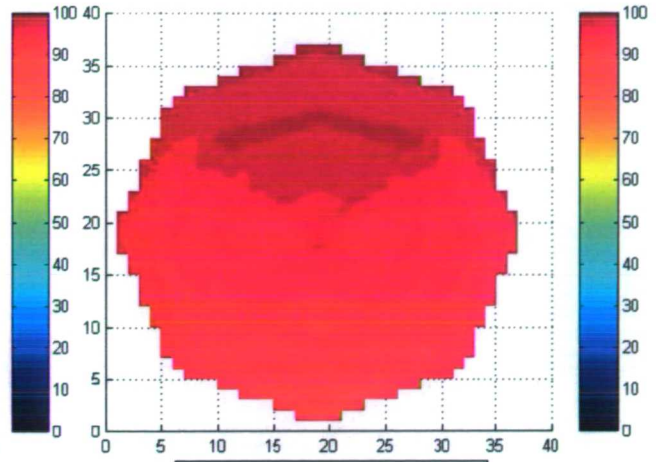
2m/s 68% input oil



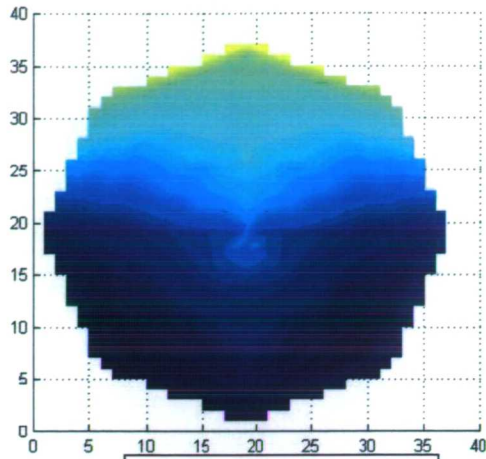
2m/s 72% input oil



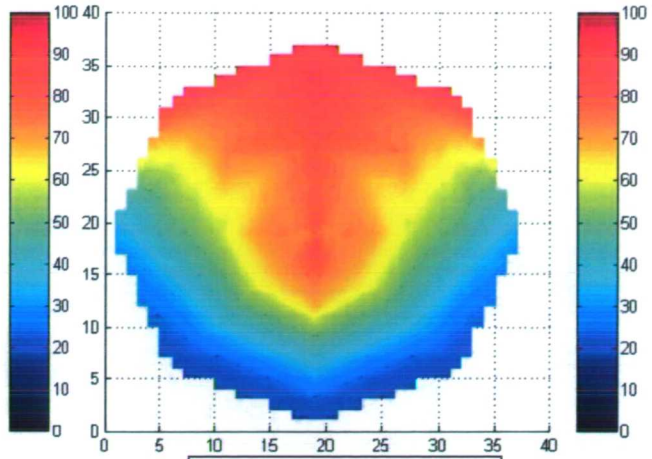
2m/s 80% input oil



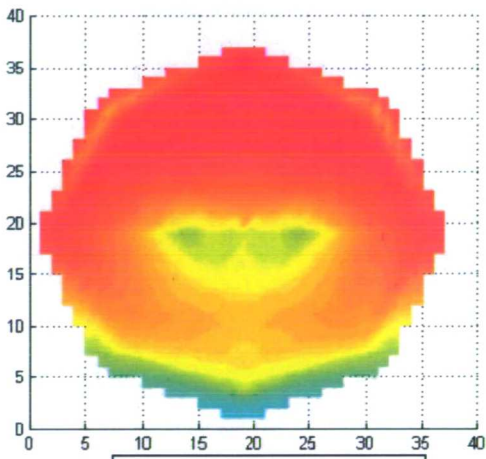
2m/s 90% input oil



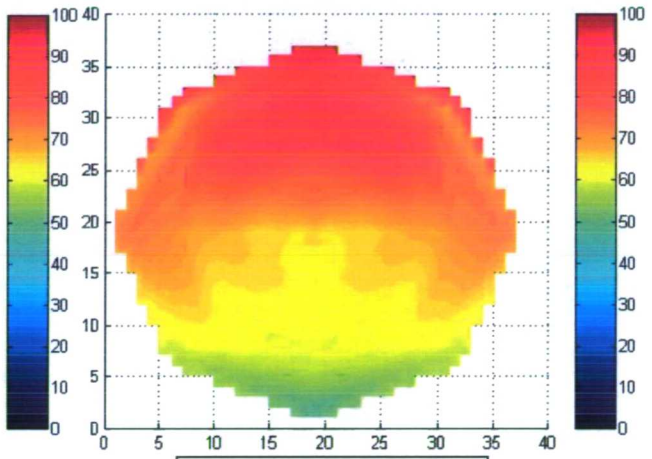
2.5m/s 20% input oil



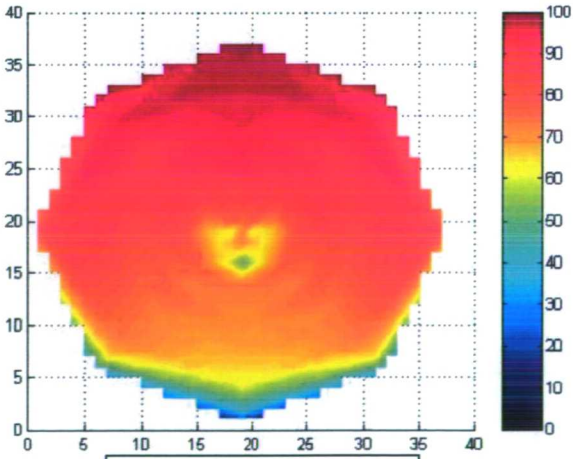
2.5m/s 50% input oil



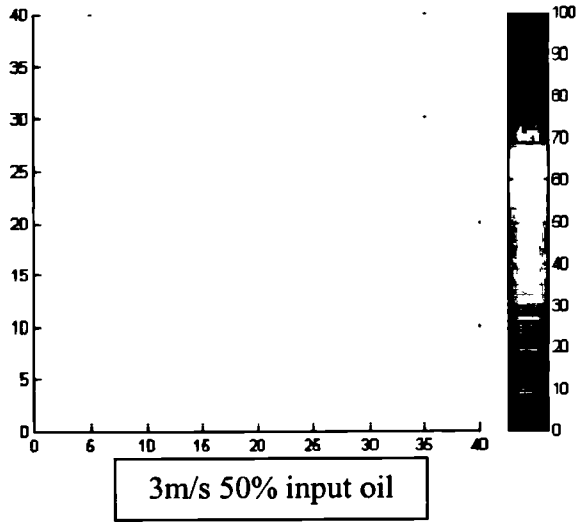
2.5m/s 68% input oil



2.5m/s 72% input oil

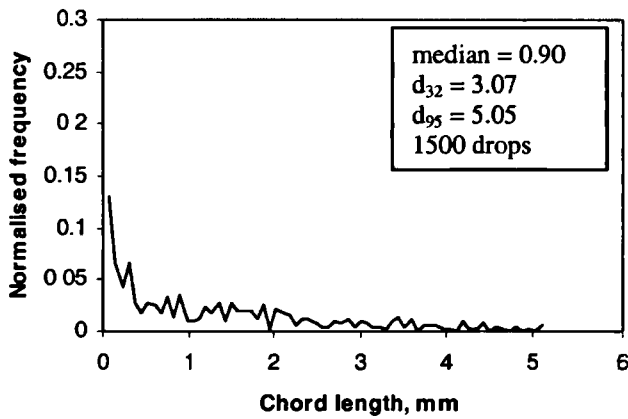
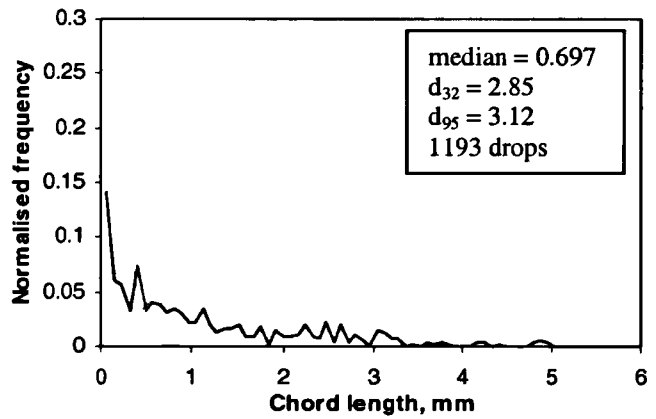
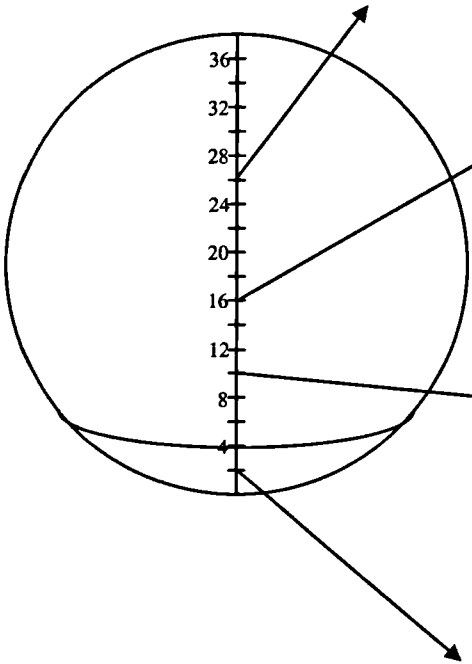
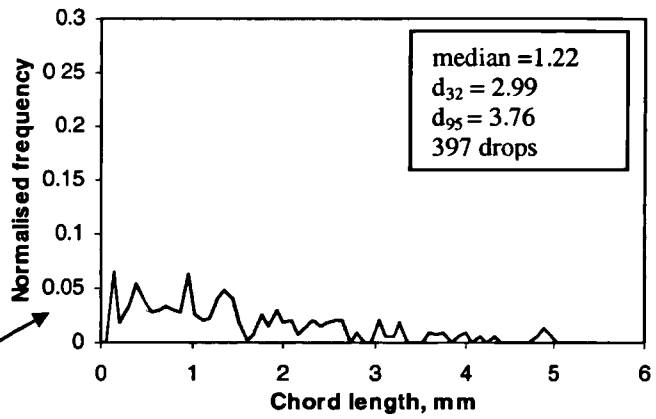
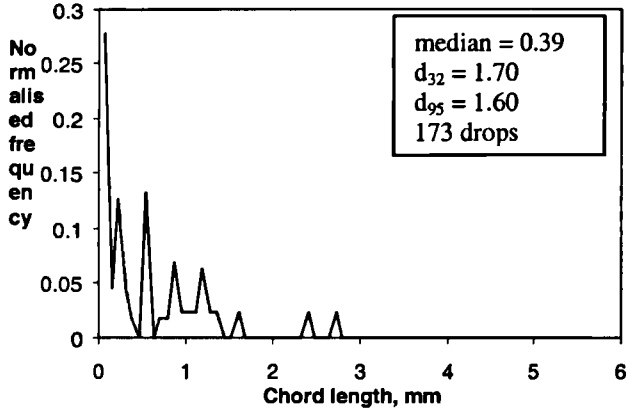


2.5m/s 80% input oil

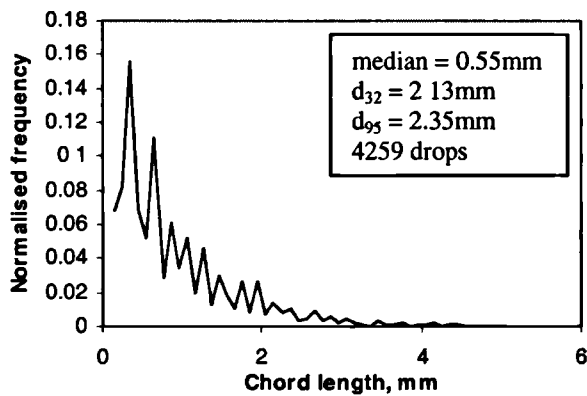
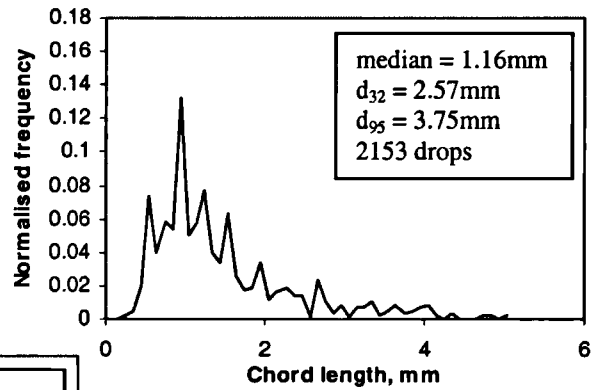
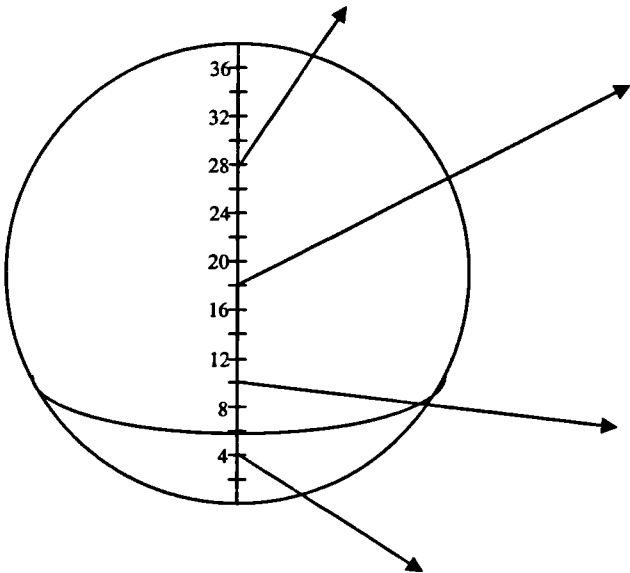
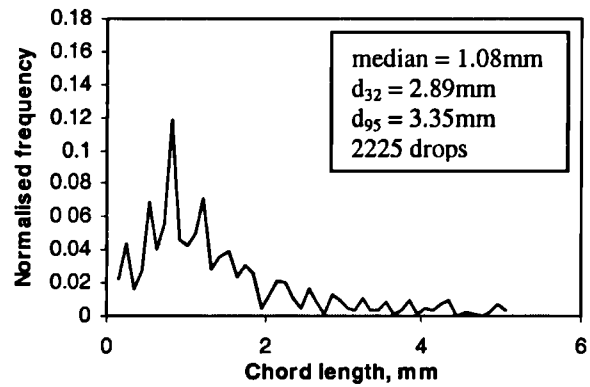
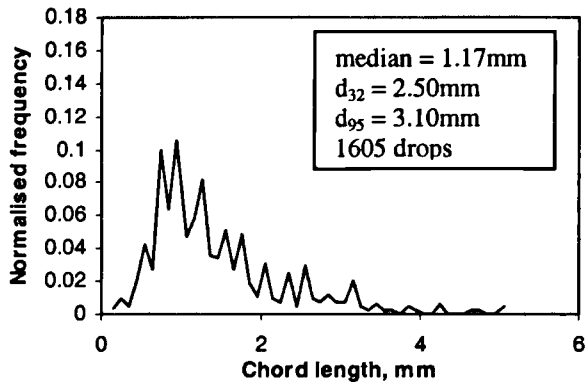


APPENDIX A5

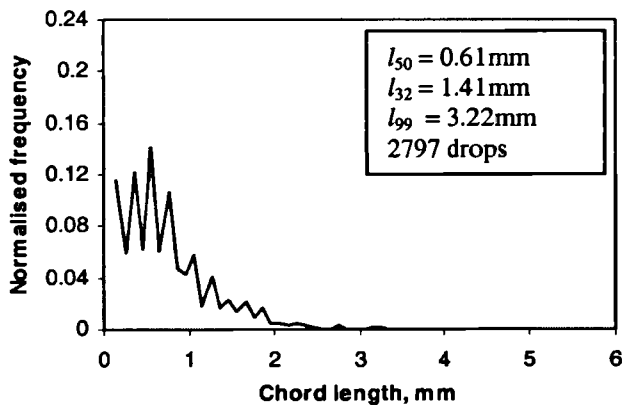
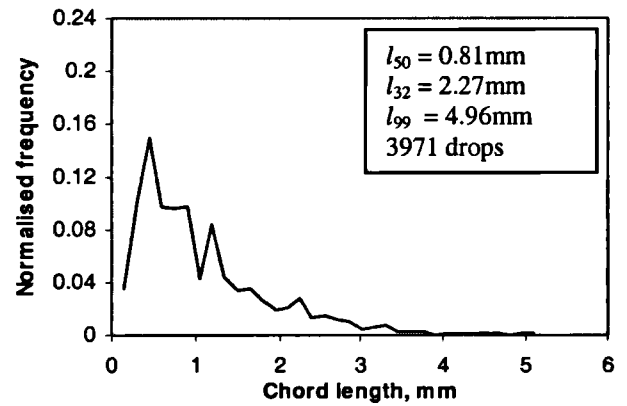
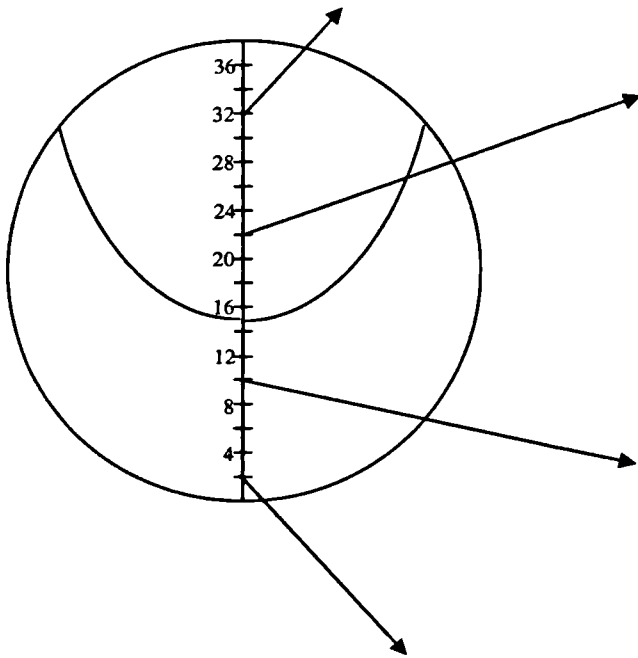
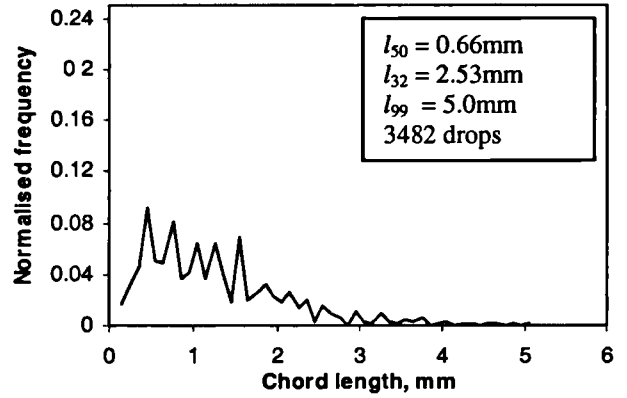
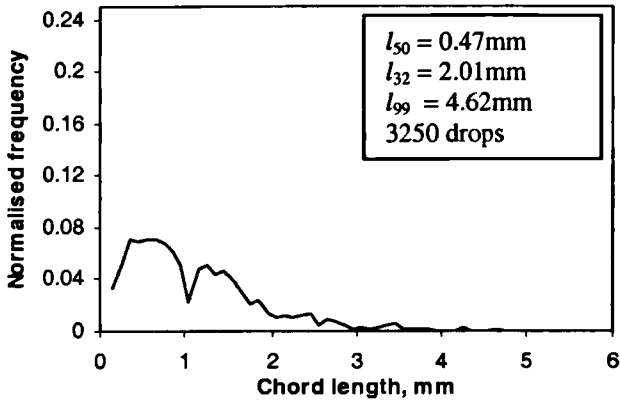
2.5m/s 80% input oil concentration



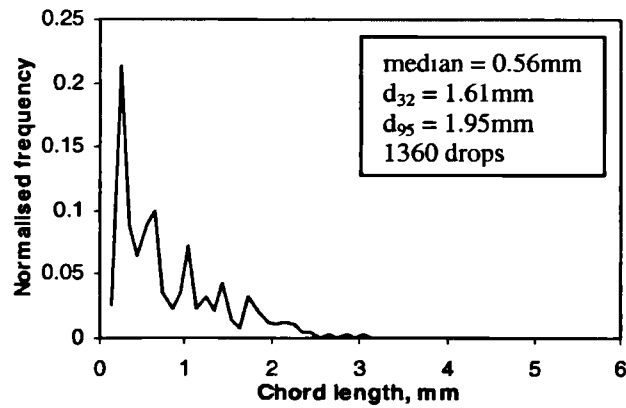
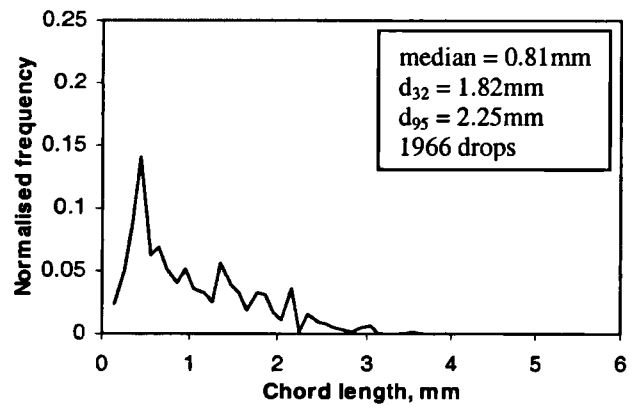
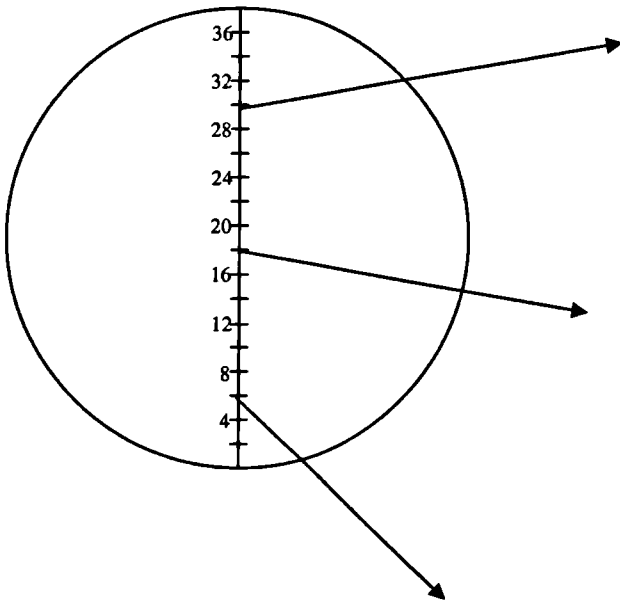
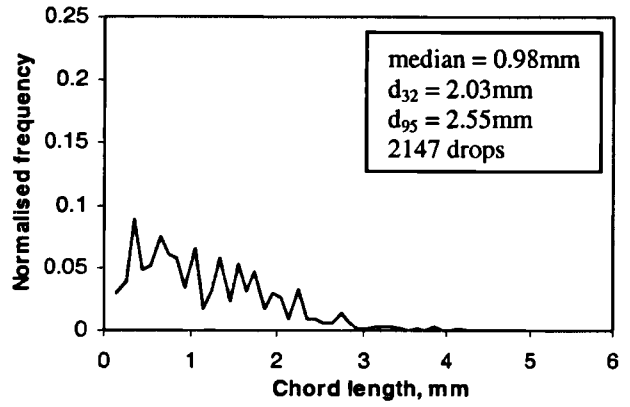
2.5m/s 68% input oil concentration



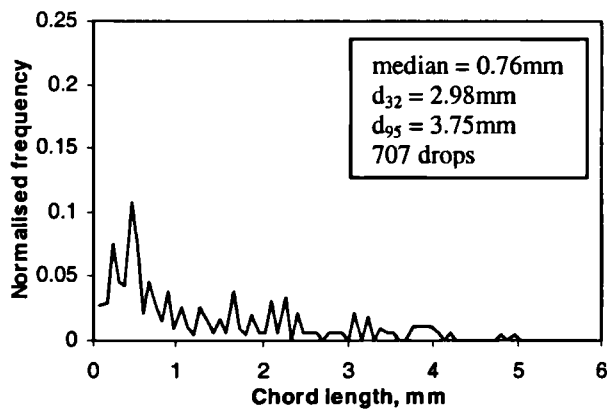
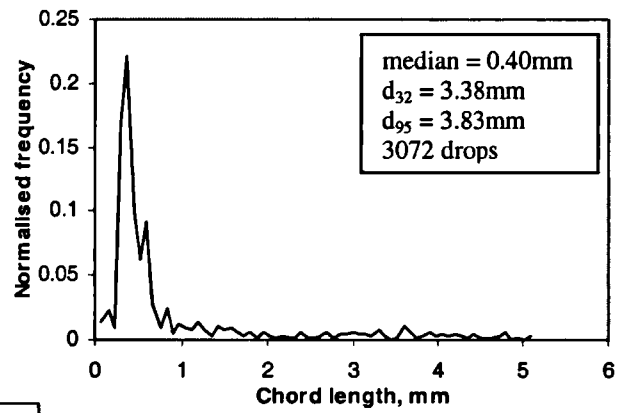
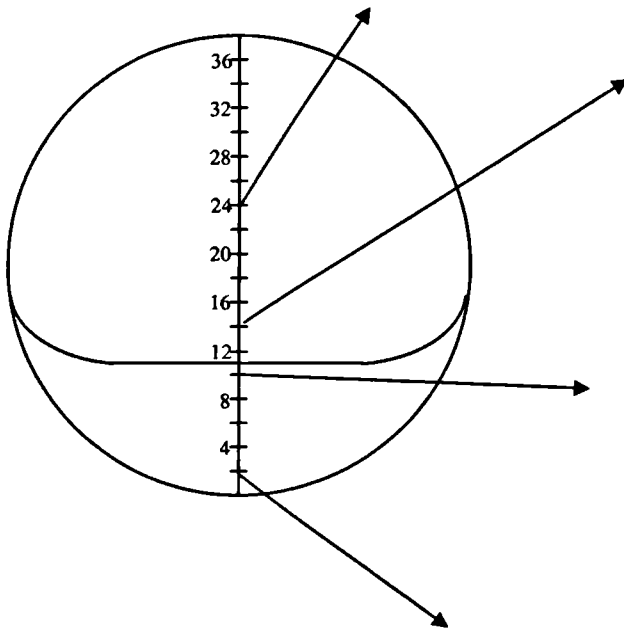
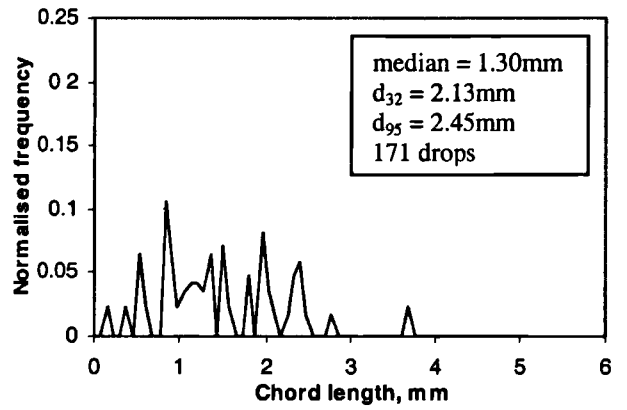
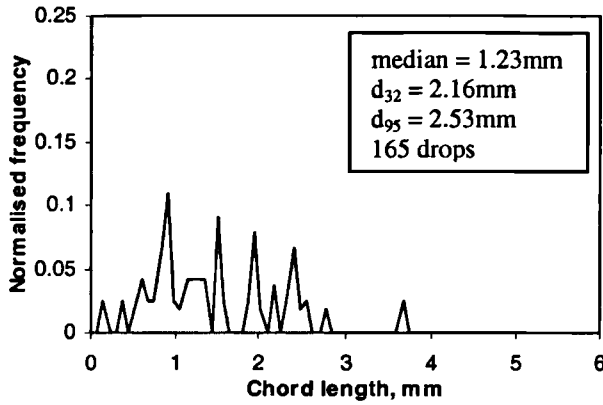
2.5m/s 50% input oil concentration



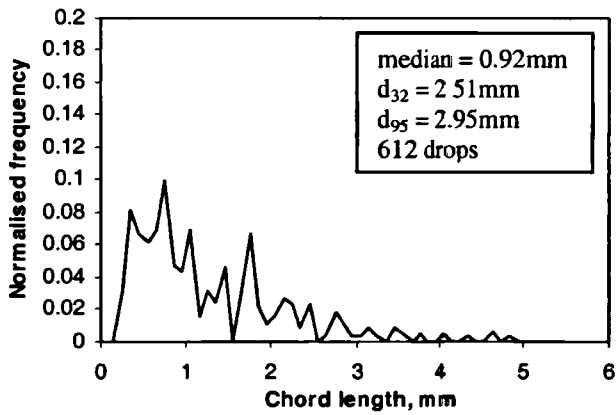
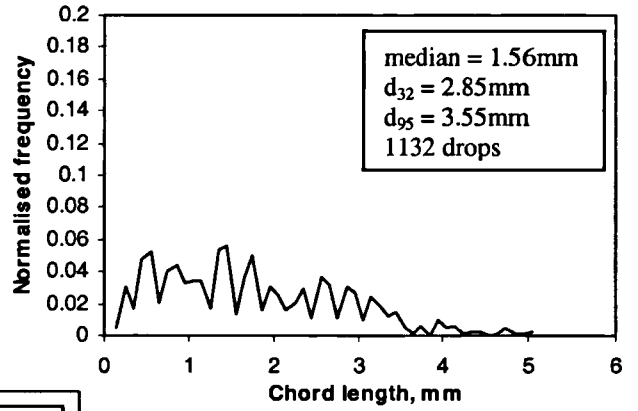
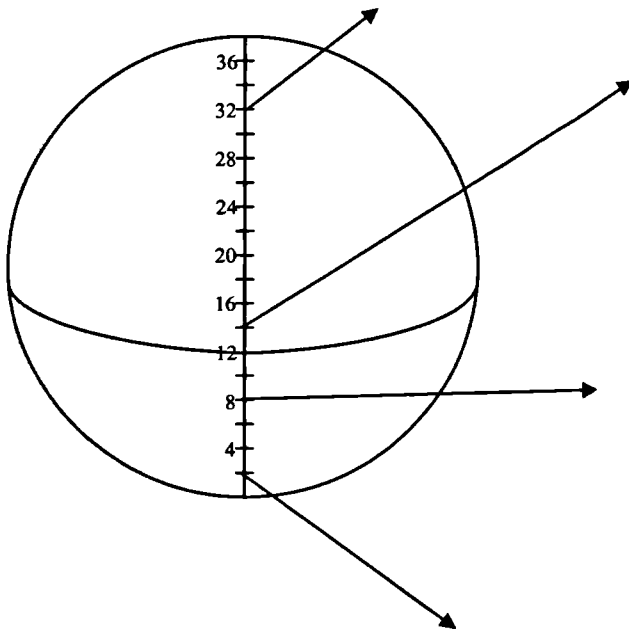
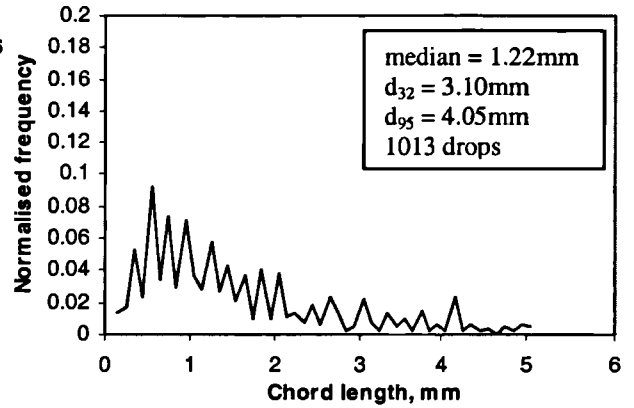
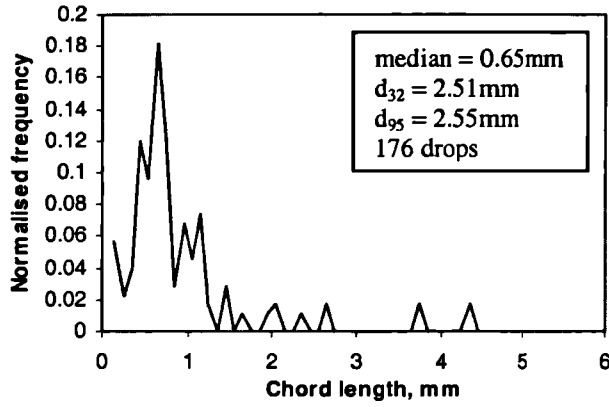
2.5m/s 20% input oil concentration



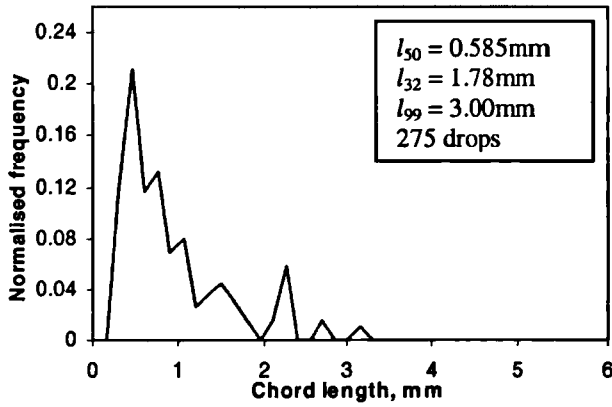
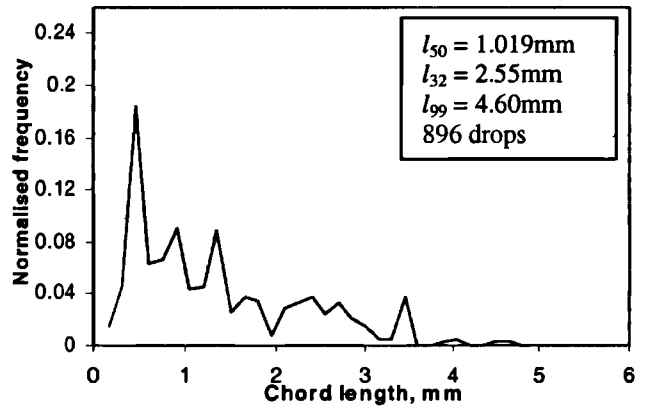
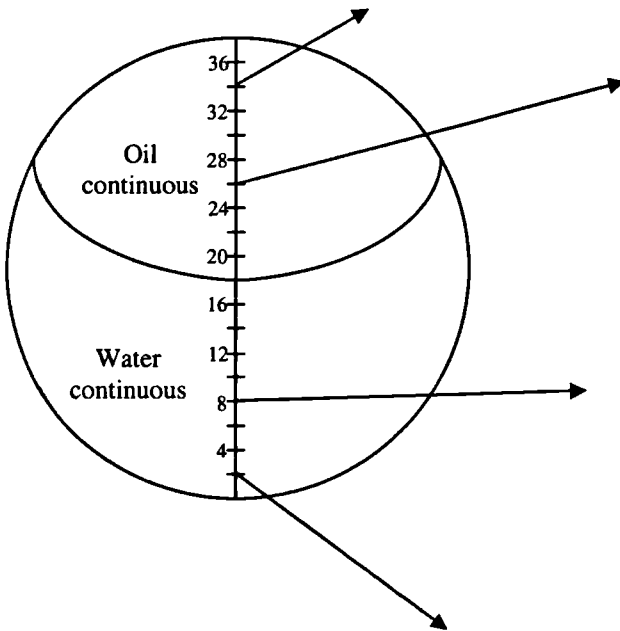
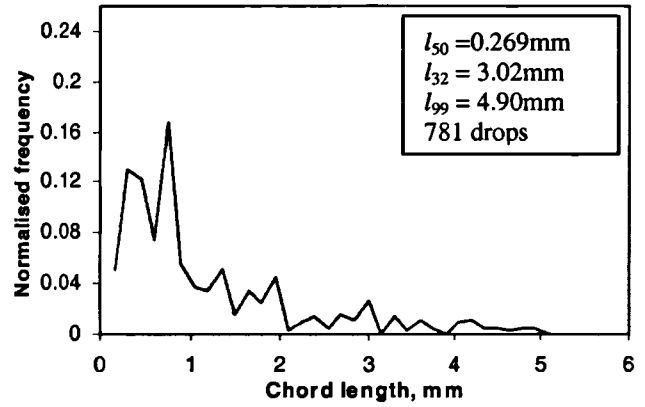
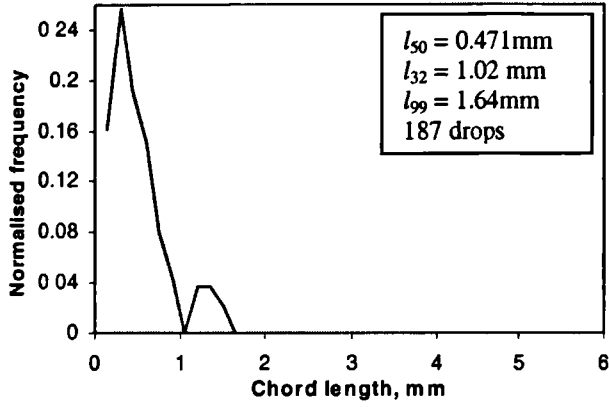
2m/s 80% input oil concentration



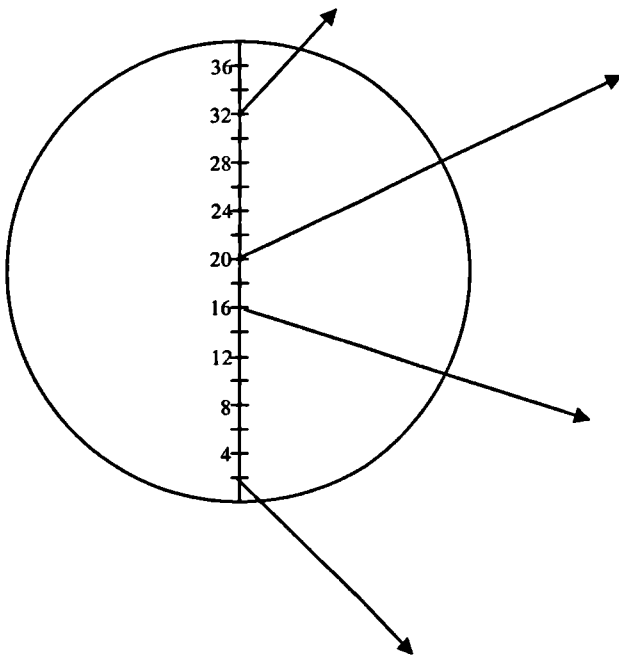
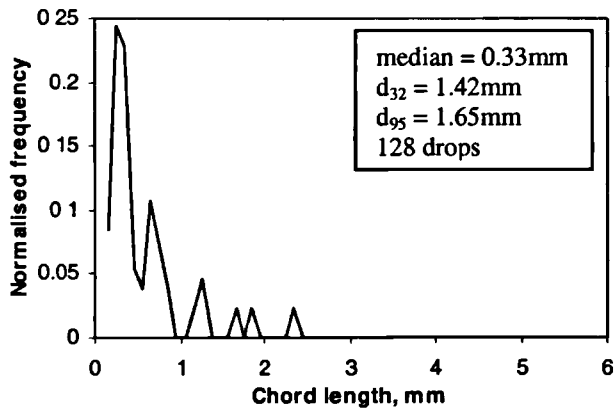
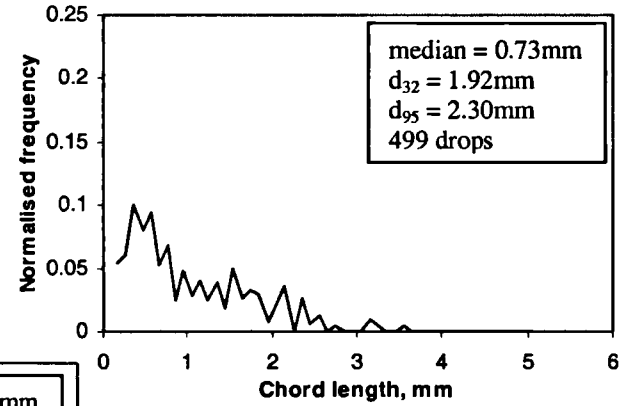
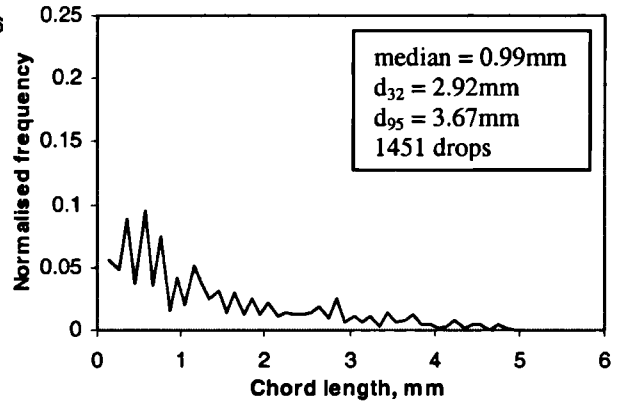
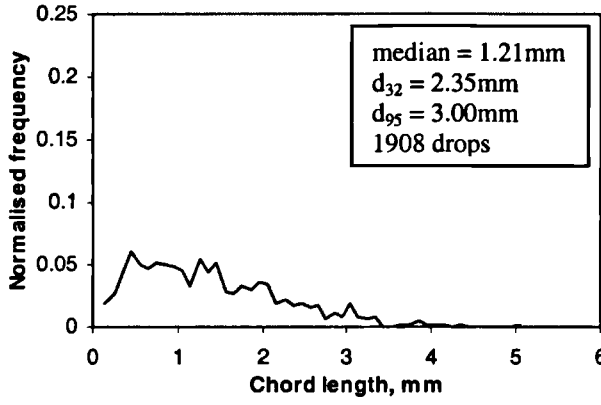
2m/s 68% input oil concentration



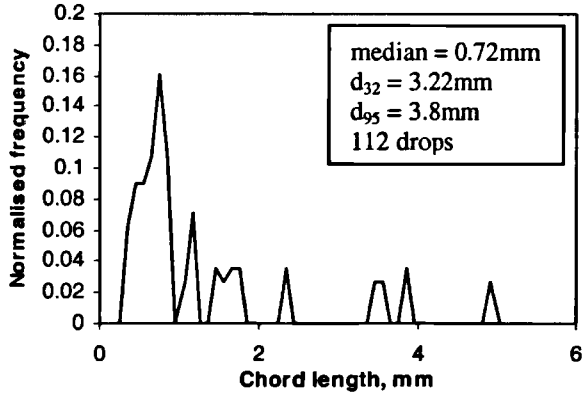
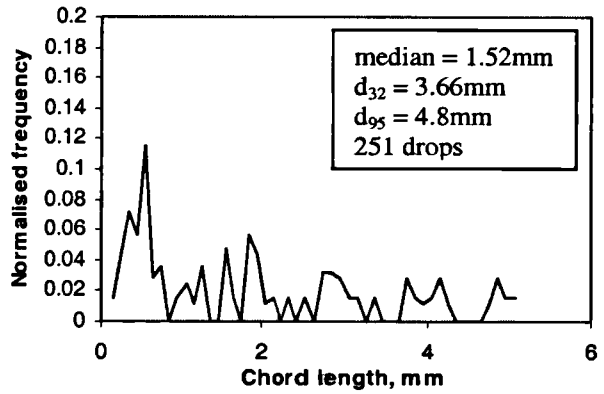
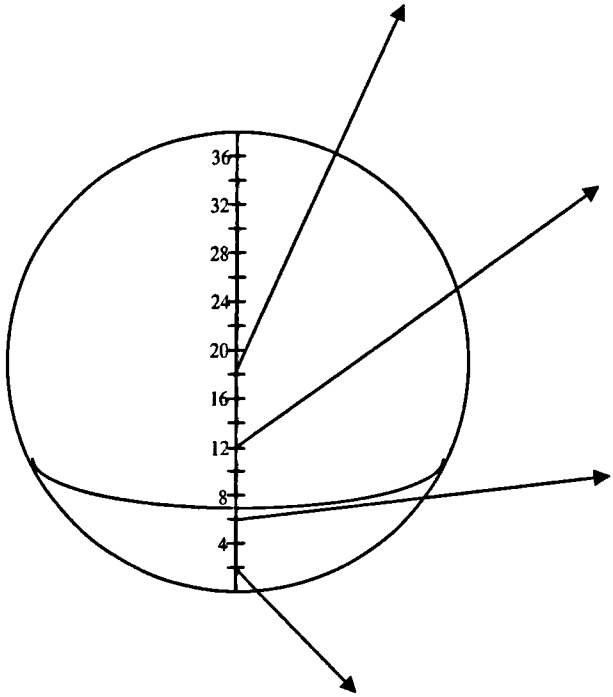
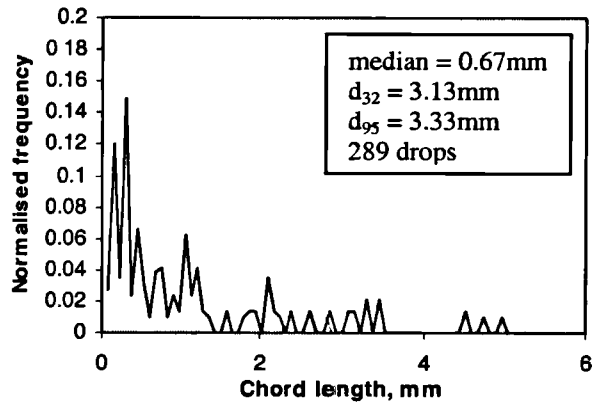
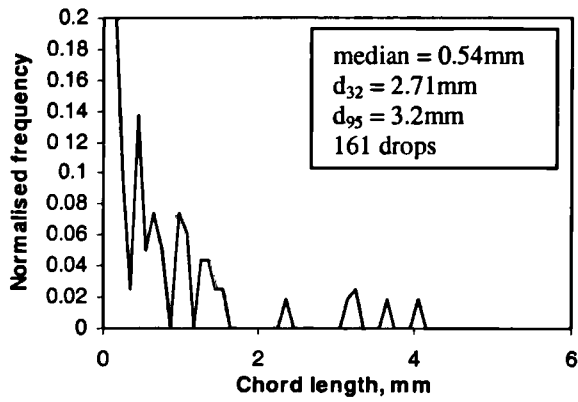
2m/s 50% input oil concentration



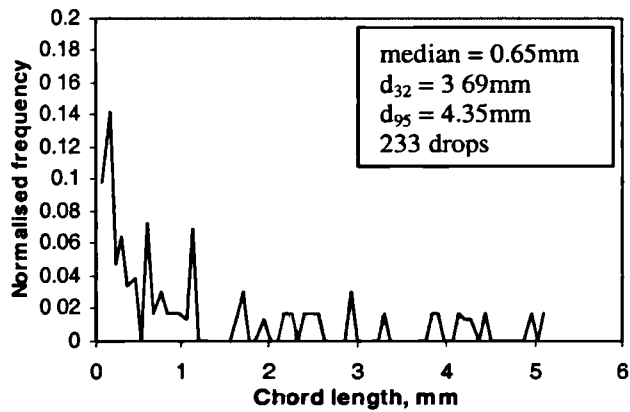
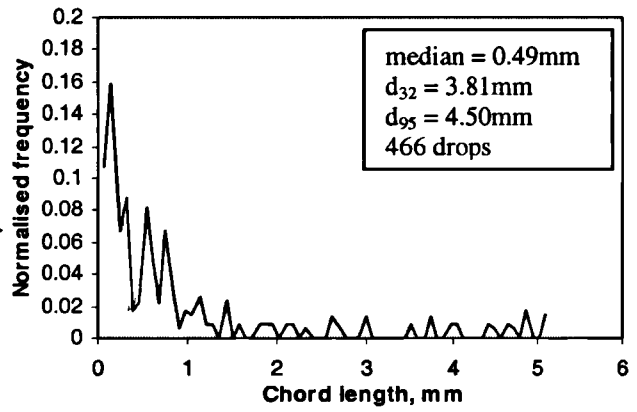
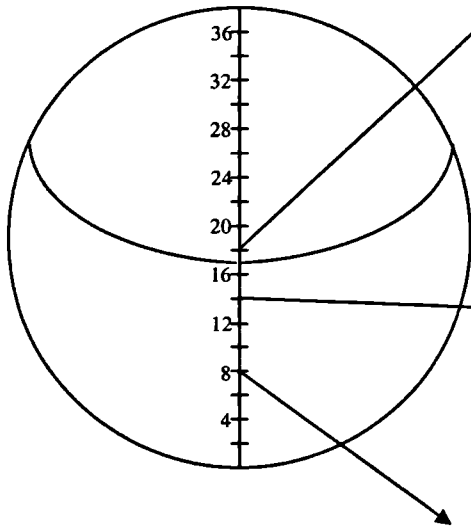
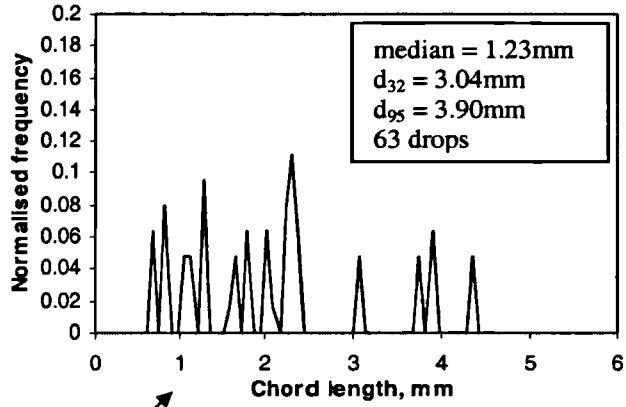
2m/s 20% input oil concentration



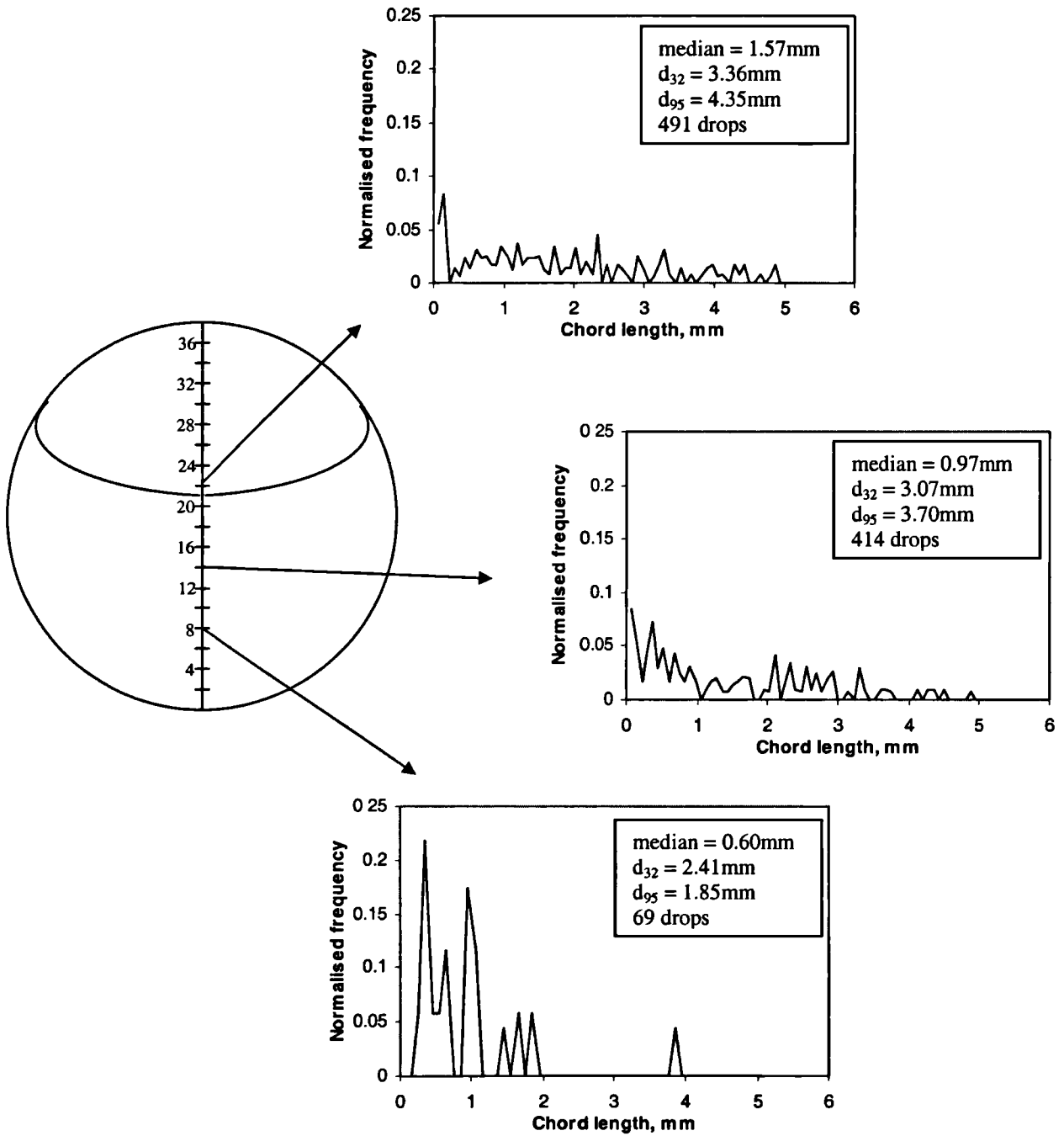
1.5m/s 80% input oil concentration



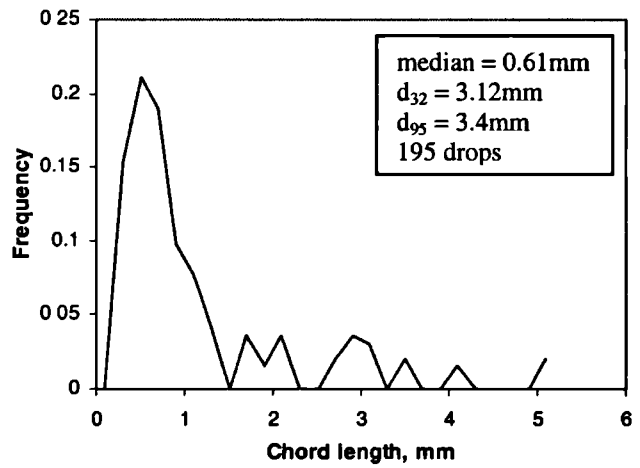
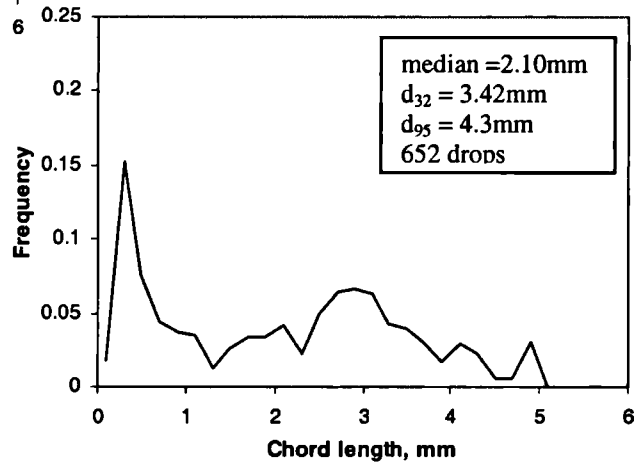
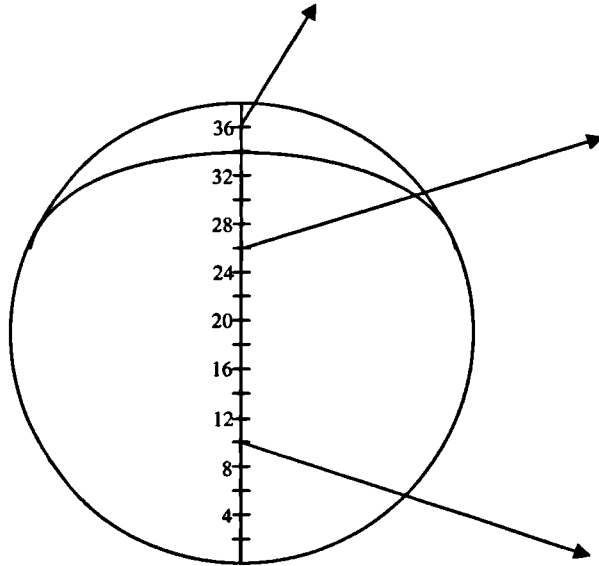
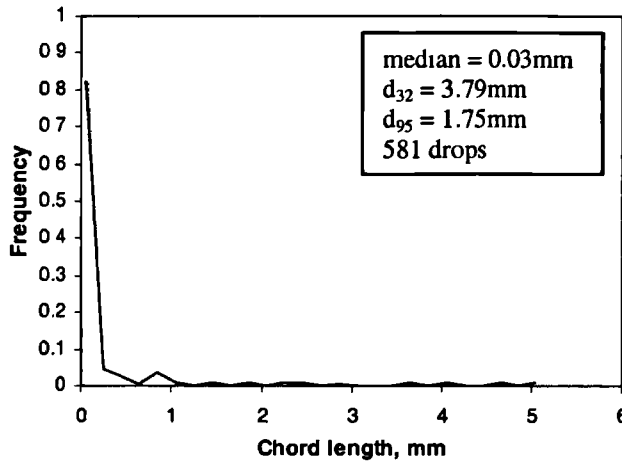
1.5m/s 68% input oil concentration



1.5m/s 50% input oil concentration



1.5m/s 20% input oil concentration



APPENDIX A6

Fortran 90 code to carry out the modified to fluid model as described in Section 6. This model includes interfacial curvature, entrainment, and the interfacial shear stress by Taitel et al. (1995). The model can also be modified to include the interfacial shear stress terms by Neogi et al. (1994) and Roberts (1996).

```
program MOD_2FLUID
implicit none

REAL H, QO, QW, QU, QL, AU, AL, UU, UL, XO, XW, RHOU, &
&RHOL, VISCU, VISCL, SU, SL, SI, XOINC, XOMAX, XOMIN, &
&XWMAX, XWMIN, XWINC, HMAX, HMIN, HINC, TU, TL, TI, &
&DPU, DPL, DP_DIFF, DP, ENTFLOW, ANSWER, THETA, &
&THETA1, THETA2, SOLUTION, HEIGHT, DP_TOT, OILENT, &
&WATENT, DP_OIL, DP_WAT, WATSTAY, OILSTAY, EU, EL, &
&UPFLOW, LOWFLOW, GAMMATERM, UPSTRESS, LOWSTRESS, &
&INTSTRESS, VELU, VELL, DENU, DENL, AREAU, GAMMA, &
&AREAL, PERU, PERI, PERL, VL, VU, FU, FL, SPDV, Y, N, &
&percent, SUP, SINT, SLOW, FRICU, FRICL, FI, FRICI, &
&AUS, AUL, ALS, ASU, CURVETERM, X, EXPFRIC
INTEGER ierror

PRINT*, 'Two Fluid Model with or without curved interface,
and with or without own'
PRINT*, 'experimental friction factor'

PRINT*, 'Use entrainment to calculate the flowrates? 1=Y,
0=N'
READ*, ENTFLOW

PRINT*, 'Use single phase density and viscosity? 1-Y, 0=N'
READ*, SPDV

PRINT*, 'Use curved interface? 0=No, 1= r=0.038, 2=
r=0.019'
READ*, CURVETERM

PRINT*, 'Use experimental wall friction factors? 0=No,
1=Yes'
READ*, EXPFRIC

OPEN(1, FILE='data.txt', STATUS='REPLACE')
```

```

DO
OPEN(2, FILE='drop15.txt', STATUS='OLD', ACTION='READ')

READ(2,*) percent
READ(2,*) QO
READ(2,*) QW
READ(2,*) EU
READ(2,*) EL
READ(2,*) HMIN
READ(2,*) HMAX
READ(2,*) HINC
READ(2,*) FU
READ(2,*) FL

IF (ENTFLOW==1) THEN
XO=- (QO*EU-QO*EL*EU-QW*EL*EU) / (QO*(EL-EU))
QU=(QO*XO)/EU
QL=(QO*(1-XO))/EL
XW=(QL-(QO*(1-XO)))/QW
ELSE IF (ENTFLOW==0) THEN
QU=QO
QL=QW
END IF

IF (SPDV>0) THEN
RHO=828
RHO=1000
VISC=0.006
VISC=0.001
ELSE
RHO=(828*EU)+(1000*(1-EU))
RHO=(828*EL)+(1000*(1-EL))
VISC=((1-(1-EU))**(-2.5))*0.006
VISC=((1-EL)**(-2.5))*0.001
END IF

SOLUTION=10000000
DO H=HMIN, HMAX, HINC

IF (CURVETERM==0) THEN !FLAT INTERFACE!
IF (H<0.019) THEN
THETA=2*ACOS((0.019-H)/0.019)
AL=0.5*(0.019**2)*(THETA-SIN(THETA))
AU=0.001134-AL
UL=QL/AL

```

```

UU=QU/AU
SL=0.019*THETA
SU=0.1194-SL
SI=2*0.019*SIN(THETA/2)
ELSE IF (H>0.019) THEN
THETA=2*ACOS((0.019-(0.038-H))/0.019)
AU=0.5*(0.019**2)*(THETA-SIN(THETA))
AL=0.001134-AU
UL=QL/AL
UU=QU/AU
SU=0.019*THETA
SL=0.1194-SU
SI=2*0.019*SIN(THETA/2)
END IF

ELSE IF (CURVETERM==1) THEN !CURVED INTERFACE WHERE
R=0.038!

IF (H<0.0139) THEN
X=((H**2)+(4*0.019*H))/((2*0.019)+(2*H))
!X is the height where the interface touches the pipe wall!
THETA1=2*ACOS((0.019-X)/0.019)
ALS=0.5*(0.019**2)*(THETA1-SIN(THETA1))
THETA2=2*ACOS((0.038-(X-H))/0.038)
AUS=0.5*(0.038**2)*(THETA2-SIN(THETA2))
AL=ALS-AUS !AL IS AREA OF WATER!
AU=0.001134-AL
UL=QL/AL
UU=QU/AU
SL=0.019*THETA1
SU=0.1194-SL
SI=0.038*THETA2

!If the interface is 'sad' at low oil fractions!
ELSE IF (H>0.027) THEN
X=((4*0.019*H)-(H**2))/((6*0.019)-(2*H))
THETA1=2*ACOS((0.019-(0.038-X))/0.019)
AUS=0.5*(0.019**2)*(THETA1-SIN(THETA1))
THETA2=2*ACOS((0.038-(H-X))/0.038)
ALS=0.5*(0.038**2)*(THETA2-SIN(THETA2))
AU=AUS-ALS
AL=0.001134-AU
UL=QL/AL
UU=QU/AU
SU=0.019*THETA1
SI=0.038*THETA2
SL=0.1194-SU

```

!If X is geater than r, but less than the point where the interface changes shape!

ELSE

```
X=((H**2)+(4*0.019*H))/((2*0.019)+(2*H))
THETA1=2*ACOS((0.019-(0.038-X))/0.019)
ALS=0.001134-(0.5*(0.019**2)*(THETA1-SIN(THETA1)))
THETA2=2*ACOS((0.038-(X-H))/0.038)
AUS=0.5*(0.038**2)*(THETA2-SIN(THETA2))
AL=ALS-AUS
AU=0.001134-AL
UL=QL/AL
UU=QU/AU
SU=0.019*THETA1
SL=0.1194-SU
SI=0.038*THETA2
END IF
```

ELSE IF (CURVETERM==2) THEN !CURVED INTERFACE WHERE
R=0.019!

IF (H>0.027) THEN

X=H/2

THETA=2*ACOS((0.019-(H-X))/0.019)

AUS=0.001134-(0.5*(0.019**2)*(THETA-SIN(THETA)))

ALS=0.5*(0.019**2)*(THETA-SIN(THETA))

AU=AUS-ALS

AL=0.001134-AU

UL=QL/AL

UU=QU/AU

SU=0.019*THETA

SI=SU

SL=0.1194-SU

!When the interface is happy at high oil fractions!

ELSE

X=((2*0.019*H)+(H**2))/(2*H)

THETA=2*ACOS((0.019-(0.038-X))/0.019)

ALS=0.001134-(0.5*(0.019**2)*(THETA-SIN(THETA)))

AUS=0.5*(0.019**2)*(THETA-SIN(THETA))

AL=ALS-AUS

AU=0.001134-AL

UL=QL/AL

UU=QU/AU

SU=0.019*THETA

SL=0.1194-SU

SI=SU

```

END IF

END IF

IF (UU/UL>1.05) THEN
IF (EXPFRIC==0) THEN

FU=0.046*(((4*AU)/(SU+SI))*UU*RHO)/VISC**(-0.2)

FL=0.046*(((4*AL)/SL)*UL*RHO)/VISCL**(-0.2)
TU=FU*(RHO*(UU**2))/2)
TL=FL*(RHO*(UL**2))/2)
ELSE IF (EXPFRIC==1) THEN
TU=FU*(RHO*(UU**2))/2)
TL=FL*(RHO*(UL**2))/2)
END IF

IF (FU>0.014) THEN
TI=FU*(RHO*((UU-UL)**2))/2)
ELSE
TI=0.014*(RHO*((UU-UL)**2))/2)
END IF

DPU=(-TU*(SU/AU))-(TI*(SI/AU))
DPL=(-TL*(SL/AL))+(TI*(SI/AL))

ELSE IF (UU/UL<0.98) THEN
IF (EXPFRIC==0) THEN

FU=0.046*(((4*AU)/SU)*UU*RHO)/VISC**(-0.2)

FL=0.046*(((4*AL)/(SL+SI))*UL*RHO)/VISCL**(-0.2)
TU=FU*(RHO*(UU**2))/2)
TL=FL*(RHO*(UL**2))/2)
ELSE IF (EXPFRIC==1) THEN
TU=FU*(RHO*(UU**2))/2)
TL=FL*(RHO*(UL**2))/2)
END IF

IF (FL>0.014) THEN
TI=FL*(RHO*((UL-UU)**2))/2)
ELSE
TI=0.014*(RHO*((UL-UU)**2))/2)
END IF

DPU=(-TU*(SU AU))+(TI*(SI/AU))

```

```

DPL=(-TL*(SL/AL))-(TI*(SI/AL))

ELSE
IF (EXPFRIC==0) THEN

FU=0.046*(((4*AU)/SU)*UU*RHO)/VISCU)**(-0.2))

FL=0.046*(((4*AL)/SL)*UL*RHO)/VISCL)**(-0.2))
TU=FU*(RHO*(UU**2))/2)
TL=FL*(RHO*(UL**2))/2)
ELSE IF (EXPFRIC==1) THEN
TU=FU*(RHO*(UU**2))/2)
TL=FL*(RHO*(UL**2))/2)
END IF

DPU=-TU*(SU/AU)
DPL=-TL*(SL/AL)

END IF

DP_DIFF=DPL-DPU

IF (DP_DIFF<1) THEN
DP_DIFF=DP_DIFF*(-1)
END IF

IF (DP_DIFF<SOLUTION) THEN
SOLUTION = DP_DIFF
HEIGHT = H
DP_TOT=DPU+DPL
DP=DP_TOT/2
DP_WAT=DPL
DP_OIL=DPU
UPFLOW=QU
LOWFLOW=QL
OILSTAY=XO
WATSTAY=XW
UPSTRESS=TU; LOWSTRESS=TL; INTSTRESS=TI
VELU=UU; VELL=UL; DENU=RHO; DENL=RHO
AREAU=AU; AREAL=AL; PERU=SU; PERI=SI; PERL=SL
VU=VISCU; VL=VISCL; SL=SLOW; SU=SUP; SI=SINT;
FRICU=FU; FRICL=FL; FRICI=FI
END IF

END DO

```

```
WRITE(1, '(13F12.6)') percent, HEIGHT, DP, QU, QL, AREAU,  
AREAL
```

```
END DO
```

```
CLOSE (1)
```

```
CLOSE (2)
```

```
end program MOD_2FLUID
```